LBL-16119

Lawrence Berkeley Laboratory
UNIVERSITY OF CALIFORNIA

Materials & Chemical
Sciences Division

Heteronuclear Dipolar Couplings, Total Spin Coherence, and Bilinear Rotations in NMR Spectroscopy

J.R. Garbow
(Ph.D. Thesis)

July 1983

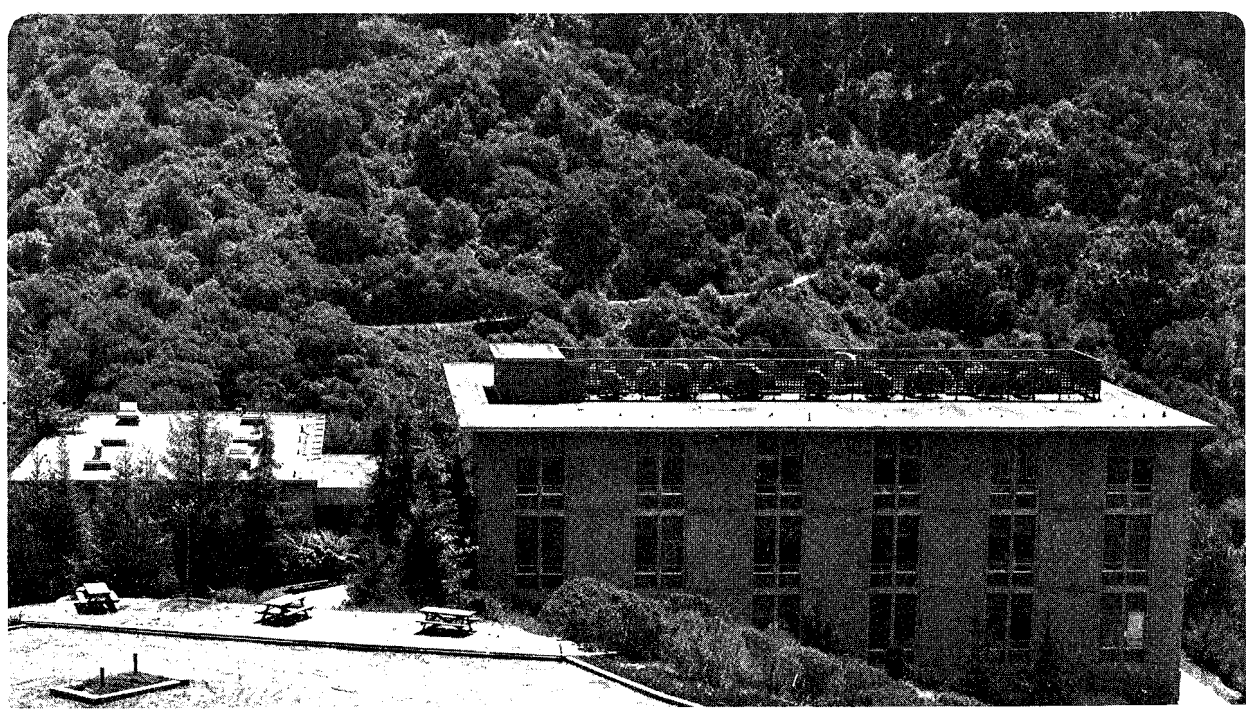

Prepared for the U.S. Department of Energy under Contract DE-AC03-76SF00098

LBL-16119

HETERONUCLEAR DIPOLAR COUPLINGS, TOTAL SPIN COHERENCE, AND BILINEAR ROTATIONS IN NMR SPECTROSCOPY

Joel Richard Garbow

Ph.D. Thesis

July 1983

Materials and Molecular Research Division

Lawrence Berkeley Laboratory

University of California

Berkeley, CA 94720

This work was supported by the Director, Office of Energy Research, Office of Basic Energy Sciences, Materials Sciences Division of the U. S. Department of Energy under Contract Number DE-AC03-76SF00098.

HETERONUCLEAR DIPOLAR COUPLINGS, TOTAL SPIN COHERENCE, AND BILINEAR ROTATIONS IN NMR SPECTROSCOPY

Joel Richard Garbow

Abstract

The past few years have produced many important developments in nuclear magnetic resonance (NMR) spectroscopy. Among the most significant of these are advancements in the field of multiple quantum (MQ) NMR. Multiple quantum spectroscopy has proven to be a very valuable technique, both as a source of enhanced resolution and by providing information not available in normal single quantum spectroscopy. This thesis is devoted to the development and experimental demonstration of several new MQ NMR methods.

In Chapter 1 a variety of different introductory topics are presented. The potential complexity of the NMR spectra of molecules dissolved in liquid crystal solvents serves to motivate the development of multiple quantum spectroscopy. The basics of MQ NMR are reviewed in Chapter 2. An experimental search procedure for the optimization of MQ pulse sequences is introduced.

Chapter 3 discusses the application of MQ NMR techniques to the measurement of dipolar couplings in heteronuclear spin systems. The advantages of MQ methods in such systems are developed and experimental results for partially oriented [1-^{13}C] benzene are presented. Several pulse sequences are introduced which employ a two-step excitation of heteronuclear MQ coherence. A new multiple pulse method, involving the simultaneous irradiation of both rare and abundant spin species, is described.

The problem of the broadening of MQ transitions due to magnetic field inhomogeneity is considered in Chapter 4. The method of total spin coherence transfer echo spectroscopy (TSCTES) is presented, with experiments on partially oriented acetaldehyde serving to demonstrate this new technique. TSCTES results in MQ spectra which are sensitive to all chemical shifts and spin-spin couplings and which are free of inhomogeneous broadening.

In Chapter 5 the spectroscopy of spin systems of several protons and a ^{13}C nucleus in the isotropic phase is discussed. The usefulness of the heteronuclear bilinear rotation as a calculational tool is illustrated. Compensated bilinear π rotations, which are relatively insensitive to timing parameter missets, are presented. A new technique for homonuclear proton decoupling, Bilinear Rotation Decoupling, is described and its success is weakly coupled systems is demonstrated.

ACKNOWLEDGEMENTS

During my graduate years at Berkeley I have had the great pleasure of working in the laboratory of Professor Alex Pines. His seemingly boundless energy, scientific creativity, and constant reminders to "have fun" have done much to further my scientific development and I thank him for his support.

Professor Shimon Vega of the Weizmann Institute has been the source of many interesting ideas and I have benefited greatly from many insightful conversations with him. I would like to thank him for his support during the time that I spent working in his laboratory in Israel. I would also like to thank Professor Mel Klein and his research group at the Melvin Calvin Laboratory, Professor Kurt Zilm of Yale University, and Professor Jeffrey Reimer for many helpful discussions.

I have been privileged to work with many outstanding graduate students in the Pines research group. Among these, special thanks are due to Dan Weitekamp, Steve Sinton, Jim Murdoch, and Gary Drobny. Their willingness to give freely of their time and energy has contributed greatly to the work in this thesis and I will always be grateful to them for their help and friendship. I am also thankful for the assistance and friendship of former students Dick Eckman, Larry Sterna, Jau Tang, Yu-Sze Yen, and Warren Warren and current Pines group members David Zax, Rob Tycko, Jean Baum, John Millar, Tony Bielecki, Herman Cho, Miriam Gochin, Baek Oh, Erika Schneider, and Ann Thayer.

Graduate students at Berkeley are fortunate to have the support of outstanding electronics, machine, and glass shops. Don Wilkinson and his colleagues in the electronics shop have been especially helpful to me. The assistance of Sid Wolfe and Herbert Zimmermann in the synthesis

and preparation of the samples studied in this work is much appreciated. The administrative and secretarial skills of Dione Carmichael are gratefully acknowledged. Cordelle Yoder's outstanding typing and Nancy Monroe's drafting skills are reflected throughout the pages of this thesis.

Last, but by no means least, I express appreciation to my family for having stood behind me through my years in graduate school. The love and support of my parents and my beloved wife, Debbie, have been a constant source of inspiration to me and this work could not have been completed without them.

TABLE OF CONTENTS

TABLE OF CONTENTS (continued)

TABLE OF CONTENTS (continued)

TABLE OF CONTENTS (continued)

TABLE OF CONTENTS (continued)

TABLE OF CONTENTS (continued)

TABLE OF CONTENTS (continued)

Chapter 1: INTRODUCTION

Since its discovery nearly forty years ago[1,2], nuclear magnetic resonance (NMR) spectroscopy has had a tremendous impact on the fields of chemistry and physics. As a probe of local nuclear environment, NMR has provided a wealth of information about molecular structure and motion. In addition, it has become a standard analytical technique useful for compound identification. Numerous texts have chronicled the development of NMR spectroscopy[3-6]. In this work we focus on a comparatively new branch of NMR spectroscopy - time domain multiple quantum (MQ) NMR. This first chapter presents several topics which serve as important background for the methods to be described in subsequent chapters.

Most of the work in this thesis is described in a density matrix formalism[7;4] and Section 1.1 introduces the statistical mechanical density operator. Its general properties and equation of motion are examined and the equilibrium density operator for a group of nuclear spins in high magnetic field is derived. Section 1.2 discusses the various terms in the spin Hamiltonian, describing the interactions of the nuclear spins with each other, with surrounding electrons, and with externally applied magnetic fields. In Section 1.3 the major features of the spectra of isotropic liquids and of molecules dissolved in liquid crystal solvents are described. Dipolar couplings, which generally dominate the spectra of partially oriented systems, are examined as a source of both structural information and spectral complexity.

Section 1.4 examines the energy level diagram for a system of coupled spins and develops an expression for the number of transitions as a function of multiple quantum order. In Section 1.5 the selection rules of

conventional NMR spectroscopy are reviewed and the resolution of single and multiple quantum spectra are compared. Section 1.6 presents a short discussion of the effects of molecular symmetry on NMR spectra. The chapter closes with an introduction to irreducible tensor operators, whose simple transformational properties under rotations are described (Sec. 1.7).

1.1 The Density Operator

1.1.1 Definition

In quantum mechanics, one seeks to find wavefunction solutions to the Schrödinger equation. A complete determination of these wavefunctions provides a complete knowledge of the quantum mechanical system. Each wavefunction represents a probability amplitude and, for an ensemble of systems each described by $|\psi(t)>$, the expectation value of any observable operator $\vec{O}$ as a function of time is given by

$$<\vec{O}(t)> = <\psi(t)|\vec{O}|\psi(t)>. \tag{1.1}$$

For an ensemble of systems described by different wavefunctions $|\psi_k(t)>$, having respective probabilities P_k, the expectation value of $\vec{O}(t)$ becomes

$$<\vec{O}(t)> = \sum_k P_k <\psi_k(t)|\vec{O}|\psi_k(t)>. \tag{1.2}$$

We can expand each wavefunction $|\psi_k(t)>$ in a complete orthonormal basis set:

$$|\psi_k(t)> = \sum_n C_n^k(t)|n> \tag{1.3a}$$

$$<\psi_k(t)| = \sum_m <m|C_m^k(t)^*, \tag{1.3b}$$

where the expansion coefficients $C_n^k(t)$ and $C_m^k(t)^*$ carry all of the time dependence of the system. Recognizing that

$$C_n^k(t) = \langle n|\psi_k(t)\rangle \tag{1.4}$$

allows us to rewrite Equation 1.2 as

$$\langle\vec{O}(t)\rangle = \sum_k P_k \Big(\sum_{m,n} \langle n|\psi_k(t)\rangle\langle\psi_k(t)|m\rangle\langle m|\vec{O}|n\rangle \Big). \tag{1.5}$$

Defining the operator $\vec{\rho}(t)$ as

$$\vec{\rho}(t) \equiv \sum_k P_k |\psi_k(t)\rangle\langle\psi_k(t)|, \tag{1.6}$$

the expression for $\langle\vec{O}(t)\rangle$ simplifies to

$$\langle\vec{O}(t)\rangle = \sum_{m,n} \langle n|\vec{\rho}(t)|m\rangle\langle m|\vec{O}|n\rangle = \mathrm{Tr}(\vec{\rho}(t)\vec{O}). \tag{1.7}$$

$\vec{\rho}(t)$ is known as the density operator and its matrix representation as the density matrix. The density operator is very important in statistical mechanics and is discussed in detail in many texts[8]. We see from Equation 1.7 that all observables of a system may be computed once $\vec{\rho}(t)$ is known.

1.1.2 Equation of Motion

The equation of motion of the density operator can be easily derived by starting from the Schrödinger equation

$$-i\hbar \frac{\partial}{\partial t}|\psi(t)\rangle = \vec{\mathcal{H}}(t)|\psi(t)\rangle. \tag{1.8}$$

The definition of $\vec{\rho}(t)$ in Equation 1.6 can be differentiated to yield

$$\dot{\vec{\rho}}(t) = \sum_k P_k \Big[\Big(\frac{d}{dt}|\psi_k(t)\rangle\langle\psi_k(t)|\Big) + \Big(|\psi_k(t)\rangle \frac{d}{dt} \langle\psi_k(t)|\Big)\Big]. \tag{1.9}$$

Inserting Equation 1.8 into the above expression produces the Von Neumann equation[9]:

$$\dot{\vec{\rho}}(t) = -(i/\hbar)[\vec{\rho}(t), \vec{\mathcal{H}}(t)]. \tag{1.10}$$

When the Hamiltonian $\vec{\mathcal{H}}$ is time independent, this differential equation is easily integrated to

$$\vec{\rho}(t) = \vec{U}(t)\ \vec{\rho}(0)\ \vec{U}^{-1}(t), \tag{1.11}$$

where

$$\vec{U}(t) = \exp(-i\vec{\mathcal{H}}t/\hbar) \tag{1.12}$$

and $\vec{\rho}(0)$ is the initial density operator at time t = 0. Equation 1.11 also provides the formal solution for a time dependent Hamiltonian $\vec{\mathcal{H}}(t)$, with the propagator $\vec{U}(t)$ given by

$$\vec{U}(t) = \exp(-iT \int_0^t \vec{\mathcal{H}}(t')dt'/\hbar), \tag{1.13}$$

where T is the Dyson time-ordering operator[10].

1.1.3 Interaction of Nuclear Spins with a Magnetic Field

In order to derive the equilibrium density operator for an ensemble of nuclear spins, we must first discuss the interaction of these spins with a magnetic field. Classically, the energy of interaction E between a magnet moment $\underset{\sim}{\mu}$ and magnetic field $\underset{\sim}{H}_0$ is

$$E = -\underset{\sim}{\mu} \cdot \underset{\sim}{H}_0. \tag{1.14}$$

We associate with the nuclear spin operator $\vec{I}$ the magnetic moment operator

$$\vec{\mu} = \gamma_I \hbar \vec{I}, \tag{1.15}$$

where γ_I is the nuclear gyromagnetic ratio. The Hamiltonian for the nuclear spin-magnetic field interaction becomes

$$\vec{\mathcal{H}} = -\gamma_I \hbar \vec{I} \cdot \underset{\sim}{H}_o. \tag{1.16}$$

The total angular momentum of a nuclear spin I is $\hbar[I(I+1)]^{\frac{1}{2}}$, the square root of the eigenvalue of $\vec{I}^2$. In addition, we may simultaneously specify the eigenvalue of one of the components of $\vec{I}$, taken by convention to be $\vec{I}_z$, since

$$[\vec{I}^2, \vec{I}_z] = 0. \tag{1.17}$$

For an I spin the eigenvalue of $\vec{I}_z$, known as the Zeeman quantum number m, can take on the $(2I+1)$ values $-I, -I+1 \ldots I-1, I$. With the static field in the z-direction, the energy of interaction between the spin and the field is, from Equation 1.14:

$$E_m = -m\hbar\omega_o^I, \tag{1.18}$$

where $\omega_o^I = \gamma_I H_o$, the I spin Larmor frequency.

Consider a spin system consisting of N spin-I nuclei (all of the same spin species). Each energy level of this system can be classified with respect to its total Zeeman quantum number m^I. This quantum number, the eigenvalue of the operator $\vec{I}_z = \sum_{i=1}^{N} \vec{I}_{zi}$, equals the sum of the individual spin Zeeman quantum numbers ($m^I = \sum_i m_i$). The energy of interaction of this spin system with the magnetic field is

$$E_{m^I} = -m^I \hbar\omega_o^I . \tag{1.19}$$

The experiments to be described in this thesis were all done in an external magnetic field of 42.7 kGauss, corresponding to a proton

resonance frequency ($\gamma_I H_o/2\pi$) of 182 MHz. For all spin-½ nuclei and many nuclei having spin $I \geq 1$, the interaction with the static field is by far the largest which the spins experience and is the only one which need be considered in determining the equilibrium density matrix.

1.1.4 Equilibrium Density Operator

We now calculate the equilibrium density operator for a spin system of N spin-I nuclei (or an ensemble of such systems). The equilibrium density matrix is diagonal, with each diagonal element given by the population of its respective Zeeman level. The relative population of each Zeeman level is given by the Boltzmann factor

$$\exp(-E_{m_I}/kT)/\Sigma_{m_I} \exp(-E_{m_I}/kT). \tag{1.20}$$

The off-diagonal density matrix elements represent coherent superpositions of states (coherences). At equilibrium, they are assumed to be zero under the "hypothesis of random phases". Recall that a representative off-diagonal element is $\overline{C_m^*(t)C_n(t)}$, where the bar represents the average expressed in Equation 1.6. This element can be rewritten as

$$|C_m||C_n|\exp(i(\alpha_n - \alpha_m)t). \tag{1.21}$$

If any of the off-diagonal terms are non-zero, there will be observable properties of the spin system which oscillate with time. Since this is contrary to the definition of thermal equilibrium, all off-diagonal elements must be zero.

The equilibrium density operator may therefore be written

$$\vec{\rho}_{EQ} = \left(\frac{1}{Z}\right) \exp(-\vec{\mathcal{H}}/kT), \tag{1.22}$$

where $Z = Tr(\exp(-\vec{\mathcal{H}}/kT))$. In the high temperature approximation, with $(\gamma_I \hbar H_o/kT) << 1$, this expression may be expanded to

$$\vec{\rho}_{EQ} \simeq \frac{1}{\sim} - (2I+1)^{-N} (\gamma\hbar H_o/kT)\vec{I}_z. \tag{1.23}$$

Only the second term in this expression contributes to an observable NMR signal. We therefore write the reduced equilibrium density matrix as $b_I\vec{I}_z$, with the temperature and magnetic field dependent constant b_I given by $-(2I+1)^{-N}(\gamma\hbar H_o/kT)$, or simply as $\vec{I}_z$. In the remainder of this thesis, explicit labeling of operators with an arrow (→) will be omitted.

1.1.5 Interaction Representation

Before concluding this section on density operators, it is useful to introduce the concept of an interaction representation. Consider the transformation from the laboratory frame of reference to one defined by the transformation operator T. The Hamiltonian in this new reference frame, $\mathcal{H}^*$, can be expressed as

$$\mathcal{H}^* = T\mathcal{H}T^\dagger + iT^\dagger\dot{T}. \tag{1.24}$$

We can transform the density operator in a similar manner:

$$\rho^* = T\rho T^\dagger. \tag{1.25}$$

Using the relationships developed in Sections 1.1.1 and 1.1.2, it can be easily shown that

$$\dot{\rho}^*(t) = -\frac{i}{\hbar}[\rho^*(t), \mathcal{H}^*(t)] \tag{1.26a}$$

and

$$\langle O^*(t)\rangle = Tr(\rho^*(t)O), \tag{1.26b}$$

where $\langle O^*(t) \rangle$ is the expectation value of the operator O viewed in this transformed frame of reference.

For NMR purposes, a particularly useful transformation operator is given by

$$T = \exp(-i\omega I_z t), \tag{1.27}$$

where ω is the carrier frequency of the applied radio frequency radiation, as discussed in Section 1.2.2. This frame of reference is known as the rotating frame and corresponds to observing the spin system from a frame rotating at angular velocity ω about the z-axis. In the rotating frame, the interaction between the nuclear spins and magnetic field becomes

$$\mathcal{H}^* = -(\omega_o^I - \omega) I_z = -\Delta\omega^I I_z, \tag{1.28}$$

where $\Delta\omega^I$ is referred to as the I spin resonance offset. In the remainder of this work all density matrices and Hamiltonians will refer to this rotating frame and the asterisk will be dropped.

1.2 The Spin Hamiltonian

In this section we discuss the various terms in the spin Hamiltonian, which describe the interaction of the nuclear spins with themselves, with surrounding electrons, and with applied magnetic fields. Before doing this, however, we address the question of units. Throughout this thesis the spin Hamiltonian is expressed in rad·sec^{-1}, since these are the convenient units for calculating the evolution of the density matrix. The resonance offset, chemical shifts, and spin-spin couplings measured in NMR experiments are expressed in units of Hz, however. In order to reconcile this discrepancy, the following convention is adopted. Coupling constants which are primed (D'_{ij}, J'_{ij}) are in units of rad·sec^{-1}, while

unprimed coupling constants (D_{ij}, J_{ij}) are in Hz. Similarly, chemical shifts ω_i and resonance offsets $\Delta\omega$ are expressed in rad·sec^{-1}, while $\nu_i = \omega_i/2\pi$ and $\Delta\nu = \Delta\omega/2\pi$ are in Hz.

1.2.1 Zeeman Interaction

As noted in Section 1.1.3, in many systems the interaction with the static external field $\underset{\sim}{H}_o$ is by far the largest which the spins experience. Although of great historical importance, this interaction is largely uninteresting in modern magnetic resonance studies, however, and simply provides a measure of $\omega_o^I = \gamma_I H_o$. In the rotating frame, this interaction is largely removed and the coupling between the spin system and an homogeneous external magnetic field is given by Equation 1.28. An additional term, $-\omega(\underset{\sim}{r})I_z$, must be added to this equation to account for the spatial inhomogeneity of the external field. This term is subject to the constraint

$$\int \omega(\underset{\sim}{r})d\underset{\sim}{r} = 0. \tag{1.29}$$

The Zeeman Hamiltonian $\mathcal{H}_I^{ZEEMAN}$ thus becomes

$$\mathcal{H}_I^{ZEEMAN} = -(\Delta\omega^I + \omega(\underset{\sim}{r}))I_z. \tag{1.30a}$$

A similar expression holds for a second spin species S when it is present:

$$\mathcal{H}_S^{ZEEMAN} = -(\Delta\omega^S + (\gamma_S/\gamma_I)\omega(\underset{\sim}{r}))S_z. \tag{1.30b}$$

In this equation the resonance offset $\Delta\omega^S$ is defined with respect to the frequency of the S spin r.f. field. (When two spin species are present, we transform into a doubly rotating frame defined by the frequencies of the r.f. fields of both species.) Although the Zeeman interaction arises from the coupling of the spins to an external field, it will often prove

convenient to include it in the internal spin Hamiltonian, $\mathcal{H}_{INT}$, as discussed in Section 1.2.3.1.

The other terms in the spin Hamiltonian can be divided into two parts:

$$\mathcal{H} = \mathcal{H}_{rf} + \mathcal{H}_{INT}, \tag{1.31}$$

where $\mathcal{H}_{rf}$ describes the effects of externally applied radio frequency fields, and $\mathcal{H}_{INT}$ those interactions which are internal to the spin system. Contributions to $\mathcal{H}_{INT}$ include those from chemical shifts, direct and indirect spin-spin couplings, and quadrupolar couplings. Each of these different interactions is discussed in Section 1.2.3.

1.2.2 Radio Frequency Fields ($\mathcal{H}_{rf}$)

The nuclear spins can couple to an oscillating radio frequency (r.f.) field applied perpendicular to the static field. This interaction has the form

$$-2\gamma_I H_1 I_y \cos(\omega t + \phi) \tag{1.32}$$

for an r.f. field of frequency ω, amplitude $2H_1$, and phase ϕ. It is at first surprising that the r.f. field should be capable of nutating the spins at all for the usual case $H_1 << H_0$. It is in fact only for a frequency $\omega \sim \omega_o^I$ that the r.f. is effective. In the rotating frame, the r.f. Hamiltonian is

$$\mathcal{H}_{rf} = -\omega_1 I_\phi, \tag{1.33}$$

where

$$I_\phi = I_y \cos\phi - I_x \sin\phi \tag{1.34}$$

and $\omega_1 = \gamma_I H_1$. In Equation 1.32, the counter-rotating component of the radiation, oscillating at frequency 2ω, has been ignored. Analogous expressions hold for the interaction of an S spin with an oscillating r.f. field.

1.2.3 $\mathcal{H}_{INT}$

Each of the terms of $\mathcal{H}_{INT}$ is conveniently written as a second rank tensor coupling between two vectors. Expressed in Cartesian coordinates, the coupling Hamiltonian is

$$\mathcal{H} = \underset{\sim}{X} \cdot \underset{\approx}{A} \cdot \underset{\sim}{Y} = \sum_{i,j}^{x,y,z} X_i A_{ij} Y_j, \tag{1.35}$$

where $\underset{\approx}{A}$ is a 3×3 matrix. Each internal Hamiltonian interaction must be properly summed over all spins in the spin system. Throughout this thesis, the spin system will consist of N coupled protons ($I = \frac{1}{2}$ spins) and perhaps a single ^{13}C nucleus ($S = \frac{1}{2}$ spin).

1.2.3.1 Chemical Shifts

In addition to the applied magnetic field H_o, each nucleus experiences a small local field due to the electrons surrounding it. This shielding effect, the chemical shift, can be written as

$$\mathcal{H}_{CS}^{I} = -\gamma_I \sum_i \underset{\sim}{I}_i \cdot \underset{\approx}{\sigma}_i \cdot \underset{\sim}{H}_o \tag{1.36}$$

In high field, only the secular part of $\mathcal{H}_{CS}$ (the part which commutes with I_z) is retained:

$$\mathcal{H}_{CS}^{I} = -\omega_o^I \sum_i \sigma_{zzi} I_{zi} = -\sum_i \omega_i I_{zi}. \tag{1.37}$$

By convention, we take the sum of the chemical shifts to be zero ($\sum_i \omega_i = 0$). It is convenient to combine the chemical shift Hamiltonian

with $\mathcal{H}_I^{ZEEMAN}$ (Eq. 1.30a):

$$\mathcal{H}_I^Z = -\sum_i \omega_i I_{zi} - (\Delta\omega^I + \omega(\underset{\sim}{r}))I_z. \tag{1.38}$$

Collectively the interactions in this equation will be referred to as the Zeeman terms. An analogous expression holds for the S spin Zeeman term:

$$\mathcal{H}_S^Z = -\omega_S S_z - (\Delta\omega^S + \left(\frac{\gamma_S}{\gamma_I}\right)\omega(\underset{\sim}{r}))S_z. \tag{1.39}$$

1.2.3.2 Dipolar Couplings ($\mathcal{H}^D$)

As described earlier (Eq. 1.15), we associate with each nuclear spin $\underset{\sim}{I}$ a magnetic moment $\underset{\sim}{\mu}$. The direct interaction of these moments with one another is described by the dipolar coupling Hamiltonian $\mathcal{H}^D$:

$$\mathcal{H}_{II}^D = -\sum_{i<j} \underset{\sim}{I}_i \cdot \underset{\approx}{D}'_{ij} \cdot \underset{\sim}{I}_j. \tag{1.40}$$

The dipolar coupling between spins i and j involves products of the components of their respective angular momentum operators, and is therefore termed a bilinear interaction. The subscript on $\mathcal{H}_{II}^D$ emphasizes the bilinear quality of this Hamiltonian. The elements of the coupling matrix $\underset{\approx}{D}'_{ij}$ are

$$D'_{ijab} = \frac{-\gamma_I^2 \hbar}{r_{ij}^3}(3\cos\theta_{ija}\cos\theta_{ijb} - \delta_{ab}), \qquad a,b = x,y,z \tag{1.41}$$

where r_{ij} is the distance between nuclei i and j, θ_{ija} is the angle between the i-j internuclear vector and the laboratory a-axis, and δ_{ab} is the Kronecker delta. Retaining only the secular terms, the homonuclear dipole-dipole interaction becomes

$$\mathcal{H}_{II}^{D} = -\sum_{i<j} D'_{ij}(3I_{zi}I_{zj} - \underset{\sim}{I}_i \cdot \underset{\sim}{I}_j), \tag{1.42}$$

where

$$D'_{ij} = -(\gamma_I^2\hbar/r_{ij}^3)(\tfrac{1}{2})(3\cos^2\theta_{ijzz}-1). \tag{1.43}$$

When two different nuclear species are involved, the spin function part of Equation 1.42 must be modified. This is because flip-flop terms between unlike spins, which do not conserve energy, are forbidden. For heteronuclear spin pairs

$$\mathcal{H}_{IS}^{D} = -\sum_{i} 2D'_{iSzz}I_{zi}S_z, \tag{1.44}$$

where

$$D'_{iS} = -(\gamma_I\gamma_S\hbar/r_{iS}^3)(\tfrac{1}{2})(3\cos^2\theta_{iSzz}-1). \tag{1.45}$$

1.2.3.3 Scalar (J) Couplings ($\mathcal{H}^J$)

In addition to the direct coupling between nuclear magnetic moments, there is also an indirect coupling between spins via the electrons. This interaction is referred to as the scalar or J coupling:

$$\mathcal{H}_{II}^{J} = -\sum \underset{\sim}{I}_i \cdot \underset{\approx}{J}'_{ij} \cdot \underset{\sim}{I}_j. \tag{1.46}$$

As indicated by its subscript, the scalar coupling Hamiltonian, $\mathcal{H}_{II}^{J}$, is also a bilinear interaction. The secular part of this coupling is

$$-\sum_{i<j} [J'_{ijzz}I_{zi}I_{zj} + \tfrac{1}{4}(J'_{ijxx}+J'_{ijyy})(I_{+i}I_{-j}+I_{-i}I_{+j})]. \tag{1.47}$$

By algebraic rearrangement, this expression can be broken into isotropic and anisotropic parts

$$\mathcal{H}^{J}_{II} = -\sum_{i<j} J'_{ij}\underset{\sim}{I}_i \cdot \underset{\sim}{I}_j - (\tfrac{1}{2}) \sum_{i<j} J^{ANISO}_{ij}(3I_{zi}I_{zj} - \underset{\sim}{I}_i \cdot \underset{\sim}{I}_j), \qquad (1.48)$$

where

$$J'_{ij} = \frac{1}{3}\,\mathrm{Tr}(\underset{\approx}{J}'_{ij}), \qquad (1.49a)$$

and

$$J^{ANISO}_{ij} = \frac{2}{3} J'_{ijzz} - \frac{1}{3}(J'_{ijxx} + J'_{ijyy}) \qquad (1.49b)$$

The spin operator part of the anisotropic term has exactly the same form as the dipolar Hamiltonian $\mathcal{H}^{D}_{II}$ (Eq. 1.42). For protons, this term is usually quite small and can be ignored. The high field homonuclear J-coupling becomes

$$\mathcal{H}^{J}_{II} = -\sum_{i<j} J'_{ij}\underset{\sim}{I}_i \cdot \underset{\sim}{I}_j. \qquad (1.50)$$

In describing the scalar coupling between heteronuclear spins, the non-energy conserving flip-flop terms must once again be suppressed. The heteronuclear J-coupling Hamiltonian, $\mathcal{H}^{J}_{IS}$, is

$$\mathcal{H}^{J}_{IS} = -\sum_{i} J'_{iS}I_{zi}S_z \qquad (1.51)$$

with $J'_{iS} = J'_{iSzz}$. Because their spin operator parts are the same, it is convenient to combine the heteronuclear dipolar and J-coupling Hamiltonians into a single term $\mathcal{H}_{IS}$:

$$\mathcal{H}_{IS} = \mathcal{H}^{D}_{IS} + \mathcal{H}^{J}_{IS} = -\sum_{i} 2F'_{iS}I_{zi}S_z, \qquad (1.52)$$

where

$$F'_{iS} = 2\pi F_{iS} = \frac{1}{2}(J'_{iS} + 2D'_{iS}). \qquad (1.53)$$

1.2.3.4 Quadrupolar Coupling

For nuclei having spin $I \geq 1$, there is an additional Hamiltonian term resulting from the interaction between the nuclear quadrupolar moment and electric field gradients arising from surrounding electrons and nuclei. This coupling takes the form

$$\mathcal{H}^{Q}_{II} = \sum_{i} \underset{\sim}{I}_i \cdot \underset{\approx}{V}_i \cdot \underset{\sim}{I}_i . \tag{1.54}$$

In high field, the quadrupolar Hamiltonian becomes

$$\mathcal{H}^{Q}_{II} = \sum_{i} (eQ_i V_{izz}/4I_i(2I_i - 1))(3I^2_{zi} - I_i(I_i + 1)), \tag{1.55}$$

where Q_i is the quadrupolar coupling constant of nucleus i, and V_{izz} the second derivative of the potential with respect to z at the nucleus, $\frac{\partial^2 V}{\partial z^2}$.

1.3 Information Content of NMR Spectra

Having described the different interactions which comprise the spin Hamiltonian, we discuss briefly the information content of NMR spectra. The terms of the internal Hamiltonian of Section 1.2.3 depend on particular laboratory frame components of different second rank tensors. The transformation from a molecule-fixed axis system into the laboratory frame is of utmost importance in determining the sensitivity of an NMR experiment to the different components of the spin Hamiltonian. This transformation in turn depends on the thermodynamic phase of the sample being investigated. We consider the two phases which are of importance in this work: (1) isotropic liquids and (2) liquid crystals. NMR spectroscopy in solids has been discussed in considerable detail elsewhere[6,11-13].

1.3.1 Isotropic Liquids

In liquids, molecules are undergoing rapid isotropic motion. This completely averages away all couplings between molecules. In addition, for each intramolecular spin Hamiltonian term only the isotropic average, given by the trace of the respective second rank tensor, survives this motion. The dipolar and quadrupolar interactions are traceless and therefore average to zero, along with the anisotropic part of the chemical shift. The NMR spectra of isotropic liquids are thus determined by resonance offset, J-couplings, and isotropic chemical shifts.

1.3.2 Liquid Crystals

1.3.2.1 Partial Ordering and Anisotropic Motion

The NMR spectroscopy of liquid crystals and of molecules dissolved in liquid crystals has been the subject of several reviews[14,15] and is discussed in greater detail in Appendix A. Here we make a few general observations which allow the important features of such spectra to be described. When placed in a large magnetic field, liquid crystals become partially oriented, as do most dissolved solute molecules. This ordering is describable by a set of motional constants, or order parameters, and the spin Hamiltonian becomes a function of these constants. As in isotropic liquids, rapid translational diffusion in liquid crystal systems averages out the couplings between molecules. Unlike the liquid case, however, the motion of individual molecules is anisotropic. Due to this anisotropy, the averaging of the dipolar and quadrupolar interaction tensors is incomplete and these terms contribute to the spin Hamiltonian.

1.3.2.2 Dipolar Couplings and Structural Information

In this thesis, we are primarily interested in systems of

coupled spin-½ nuclei (protons and ^{13}C) for which the quadrupolar interaction vanishes and the dipolar couplings are the principal unknowns of interest. As described in Section 1.2.3.2, these spin-spin couplings carry with them direct structural information through the terms r_{ij}^{-3} and θ_{ij}. The proton NMR spectrum of most liquid crystal molecules themselves tend to be very broad, with little observable fine structure. Small molecules dissolved in liquid crystals, however, produce relatively sharp-line spectra, as first reported by Saupe and Englert in 1963[16,17]. Although these generally have a spectral width of several kHz, the width of individual lines may be as little as 1 or 2 Hz. These spectra are usually dominated by intramolecular dipolar couplings amongst the spins.

An illustration of NMR's sensitivity to molecular structure is provided by Figure 1.1, the proton spectrum of benzene dissolved in a liquid crystal. Also shown are spectral simulations based on several different models for the structure of benzene. The isotropic NMR spectrum of each of these models shows the single line characteristic of liquid benzene. Based on these simulations, it is very easy to identify the "correct" structure of benzene.

1.3.2.3 Spectral Complexities

While serving to illustrate the usefulness of studying molecules in liquid crystal solvents, Figure 1.1 also serves to warn us of the potential complexity of such spectra. The spectrum of the highly symmetric 6-spin benzene molecule contains many non-degenerate transitions (one expects, in fact, a total of 38 pairs of lines). For molecules containing a greater number of spins or possessing less overall symmetry, the number of observed transitions rapidly increases. This is illustrated in Figure 1.2, which shows the spectra of a variety of different solute

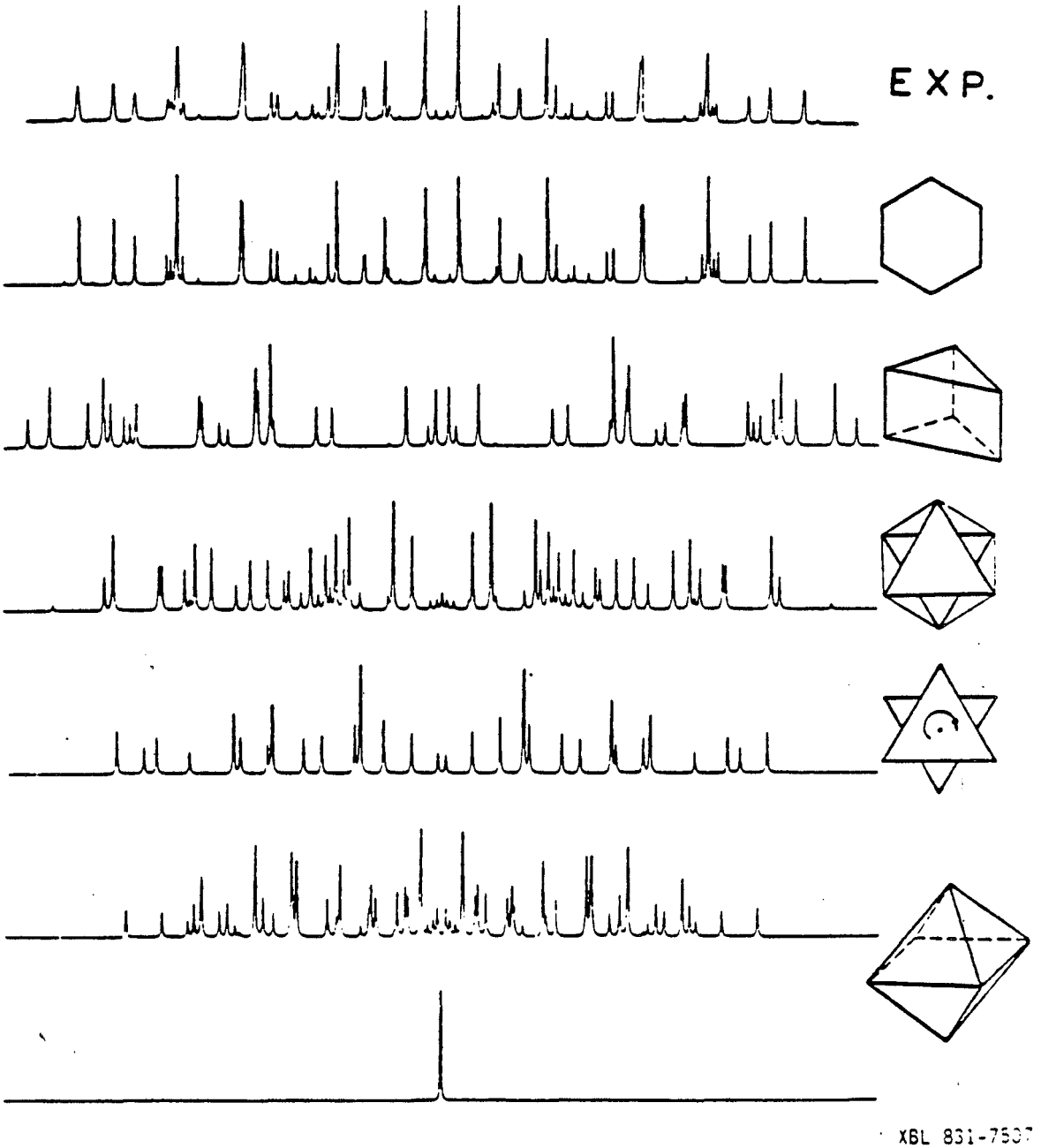

Figure 1.1. Single quantum proton NMR spectra of benzene dissolved in a liquid crystal solvent. An experimental spectrum is shown at the top. Below are several suggested models for the structure of benzene along with a simulated spectrum for each. The isotropic spectrum of each of these proposed structures is consistent with the known single-line spectrum of liquid benzene. The sensitivity of the spectra of molecules dissolved in a liquid crystal to solute geometry can be clearly seen, and the "correct" structure of benzene easily identified.(Figure courtesy of Professor Zeev Luz.)

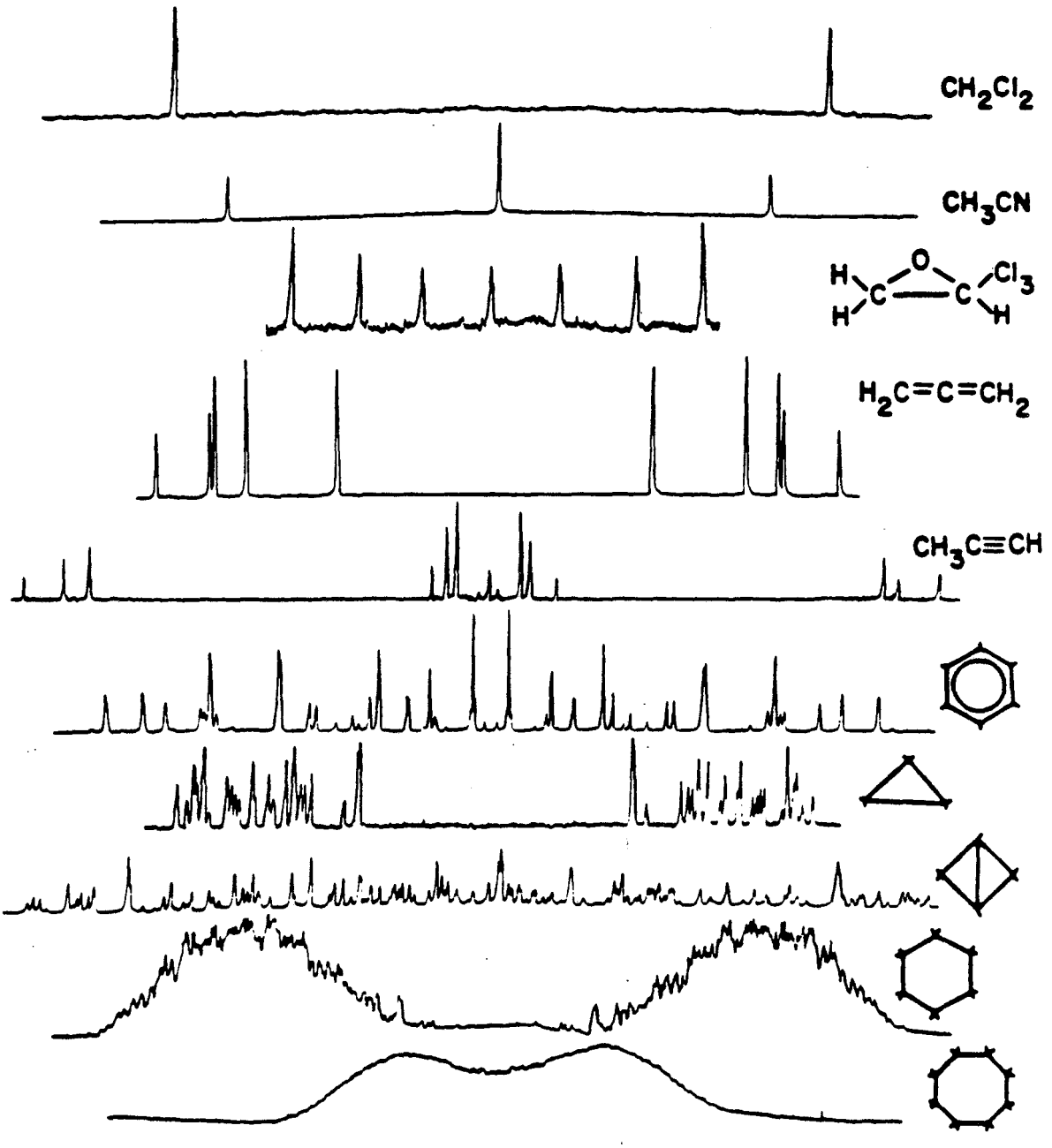

Figure 1.2. Proton NMR spectra of several different molecules dissolved in liquid crystal solvents. The spectral complexity is seen to increase very rapidly with the size of the solute molecule. (Figure courtesy of Professor Zeev Luz.)

molecules dissolved in liquid crystals. The complexity of the spectra rapidly increases from top to bottom in this figure to the point that individual transitions are no longer resolved. The inability to resolve individual transitions clearly limits the size of the spin system which can be studied and has provided much of the motivation behind the development of multiple quantum NMR in dipolar coupled systems[18-21]. By reducing the number of observed transitions, multiple quantum NMR enhances spectral resolution and thereby makes possible the analysis of larger and more complex spin systems.

1.4 Coupled Spin Systems

1.4.1 Energy Level Diagram

In describing NMR spectroscopy in coupled spin systems it is useful to refer to an energy level diagram, such as that of Figure 1.3. The labeling of Zeeman manifolds in this figure is appropriate for a system of N coupled spin-½ nuclei, with energy levels sorted according to their total Zeeman quantum number, m^I. In the high field limit, where $[\mathcal{H}_{INT}, I_z] = 0$, m^I is a good quantum number during free evolution of the system. Within each Zeeman manifold splittings arise due to chemical shifts and spin-spin couplings. The total number of energy levels is 2^N, with the number in each manifold given by the binomial coefficient

$$\left(\begin{matrix} N \\ \frac{N}{2} - m^I \end{matrix} \right). \tag{1.56}$$

Consider the transition between a pair of energy levels i and j. The order of this transition, n_{ij}^I, is defined as the difference in Zeeman quantum numbers between the two states

$$n_{ij}^I \equiv (m_i^I - m_j^I). \tag{1.57}$$

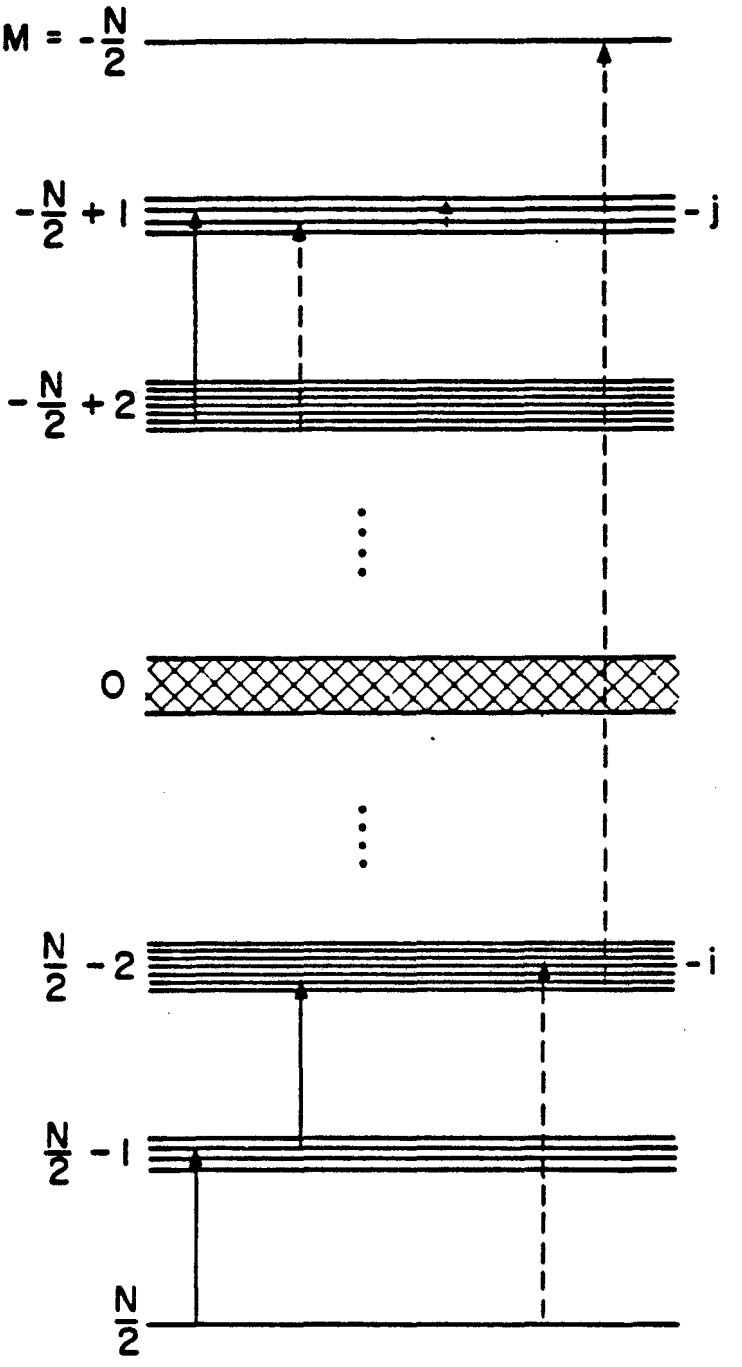

Figure 1.3. Energy level diagram for a system of coupled nuclear spins. The labeling of the energy levels is appropriate for a system of N coupled spins ½. Eigenstates are sorted by their total Zeeman quantum number m^I. Splittings within a Zeeman manifold are due to chemical shifts and spin-spin couplings. Allowed single quantum transitions, indicated by solid arrows, occur between adjacent Zeeman manifolds. The dashed arrows represent examples of normally forbidden multiple quantum transitions.

Single quantum transitions ($n^I_{ij} = \pm 1$), indicated in Figure 1.3 by solid arrows, are between adjacent Zeeman manifolds. The dashed arrows in the figure provide several examples of multiple quantum transitions, which are forbidden in conventional NMR experiments. In a general sense we will use the term multiple quantum transitions to refer to all possible transitions within a spin system, including those characterized by $n^I = \pm 1$.

1.4.2 Enumeration of Transitions

Consideration of Figure 1.3 allows us to enumerate the number of possible transitions of each order. For a system of N coupled protons in the absence of any molecular symmetry, the number of transitions of order n^I, Z_{n^I}, is (excluding zero quantum):

$$Z_{n^I} = \sum_{i=0}^{N-n^I} \binom{N}{i}\binom{N}{i+n^I} . \tag{1.58a}$$

This is equivalent to the formula of Wokaun and Ernst[22]:

$$Z_{n^I} = \binom{2N}{N-n^I} . \tag{1.58b}$$

The number of zero quantum transitions is

$$Z_{(n^I = 0)} = \frac{1}{2}\left[\binom{2N}{N} - 2^N\right] . \tag{1.59}$$

1.5 Selection Rules and Spectral Resolution

1.5.1 Conventional NMR Spectroscopy

In conventional NMR spectroscopy, all allowed transitions are characterized by the selection rule $\Delta m^I = \pm 1$. In CW experiments, this selection rules derives from first order perturbation theory and results

from the relative weakness of the applied H_1 field[23]. An equivalent spectrum is obtained by Fourier transformation of the time domain signal collected following a radio frequency pulse of nutation angle $\frac{\pi}{2}$[24]. In the Fourier transform experiment, the single quantum selection rule is a result of the initial density operator being I_z and is independent of the strength of H_1[21]. This is discussed further in Sections 1.7.2 and 2.1.

In the absence of symmetry the number of single quantum transitions is, from Equations 1.58, $\binom{2N}{N-1}$. The number of unique dipole couplings, on the other hand, cannot exceed $N(N-1)/2$. Since the number of spectral lines greatly exceeds the number of couplings, the single quantum spectrum contains much redundant information. As demonstrated by Figure 1.2, this "overabundance" of information leads to a rapid loss of spectral resolution with increasing spin system size.

1.5.2 Multiple Quantum (MQ) NMR Spectroscopy

Multiple quantum transitions were first observed in the CW spectra of liquids[25,26]. Theoretically such spectra can be explained by means of higher order perturbation theory[27]. Both the transition frequencies and lineshapes of these MQ lines are strongly dependent on the applied r.f. field strength H_1. The proportionality of MQ line intensity to powers of H_1, given by $H_1^{(2n^I-1)}$, is in fact the only means by which different multiple quantum orders can be distinguished in CW experiments. This dependence on r.f. field strength makes both the excitation and interpretation of multiple quantum transitions by CW irradiation difficult and has served to severely limit the usefulness of the technique.

The past decade has seen the development of the much more powerful and useful methods of time domain multiple quantum NMR, which have been

the subject of two recent reviews[21,28]. The principles of multiple quantum NMR in dipolar coupled systems are reviewed in Chapter 2 and form the basis for the development of the method in heteronuclear spin systems (Chap. 3) and for the technique of total spin coherence transfer echo spectroscopy (TSCTES) described in Chapter 4. Here we merely point out the potential advantages of MQ NMR with respect to spectral resolution. As described by Equation 1.58b, higher order multiple quantum spectra contain many fewer lines than their single quantum counterparts. At the same time these spectra contain enough lines to allow the various dipolar couplings to be determined. Thus they provide enhanced spectral resolution without a loss of information and, in fact, can sometimes provide additional information which is absent from the normal single quantum spectra[21,28].

1.6 Effects of Molecular Symmetry

In this section, we present a brief discussion of molecular symmetry. As discussed in numerous texts[29,30], symmetry plays a crucial role in determining NMR spectra and we will make frequent use of the principles of group theory and symmetry in subsequent chapters of this work. The importance of molecular symmetry stems from the fact that both single quantum and multiple quantum transition operators are totally symmetric in nature. This means that only transitions between states belonging to the same representation are allowed. In the absence of relaxation processes, which may be of lower symmetry and therefore able to induce transitions between states of different symmetries, each irreducible representation may therefore be treated separately.

For applications to NMR spectroscopy, a proper group theory treatment involves consideration of the spin system's permutation symmetry.

This is determined by enumerating all permutations of the nuclei to which the internal Hamiltonian is invariant. Often the spin systems of interest in NMR experiments are undergoing various intramolecular motions, including internal vibrations, rotations about carbon-carbon single bonds, and interconversion between different molecular conformers. If this motion is sufficiently fast, motional averaging may in effect increase the symmetry of $\mathcal{H}_{INT}$. In liquid crystals, this motion may also effect the degree of molecular ordering, as discussed in Appendix A.

The permutation symmetry can be quite different from that of the molecule as a whole. Often a permutation group is found to be isomorphic with a standard molecular point group. Once the permutation group has been determined, symmetry-adapted eigenstates can be generated. Within each irreducible representation, the number of transitions of each order is then easily counted. For systems of N coupled protons in the absence of chemical shifts, a simpler procedure for determining the number of (N-1) and (N-2) quantum lines has been described[31].

1.7 Irreducible Tensor Operators

1.7.1 Definition and Properties

We conclude this chapter with an introduction to irreducible tensor operators. Although most of the experiments in this thesis are treated using standard angular momentum operators, it will occasionally prove convenient to use irreducible tensor operators because of their easily calculated behavior under rotations. An irreducible angular momentum tensor operator of rank ℓ is defined[32] to be a set of $(2\ell+1)$ operators $T^{\ell}_{n}(-\ell \leq n \leq \ell)$ which transform under rotations according to

$$D(\alpha\beta\gamma)T^{\ell}_{n}\,D^{-1}(\alpha\beta\gamma) = \sum_{n'} T^{\ell}_{n'}\,\mathcal{D}^{(\ell)}_{n',n}(\alpha\beta\gamma), \tag{1.60}$$

where the terms $\mathcal{D}^{(\ell)}_{n',n}(\alpha\beta\gamma)$ are Wigner rotation matrix elements and

$$D(\alpha\beta\gamma) \equiv \exp(i\gamma I_z)\, \exp(i\beta I_y)\, \exp(i\alpha I_z). \tag{1.61}$$

Racah's original definition of the operators T^{ℓ}_{n} by the commutation relationships

$$[I_z,\ T^{\ell}_{n}] = nT^{\ell}_{n} \tag{1.62a}$$

$$[I_{\pm},\ T^{\ell}_{n}] = T^{\ell}_{n\pm1}\ [(\ell \mp n)(\ell \pm n + 1)]^{\frac{1}{2}} \tag{1.62b}$$

is equivalent to that of Equation 1.60.

The coupling of commuting irreducible tensor operators is mathematically identical to the coupling of angular momenta. As an example, the direct product of two first-rank tensor operators, each operating on a different spin, is a second-rank tensor operator, a first-rank tensor operator, and a scalar ($T^1 \otimes T^1 = T^2 + T^1 + T^0$). More generally, for the coupling of two commuting tensor operators:

$$(T^{\ell_1}(i) \otimes T^{\ell_2}(j))^{\ell}_{n} = \sum_{n_1,n_2} \langle \ell_1 n_1 \ell_2 n_2 | \ell_1 \ell_2 \ell n \rangle\ T^{\ell_1}_{n_1}(i)\ T^{\ell_2}_{n_2}(j), \tag{1.63}$$

where the quantity in angular brackets is a Clebsch-Gordon coefficient and (i,j) label the spins. Table of Clebsch-Gordon coefficients and analytical expressions for their evaluation can be found elsewhere[30,32-34]. Here we simply note that the coefficient $\langle \ell_1 n_1 \ell_2 n_2 | \ell_1 \ell_2 \ell n \rangle$ is non-zero only for $|\ell_1 - \ell_2| \le \ell \le \ell_1 + \ell_2$ and $n_1 + n_2 = n$.

When dealing with spin operators, we are often concerned specifically with rotations due to applied r.f. pulses. Each r.f. pulse is described by a nutation angle θ and a phase ϕ, and corresponds mathematically to a rotation by θ about an axis in the xy plane. For r.f. pulses, Equation 1.60 can be simplified to

$$D(\theta,\phi)T_n^{\ell}\, D^{-1}(\theta,\phi) = \sum_{n'} T_{n'}^{\ell}\, d_{n',n}^{(\ell)}(\theta)\, \exp(i(n-n')\phi), \tag{1.64}$$

where

$$D(\theta,\phi) = \exp(i\theta I_{\phi}), \tag{1.65a}$$

$$I_{\phi} = \exp(-i\phi I_z) I_y \exp(i\phi I_z), \tag{1.65b}$$

and the $d_{n',n}^{(\ell)}(\theta)$ are reduced Wigner rotation matrix elements ($d_{n',n}^{(\ell)}(\theta) = \mathcal{D}_{n',n}^{(\ell)}(0,\theta,0)$).

1.7.2 Single Quantum Selection Rule

As described in Section 1.1.4, the equilibrium density matrix for a spin system in high magnetic field is proportional to the operator I_z ($\rho_{EQ} = b_I I_z$). The angular momentum operator I_z corresponds to the irreducible tensor operator T_0^1. Following the application of an arbitrarily strong r.f. pulse, the density operator can contain (from Equation 1.64) only the terms T_0^1, $T_{\pm 1}^1$, with appropriate coefficients. We now ask which spin states this density operator connects. Expressing these spin states as angular momentum eigenfunctions $|\ell m\rangle$, the matrix element $\langle \ell_2 m_2 | T_n^{\ell} | \ell_1 m_1 \rangle$ can be evaluated by means of the Wigner-Eckart theorem[32-34]. According to this theorem

$$\langle \ell_2 m_2 | T_n^{\ell} | \ell_1 m_1 \rangle = \langle \ell_1 m_1 \ell n | \ell_1 \ell \ell_2 m_2 \rangle \langle \ell_1 \| T^{\ell} \| \ell_2 \rangle, \tag{1.66}$$

where the first factor on the right-hand side is a Clebsch-Gordon coefficient and the second factor is a reduced matrix element which is independent of magnetic quantum numbers. Since $\langle \ell_1 m_1 \ell n | \ell_1 \ell \ell_2 m_2 \rangle = 0$ unless $n = (m_1 - m_2)$, T_n^{ℓ} is an n-quantum operator. Thus, as noted in Section 1.5.1, a single r.f. pulse applied to a spin system at equilibrium excites only single quantum ($T_{\pm 1}^1$) transitions.

The creation of multiple quantum coherence requires a minimum of two r.f. pulses. The first results in a density operator composed of the irreducible tensor operators $T^1_{0,\pm1}$. The evolution of this density operator under a bilinear Hamiltonian ($\mathcal{H}^D_{II}$, $\mathcal{H}^J_{II}$) can produce operators $T^\ell_{0,\pm1}$ of rank $\ell \geq 2$. Application of a second r.f. pulse then generates operators T^ℓ_n of rank $|n| \geq 2$ which connect spin states differing by greater than ±1 in total Zeeman quantum number.

1.8 Summary

In this chapter several important topics have been discussed. Density operators and irreducible tensor operators have been introduced and the different spin Hamiltonian interactions described. In high magnetic field, a spin system at equilibrium can be described by the reduced density operator I_z. The single quantum selection rule observed in single-pulse Fourier transform NMR experiments is a direct consequence of this fact.

The NMR spectra of molecules dissolved in liquid crystal solvents are a rich source of structural and motional information. These spectra become increasingly complex as the size of the spin system increases or its symmetry decreases, however, to the point that individual transitions are no longer resolved. By reducing the number of observed transitions, time domain multiple quantum NMR can greatly enhance spectral resolution. Furthermore, this enhancement can be achieved with no loss of information about the parameters of the internal spin Hamiltonian $\mathcal{H}_{INT}$. Chapter 2 of this thesis introduces multiple quantum NMR in dipolar coupled systems and provides necessary background for the heteronuclear MQ experiments of Chapter 3 and the TSCTES technique of Chapter 4.

Chapter 2: MULTIPLE QUANTUM NMR

In this chapter, some of the basics of multiple quantum (MQ) NMR are introduced. This subject has been discussed in considerable detail in the literature[28,21,18-20,22,35-45] as well as in several recent Ph.D. theses[13,46-51]. Emphasis here is placed on those aspects of multiple quantum NMR which are important in subsequent chapters of this work.

In Section 2.1, the single quantum NMR experiment is reviewed. The basics of two-dimensional (2-D) NMR techniques are introduced in Section 2.2. Section 2.3 deals with the preparation and detection of multiple quantum transitions. A variety of different pulse sequences for accomplishing this excitation are introduced. The problems of inhomogeneous broadening of MQ transitions and of separating MQ orders are discussed in Section 2.4. The sensitivity of a multiple quantum transition to magnetic field inhomogeneity is shown to be proportional to the order of that transition, n^I. Techniques for distinguishing MQ orders are described which depend on this sensitivity and on the behavior of MQ coherence under phase shifts of the r.f. irradiation. In Section 2.5, the question of multiple quantum line intensities is addressed. An experimental search procedure useful in optimizing MQ excitation sequences, parameter proportional phase incrementation (PPPI), is introduced and its effectiveness demonstrated.

2.1 Single Quantum Fourier Transform NMR

The typical Fourier transform NMR experiment begins with the application of a $\frac{\pi}{2}$ pulse to the equilibrium spin system ($\rho(0)=I_z$). Taking this pulse to be of phase $\bar{y}$, the density matrix following the pulse, $\rho(0)_+$, is

$$\rho(0)_+ = \exp(-i\,\frac{\pi}{2}\,I_y)I_z\,\exp(i\,\frac{\pi}{2}\,I_y) = I_x. \qquad (2.1)$$

Free evolution of the spin system under the internal Hamiltonian yields for ρ as a function of time:

$$\rho(t) = \exp(-i\mathcal{H}_{INT}t)I_x\,\exp(i\mathcal{H}_{INT}t). \qquad (2.2)$$

For a spectrometer having quadrature detection, the two orthogonal channels of information can be represented by the detection operator $I_+ = I_x + iI_y$. From Equation 1.26b the observable signal as a function of time, $S_+(t)$, is

$$S_+(t) = \mathrm{Tr}(\rho(t)I_+) = \mathrm{Tr}(\exp(-i\mathcal{H}_{INT}t)I_x\,\exp(i\mathcal{H}_{INT}t)I_+). \qquad (2.3)$$

Expanding this trace in the eigenbasis of $\mathcal{H}_{INT}$ yields

$$S_+(t) = \sum_{i,j} \langle i|\exp(-i\mathcal{H}_{INT}t)|i\rangle\langle i|I_x|j\rangle\langle j|\,\exp(i\mathcal{H}_{INT}t)|j\rangle\langle j|I_+|i\rangle$$

$$= \sum_{i,j} \langle i|I_x|j\rangle\langle j|I_+|i\rangle\,\exp(i\omega_{ji}t), \qquad (2.4)$$

where $\omega_{ji} = (\omega_j - \omega_i)$ and $\omega_j = \langle j|\exp(i\mathcal{H}_{INT}t)|j\rangle$. This can be readily simplified to

$$S_+(t) = \frac{1}{2}\sum_{i<j} |\langle i|I_+|j\rangle|^2\,\exp(i\omega_{ji}t). \qquad (2.5)$$

Upon Fourier transformation, the signal as a function of frequency becomes

$$S(\omega) = \frac{1}{2}\sum_{i<j} |\langle i|I_+|j\rangle|^2\,\delta(\omega - \omega_{ji}). \qquad (2.6)$$

Several significant points are worth noting. Since I_+ only connects states differing by 1 in their total Zeeman quantum number ($\langle i|I_+|j\rangle = 0$ unless $m_i^I - m_j^I = 1$), Equation 2.6 demonstrates that only single quantum

transitions are observed. (This same result was derived using irreducible tensor operators in Section 1.7.2). This result reflects the following facts: (1) The density matrix following a single pulse contains only single quantum coherence and (2) the spectrometer only detects oscillating magnetic dipole radiation, corresponding to single quantum transitions. These two facts are important in the design of pulse sequences for the excitation and detection of multiple quantum coherence, as discussed in the next section. Equation 2.6 also demonstrates that all single quantum lines have the same relative phase. In addition, intensities of individual transitions are readily calculated once I_+ is expressed in the eigenbasis of $\mathcal{H}_{INT}$.

2.2 Two-Dimensional NMR Techniques

2.2.1 General Considerations

Time domain multiple quantum NMR is one example of a general class of techniques known as two-dimensional (2-D) NMR. The concept of 2-D experiments was first introduced approximately ten years ago in an unpublished lecture[52]. Since that time a wide variety of 2-D experiments have been developed[53] and several reviews have appeared in the literature[54-57]. A schematic representation of the general 2-D experiment is shown in Figure 2.1.

The propagator U acts on $\rho(0)$ to produce a non-equilibrium initial condition. The system is then allowed to evolve for the variable time period t_1. No attempt is made to monitor the signal during this time. The propagator V serves to correlate the evolution during t_1 with the time period t_2, during which signal is collected. The experiment is repeated many times, with t_1 being incremented by an amount Δt_1 with each acquisition. The resulting two-dimensional data array expresses the

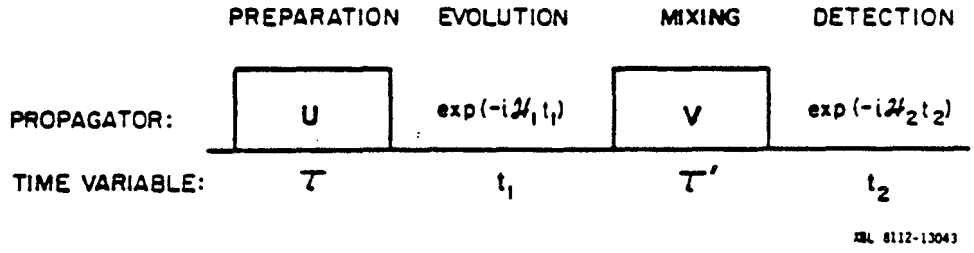

Figure 2.1. Schematic diagram of the general 2-D NMR experiment. Each of the four labeled time periods is characterized by its respective propagator and time variable. The propagator $U(\tau)$ prepares a non-equilibrium initial condition which evolves for the variable time t_1 under the Hamiltonian $\mathcal{H}_1$. The propagator $V(\tau')$ serves to correlate this t_1-evolution with the time period t_2 (characterized by the Hamiltonian $\mathcal{H}_2$), during which signal is collected.

observed signal as a function of time variables t_1 and t_2, $S(t_1,t_2)$. By performing a double Fourier transformation with respect to both t_1 and t_2, a full 2-D spectrum, $S(\omega_1,\omega_2)$, is obtained. The great power of this method is in its ability to correlate the evolution of the system in an unseen time dimension (t_1) with the detected t_2-dependent signal. By changing the propagators U and V as well as perhaps manipulating the Hamiltonians during t_1 and t_2 ($\mathcal{H}_1$ and $\mathcal{H}_2$, respectively), an endless variety of 2-D experiments can be designed.

2.2.2 The Multiple Quantum Experiment

Multiple quantum NMR experiments are inherently two-dimensional in nature. This is because, as noted in Section 2.1, multiple quantum transitions cannot be detected directly with the spectrometer. They must instead be monitored by their modulating effects on the various single quantum transitions detected during t_2. For all of the multiple quantum experiments in this thesis, a single point at $t_2 = 0$ is sampled for each t_1 value. The propagator U serves to generate multiple quantum coherence, while V mixes this coherence back to single quantum observables.

The density matrix as a function of $U(\tau)$, t_1, and $V(\tau')$ can be written

$$\rho(\tau,\tau',t_1) = V(\tau')\exp(-i\mathcal{H}_1 t_1)U(\tau)\rho(0)U^{\dagger}(\tau)\exp(i\mathcal{H}_1 t_1)V^{\dagger}(\tau'). \quad (2.7)$$

Treating the x and y data channels separately, the observed signal $S_\alpha(\tau,\tau',t_1)$ becomes

$$\begin{aligned} S_\alpha(\tau,\tau',t_1) &= \mathrm{Tr}(\rho(\tau,\tau',t_1)\times I_\alpha);\ \alpha = x,y \\ &= \mathrm{Tr}[V(\tau')\exp(-i\mathcal{H}_1 t_1)U(\tau)\rho(0)U^{\dagger}(\tau)\exp(i\mathcal{H}_1 t_1)V^{\dagger}(\tau')I_\alpha]. \end{aligned} \quad (2.8)$$

Defining

$$\rho(\tau) \equiv U(\tau)\rho(0)U^{\dagger}(\tau) \tag{2.9a}$$

and

$$\alpha(-\tau') \equiv V^{\dagger}(\tau')I_{\alpha} V(\tau'), \tag{2.9b}$$

the trace in Equation 3.8 can be expanded in the eigenbasis of $\mathcal{H}_1$ to

$$S_{\alpha}(\tau,\tau',t_1) = \sum_{i,j} \langle i|\rho(\tau)|j\rangle\langle j|\alpha(-\tau')|i\rangle \exp(i\omega_{ji}t_1). \tag{2.10}$$

The Fourier transform with respect to t_1 contains all of the frequencies ω_{ji} for which the product $\langle i|\rho(\tau)|j\rangle\langle j|\alpha(-\tau')|i\rangle$ is non-zero. Unlike the signal following a single r.f. pulse, we are no longer restricted to the observation of single quantum transitions. Instead, subject to the properties of the propagators $U(\tau)$ and $V(\tau')$, all multiple quantum orders can be observed. As an example, Figure 2.2a shows the zero through eight quantum proton spectra of the pure liquid crystal pentylcyanobiphenyl-d_{11} in the nematic phase. In the next section, we examine the properties of a number of different pulse sequences used for the excitation and detection of multiple quantum transitions. A more complete discussion of multiple quantum transition intensities is postponed until Section 2.5.

2.3 Preparation and Detection of Multiple Quantum Coherence

2.3.1 The Generalized Three Pulse Experiment

In this section we consider the preparation and detection of multiple quantum transitions. The simplest multiple quantum pulse sequence, illustrated in Figure 2.3a, consists of three r.f. pulses. The first two, separated by a fixed delay τ, constitute the preparation period which serves to create multiple quantum coherences. Following evolution for a time t_1, the third pulse mixes the multiple quantum transitions

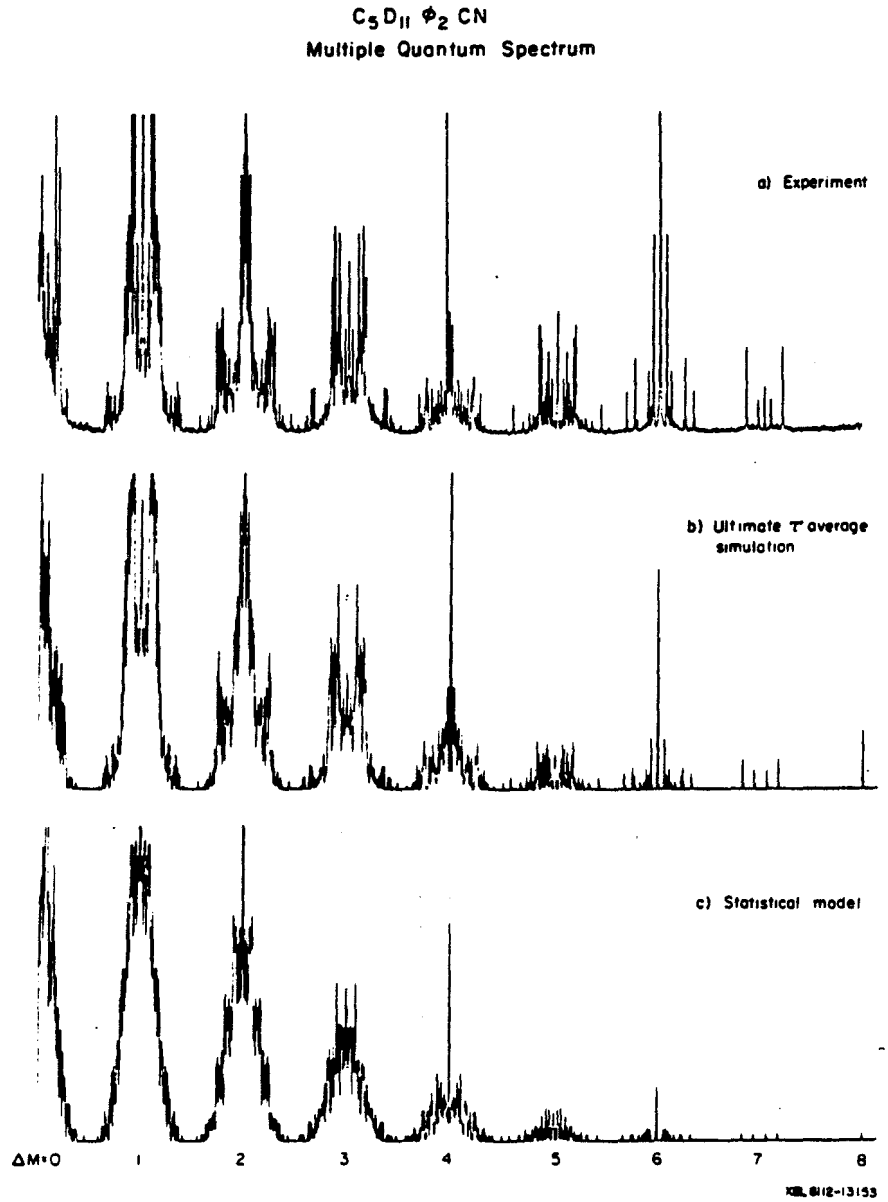

Figure 2.2. Proton multiple quantum spectra of the liquid crystal pentylcyanobiphenyl-d_{11} in the nematic phase. In all three, the strongest 0, 1, 2, and 4 quantum lines have been truncated. (a) An experimental spectrum, displayed in magnitude mode, is the average of six such spectra collected with preparation times τ ranging from 0.4 to 1.4 msec. Only one half of the spectrum, which is symmetric about its center, is shown. Separation of multiple quantum orders was achieved by TPPI (Sec. 2.4.2.2). (b) An ultimate τ average (Sec. 2.5.2). (c) A simulated spectrum, based upon the statistical model (Sec. 2.5.3). (Figure courtesy of Steve Sinton and Jim Murdoch.)

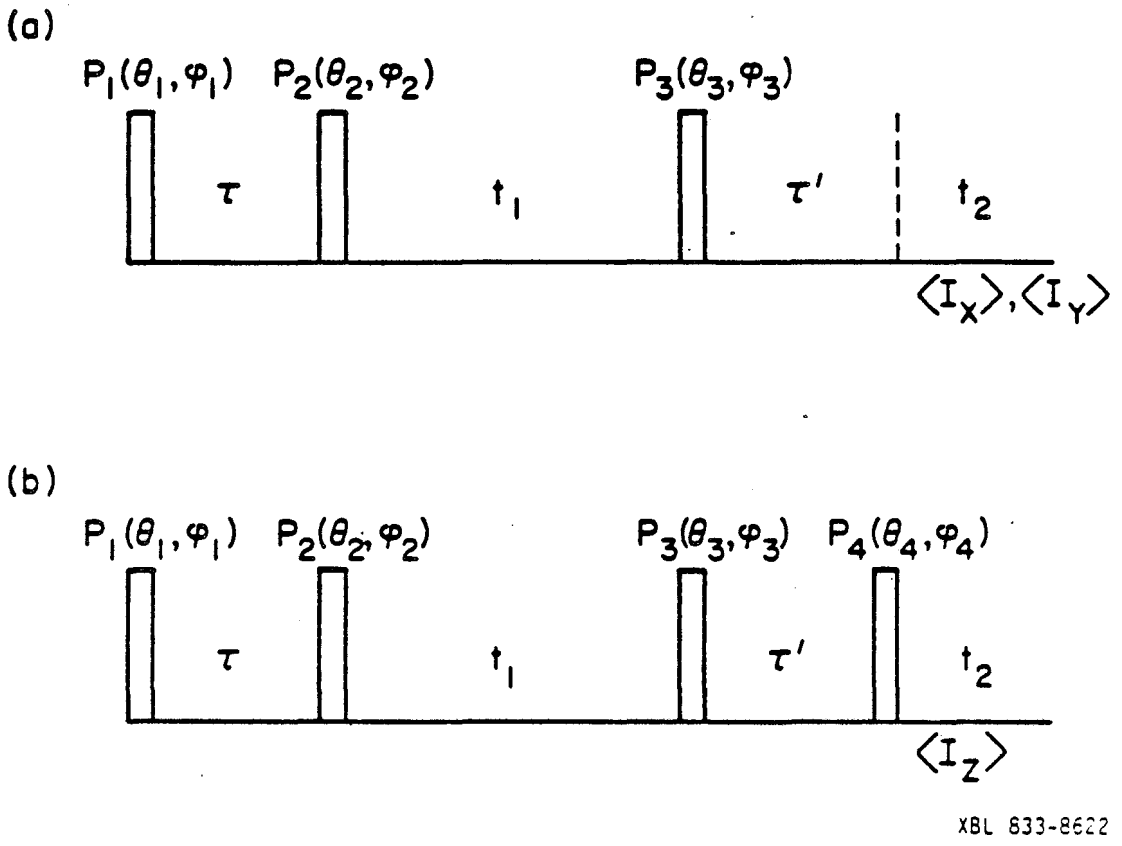

Figure 2.3(a). The basic three-pulse multiple quantum pulse sequence. Each pulse is characterized by a flip angle θ and phase ϕ. Transverse magnetization components I_x and I_y are sampled during t_2. (b) The symmetry of the preparation and mixing periods is emphasized by imagining the multiple quantum experiment to be a four-pulse experiment with I_z the detected operator.

back into single quantum transitions. These then evolve into observable signal after a fixed time τ'. The preparation and mixing periods are referred to jointly as excitation periods.

Much of the following discussion describes properties of the multiple quantum preparation period. Because of the basic symmetry of preparation and mixing periods[20,21], the same considerations govern the choice of pulse and timing parameters in each and the conclusions reached apply equally well to both excitation periods. This preparation/mixing period symmetry is most easily visualized by imagining the basic multiple quantum experiment to be a four pulse experiment with I_z the detected operator (Fig. 2.3b). (The same conclusions which are drawn for this pulse sequence also apply to the sequence of Figure 2.3a, where transverse magnetization components are detected.) For this experiment, the intensity of a transition i-j is given (from Eq. 2.10) by the product

$$\rho_{ij}(\tau)Z_{ji}(-\tau') = \langle i|U(\tau)I_zU^{\dagger}(\tau)|j\rangle\langle j|V^{\dagger}(\tau')I_zV(\tau')|i\rangle. \qquad (2.11)$$

This intensity is maximized when $V(\tau') = U^{\dagger}(\tau)$, for which

$$\rho_{ij}(\tau)Z_{ji}(-\tau') = |\rho_{ij}(\tau)|^2. \qquad (2.12)$$

The condition $V(\tau') = U^{\dagger}(\tau)$ requires reversing the phases of all r.f. pulses as well as "choosing" $\tau' = -\tau$. The ability to effectively "reverse time" by changing the sign of the effective Hamiltonian has been demonstrated[58,59]. For spectra of non-overlapping lines, equivalent intensities are obtained for the more easily achieved condition $V(\tau') = U(\tau)$. Each line now has its own phase factor, however, and spectra must be displayed in magnitude mode. For spectra containing overlapping transitions, these differing phase factors lead to a cancellation of intensity

and time-reversal methods must be employed[13,45].

2.3.2 Specific Three-Pulse Sequences

We now evaluate the pulse sequence of Figure 2.3a for different combinations of flip angles and phases. As described previously, the spin Hamiltonian for a set of coupled protons contains terms due to chemical shifts, resonance offset, dipolar couplings, and scalar couplings. The problem of calculating the evolution of the spin system under this Hamiltonian is a difficult one which generally requires use of a computer. For molecules dissolved in liquid crystalline solvents, the dipolar couplings are usually dominant. For the present, we assume that the only terms present in the Hamiltonian are due to dipolar couplings and perhaps a resonance offset, i.e., $\mathcal{H}_{INT} = \mathcal{H}^D_{II} - \Delta\omega I_z$. In Section 2.3.3 the consequences of relaxing this assumption are discussed.

The propagator $U(\tau)$ associated with two r.f. pulses having flip angles θ_1 and θ_2 and phases ϕ_1 and ϕ_2, respectively, which are separated in time by a delay τ is

$$U(\tau) = \exp(i\theta_2 I_{\phi_2}) \exp(-i\mathcal{H}_{INT}\tau) \exp(i\theta_1 I_{\phi_1}). \qquad (2.13)$$

In evaluating this propagator it is convenient to allow the pulses to act directly on the term $\exp(-i\mathcal{H}_{INT}\tau)$. Recall from Equation 1.42 that the dipolar Hamiltonian can be written

$$\mathcal{H}^D_{II} = -\sum_{i<j} D'_{ij}(3I_{zi}I_{zj} - \underset{\sim}{I}_i \cdot \underset{\sim}{I}_j). \qquad (2.14)$$

Labeling this as $\mathcal{H}^D_{zz}$, we define $\mathcal{H}^D_{xx}$ and $\mathcal{H}^D_{yy}$ as the dipolar Hamiltonian, $\mathcal{H}^D_{II}$, rotated by $\frac{\pi}{2}$ pulses of phases $\bar{y}$ and $\bar{x}$, respectively:

$$\mathcal{H}^D_{xx} = \exp(-i\frac{\pi}{2}I_y)\mathcal{H}^D_{II}\exp(i\frac{\pi}{2}I_y) = -\sum_{i<j} D'_{ij}(3I_{xi}I_{xj} - \underset{\sim}{I}_i \cdot \underset{\sim}{I}_j), \quad (2.15a)$$

$$\mathcal{H}^D_{yy} = \exp(-i\frac{\pi}{2}I_x)\mathcal{H}^D_{II}\exp(i\frac{\pi}{2}I_x) = -\sum_{i<j} D'_{ij}(3I_{yi}I_{yj} - \underset{\sim}{I}_i \cdot \underset{\sim}{I}_j). \quad (2.15b)$$

Simple algebraic manipulation allows these to be rewritten

$$\mathcal{H}^D_{xx} = -\frac{1}{2}\mathcal{H}^D_{zz} - \frac{3}{4}\sum_{i<j} D'_{ij}(I_{+i}I_{+j} + I_{-i}I_{-j}), \quad (2.16a)$$

$$\mathcal{H}^D_{yy} = -\frac{1}{2}\mathcal{H}^D_{zz} + \frac{3}{4}\sum_{i<j} D'_{ij}(I_{+i}I_{+j} + I_{-i}I_{-j}). \quad (2.16b)$$

Thus the rotated dipolar Hamiltonian is a pure zero/two quantum operator. The consequences of this will be explored below.

In describing the prepared density matrix $\rho(\tau)$ it is convenient to use a power series expansion:

$$\begin{aligned}\rho(\tau) &= \exp(-i\mathcal{H}'_{INT}\tau)\rho(0)\exp(i\mathcal{H}'_{INT}\tau) \\ &= \rho(0) + i\tau[\rho(0),\mathcal{H}'_{INT}] - \frac{\tau^2}{2}[[\rho(0),\mathcal{H}'_{INT}],\mathcal{H}'_{INT}] + \ldots \quad (2.17)\end{aligned}$$

where

$$\mathcal{H}'_{INT} = \exp(i\theta_2 I_{\phi_2})\mathcal{H}_{INT}\exp(i\theta_1 I_{\phi_1}). \quad (2.18)$$

We will assume that the first r.f. pulse is a $(\frac{\pi}{2})_x$ pulse ($\theta_1 = \frac{\pi}{2}, \phi_1 = x$) and examine $\rho(\tau)$ for different choices of θ_2 and ϕ_2.

2.3.2.1 $\theta_2 = \frac{\pi}{2}$, $\phi_2 = \bar{x}$, $\Delta\omega = 0$

The sequence $(\frac{\pi}{2})_x - \tau - (\frac{\pi}{2})_{\bar{x}}$ (Fig. 2.4a), in the absence of a resonance offset, excites only even-quantum coherence[46,60]. For this pulse sequence the Hamiltonian $\mathcal{H}'_{INT}$ is given by $\mathcal{H}^D_{yy}$. With $\rho(0) = I_z$, the prepared density matrix can be expanded according to Equation 2.17 as

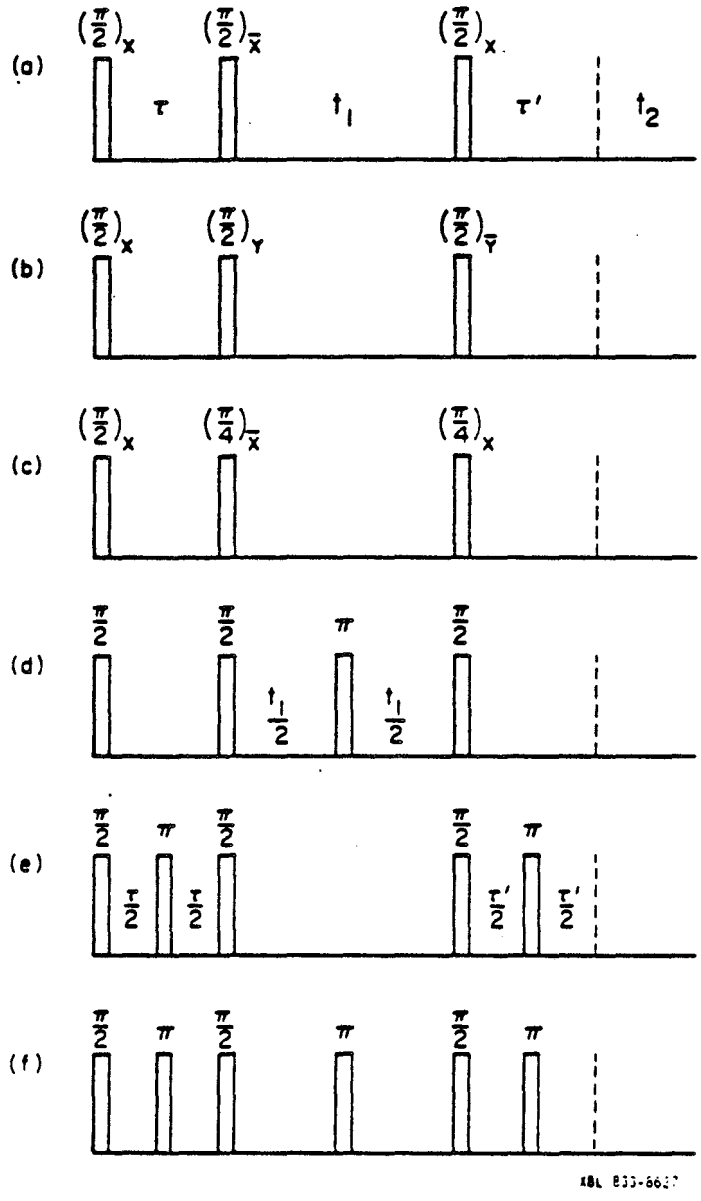

Figure 2.4. Multiple quantum pulse sequences. (a) For $\Delta\omega = 0$, this sequence excites only even-quantum coherence. (b) For $\Delta\omega = 0$, this sequence excites only odd-quantum coherence. (c) This sequence excites both even and odd-quantum coherence. (d)-(f) Examples of multiple quantum sequences incorporating π pulses into the preparation, evolution, and mixing periods.

$$\rho(\tau) = I_z + i\tau[I_z,\mathcal{H}^D_{yy}] - \frac{\tau^2}{2}[[I_z,\mathcal{H}^D_{yy}],\mathcal{H}^D_{yy}] + \ldots \qquad (2.19)$$

As a direct result of the bilinear nature of $\mathcal{H}^D_{yy}$ (Eq. 2.16b), $\rho(\tau)$ is found to contain only even-quantum coherence (including zero) when these commutators are evaluated. Zero quantum coherence first appears in the τ^2 term in this expansion, while other even n-quantum coherences are first observed in the term proportional to $\tau^{(n-1)}$[47,61].

2.3.2.2 $\theta_2 = \frac{\pi}{2}$, $\phi_2 = y$, $\Delta\omega = 0$

In the absence of a resonance offset, the sequence $(\frac{\pi}{2})_x - \tau - (\frac{\pi}{2})_y$ (Fig. 2.4b) excites only odd-quantum coherence[46,60]. This is most easily seen by inserting the identity $\exp(-i\frac{\pi}{2}I_y)\exp(i\frac{\pi}{2}I_y)$ immediately after the propagator for the initial $(\frac{\pi}{2})_x$ pulse. The prepared density operator becomes

$$\rho(\tau) = \exp(-i\mathcal{H}^D_{xx}\tau)\exp(i\tfrac{\pi}{2}I_y)\exp(i\tfrac{\pi}{2}I_x)I_z\exp(-i\tfrac{\pi}{2}I_x)\exp(-i\tfrac{\pi}{2}I_y)$$

$$\times \exp(i\mathcal{H}^D_{xx}\tau) = \exp(-i\mathcal{H}^D_{xx}\tau)I_y\exp(i\mathcal{H}^D_{xx}\tau). \qquad (2.20)$$

Expanding $\rho(\tau)$ in a series yields

$$\rho(\tau) = I_y + i\tau[I_y,\mathcal{H}^D_{xx}] - \frac{\tau^2}{2}[[I_y,\mathcal{H}^D_{xx}],\mathcal{H}^D_{xx}] + \ldots \qquad (2.21)$$

which, upon evaluating the commutators, is seen to contain only odd-quantum coherence. This selectivity results from the action of the bilinear operator $\mathcal{H}^D_{xx}$ (Equation 2.16a) on the single quantum initial condition I_y. Obviously, single quantum coherence first appears in the τ-independent term, while other odd n-quantum coherence is first observed in the term proportional to $\tau^{(n-1)}$[47,61].

2.3.2.3 $\theta_2 = \frac{\pi}{4}$ $\phi_2 = \bar{x}$, $\Delta\omega = 0$

The sequence $(\frac{\pi}{2})_x - \tau - (\frac{\pi}{4})_{\bar{x}}$ (Fig. 2.4c) excites both even and odd-quantum coherence. If the initial $(\frac{\pi}{2})_x$ pulse is viewed as a pair of $(\frac{\pi}{4})_x$ pulses, the prepared density matrix can be written as

$$\rho(\tau) = \exp(-i\tfrac{\pi}{4} I_x) \exp(-i\mathcal{H}^D_{II}\tau) \exp(i\tfrac{\pi}{4} I_x)[\tfrac{1}{\sqrt{2}}(I_z + I_y)]$$

$$\times \exp(-i\tfrac{\pi}{4} I_x) \exp(i\mathcal{H}^D_{II}\tau) \exp(i\tfrac{\pi}{4} I_x). \qquad (2.22)$$

The rotated dipolar coupling Hamiltonian $\exp(-i\frac{\pi}{4} I_x)\mathcal{H}^D_{II} \exp(i\frac{\pi}{4} I_x)$ equals $\frac{1}{\sqrt{2}}(\mathcal{H}^D_{zz} + \mathcal{H}^D_{yy})$, which is itself a 0, ±2 quantum operator. With an initial density matrix which is a linear combination of those of Sections 2.3.2.1 and 2.3.2.2, it is easily seen that the expansion of $\rho(\tau)$ will contain all orders of coherence.

2.3.2.4 $\Delta\omega \neq 0$

The pulse sequences considered thus far have been analyzed assuming no resonance offset. With $\theta_1 = \frac{\pi}{2}$, $\phi_1 = x$, the preparation sequence can be made to excite only even-quantum coherence, only odd-quantum coherence, or both, depending on the choice of flip angle θ_2 and phase ϕ_2. In the presence of a resonance offset, the pulse sequences $(\frac{\pi}{2})_x - \tau - (\frac{\pi}{2})_{\bar{x}}$ and $(\frac{\pi}{2})_x - \tau - (\frac{\pi}{2})_y$ themselves give a mixture of even and odd-quantum coherence depending upon the value of $(\Delta\omega\tau)$.

Consider the even-quantum selective sequence of Figure 2.4a for $\Delta\omega \neq 0$. The prepared density matrix is

$$\rho(\tau) = \exp(-i\tfrac{\pi}{2} I_x) \exp(-i(\mathcal{H}^D_{II} - \Delta\omega I_z)\tau) \exp(i\tfrac{\pi}{2} I_x) I_z \exp(-i\tfrac{\pi}{2} I_x)$$

$$\times \exp(i(\mathcal{H}^D_{II} - \Delta\omega I_z)\tau) \exp(i\tfrac{\pi}{2} I_x). \qquad (2.23)$$

Since the secular dipolar Hamiltonian, by definition, commutes with I_z

$$\exp(-i(\mathcal{H}^D_{II} - \Delta\omega I_z)\tau) = \exp(-i\mathcal{H}^D_{II}\tau)\ \exp(i\Delta\omega I_z\tau). \qquad (2.24)$$

Equation 2.23 can therefore be simplified:

$$\rho(\tau) = \exp(-i\mathcal{H}^D_{yy}\tau)\ \exp(-i\Delta\omega I_y\tau) I_z\ \exp(i\Delta\omega I_y\tau)\ \exp(i\mathcal{H}^D_{yy}\tau) \qquad (2.25a)$$

$$= \exp(-i\mathcal{H}^D_{yy}\tau)[I_z\ \cos(\Delta\omega\tau) + I_x\ \sin(\Delta\omega\tau)]\ \exp(i\mathcal{H}^D_{yy}\tau). \qquad (2.25b)$$

This is reminiscent of Equation 2.22, with a bilinear operator acting upon an initial density matrix which is a linear combination of I_z and I_x. When $\Delta\omega\tau = m\pi$ only even-quantum coherence is observed, while pure odd-quantum appears for $\Delta\omega\tau = m\pi/2$. For intermediate values $\rho(\tau)$ contains a mixture of even and odd coherence.

2.3.3 Sequences Incorporating One or More π Pulses

Beginning with the basic three-pulse experiment of Figure 2.2a, a wide variety of different multiple quantum pulse sequences can be designed. A most common modification is the addition of π pulses in the middle of the preparation and mixing period (at times $\frac{\tau}{2}$ and $\frac{\tau'}{2}$, respectively) as well as in the middle of the evolution period, at time $t_1/2$ (Figs. 2.4d-f). The effect of these π pulses is to change the sign of all spin Hamiltonian terms which are linear in I_z: (1) resonance offset, (2) chemical shift, and (3) magnetic field inhomogeneity. The evolution period π pulse is discussed in greater detail in Section 4.1.1. Here we focus on the inclusion of π pulses in the multiple quantum preparation and mixing periods.

Equation 2.25b emphasizes the sensitivity of even/odd selective experiments to resonance offset, Δω. Incorporation of π pulses into the preparation and mixing periods insures that the arguments of Sections

2.3.2.1 and 2.3.2.2 remain valid in the presence of a non-zero resonance offset. In addition, these pulses remove the effects of magnetic field inhomogeneity, $-\omega(\underset{\sim}{r})I_z$.

2.3.4 Spin Systems Having Chemical Shifts

Until now, we have limited ourselves to a spin Hamiltonian composed of dipolar couplings and a possible resonance offset. We now ask about the preparation and detection of multiple quantum coherence in systems having chemical shift differences between the spins. In isotropic systems, these chemical shift differences are required in order that the bilinear J-coupling be capable of exciting multiple quantum transitions. In anisotropic systems, non-zero chemical shifts allow the scalar couplings to contribute to multiple quantum excitation. Due to the relative size of dipolar and scalar couplings, however, we will continue to neglect the J-couplings in the qualitative discussion of this section. Because the scalar couplings are themselves bilinear operators, their inclusion would not alter any of the conclusions drawn.

In the presence of chemical shifts, the multiple quantum sequences of Figures 2.4a and b are no longer even/odd selective. As with a non-zero resonance offset, this is because the spin Hamiltonian now contains single spin operator terms. Unlike the resonance offset, however, the chemical shift Hamiltonian does not commute with $\mathcal{H}^D_{II}$ and a simplification like that of Equation 2.24 cannot be made. Moreover, this lack of commutivity precludes the removal of chemical shift terms by inclusion of single π pulses, as in Figures 2.4d-f. The implications of this fact with regard to the evolution period t_1 are the subject of Chapter 4 on total spin coherence transfer echo spectroscopy. In terms of the excitation periods, it means that even/odd selectivity cannot be

restored by π pulses at $\frac{\tau}{2}$ and $\frac{\tau'}{2}$. These 'deviations' from even/odd selectivity increase with increasing chemical shift magnitudes. This selectivity can be restored, even in systems with large chemical shifts, by using a train of closely spaced π pulses in both preparation and mixing.

2.4 Inhomogeneous Broadening of MQ Lines/Separation of MQ Orders

In this section, the problems of the inhomogeneous broadening of multiple quantum lines and separation of multiple quantum orders are addressed. At first, the connection between these two subjects may not be apparent. As will be demonstrated, however, both involve a consideration of the evolution of multiple quantum transitions under Hamiltonians proportional to the operator I_z. It is the order-dependent behavior of multiple quantum lines under such Hamiltonians which both account for the increasing susceptibility of higher order transitions to magnet inhomogeneity and allow the separation of multiple quantum spectra by order.

2.4.1 Sensitivity to Magnetic Field Inhomogeneity

Recall from Section 2.2.2 that the observed signal in a multiple quantum NMR experiment can be written

$$S_\alpha(\tau,\tau',t_1) = \sum_{i<j} \rho_{ij}(\tau)\alpha_{ji}(-\tau')\langle i|\exp(-i\mathcal{H}_1 t_1)|i\rangle\langle j|\exp(i\mathcal{H}_1 t_1)|j\rangle. \quad (2.26)$$

Let's assume that the Hamiltonian $\mathcal{H}_1$ contains no off-resonance term and examine the effect of its explicit introduction into the evolution period. Since $\mathcal{H}_1$ commutes with the off-resonance term $-\Delta\omega I_z$,

$$\exp(-i(\mathcal{H}_1 - \Delta\omega I_z)t_1) = \exp(-i\mathcal{H}_1 t_1)\exp(i\Delta\omega I_z t_1) \quad (2.27)$$

and Equation 2.26 becomes

$$S_\alpha(\tau,\tau',t_1) = \sum_{i<j} \rho_{ij}(\tau)\alpha_{ji}(-\tau')\langle i|\exp(-i\mathcal{H}_1 t_1)|i\rangle\langle i|\exp(i\Delta\omega I_z t_1)|i\rangle$$

$$\times \langle j|\exp(i\mathcal{H}_1 t_1)|j\rangle\langle j|\exp(-i\Delta\omega I_z t_1)|j\rangle \qquad (2.28a)$$

$$= \sum_{i<j} \rho_{ij}(\tau)\alpha_{ji}(-\tau')\exp(i\omega_{ji}t_1)\exp(i\Delta\omega(m_i^I - m_j^I)t_1). \qquad (2.28b)$$

Thus a resonance offset of $\Delta\omega$ appears n_{ij}^I times as large to a multiple quantum transition. The same is true of the magnetic field inhomogeneity, $\omega(\underline{r})$. Multiple quantum lines are broadened by an amount proportional to the order of the transition[53]. This means that the homogeneity of the magnetic field can limit the attainable resolution in multiple quantum spectra in situations where it is not resolution limiting in single quantum spectroscopy. A π pulse placed at the midpoint of the evolution period will remove the inhomogeneous broadening due to the magnet, but often introduces other complications, as discussed in Chapter 4. This fact provides one of the primary motivations for the development of the TSCTES method. Equation 2.28b also reveals that zero-quantum transitions are unaffected by magnetic field inhomogeneity[53] and as such are a convenient observable for the measurement of transverse relaxation times T_2[22].

2.4.2 Separation of Multiple Quantum Orders

In interpreting multiple quantum spectra, it is convenient to sort out transitions according to changes in the total Zeeman quantum number, n^I. At first, it might seem that this separation should be an easy matter, since transitions of differing order differ in energy by multiples of the Larmor frequency, ω_o^I (Fig. 1.3). However, it is precisely these

large energy differences which are removed in the resonant rotating frame (Sec. 1.1.5). In this frame, transition frequencies are determined by chemical shifts and spin-spin interactions and transitions of all orders overlap completely. A variety of different approaches have been designed which address the problem of separating multiple quantum orders. These include shifts in the spectrometer reference frequency[46], phase shifts of the applied r.f. pulses[37,19,41,62] and applications of pulsed magnetic field gradients[63-66,21].

2.4.2.1 Resonance Offset

Perhaps the simplest approach to the separation of multiple quantum orders makes use of a resonance offset $\Delta\omega$. According to Equation 2.28b a transition i-j evolves under an effective offset given by $n^I_{ij}\Delta\omega$. By choosing $\Delta\omega$ greater than the spectral width of an individual order, separation of transitions according to total change in Zeeman quantum number is achieved. Transitions of order n^I are centered about a frequency which is offset from zero by an amount $n^I\Delta\omega$. The increment in t_1 must be chosen to allow sufficient bandwidth for a total of $(2N+1)$ orders.

There are problems associated with using resonance offsets to separate multiple quantum spectra, however. If the receiver reference frequency also serves as the carrier frequency for the r.f. pulses, going far off-resonance may lead to an inability to excite the entire bandwidth of transitions. This difficulty can be overcome through the use of two different frequency sources. A more fundamental objection to separating orders by a resonance offset is its incompatibility with experiments which employ a spin echo during t_1. Since the resonance

offset and magnet inhomogeneity terms are of the same form, any pulse sequence which removes $\omega(\underline{r})$ will simultaneously remove the offset $\Delta\omega$. In obtaining spectra which are free of inhomogeneous broadening, the separation of multiple quantum orders is lost.

2.4.2.2 Time Proportional Phase Incrementation (TPPI)

Clearly, alternative approaches for distinguishing between orders are desirable. Two closely related methods take advantage of the response of multiple quantum coherence to phase shifts in the irradiating r.f. field. In Equation 1.34 the phase of the r.f., ϕ, was defined by

$$I_\phi = I_y\cos\phi - I_x\sin\phi. \tag{2.29}$$

As this equation implies, a phase shift $\Delta\phi$ corresponds to a rotation about I_z:

$$I_{\phi+\Delta\phi} = \exp(-i\Delta\phi I_z)I_\phi \exp(i\Delta\phi I_z). \tag{2.30}$$

If each of the pulses of the preparation period is phase shifted by an amount $\Delta\phi$, the effect can be described by an overall phase shift of the propagator $U(\tau)$:

$$U_{\Delta\phi}(\tau) = \exp(-i\Delta\phi I_z)U(\tau) \exp(i\Delta\phi I_z). \tag{2.31}$$

The effect on the detected signal S_α is easily calculated:

$$S_\alpha(\tau,\tau',t_1,\Delta\phi) = \sum_{i<j} \rho_{ij}(\tau)\alpha_{ji}(-\tau')\langle i|\exp(-i\Delta\phi I_z)|i\rangle \times \langle j|\exp(i\Delta\phi I_z)|j\rangle \exp(i\omega_{ji}t_1) \tag{2.32a}$$

$$= \sum_{i<j} \rho_{ij}(\tau)\alpha_{ji}(-\tau') \exp(in^I_{ji}\Delta\phi) \exp(i\omega_{ji}t_1). \tag{2.32b}$$

Thus phase shifting the r.f. introduces an order-dependent phase factor into the observed signal.

Suppose that the phase of each pulse in the preparation period is incremented by $\Delta\phi$ with each increment in t_1. We may then associate with the phase shift $\Delta\phi$ a pseudo-resonance offset $\Delta\omega'$, defined by $\Delta\omega' = \frac{\Delta\phi}{\Delta t_1}$. This technique is known as time proportional phase incrementation (TPPI)[19,41] and the signal S_α is given by

$$S_\alpha(\tau,\tau',t_1,\Delta\phi) = \sum_{i<j} \rho_{ij}(\tau)\alpha_{ji}(-\tau') \exp(in^I_{ji}\Delta\omega' t_1) \exp(i\omega_{ji}t_1). \quad (2.33)$$

A simple TPPI multiple quantum pulse sequence is illustrated in Figure 2.5a. As with an actual resonance offset, the center of each multiple quantum order in a TPPI experiment is shifted by an amount $n^I_{ji}\Delta\omega'$. Unlike a real offset, however, separation of orders is not lost if a spin echo is used during the evolution period. To prevent foldback of higher order spectra, $\Delta\phi$ should be chosen $\leq \frac{\pi}{N}$, while Δt_1 must be chosen to provide a bandwidth which is sufficient to accommodate $(2N+1)$ orders. TPPI was used in acquiring the spectra of Figure 2.2a.

2.4.2.3 Phase Fourier Transformation (PFT)

An alternate method for separating multiple quantum orders based upon phase shifting the r.f. pulses is known as phase Fourier transformation (PFT)[37]. Under this technique a series of experiments are performed and the gathered free induction decays co-added. Within each experiment the phases of the preparation period pulses are held constant while a phase shift of all of these pulses by an amount $\Delta\phi$ is performed between experiments. As an example, co-addition of signal from two experiments having relative preparation phases of 0 and π retains

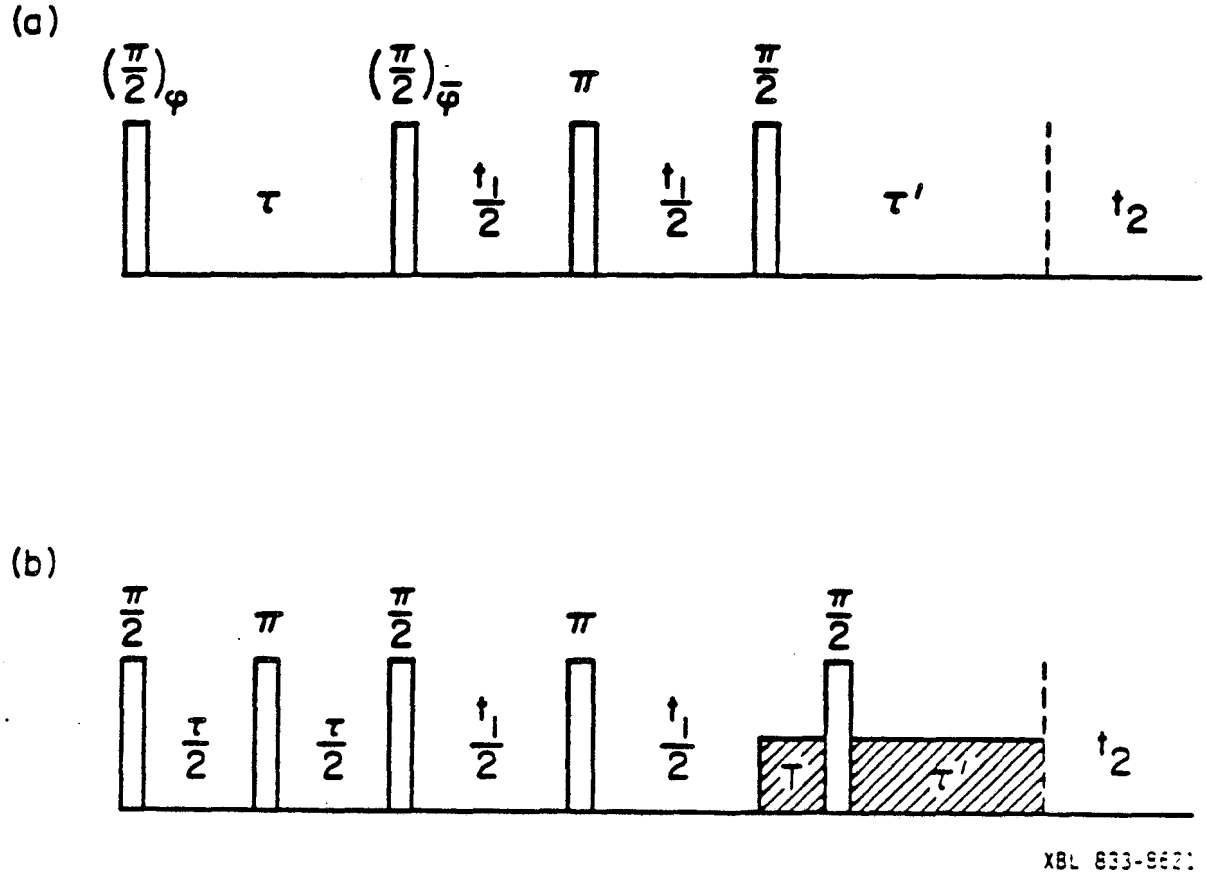

Figure 2.5. (a) TPPI pulse sequence to allow separation of signal from different multiple quantum orders. The phases of the two preparation period $\pi/2$ pulses are incremented with each increment in t_1 while the phases of the pulses in the evolution and mixing periods are fixed throughout. (b) CTEF pulse sequence to allow selection of signal from a single multiple quantum order. In this sequence the time period T is fixed and the cross-hatched areas represent application of a pulsed magnetic field gradient. τ' is set equal to $|n^I|T$, where n^I is the multiple quantum order of interest. A coherence transfer echo is created at time $t_2 = 0$ for this order only.

only even-quantum transitions (odd quantum transitions can be obtained by subtracting the f.i.d.'s from one another). This method is easily generalized to allow other combinations of orders to be sorted. A total of (2N+1) experiments must be performed to allow each multiple quantum order to be individually distinguished. The time and storage requirements for such a series of experiments are approximately the same as in the corresponding TPPI experiment. PFT and TPPI can also be combined together as a means, for example, of separating and displaying only even orders of coherence.

2.4.2.4 Coherence Transfer Echo Filtering (CTEF)

We discuss in this section a final means for separating the various multiple quantum orders. Relying on the order-dependent behavior of multiple quantum coherence under the influence of the magnetic field inhomogeneity $-\omega(\underset{\sim}{r})I_z$, the method is known as coherence transfer echo filtering (CTEF)[21]. A typical multiple quantum pulse sequence incorporating CTEF is shown in Figure 2.5b. π pulses at $\frac{\tau}{2}$ and $t_1/2$ insure that all dephasing due to $-\omega(\underset{\sim}{r})I_z$ has been refocussed at time t_1. Multiple quantum coherence is allowed to evolve freely for an additional time T. Depending upon the homogeneity of H_o, a field-spoiling gradient may be required during this time. During T each multiple quantum order accumulates a "dephasing" factor given by

$$\exp(+in^I\omega(\underset{\sim}{r})T). \tag{2.34}$$

As in other multiple quantum sequences, the final $\frac{\pi}{2}$ pulse transfers coherence and rephasing as single quantum coherence begins. After a time τ', the accumulated phase factor is

$$\exp(-i\omega(\underset{\sim}{r})\tau'). \qquad (2.35)$$

When $n^I T = \tau'$ a coherence transfer echo[35,63] occurs and the signal at this point is free of magnet inhomogeneity. Clearly a different τ' is required to satisfy the echo condition for each multiple quantum order n^I. By choosing τ' appropriately and sampling at the point $t_2 = 0$, only signal resulting from coherence which was n^I-quantum during t_1 is detected. In order for this method to be effective, $\omega(\underset{\sim}{r})T$ must be large enough that the echoes in τ' resulting from the different multiple quantum orders are well separated from one another. By sampling the signal at several points in τ' (each satisfying the condition $\tau' = n^I T$ for a different n^I) it is possible, after some rearrangement of the data, to obtain spectra for several multiple quantum orders simultaneously. In practice, however, the spectra presented in Chapters 3 and 4 were each obtained in separate experiments.

There are a couple of advantages to using CTEF to detect the different multiple quantum orders individually. One of these relates to the concept of two-dimensional or t_1 noise[21]. In addition to thermal noise, which is an inevitable part of all NMR experiments, multiple quantum experiments suffer from noise as a result of their two-dimensional nature. This t_1 noise can result from any spectrometer instabilities which cause the preparation and mixing sequences to fluctuate from one acquisition to the next during an experiment. This noise has been shown to be multiplicative in nature, being proportional to the magnitude of the detected signal[21]. By limiting the detected signal to the order of interest only, CTEF helps to reduce t_1 noise. Additional advantages which result from detecting a single multiple quantum order are savings in computer storage space and, perhaps, experimental running time.

2.5 Multiple Quantum Line Intensities

2.5.1 Ensemble Averaging

We return now to the question of line intensities in multiple quantum experiments. In order to take advantage of the enhanced resolution of multiple quantum spectra, it is necessary to excite with appreciable intensity the higher order multiple quantum transitions. In a system of many coupled spins, the dynamics of the preparation and mixing periods are exceedingly complex and it is unlikely that a single value of τ will suffice to excite all of the desired transitions. Instead a series of experiments are generally performed for a variety of different τ's. Fourier transforms and magnitude spectra are calculated for each and the magnitude spectra are co-added. It is hoped that the resulting ensemble average contains more high-order lines with sizeable intensities than the spectrum for any single preparation/mixing time alone. An experimental search procedure which is very useful in choosing favorable values for τ is described in Section 2.5.5.

2.5.2 Line Intensity Computation

The complexities of the excitation period dynamics pose computational as well as experimental difficulties. Analytical formulae have been given for multiple quantum line intensities in several simple spin-½ systems. These include three-pulse excitation of AB[53,39,67], A_2[39], and A_N[61] spin systems and AB systems under excitation sequences incorporating π pulses in preparation/mixing[68] and in evolution[69]. Recently, computer programs have been written which can calculate line intensities for systems of up to eight spin-½ nuclei under a wide variety of excitation sequences[51,61,70]. For non-selective sequences, these programs are capable of performing two different types of computations.

The first are exact dynamics calculations based upon a particular set of excitation parameters. The intensities thus generated can be compared directly with those observed in an experimental spectrum with the same parameters. A second approach involves calculating a so-called ultimate tau-averaged spectrum[51,61]. As the name implies, the computed quantities are average line intensities which result from integrating over all values of the preparation/mixing parameter τ. Analytical expressions for the required integrals over τ are readily obtained, making computation of the ultimate tau-average straightforward. The savings in computational time when compared to making separate calculations for many different τ's are considerable and, as illustrated in Figure 2.2b, ultimate tau-averaged intensities compare favorably with those from an ensemble-averaged set of experiments. The discrepancies in this figure between calculated and experimental intensities are due largely to having considered a limited number of experimental τ's.

2.5.3 Statistical Model for Line Intensities

Both the analytical formulae and computer programs described in the previous section require a knowledge of the parameters of the spin Hamiltonian in order to compute line intensities. However, these chemical shifts and spin-spin couplings are often the unknowns of interest in multiple quantum experiments. In such cases, intensities serve to confirm the correctness of the spin Hamiltonian parameter assignments, which are generally made based upon transition frequencies alone. This leads to the question of whether a model exists which can give some general information about expected intensities without requiring a detailed consideration of the excitation dynamics.

A particularly simple model for multiple quantum line intensities, the statistical model, assumes all symmetry allowed transitions (transitions between states belonging to the same irreducible representation) to be equal in magnitude. The number of n^I-quantum transitions in a general system of N spin-½ nuclei was given in Equation 1.58b as

$$Z_{n^I} = \binom{2N}{N - n^I} . \tag{2.36}$$

For large N, this equation can be approximated as

$$Z_{n^I} \simeq 4^N \exp[-(n^I)^2/N]. \tag{2.37}$$

Thus, in the absence of any molecular symmetry, the number of transitions per order has a Gaussian distribution. The statistical model therefore predicts that the integrated intensity should fall off very rapidly with increasing order, owing to the relatively few number of higher order transitions. A similar conclusion is reached for systems having permutation symmetry, if the available magnetization is divided equally among all symmetry allowed transitions.

While providing a good qualitative estimate of line intensities, the statistical model fails from a quantitative point of view (Fig. 2.2c). In particular, it tends to underestimate the intensities of the higher order transitions, especially in spin systems in which most of the dipole couplings have the same algebraic sign[61]. It is certainly correct in its prediction that most of the available magnetization is distributed amongst transitions of low order, however. This fact, in turn, has provided much of the motivation behind the development of the techniques of selective excitation.

2.5.4 Selective Excitation

Selective excitation[70-73,20,47,44,21] involves the design and use of preparation and mixing sequences which excite only multiple quantum transitions of a particular (high) order. Selective excitation sequences consist of long trains of carefully spaced, phase shifted r.f. pulses. These sequences are quite demanding experimentally[47,72,73], though the potential gains in signal-to-noise for high-order transitions are substantial[47,20,21]. Selective excitation sequences were not used for any of the experiments described in this thesis.

2.5.5 Parameter Proportional Phase Incrementation (PPPI)

2.5.5.1 Motivation

Many experiments require the excitation of transitions of one or more high multiple quantum orders. The task of choosing preparation and mixing period parameters which excite these transitions with appreciable intensities is particularly important in light of the observation that most of the available magnetization is distributed among the lower orders. As noted previously, incomplete knowledge of the spin Hamiltonian often precludes the use of a computer to aid in this task. One is basically left with an experimental search problem. To this end, we have developed a procedure for rapid search over excitation sequence parameters which is called the parameter proportional phase incrementation (PPPI)[74] method. This search procedure is related to another which has been described recently[75]. In close analogy to the TPPI method (Sec. 2.4.2.2), the PPPI experiment involves the simultaneous incrementation of the search parameter and phase of the preparation period pulses with each acquisition of a two-dimensional experiment. In this work, the

parameter most commonly searched over is the multiple quantum preparation time τ and the PPPI procedure is discussed in terms of this parameter.

2.5.5.2 Description and Experimental Demonstration

The generalized schematic representation of the two-dimensional experiment shown in Figure 2.1 applies equally well to PPPI experiments and is repeated for convenience in Figure 2.6a. The search over τ is made by fixing the value of t_1 and incrementing τ and $\tau'(=\tau)$ on successive shots. That τ and τ' can be varied simultaneously is a direct result of the aforementioned symmetry of preparation and mixing periods. We demonstrate the method on the four spin acetaldehyde molecule dissolved in the liquid crystal p-octylphenyl 2-chloro-4-(p-heptylbenzoyloxy)-benzoate (Eastman 15320). The actual pulse sequence used is shown in Figure 2.6b with a single magnetization point at $t_2 = 0$ sampled for each value of τ.

Figure 2.7a shows one channel of the resulting proton NMR signal with $\tau/2$ varied from 12.80 to 17.92 msec. One component of the complex Fourier transform of this signal is displayed in Figure 2.7b. The contribution to this transform from the various orders of coherence $-4 \leq n^I \leq 4$ are well separated due to the r.f. phase shifts associated with each increment of τ. The contribution from one value of n^I is shifted to the origin, all other orders are cleared, and an inverse Fourier transform is then performed. The result is again a complex function of τ which is now specific to a particular order n^I and free of the extraneous modulation which the phase shifting introduced. The magnitude of this function is shown in Figure 2.7d for $n^I = 4$, the total spin coherence (Sec. 4.1.2). This is an excitation function, describing the magnitude of the $n^I = 4$ coherence for each value of $\frac{\tau}{2}$. Additional

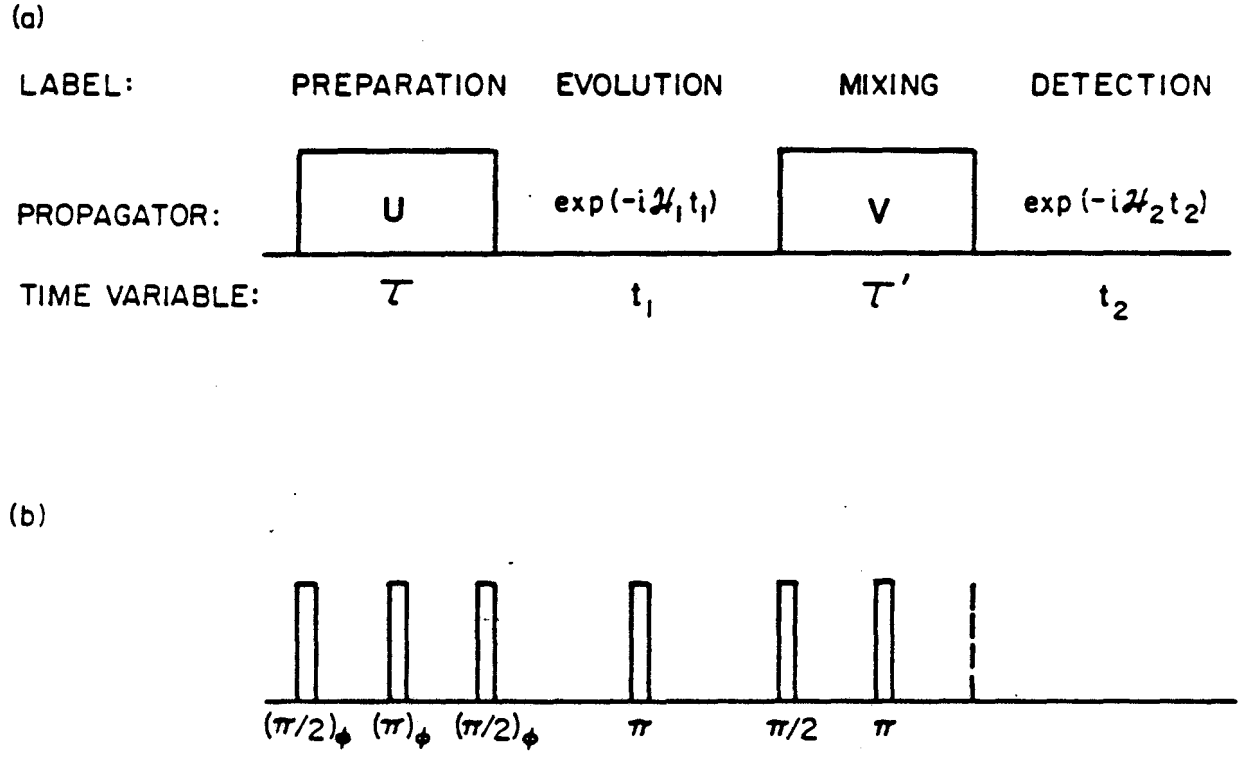

Figure 2.6. The PPPI experiment. (a) Generalized schematic diagram of the 2-D NMR experiment, reproduced from Figure 2.1. In the PPPI experiment, the r.f. phase of U and the search parameter characterizing both U and V are incremented from one shot to the next. The signal is collected in t_2 for a fixed value of t_1. (b) Actual pulse sequence used for the PPPI search over the excitation parameter τ. The phase of the first three r.f. pulses is incremented along with the excitation time $\tau = \tau'$. The other times and pulse phases are held constant. For each value of τ, a single magnetization point is sampled at $t_2 = 0$.

Figure 2.7. Collection and processing of data from a PPPI experiment. (a) One channel of the proton NMR signal of partially oriented acetaldehyde collected using the pulse sequence of Figure 2.6b, with preparation time variable $\tau/2$ ranging from 12.80 to 17.92 msec. (b) One component of the complex Fourier transform of the signal showing contributions from the various multiple quantum orders n^I, $-4 \leq n^I \leq 4$, well separated by incrementation of the phase of the preparation pulses. (c) Response of a single order ($n^I = 4$) shifted back to the origin to remove the apparent offset attributable to phase incrementation. (d) Display of the magnitude of the inverse Fourier transform of the response in (c). From this excitation function, the best values of the search parameter τ for the selected order may be chosen.

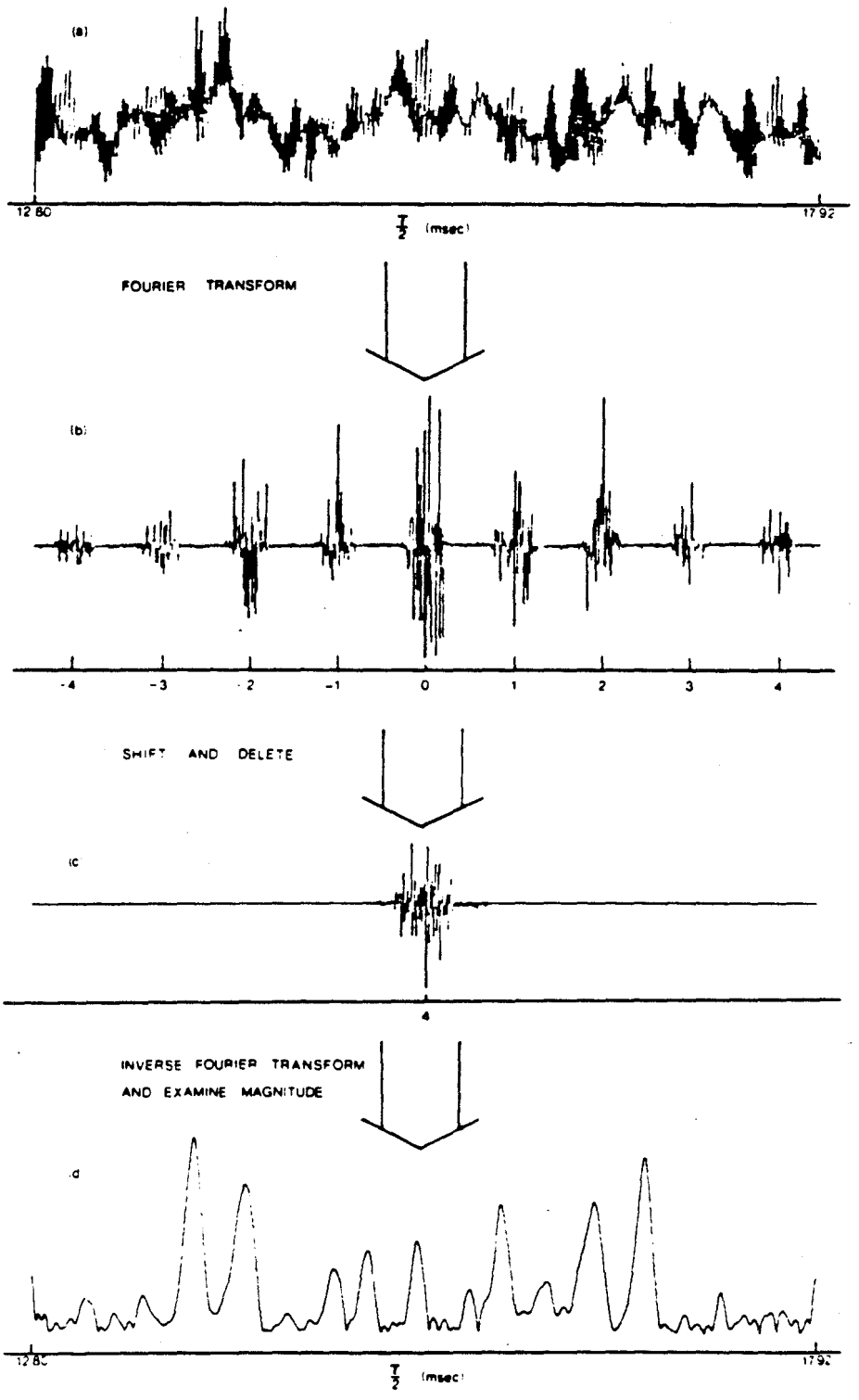
(a)
12.80
17.92
T/2 (msec)
FOURIER TRANSFORM
(b)
-4
-3
-2
-1
0
1
2
3
4
SHIFT AND DELETE
(c)
4
INVERSE FOURIER TRANSFORM
AND EXAMINE MAGNITUDE
(d)
12.80
17.92
T/2 (msec)

XBL 814-9049

excitation functions for n^I = 2 and 4 over the range τ = 2.0-14.0 msec are shown in Figure 2.8, along with computer simulations of these functions.

Figure 2.9 demonstrates the success of the PPPI search procedure. The upper trace is the excitation function of Figure 2.7d, the lower trace a section of this function on an expanded time scale. Superimposed are discrete measurements of the n^I = 4 line magnitude from a series of TPPI multiple quantum spectra using the pulse sequence of Figure 2.6b with fixed τ and variable t_1.

2.5.5.3 Limitations

The use of PPPI to find a satisfactory excitation sequence for the total spin coherence represents a particularly simple case, because this coherence is always associated with a single transition frequency. Within each multiple quantum order n^I the excitation function measures

$$\left| \sum_{i,j}{}' \rho_{ij}(\tau) \right|^2, \tag{2.38}$$

where the sum is restricted to i,j such that $(m_i^I - m_j^I) = n^I$. For spectra containing non-overlapping transitions, however, the quantity which we would like to maximize is

$$\sum_{i,j}{}' \left| \rho_{ij}(\tau) \right|^2, \tag{2.39}$$

the sum of the magnitudes of all of the n^I-quantum lines. For the total spin coherence, expressions (2.38) and (2.39) are equal and the PPPI search procedure accurately measures the transition magnitude.

The situation for n^I other than the total spin coherence is more complicated. Recall that the terms $\rho_{ij}(\tau)$ are themselves complex numbers

Figure 2.8. Experimental and simulated excitation functions for partially oriented acetaldehyde. Experimental functions were collected using the pulse sequence of Figure 2.6b with τ ranging from 2.0 to 14.0 msec. Computer simulations, shown below the experimental results, were generated using program EXFUNK[51]. Parameters used in the simulation of this AB_3 spin system are J_{AB} = 2.8 Hz, D_{AB} = -179.0 Hz, D_{BB} = 458.6 Hz, and ν_{AB} = 1360.9 Hz. These simulations reflect the computed quantity $|\Sigma' \rho_{ij}(\tau)|^2$, where the sum is restricted to those elements ρ_{ij} for which $m_i^I - m_j^I = n^I$. (a) $n^I = 2$ excitation functions. (b) $n^I = 4$ excitation functions. (In order to achieve the observed fit between experimental and simulated excitation functions, it was necessary to shift their time scales by 50 μsec with respect to one another. This is attributed to possible experimental timing errors.)

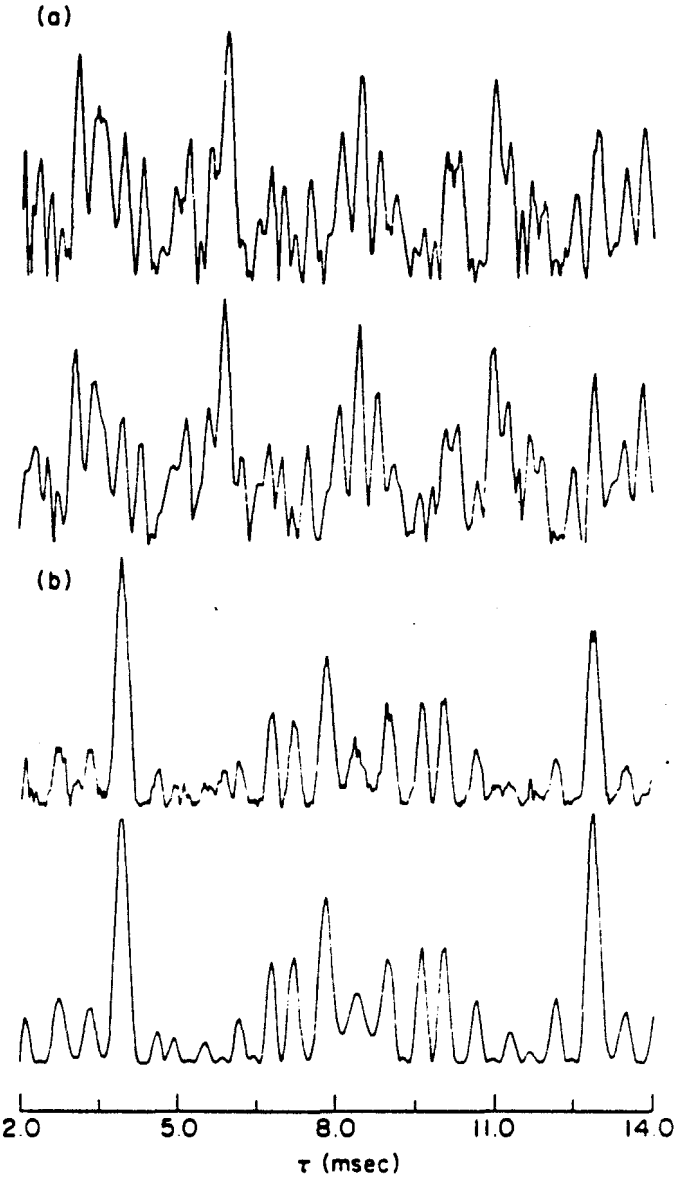

XBL 831-7512

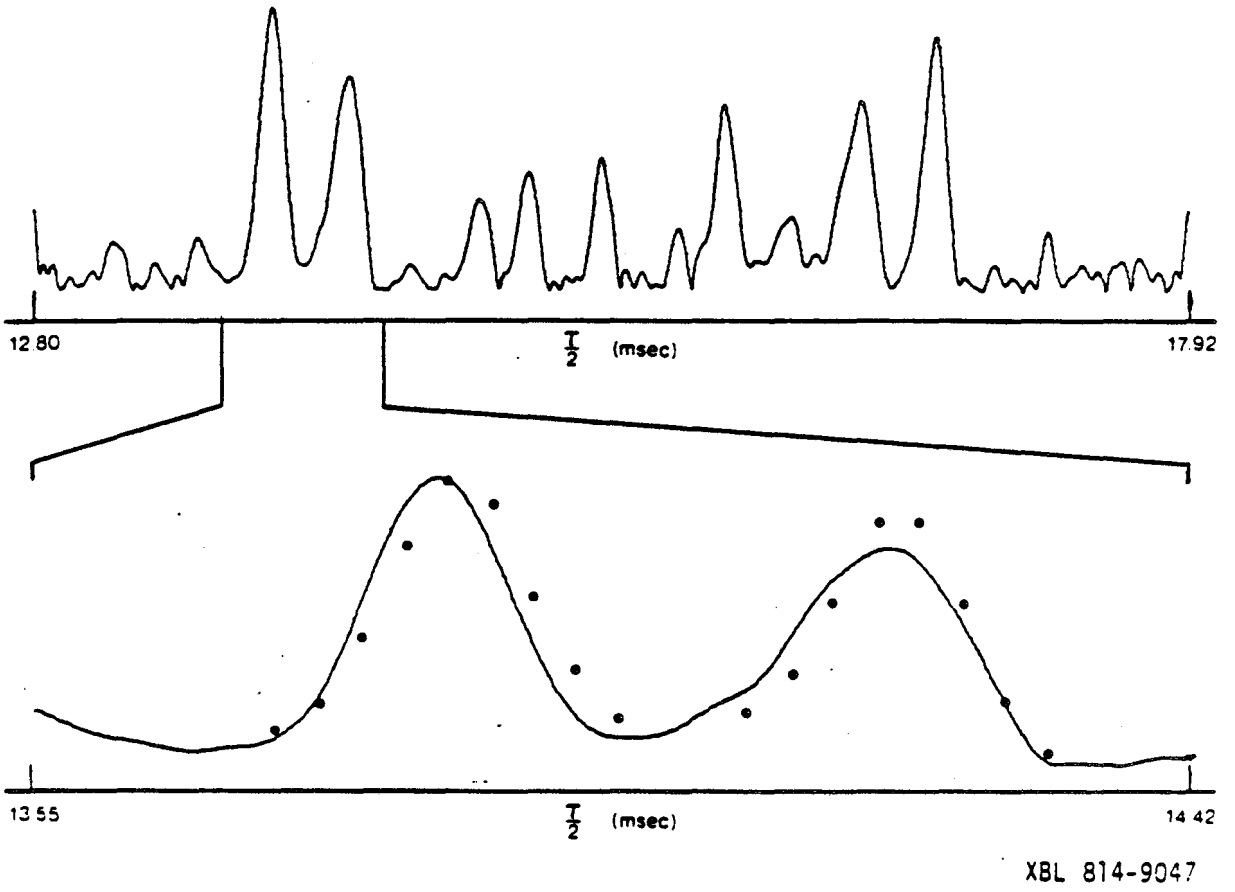

Figure 2.9. The $n^I = 4$ excitation function of partially oriented acetaldehyde with excitation time variable $\tau/2$ ranging from 12.80 to 17.92 msec, reproduced from Figure 2.7d. (b) Magnitude of the four-quantum line intensity obtained from a series of normal multiple quantum experiments with fixed τ and variable t_1. The points for individual experiments are superimposed on an expanded image of the relevant portion of the $n^I = 4$ excitation function.

with generally different unknown phases. The situation can then arise that for some fixed values of t_1, $|\Sigma' \rho_{ij}(\tau)|^2$ is small even though several of the individual terms have sizeable amplitudes. This is illustrated in Figures 2.10a and b which show two and three-quantum average excitation function magnitudes ($|\Sigma' \rho_{ij}(\tau)|^2$) and average squared coherence magnitudes ($\Sigma'|\rho_{ij}(\tau)|^2$) calculated for partially oriented acetaldehyde.

The amount of n^I-quantum coherence actually excited is always greater than or equal to that measured by the excitation function. As might be expected by considering the $\rho_{ij}(\tau)$ as random variables, this effect becomes more pronounced as the number of transitions in the order of interest increases. Because of phase cancellation it is possible to miss favorable preparation times τ using the PPPI method. On the other hand, one can be assured that a given τ will always be at least as good as measured by the excitation function and perhaps considerably better. For orders containing several transitions, the choice of a τ which is an excitation function maximum does not guarantee that each of the transitions will appear with appreciable intensity. It may therefore still be necessary to ensemble average together several different τ values to assure that all lines are represented. The PPPI method is then helpful in selecting a set of τ's for this ensemble average.

The PPPI method has been demonstrated by a search over the single timing parameter τ. It has been used repeatedly in the experiments of subsequent chapters to optimize the excitation sequence. For spin systems which are smaller than about eight spins, it generally proves possible to experimentally locate τ's for which non-selective experiments give line intensities much greater than their average values. In larger spin systems, selective excitation sequences (Sec. 2.5.4) may be required

Figure 2.10. Computed average excitation function magnitudes and average squared coherence magnitudes for partially oriented acetaldehyde. The former are described by $|\Sigma'\rho_{ij}(\tau)|^2$, the latter by $\Sigma'|\rho_{ij}(\tau)|^2$, where the restricted sums are over all elements ρ_{ij} for which $m_i^I - m_j^I = n^I$. These curves were generated by computer program EXFUNK[51] using the parameters of Figure 2.8. As demonstrated in that figure, it is the average excitation function magnitude which is the measured quantity in a PPPI experiment. For multiple quantum spectra in which all lines are resolved, however, it is the average squared coherence magnitude which we would like to maximize. Because the individual elements $\rho_{ij}(\tau)$ are themselves complex numbers, the average squared coherence magnitude always places an upper bound on the value of the average excitation function magnitude. (a) $n^I = 3$ average magnitudes. (b) $n^I = 2$ average magnitudes.

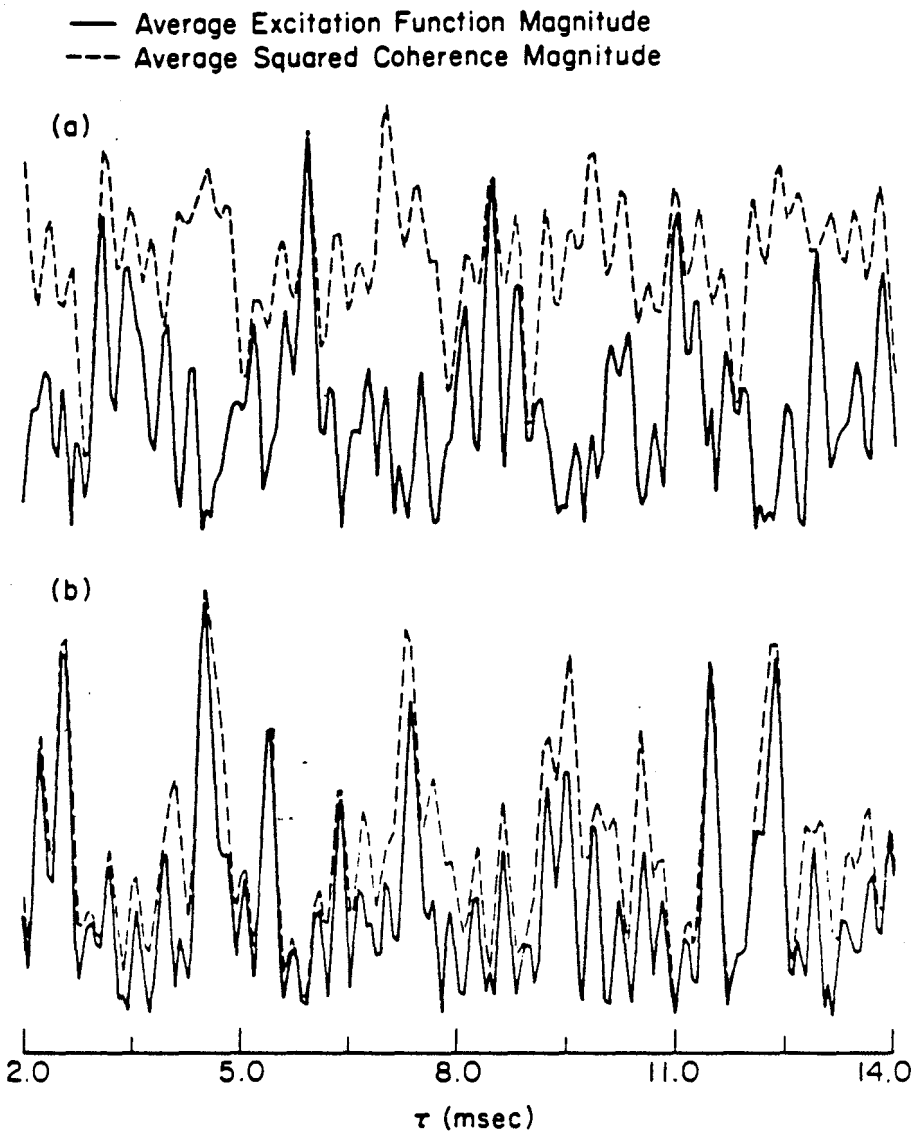
Average Excitation Function Magnitude
Average Squared Coherence Magnitude
(a)
(b)
2.0
5.0
8.0
11.0
14.0
τ (msec)

XBL 831-7511

to produce this same result. As previously described, these sequences may depend on several pulse and timing parameters and PPPI should also prove useful in optimizing these parameters.

Chapter 3: DETERMINATION OF DIPOLAR COUPLING CONSTANTS USING HETERONUCLEAR MULTIPLE QUANTUM NMR

To this point, only homonuclear spin systems consisting of N coupled protons have been considered. In this chapter we discuss the measurement of dipolar coupling constants in partially oriented heteronuclear spin systems of several protons and a single nucleus of another spin species. In particular, we consider systems consisting of N protons (I spins) and a randomly placed ^{13}C nucleus (S spin). This is the situation commonly encountered in organic molecules where the 1% natural abundance of ^{13}C implies that it is highly unlikely that two carbon-13 nuclei will be found in the same molecule. Other heteronuclear spins could also be considered, though we assume throughout that S is a spin-½ nucleus.

In Section 3.1 we motivate the development of heteronuclear multiple quantum (HMQ) NMR methods for the measurement of dipolar couplings[76]. The advantages of studying heteronuclear spin systems are considered and a schematic representation of both the single quantum and multiple quantum experiments is given. A formalism for describing the behavior of spin systems under a time-dependent Hamiltonian, average Hamiltonian theory[77-78], is reviewed in Section 3.2. The technique of S spin single quantum local field spectroscopy[79-93] and the less familiar I spin analog are considered in Section 3.3, with particular attention given to their resolution limitations.

Section 3.4 summarizes previous work on HMQ NMR and develops theoretically its advantages for the determination of heteronuclear dipolar couplings in anisotropic systems. The information content of a variety of HMQ experiments is discussed. Heteronuclear multiple quantum methods are experimentally demonstrated in Section 3.5 through excitation of the

high quantum spectra of partially enriched [1-^{13}C] benzene. Excitation sequences are described which allow relative line intensities to be easily calculated. Section 3.6 introduces the concept of scalar heteronuclear recoupled interactions by multiple pulse (SHRIMP) and discusses the incorporation of this new coherent averaging technique into the evolution period of HMQ experiments. In Section 3.7 we discuss how the HMQ spectra arising from different molecular species may be separated from one another by introducing the S spin chemical shift into the evolution period.

3.1 Motivation

3.1.1 Advantages of Heteronuclear Spin Systems

In Chapter 1 we observed that NMR spectra grow increasingly complex as the size of the coupled spin system is increased or its symmetry reduced. It is therefore, perhaps, surprising that one would wish to study heteronuclear spin systems at all. However, there are several recognized reasons why the apparent complication of introducing a heteronuclear spin can actually simplify the problem. These reasons provide much of the motivation behind the development of heteronuclear multiple quantum methods.

The first possible advantage of the heteronuclear system over the purely homonuclear case is that the number of heteronuclear couplings is N, in contrast to N(N-1)/2 homonuclear couplings. Consequently, both the simulation and interpretation of a spectrum which is determined only by heteronuclear unknowns are greatly simplified. While yielding a simpler spectrum, the reduced number of heteronuclear couplings poses one potential problem: there is less total information. However, this information is reobtained if the S spins are randomly distributed among different sites throughout the molecule. In the absence of isotopic

enrichment, this is always the case with ^{13}C nuclei.

A second advantage to studying heteronuclear spin systems derives from the fact that the spectrum of $\mathcal{H}_{IS}$ (Eq. 1.52) alone is particularly simple[79], because the individual terms of this Hamiltonian commute with one another. As noted previously, this commutation reflects the absence of non-energy-conserving flip-flop terms. There are fewer transitions and the relationships between transition frequencies and couplings are simpler than for a sum of non-commuting terms (as is found for the homonuclear case).

A third advantage to the study of heteronuclear systems is that the heteronuclear spin (e.g., ^{13}C, ^{15}N, ^{31}P) will often have a large chemical shift range, which can serve as a spreading parameter in the ω_2 dimension of a 2-D experiment. In the 2-D experiment, each observed dipolar splitting in ω_1 can then be correlated with an S spin chemical shift in ω_2. In this manner heteronuclear dipolar couplings can be associated with specific sites within the molecule.

The preceding paragraphs are not meant to suggest that the study of heteronuclear spin systems need always be considered as an alternative to studying purely homonuclear systems. In many cases, the measurement of heteronuclear dipolar couplings can be used to supplement the measured homonuclear couplings. As described further in Appendix A, each observed dipolar coupling for a partially oriented molecule is a function of both the elements of a dipolar Hamiltonian matrix and a set of order parameters. Furthermore (Section A.2.3), for non-rigid molecules it may be necessary to specify a relative probability and one or more order parameters for each of several different molecular conformations. For the homonuclear spin system alone, the problem of calculating all of the unknowns of

interest may be underdetermined. Consideration of the heteronuclear couplings can then provide additional needed information, allowing a more complete solution to be obtained.

3.1.2 Physical Picture of Single Quantum and Multiple Quantum Methods

As with the measurement of other parameters, accurate determination of heteronuclear dipolar couplings is dependent upon the ability to obtain well-resolved spectra which in turn are highly sensitive to these particular spin interactions. Measurement of heteronuclear couplings can be complicated by homonuclear couplings among the abundant spins, which can be comparable in size to the heteronuclear interactions. This limitation provided much of the motivation for the technique of ^{13}C local field spectroscopy[79-93] (Section 3.3.2), which focuses on the use of multiple pulse sequences to remove the dipolar couplings between abundant spins. A schematic representation of the single quantum local field experiment is given in Figure 3.1a. The proton spins independently experience the local field of the ^{13}C nucleus and vice versa. Couplings between protons are assumed to be effectively absent, which simplifies analysis considerably.

Even with this idealized removal of homonuclear interactions, the ^{13}C spectrum consists of 2^N transition frequencies, corresponding to the different ways of arranging the N proton spins up and down. Absent from the single quantum local field spectrum of either spin species are the algebraic signs of the heteronuclear couplings.

These difficulties are overcome through the use of heteronuclear multiple quantum techniques. Instead of attempting to remove the homonuclear couplings, we take advantage of these couplings to excite the protons as a coherent group, as suggested by Figure 3.1b. This grouping

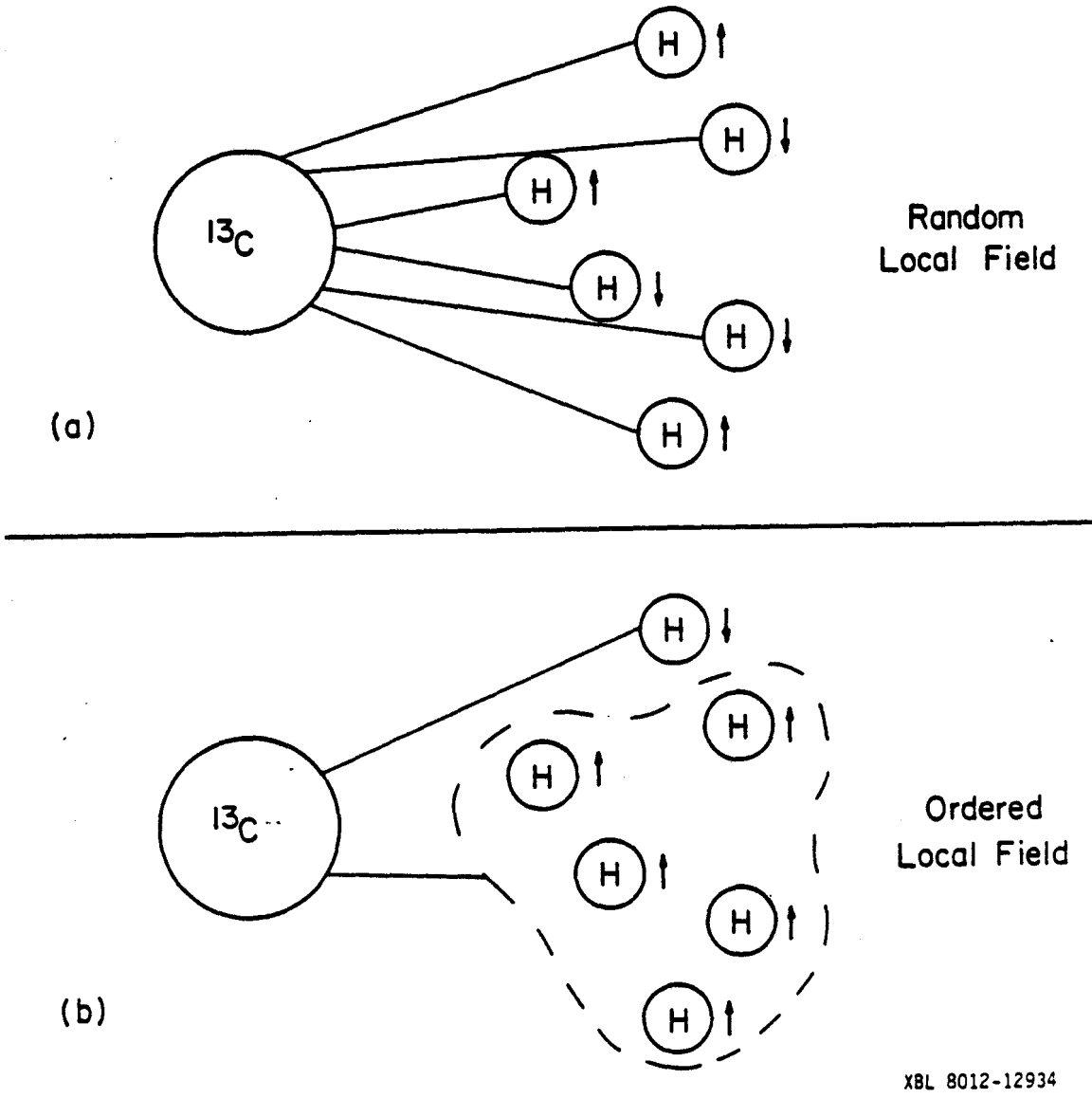

Figure 3.1. Schematic representation of the single quantum random local field and multiple quantum ordered local field for a system of one ^{13}C and N protons. (a) In the single quantum experiment the protons are assumed to be uncoupled from one another. A total of 2^N different proton configurations are possible, one of which is shown. The carbon spin may experience any of these different proton local fields. (b) In the heteronuclear multiple quantum experiment the protons are excited as a coherent group. One of the six possible groups of five protons is illustrated. This fewer number of ordered local fields enhances spectral resolution by reducing the number of possible transition frequencies. These frequencies measure sums and differences of individual heteronuclear couplings.

leads to an ordered field interaction between the protons and the ^{13}C spin. Transition frequencies are determined by sums of local fields, thereby providing information on the relative signs of heteronuclear coupling constants. The few distinct ways in which a large number of the protons can be grouped restricts the number of possible transitions, leading to increased spectral resolution.

3.2 Average Hamiltonian Theory

In much of what follows, we will want to consider the evolution of a spin system in the presence of a time-dependent r.f. field. This is the domain of coherent averaging theory, which is also known as average Hamiltonian theory[77,78,11,6]. When the irradiation sequence is periodic and cyclic, as defined below, average Hamiltonian theory prescribes a means by which the irradiation can be replaced by an effective, time-independent Hamiltonian. Average Hamiltonian theory has been reviewed in two recent texts[11,6] and the brief account given here, which relies heavily on the treatment of Haeberlen[11], serves only to outline the framework and notation of the method.

To begin, the Hamiltonian is separated into two terms

$$\mathcal{H}(t) = \mathcal{H}_{rf}(t) + \mathcal{H}_{INT}, \tag{3.1}$$

where the time-dependent r.f. is under the control of the experimenter and the internal Hamiltonian is assumed to be time-independent. In analogy to the transformation from laboratory to rotating frames (Section 1.1.5), we then go into an interaction representation defined by the r.f.:

$$U_{rf}(t) = T \exp[-i \int_0^t \mathcal{H}_{rf}(t')dt'], \tag{3.2}$$

where T is the Dyson time-ordering operator. In this representation, the density matrix, in the absence of $\mathcal{H}_{INT}$, remains stationary. The density matrix in this so-called toggling frame, $\tilde{\rho}(t)$, evolves according to

$$\tilde{\rho}(t) = U_{INT}(t)\ \tilde{\rho}(0)U_{INT}^{-1}(t), \tag{3.3}$$

where ($\hbar = 1$)

$$U_{INT}(t) = T \exp[-i \int_0^t \tilde{\mathcal{H}}_{INT}(t')dt'] \tag{3.4a}$$

and

$$\tilde{\mathcal{H}}_{INT}(t) = U_{rf}^{-1}(t)\mathcal{H}_{INT}U_{rf}(t). \tag{3.4b}$$

Defining

$$U(t) \equiv U_{rf}(t)U_{INT}(t), \tag{3.5}$$

Equation 3.3 in the normal rotating frame becomes

$$\rho(t) = U(t)\rho(0)U^{-1}(t). \tag{3.6}$$

For a general, time-dependent r.f. field, evaluation of the propagator U(t) can be most tedious. Calculation of this propagator becomes simpler if the Hamiltonian $\mathcal{H}_{rf}(t)$ is cyclic. In this case $U_{rf}(t)$ becomes periodic with cycle time t_c:

$$U_{rf}(t + t_c) = U_{rf}(t). \tag{3.7}$$

In particular, since $U_{rf}(0) = 1$, the r.f. propagator is also unity for all integer multiples of t_c. Furthermore, when $\mathcal{H}_{rf}(t)$ is cyclic, the toggling frame internal Hamiltonian is also periodic:

$$\tilde{\mathcal{H}}_{INT}(t+t_c) = \tilde{\mathcal{H}}_{INT}(t), \tag{3.8}$$

allowing the propagator for multiples of t_c to be written

$$U_{INT}(Nt_c) = [U_{INT}(t_c)]^N. \tag{3.9}$$

The evolution of the density matrix is then given as:

$$\rho(Nt_c) = [U_{INT}(t_c)]^N \rho(0) [U_{INT}^{-1}(t_c)]^N. \tag{3.10}$$

This equation states the very important result that the long time evolution of the system can be calculated by considering the propagator $U_{INT}(t)$ over a single cycle.

In evaluating $U_{INT}(t_c)$, it would be convenient to be able to write this propagator as a single exponential. This can be done using the Magnus expansion[94]:

$$\begin{aligned} U_{INT}(t_c) &= T \exp[-i \int_0^{t_c} \tilde{\mathcal{H}}_{INT}(t)dt] \\ &= \exp(-i(\bar{\mathcal{H}}^{(0)} + \bar{\mathcal{H}}^{(1)} + \bar{\mathcal{H}}^{(2)} + \ldots)t_c), \end{aligned} \tag{3.11}$$

where

$$\bar{\mathcal{H}}^{(0)} = \frac{1}{t_c} \int_0^{t_c} \mathcal{H}_{INT}(t)dt \tag{3.12a}$$

$$\bar{\mathcal{H}}^{(1)} = \frac{-i}{2t_c} \int_0^{t_c} dt_2 \int_0^{t_2} dt_1 [\tilde{\mathcal{H}}_{INT}(t_2), \mathcal{H}_{INT}(t_1)] \tag{3.12b}$$

$$\begin{aligned} \bar{\mathcal{H}}^{(2)} = \frac{-1}{6t_c} \int_0^{t_c} dt_3 \int_0^{t_3} dt_2 \int_0^{t_2} dt_1 \{ &[\tilde{\mathcal{H}}_{INT}(t_3), [\tilde{\mathcal{H}}_{INT}(t_2), \tilde{\mathcal{H}}_{INT}(t_1)]] \\ &+ [\tilde{\mathcal{H}}_{INT}(t_1), [\tilde{\mathcal{H}}_{INT}(t_2), \tilde{\mathcal{H}}_{INT}(t_3)]] \}. \end{aligned} \tag{3.12c}$$

The term $\bar{\mathcal{H}}^{(0)}$ is known as the average Hamiltonian while $\bar{\mathcal{H}}^{(n)}$ $(n \geq 1)$ is referred to as the n^{th} order correction term to the average Hamiltonian.

If $\tilde{\mathcal{H}}_{INT}(t)$ commutes with itself at all times, $\bar{\mathcal{H}}^{(0)}$ suffices to describe the evolution of the system. Otherwise, other terms in the expansion must be considered. For symmetric cycles having $\tilde{\mathcal{H}}_{INT}(t) = \tilde{\mathcal{H}}_{INT}(t_c - t)$, all odd-order corrections terms $\bar{\mathcal{H}}^{(n)}$ vanish[11].

3.3 Spectral Resolution of Single Quantum Methods

3.3.1 The Number of Transitions

In this section, the spectral resolution attainable by a variety of single quantum methods is reviewed. As described previously with regards to NMR in homonuclear spin systems, a convenient estimate of achieveable resolution is obtained by enumerating the number of transitions allowed with a certain technique. The ability to resolve individual transitions requires roughly that

$$Z < M_2^{\frac{1}{2}} T_2, \tag{3.13}$$

where Z is the number of allowed transitions, $M_2^{\frac{1}{2}}$ is the square root of the second moment of the spectrum, and T_2 is the relaxation time which determines the width of individual transitions. For a typical molecule dissolved in a liquid crystalline solvent, the T_2 relaxation sets an upper limit of $10^2 - 10^3$ on Z.

Figure 3.2a illustrates the increase in spectral complexity which accompanies an increase in the number of proton spins. The spin system considered in this figure consists of N protons and a ^{13}C nucleus, in the absence of any symmetry. The number of single quantum ^{13}C transitions in such a system is $\binom{2N}{N}$, while the number of single quantum proton transitions is $2\binom{2N}{N-1}$, twice the number found in the absence of the carbon spin. The logarithm of the number of allowed transitions Z as a function of N for both ^{13}C and ^{1}H spectra is plotted in this figure. In both cases,

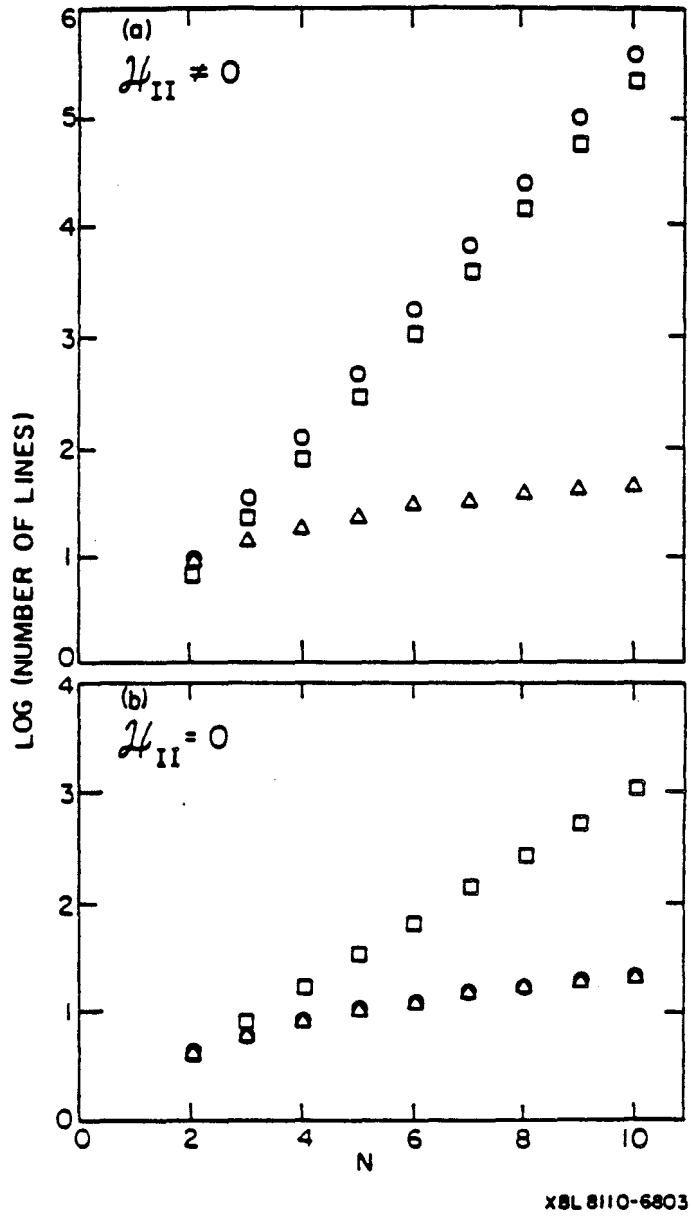

Figure 3.2. Graph of $\log_{10}$ (number of spectral lines) vs. number of I spins (N) for the I spin single quantum spectrum (○), the S spin single quantum spectrum (□), and the ($n^I = N-1$, $n^S = 0$) HMQ spectrum (△). (a) $\mathcal{H}_{II} \neq 0$, the case in which homonuclear dipolar couplings are not removed or scalar couplings are not negligible. (b) $\mathcal{H}_{II} = 0$, the case in which all homonuclear couplings are zero. Although this limit is approached when $\mathcal{H}_{II}^D$ is removed in local field spectra, the scalar terms $\mathcal{H}_{II}^J$ prevent its precise realization.

Z grows exponentially with N, quickly resulting in spectra having far too many lines to allow extraction of useful coupling information. This point is further illustrated by Figure 3.3a which shows a simulation of the single quantum carbon spectrum of partially oriented [1 - ^{13}C] benzene. Individual transitions are just barely resolved for this six proton spin system.

3.3.2 S Spin Local Field Spectroscopy

Over the past few years, several groups have addressed the problem of extracting heteronuclear dipolar coupling constants in solids[80-84] and in liquid crystals[85] using the technique of ^{13}C local field spectroscopy. Recently this technique has also been applied to powder samples rotating at the magic angle[86-93]. As mentioned previously, it is couplings among the protons which are responsible for much of the carbon spectral complexity. In ^{13}C local field spectroscopy, one uses multiple pulse sequences[77,78,95-98] or magic angle irradiation[99] to remove the proton homonuclear dipolar couplings. In addition, spectra due to inequivalent ^{13}C's are sorted out by collecting proton decoupled carbon spectra in a second time dimension. Double Fourier transformation of the resulting two-dimensional data array yields ^{13}C spectra in the absence of proton-proton dipolar couplings and separated in ω_2 by their carbon chemical shifts. Figure 3.4a shows a typical S spin local field spectroscopy pulse sequence.

Figure 3.3b is a simulation of an ideal single quantum ^{13}C local field spectrum of partially oriented [1 - ^{13}C] benzene. A common feature of all published pulse sequences designed to remove homonuclear dipolar couplings is a scaling of the proton chemical shifts and heteronuclear interactions ($\mathcal{H}_{IS}$) by a common factor $K \leq \frac{1}{\sqrt{3}}$. This accounts for the

Figure 3.3. Simulations of ^{13}C single quantum spectra of partially oriented [1 - ^{13}C] benzene, generated by computer program CARBOY[51]. The parameters used are those of reference [102], with all couplings expressed in Hz: D_{12} = -403.854, D_{13} = -77.498, D_{14} = -50.257, D_{15} = -1119.617, D_{25} = -153.006, D_{35} = -39.280, D_{45} = -26.489; J_{12} = 7.549, J_{13} = 1.378, J_{14} = 0.650, J_{15} = 157.914, J_{25} = 1.052, J_{35} = 7.653, J_{45} = -1.257. (a) Stick simulation of normal spectrum with $\mathcal{H}_{II}$ fully operative. The presence of homonuclear dipolar couplings makes extraction of heteronuclear coupling constants difficult. (b) Stick simulation of local field spectrum with $\mathcal{H}_{II}^{D}$ = 0. The multiple pulse scale factor is $1/\sqrt{3}$. Although the total number of transitions has been greatly reduced relative to (a), the density of lines within each of the two well-resolved groups is comparable.

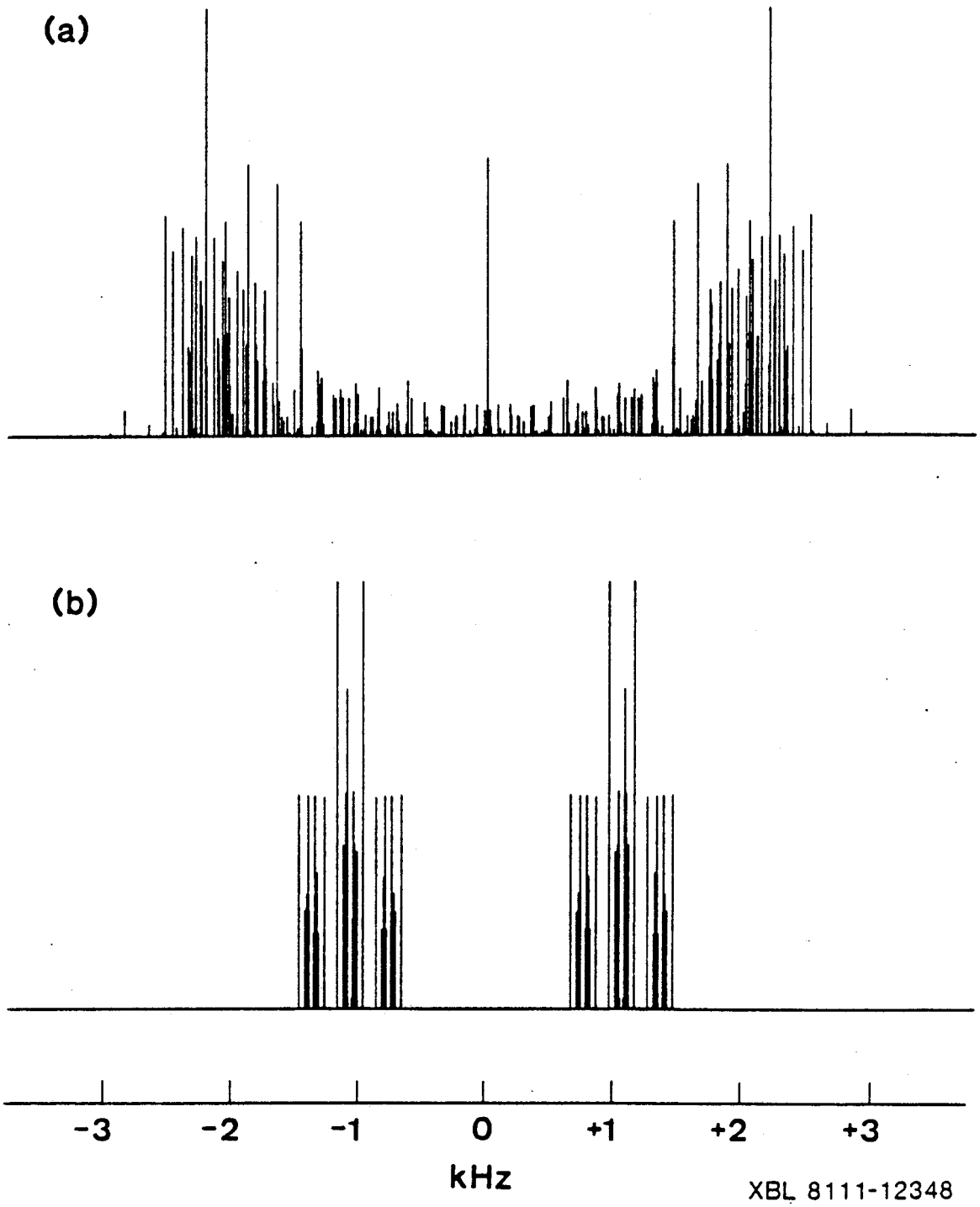
(a)
(b)
-3
-2
-1
0
+1
+2
+3
kHz
XBL 8111-12348

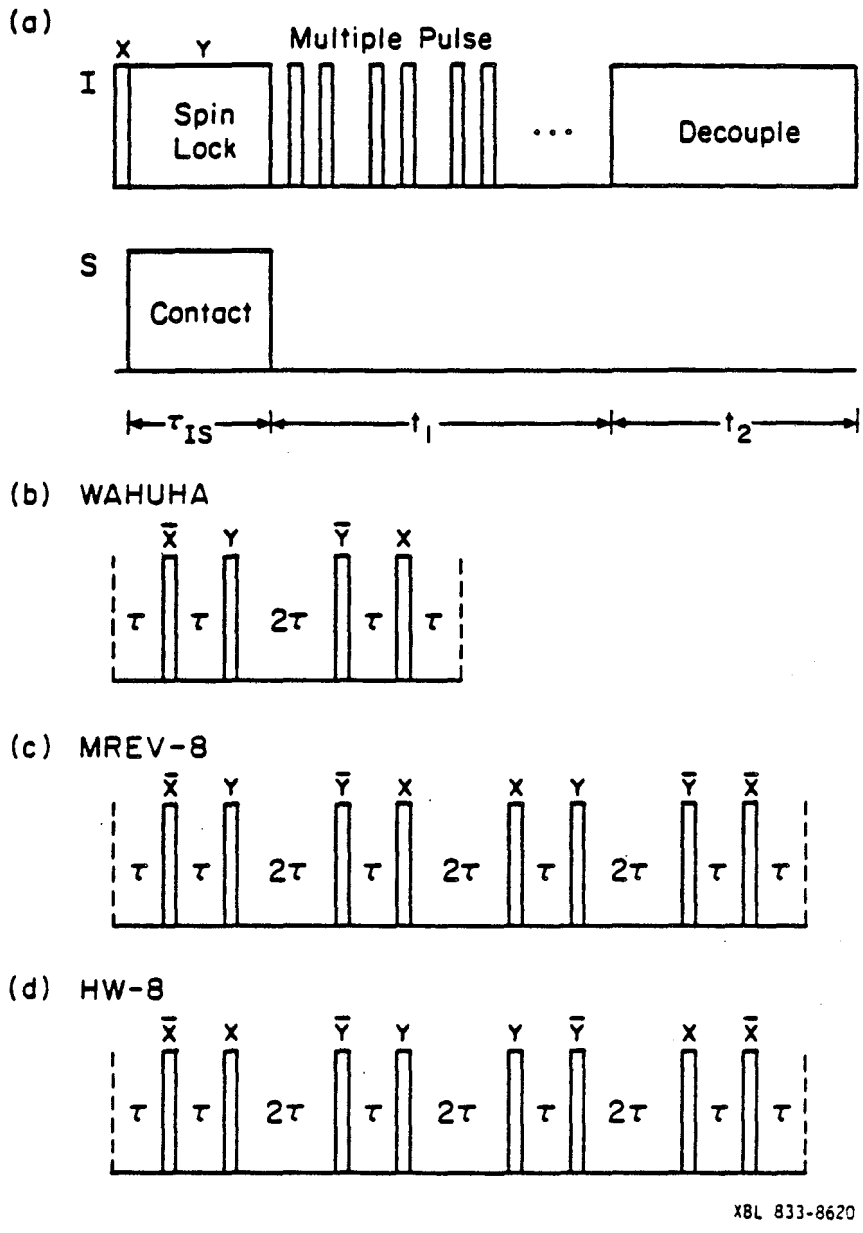

Figure 3.4. (a) S spin local field spectroscopy pulse sequence[80-84]. The S spins are first cross polarized during τ_{IS}. They evolve for the variable time t_1 with a multiple pulse sequence applied to the protons. For each value of t_1, a proton-decoupled free induction decay is collected during t_2. Figures (b)-(d) provide 3 examples of possible proton multiple pulse sequences. (b) WAHUHA[77,78]; this four pulse sequence has a cycle time $t_c = 6\tau$ and a scale factor $K = 1/\sqrt{3}$. (c) MREV-8[96]; this eight pulse sequence has $t_c = 12\tau$ and $K = \sim\sqrt{2}/3$. (d) HW-8[78]; this eight pulse sequence has $t_c = 12\tau$ and $K = 1/3$. In addition, the resulting average Hamiltonian $\bar{\mathcal{H}}^{(0)}$ for this sequence is secular.

decreased spectral width observed in this spectrum. Even for this relatively simple spin system the tendency of the transitions to cluster into unresolvable multiplets is apparent. Within the two well-resolved groups of lines, the line density is similar to that of the unperturbed spectrum of Figure 3.3a.

The high line density in Figure 3.3a can be traced to two different sources. Owing to their scalar nature, the homonuclear J-couplings are not removed by the multiple pulse sequences designed to average $\mathcal{H}_{II}^{D}$ to zero. In addition, as demonstrated in Figure 3.2b, the number of transitions increases exponentially with the number of protons N whether or not the protons are coupled to one another. As a result, only the largest proton-carbon coupling is usually resolved. This coupling, corresponding in [1 - ^{13}C] benzene to the interaction between the carbon and its bound proton, is measured directly by the splitting between the centers of the two groups of lines in Figure 3.3b. The smaller couplings appear only as a line broadening, which is difficult to analyze quantitatively.

3.3.3 I Spin Local Field Spectroscopy

An alternate version of the single quantum local field experiment would be to measure the parameters of $\mathcal{H}_{IS}$ by observing the abundant I spins while again removing homonuclear dipolar couplings by means of a multiple pulse sequence. Studies of this type have been made on protons in solid state powder samples[100,101]. We consider here the resolution potential of this technique in studies of partially oriented molecules.

In the limit that $\mathcal{H}_{II} = 0$, the proton local field spectrum consists of N pairs of lines. This dependence of the number of lines on N is indicated in the lowest curve of Figure 3.2b. Each pair of lines is the spectrum of a single proton, with a splitting given by $2K|F_{iS}|$. Thus

the parameters of $\mathcal{H}_{IS}$ are available directly once the multiple pulse scaling factor K is established. The resolution enhancement over the ^{13}C local field spectrum is considerable, since the same information formerly present in 2^N lines is now present in only 2N lines. Still missing from the spectrum, however, is information concerning the relative signs of the F_{iS} parameters.

As discussed in Section 3.3.2, the limit $\mathcal{H}_{II} = 0$ is never actually reached due to the homonuclear J-couplings. This is illustrated in Figure 3.5a, the simulation of an idealized proton local field spectrum of oriented [1-^{13}C] benzene. The unperturbed proton spectrum of this compound has been previously reported[102]. Although the largest proton-proton scalar coupling is less than 10 Hz, the spectrum of Figure 3.5a consists of multiplets spanning several times this value. Figure 3.5b illustrates the spectrum of this molecule in the absence of any proton-proton couplings. Comparison of these two spectra clearly indicates that the homonuclear scalar couplings limit the accuracy with which the couplings F_{iS} can be measured by proton local field spectroscopy. Nonetheless, comparison of Figures 3.5a and 3.3b does demonstrate the potential resolution advantage of I spin local field spectra over the S spin version for the measurement of small heteronuclear couplings.

3.4 Heteronuclear Multiple Quantum NMR

3.4.1 Background

The principal focus of heteronuclear multiple quantum NMR experiments to date has been the observation of dilute S spin transitions with the greater sensitivity afforded by the abundance and larger gyromagnetic ratio of protons. In solids, the multiple quantum transitions of the S = 1 spins deuterium[103,104] and ^{14}N[105,106] and the $S = \frac{3}{2}$ spin ^{23}Na[107]

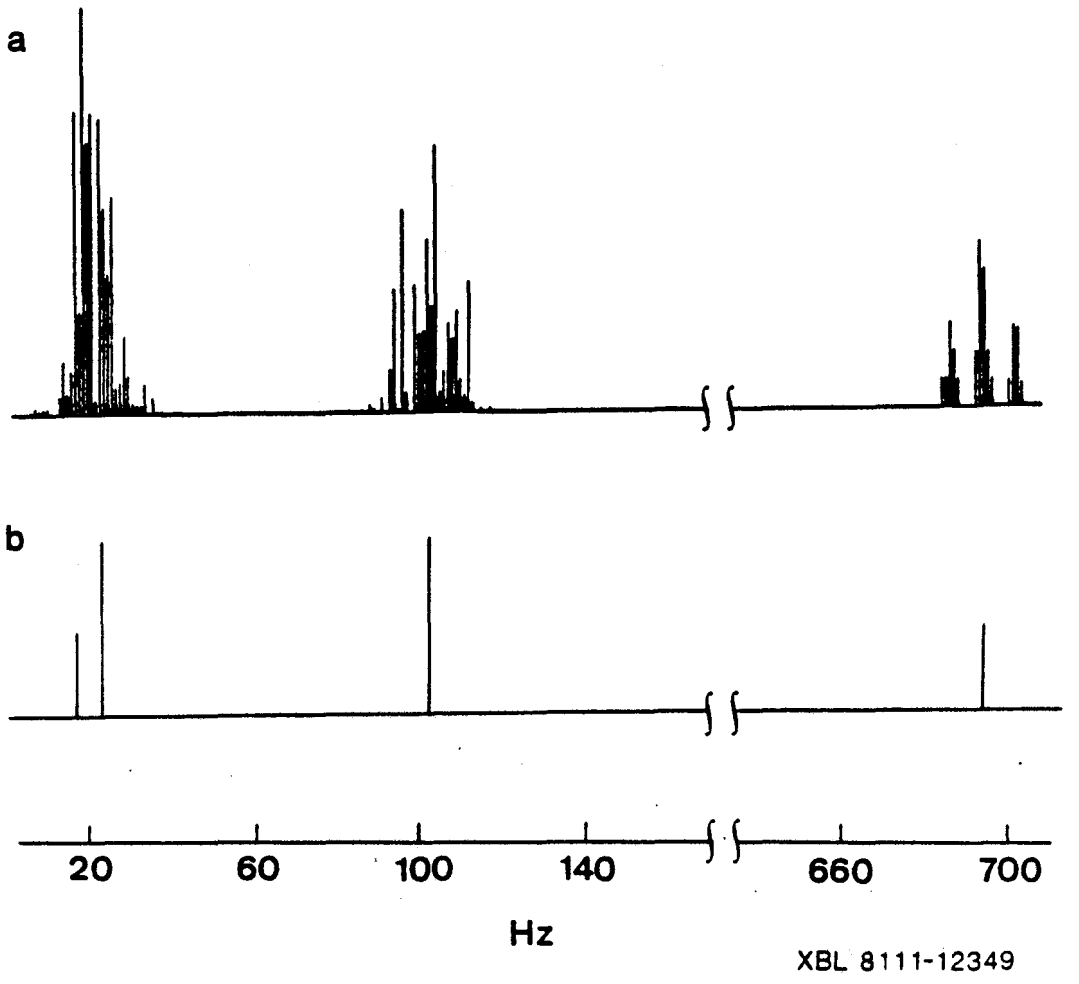

Figure 3.5. Simulations of ^{1}H single quantum spectra of partially oriented [1 - ^{13}C] benzene. Parameters are again those of reference [102]. (a) Local field spectrum with $\mathcal{H}_{II}^{D} = 0$, multiple pulse scale factor = $1/\sqrt{3}$. The information content relative to the corresponding ^{13}C local field experiment (Fig. 3.3b) is considerably improved. The two largest F_{iS} are given by the positions of the two rightmost multiplets. Still, the homonuclear scalar couplings, which are responsible for the dense packing of spectral lines, limit the accuracy with which F_{iS} may be determined. (b) The hypothetical local field spectrum in the absence of all homonuclear couplings ($\mathcal{H}_{II} = 0$).

have been observed with the aid of proton cross polarization. In these samples the spin system is of macroscopic dimension and the coherence transfer is treated with a spin temperature formalism.

In liquids, HMQ experiments on I_nS(I,S = spin-½ nuclei) systems have demonstrated such fundamental multiple quantum phenomena as the relaxation of forbidden and degenerate coherences[108-110], heteronuclear coherence transfer echoes[63], and the indirect detection of dilute spin chemical shifts with enhanced sensitivity[111]. Recently the double quantum transitions of ^{14}N and deuterium have been observed. The ^{14}N double quantum spectrum of ammonium ion in aqueous solution has been detected using only ^{14}N magnetization by spin-tickling the protons[112] and through transfer of coherence from the protons[66]. A similar coherence transfer has been applied to the study of deuterochloroform and perdeuterated glycerol[113].

In liquid crystals, the deuterium double quantum transition of partially oriented CH_2DCN has been detected[114] through proton magnetization using a variety of different preparation and detection schemes, including pulsed coherence transfer.

3.4.2 Formalism

Since the heteronuclear coupling Hamiltonian $\mathcal{H}_{IS}$ contains no flip-flop terms, the total Zeeman quantum numbers for each spin species separately are good quantum numbers for free evolution of the system. It is therefore useful to characterize elements of the density matrix describing the system by the quantities n^I and n^S defined such that

$$\rho(\tau) = \sum_{n^I} \sum_{n^S} \rho_{n^I,n^S}(\tau) \qquad (3.14)$$

$$\left[I_z, \rho_{n^I, n^S}\right] = n^I \rho_{n^I, n^S} \tag{3.15}$$

$$\left[S_z, \rho_{n^I, n^S}\right] = n^S \rho_{n^I, n^S}. \tag{3.16}$$

As before, n^I is the difference in total I spin Zeeman quantum number between the connected states; n^S plays an analogous role for the Zeeman quantum number of the S spin. The defining commutation relations of Equations 3.15 and 3.16 insure that each set of indices represents a separate spectrum which may be isolated by the techniques of TPPI, PFT, and CTEF described in Chapter 2. The generalized diagram of Figure 2.1 applies equally well to HMQ experiments where now the propagators U and V may involve irradiation of both spin species.

While the initial magnetization and detected magnetization can be that of either I or S spins, the signal-to-noise advantage[111,114,66] of using the magnetization of the spin with the greater gyromagnetic ratio is considerable. In most cases of interest, the I spins are protons and only their magnetization need be considered. As discussed in Section 3.7, this is not inconsistent with making use of the S spin chemical shift as a spreading parameter.

For $S = \frac{1}{2}$, a convenient operator basis for describing the dynamics of the combined I-S coherence is the simple products, one factor for each spin, of the single spin operators

$$S_+ = |\alpha\rangle\langle\beta| \qquad S_- = |\beta\rangle\langle\alpha| \qquad S_0^+ = |\alpha\rangle\langle\alpha|$$

$$S_0^- = |\beta\rangle\langle\beta|. \tag{3.17}$$

An analogous definition holds for the individual I spin operators: I_{+i}, I_{-i}, I_{0i}^+, I_{0i}^-; i = 1 to N. Any product of one such operator for each

spin may be classified with respect to the quantum number n^I by adding up the subscripts of the I spin factors. The quantum number n^S is the subscript of the S spin factor. The usefulness of this operator basis is that each of its members is an eigenoperator for evolution under $\mathcal{H}_{IS}$ and that it provides a compact description for the relevant part of the prepared density operator for several of the experiments to be described.

3.4.3 Higher Order HMQ Spectra

The heteronuclear multiple quantum spectra characterized by $n^I = N$, $N-1$ and $n^S = 0, \pm 1$ are of particular interest because they have the fewest number of transitions compatible with full determination of the heteronuclear couplings F_{iS}. Each of these spectra will be discussed for $S = \frac{1}{2}$ with regard to the number of transitions and to the transition frequencies in the limit that $\mathcal{H}_{II} = 0$. The transition frequencies are approximate, since $\mathcal{H}^J_{II}$ is neglected. The important point is that the number of transitions does <u>not</u> increase drastically when $\mathcal{H}^J_{II}$ is admitted, unlike the situation observed for single quantum I spin local field spectroscopy Section 3.3.3. Thus numerical inclusion of $\mathcal{H}^J_{II}$, whose parameters may be closely approximated by the liquid state values, does not seriously affect the resolution and perturbs the frequencies only slightly from the analytical forms given below.

As noted in Section 3.3.2, the experimental removal of $\mathcal{H}^D_{II}$ by multiple pulse sequences results in a scaling of the terms $\mathcal{H}^Z_I$ and $\mathcal{H}_{IS}$ by a common factor K. Because the discussion is simplified when n^I is a good quantum number, it will be assumed in this section that the effective Hamiltonian $\mathcal{H}_1$ during the evolution period is

$$\mathcal{H}_1 = \bar{\mathcal{H}}^{(0)}_{IS} + \mathcal{H}^J_{II} = -K \sum_i 2F_{iS} I_{zi} S_z - \sum_{i<j} J_{ij} \underset{\sim}{I}_i \cdot \underset{\sim}{I}_j . \qquad (3.18)$$

This effective heteronuclear coupling is obtained, for example, by the secular HW-8 multiple pulse cycle[77] illustrated in Figure 3.4d, for which $K = \frac{1}{3}$. Such a pulse sequence may be augmented by simultaneous π pulses to both the I and S spins in-between cycles in order to remove the Zeeman terms, and hence the magnetic field inhomogeneity, from the evolution period. Other pulse sequences resulting in the $\mathcal{H}_1$ of Equation 3.18 are also possible.

3.4.3.1 $n^I = N$, $n^S = 1$

Consider first the evolution during t_1 of the total spin coherence (Sec. 4.1.2) of the combined I-S system. This coherence is characterized by quantum numbers $n^I = N$, $n^S = 1$ and the eigenoperator is $S_+ \prod_i I_{+i}$, which commutes with $\mathcal{H}_{IS}$. In fact, this coherence also commutes with the homonuclear spin-spin couplings, so that its evolution under the full spin Hamiltonian is determined only by the sum of the Zeeman terms.

3.4.3.2 $n^I = N$, $n^S = 0$

The simplest case which can yield dipolar coupling information is that of the two eigenoperators with $n^I = N$, $n^S = 0$. These are $S_0^{\pm} \prod_i I_{+i}$, and their commutators with $\bar{\mathcal{H}}_{IS}^{(0)}$ are given by

$$[\bar{\mathcal{H}}_{IS}^{(0)}, S_0^{\pm} \prod_i I_{+i}] = \pm K(\sum_i F_{iS})(S_0^{\pm} \prod_i I_{+i}). \qquad (3.19)$$

Since the $n^I = N$, $n^S = 0$ operators commute with the I-I couplings, they are the correct eigenoperators whether or not $\mathcal{H}_{II}$ has been removed. This commutator shows that the spectrum characterized by $n^I = N$, $n^S = 0$ consists of a pair of lines with splitting $2K|\sum_i F_{iS}|$ if a multiple pulse sequence is used, or $2|\sum_i F_{iS}|$ if only a single π pulse is applied to both spins at time $\frac{t_1}{2}$. A comparison of these two spectra provides a direct

experimental measurement of K which is free of inhomogeneous broadening.

3.4.3.3 $n^I = N-1,\ n^S = 1$

The 2N operators characterized by $n^I = N-1,\ n^S = 1$ are eigenoperators under $\bar{\mathcal{H}}_{IS}^{(0)}$ having eigenvalues determined by the commutators

$$[\bar{\mathcal{H}}_{IS}^{(0)},\ S_+ I_{0i}^{\pm} \prod_{j\neq i} I_{+j}] = (\bar{+}KF_{iS})(S_+ I_{0i}^{\pm} \prod_{j\neq i} I_{+j}). \tag{3.20}$$

This corresponds to a spectrum of N pairs of lines, each pair giving the magnitude of one of the heteronuclear couplings F_{iS}. No information regarding the relative signs of these couplings is supplied. These transitions therefore yield the same information as the S spin local field experiments of Section 3.3.2, but the information is now present in 2N rather than 2^N lines. In contrast to I spin local field spectroscopy, the presence of homonuclear I-I couplings does <u>not</u> increase the number of lines in the $n^I = N-1,\ n^S = 1$ spectrum. Therefore, experiments done without removal of homonuclear dipolar couplings, or those in which $\mathcal{H}_{II}^D$ is removed but homonuclear J-couplings are not negligible, do not suffer the loss in resolution seen in the corresponding single quantum local field experiments.

3.4.3.4 $n^I = N-1,\ n^S = 0$

Finally we consider the case where $n^I = N-1,\ n^S = 0$. There are 4N eigenoperators of $\bar{\mathcal{H}}_{IS}^{(0)}$, whose eigenvalues are determined by the commutators

$$[\bar{\mathcal{H}}_{IS}^{(0)},\ S_0^{\pm} I_{0i}^{\pm} \prod_{j\neq i} I_{+j}] = \pm K(\sum_{j\neq i} F_{jS})(S_0^{\pm} I_{0i}^{\pm} \prod_{j\neq i} I_{+j}), \tag{3.21}$$

where the sign preceding K is defined with respect to the superscript of

the S spin operator. Each eigenvalue is two-fold degenerate. The resulting spectrum consists of N pairs of lines, with splittings proportional to the sum of all but one of the I-S couplings. The one coupling absent is different for each of the N pairs. We thus have N linearly independent equations whose solutions give the N heteronuclear couplings F_{iS}, including relative signs. When $\mathcal{H}_{II} \neq 0$, the degeneracy mentioned above is lifted, and up to 2N pairs of lines are possible.

This analysis could easily be extended to lower order spectra with equally simple expressions for the various eigenvalues. In the limit that $\mathcal{H}_{II} = 0$, the spectra will always consist of pairs of lines whose splittings are proportional to sums and differences of the heteronuclear coupling constants. As is the case for a homonuclear spin system, the number of lines increases quite rapidly with decreasing n^I, leading to a loss of resolution. The heteronuclear Hamiltonian $\mathcal{H}_{IS}$ is, however, fully determined by the four spectra discussed above.

3.5 Experiments

3.5.1 Pulse Sequences and Spectra

Heteronuclear multiple quantum experiments were performed on [1 - ^{13}C] benzene enriched to 90% and dissolved at 40 mol% in Eastman 15320 nematic liquid crystal. The temperature was regulated at 26.0 ± 0.1°C. The homebuilt spectrometer, which is described in Appendix B, operates at 182 MHz proton Larmor frequency. Proton signal was detected throughout with sampling of the transverse magnetization at time $t_2 = 0$.

Figure 3.6 illustrates those portions of the [1 - ^{13}C] benzene energy level diagram relevant to these experiments. Individual states are sorted based on both their ^{13}C Zeeman quantum number, m^S, and their proton

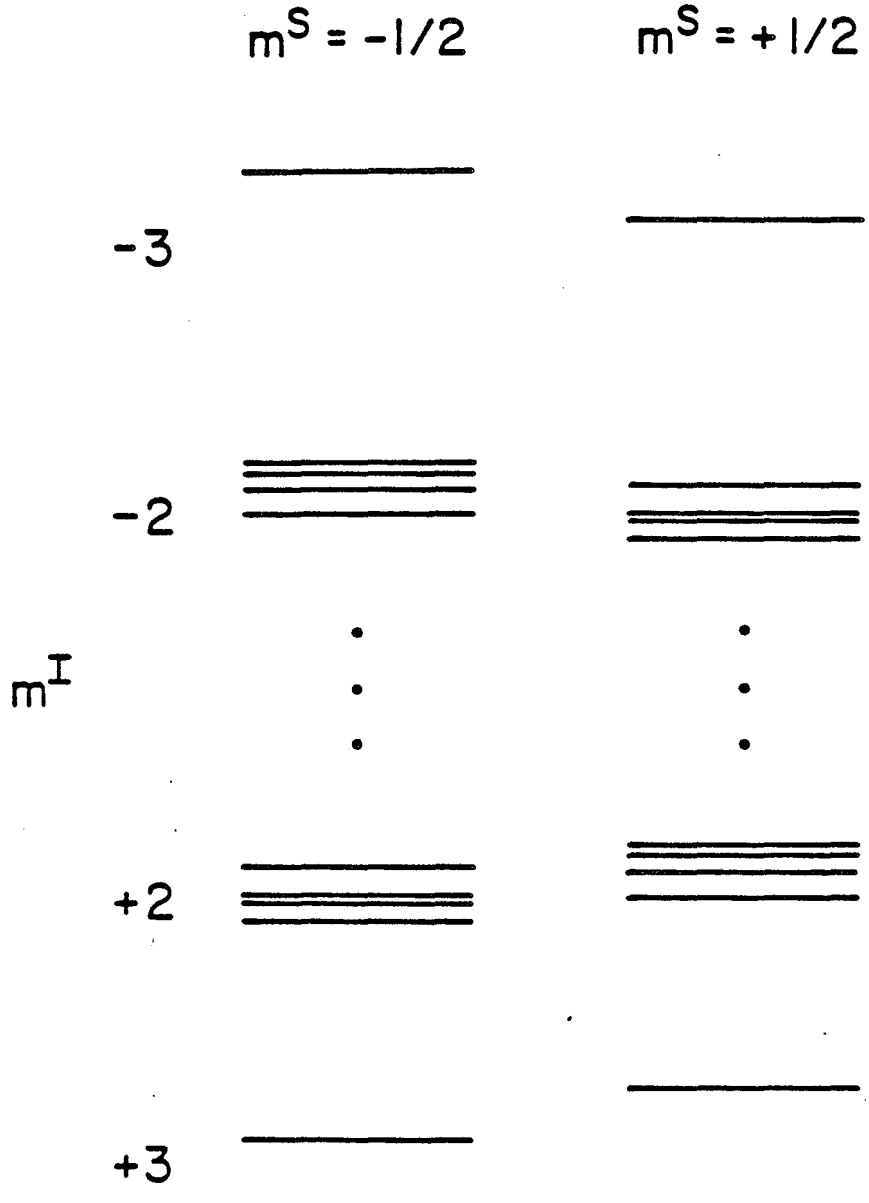

XBL 8110-7174 A

Figure 3.6. [1 - ^{13}C] benzene energy level diagram. Energy levels are sorted by total proton Zeeman quantum number (m^I) and by ^{13}C Zeeman quantum number (m^S). This is useful in that both m^I and m^S, and hence the differences $n^I = \Delta m^I$ and $n^S = \Delta m^S$, are good quantum numbers for free evolution of the spin system. Subspectra with $n^S = 0$ correspond to vertical transitions, while those with $n^S = \pm 1$ connect a state in the left hand column with one on the right.

total Zeeman quantum number, m^I. In the absence of heteronuclear flip-flop terms, both of these are good quantum numbers of the system. On this energy level diagram, spectra characterized by $n^S = 0$ correspond to vertical transitions, while those with $n^S = \pm 1$ describe diagonal transitions, connecting a state in the left-hand column with one on the right.

A simple pulse sequence for obtaining spectra characterized by $|n^I| \leq N$, $n^S = 0$ is illustrated in Figure 3.7a. The pulse sequence of Figure 3.7b employs, in addition, a pulsed magnetic field gradient to allow signal from a single n^I value to be selected by the CTEF technique described in Section 2.4.2.4. Experimental spectra obtained for $n^I = 5$ and $n^I = 6$ using this latter sequence are shown in Figure 3.8a. The $n^I = 6$ spectrum shows a doublet whose splitting measures $2 \sum_i F_{iS}$ independent of all I-I couplings. The small, central peak in this spectrum is the total spin coherence from the unlabeled molecules. The $n^I = 5$ spectrum consists of one pair of lines from the unlabeled molecules and three pairs from [1-^{13}C] benzene molecules. The energy level diagram (Fig. 3.6) suggests that there should be eight pairs of $n^I = 5$, $n^S = 0$ lines. An intensity calculation, discussed in Section 3.5.2, shows the unobserved transitions to have small intensities for the excitation sequence used. Theoretical stick spectra, with line intensities adjusted for observed differences in experimental linewidths, is shown in Figure 3.8b.

Figure 3.7c illustrates a simple pulse sequence for obtaining spectra characterized by $|n^I| \leq N$, $n^S = \pm 1$ while the sequence actually employed, shown in Figure 3.7d, incorporates CTEF. As discussed in Section 3.5.3, one generally expects to excite both $n^S = \pm 1$ and $n^S = 0$ transitions with these sequences. The spectrum obtained for $n^I = 5$,

Figure 3.7. Simple HMQ NMR pulse sequences. (a) This pulse sequence results in excitation of coherences characterized by $n^S = 0$ and all values of $|n^I| \leq N$. ^{13}C decoupling during preparation and mixing serves to remove $\mathcal{H}_{IS}$ from the excitation dynamics. (b) The application of a pulsed magnetic field gradient (cross-hatched areas) allows CTEF selection of coherence characterized by a single n^I value. (c) This pulse sequence results in excitation of coherences characterized by $n^S = 0, \pm 1$. Following excitation of the protons with $\mathcal{H}_{IS}$ removed, ^{13}C decoupling is turned off and $\mathcal{H}_{IS}$ is allowed to act for a time $\tau_{IS} \gtrsim |F_{iS}|^{-1}$. A $\pi/2$ pulse on the ^{13}C spins then changes the n^S quantum number of the HMQ from zero to ± 1. The mixing period reverses these steps, allowing detection of proton magnetization in t_2. (d) Again a pulsed gradient for purposes of CTEF.

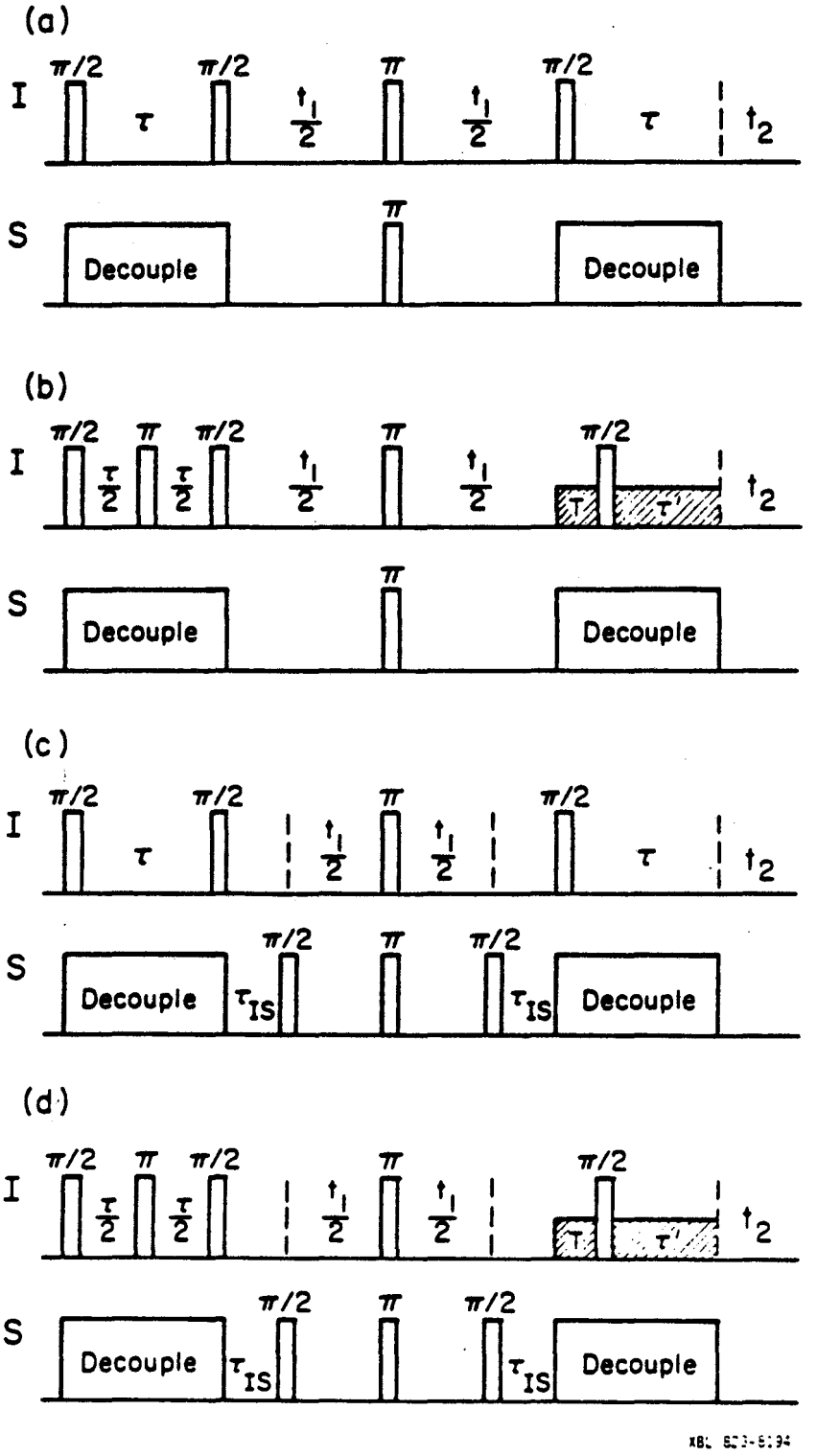
(a)
I
π/2
τ
π/2
t1/2
π
t1/2
π/2
τ
t2
S
Decouple
π
Decouple
(b)
I
π/2
τ/2
π
τ/2
π/2
t1/2
π
t1/2
π/2
τ
τ'
t2
S
Decouple
π
Decouple
(c)
I
π/2
τ
π/2
t1/2
π
t1/2
π/2
τ
t2
S
Decouple
τIS
π/2
π
π/2
τIS
Decouple
(d)
I
π/2
τ/2
π
τ/2
π/2
t1/2
π
t1/2
π/2
τ
τ'
t2
S
Decouple
τIS
π/2
π
π/2
τIS
Decouple

XBL 8C3-6194

Figure 3.8. (a) $n^I = 5$, $n^S = 0$, and $n^I = 6$, $n^S = 0$ multiple quantum spectra of partially oriented [1 - ^{13}C] benzene enriched to 90%, obtained using the pulse sequence of Figure 3.7b. Each spectrum is the average of sixteen 1024-point interferograms acquired with a recycle delay of 2 sec. The mixing period τ' was less than $|n^I|T$ due to the slow rise time of the pulsed magnetic field gradient. For the $n^I = 6$ spectrum, $\tau = 5.000$ msec, $T = 1.000$ msec, $\tau' = 4.300$ msec, and $\Delta t_1 = 100$ μsec. The $n^I = 5$ spectrum was acquired with $\tau = 6.540$ msec, $T = 1.380$ msec, $\tau' = 5.404$ msec, and $\Delta t_1 = 100$ μsec. (b) Theoretical stick simulations of $n^I = 5$, $n^S = 0$, and $n^I = 6$, $n^S = 0$ spectra. These simulations were generated using the same parameters as in Figure 3.3, with the dipolar couplings being scaled to fit the experimentally observed splitting in the $n^I = 6$ spectrum. This simple scaling is sufficient, because the ordering of benzene molecules in the nematic liquid crystal is describable by a single order parameter (Appendix A). Relative line intensities, whose calculation is described in Section 3.5.2.3, were divided by the experimentally observed linewidths to give the heights shown in the simulation.

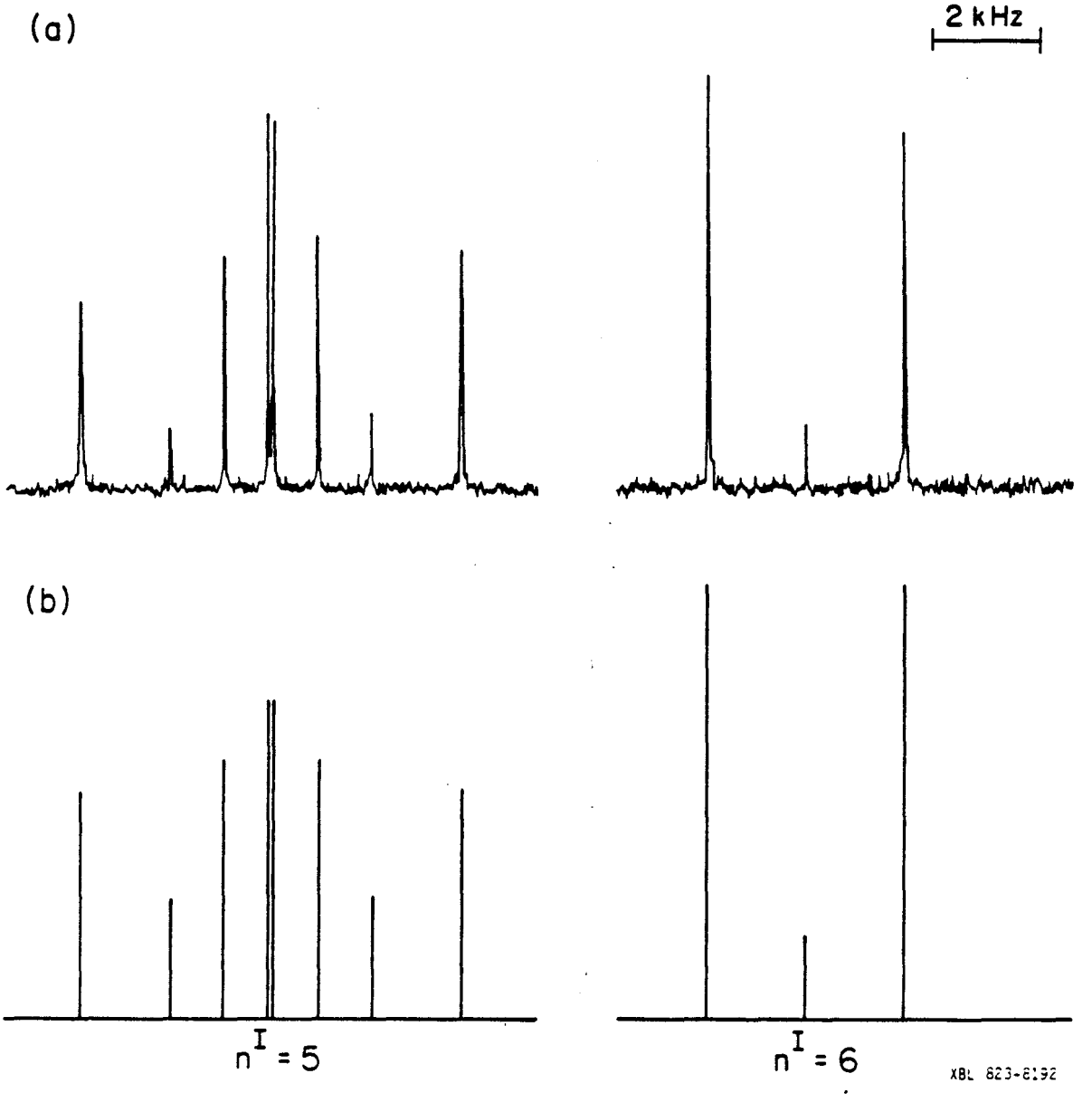
(a)
2 kHz
(b)
$n^I = 5$
$n^I = 6$
XBL 823-8192

$n^S = 0, \pm 1$ is shown in Figure 3.9, with line positions and assignments for this spectrum tabulated in Table 3-1. The $n^I = 6$, $n^S = \pm 1$ spectrum, which is not shown, consists of a single line at zero frequency.

3.5.2 Excitation Period Decoupling

3.5.2.1 Enhancement of High-Order Transitions

A significant feature of the pulse sequences of Figure 3.7 is the use of ^{13}C decoupling during the excitation periods. This has a number of advantages. By removing the ^{13}C spin from the excitation dynamics, the size of the Liouville space available to the density operator is reduced. Table 3-2 demonstrates one consequence of this reduction. The sum of the line intensities within each order n^I has been calculated for [1 - ^{13}C] benzene with and without ^{13}C decoupling. The tabulated values are ultimate τ averages (Sec. 2.5.2), representing integrals over the excitation variable τ. The ^{13}C decoupling, on average, increases the $n^I = 6$ and $n^I = 5$ intensities by factors of 3.1 and 1.1, respectively. This enhancement of the highest order coherence is particularly large for a molecule like [1 - ^{13}C] benzene, where the symmetry is, in effect, increased by ^{13}C decoupling.

3.5.2.2 Simplification of PPPI Search

The ^{13}C decoupling also simplifies considerably the PPPI search for favorable values of the excitation parameters τ and τ'. This is because the number of eigenfrequencies contributing to the excitation dynamics is reduced and, more importantly, because the signal during the search comes from unlabeled molecules as well as labeled ones. This would be particularly important in natural abundance samples where only 1% of the carbon nuclei are ^{13}C. In addition, in molecules containing

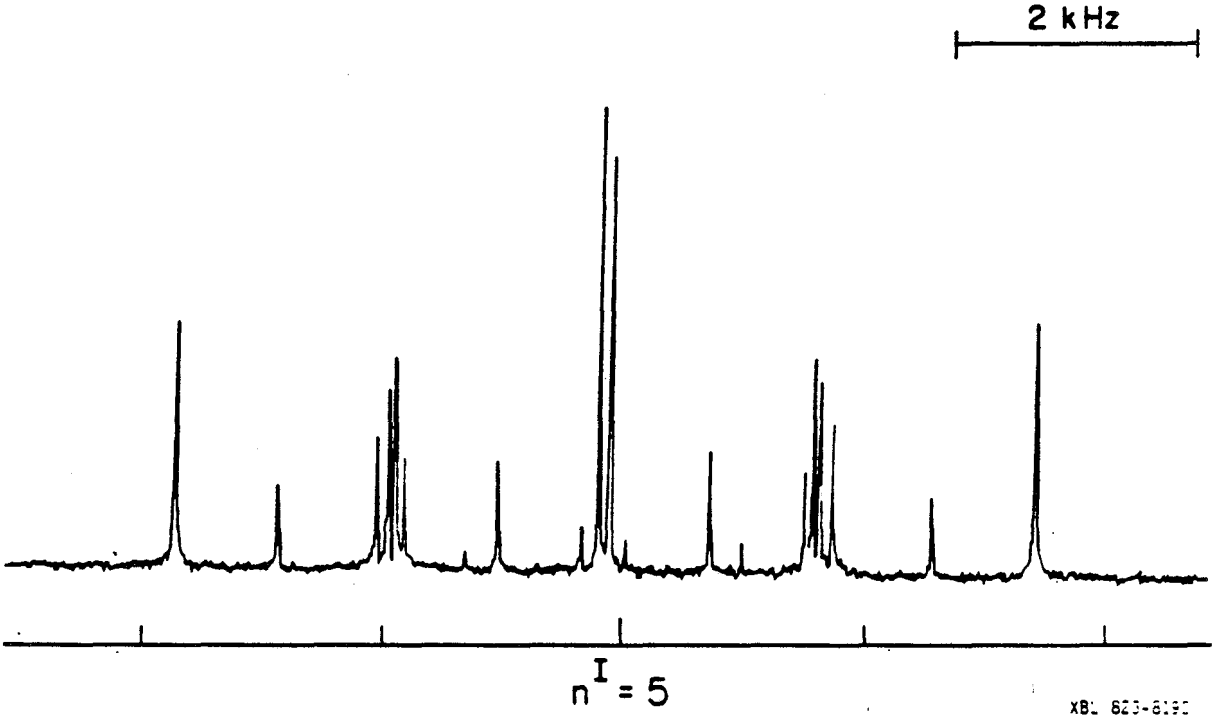

Figure 3.9. $n^I = 5$, $n^S = 0$, ±1 multiple quantum spectrum of partially oriented [1 - ^{13}C] benzene enriched to 90%, obtained using the pulse sequence of Figure 3.7d. This spectrum was recorded with τ = 6.540 msec, T = 1.380 msec, τ' = 5.404 msec, and Δt_1 = 100 μsec. The spectrum displayed here is an average of magnitude spectra obtained for five different values of τ_{IS}: 100, 200, 250, 300, and 350 μsec. Fifteen 1024-point inteferograms were recorded for each value of τ_{IS}. Line positions and assignments for this spectrum are tabulated in Table 3-1.

Table 3-1

Positions and Assignments of Lines in the $n^I = 5$, $n^S = 0, \pm 1$ Spectrum of Partially Oriented [1-^{13}C] Benzene Shown in Figure 3.9*

Observed Line Position (Hz)	Theoretical Line Position (Hz)	Assignment
49	34	$n^S = 0$
176	168	$n^S = \pm 1$
879	892	$n^S = 0$
1133	1155	$n^S = \pm 1$
1651	1673	$n^S = 0$**
1739	1760	$n^S = \pm 1$
1788	1806	$n^S = \pm 1$
1886	1914	Unlabeled molecules
2706	2733	$n^S = \pm 1$
3566	3600	$n^S = 0$

*All the lines in this spectrum occur in pairs. Accordingly, only lines at frequencies greater than 0 Hz are recorded in this table.

** This line is assigned as $n^S = 0$ based on its frequency. Its intensity here is anomalously large, however, since it does not appear in Figure 3.8.

Table 3-2

Number of Coherences and Total Magnitude Averaged Over τ per Multiple Quantum Order for [1 - ^{13}C] Benzene With and Without ^{13}C Decoupling During Preparation and Mixing

Multiple Quantum Order (n)	Number of Coherences		Total Magnitude Averaged over τ	
	Coupled	Decoupled	Coupled	Decoupled
6	1	1	0.197	0.601
5	8	2	0.804	0.905
4	38	12	2.399	3.287
3	120	34	5.946	6.005
2	263	79	11.517	11.728
1	416	116	17.252	17.090
0	210	40	7.797	4.555

two or more distinct ^{13}C sites, the carbon decoupling allows the same excitation sequence to be used to excite equally all of the "isomers".

In practice, optimal values for the excitation parameters τ and τ' in the sequences of Figure 3.7 were chosen in separate PPPI searches. (Recall that in the PPPI experiment itself τ' is always held equal to τ.) These searches were conducted with ^{13}C decoupling during both preparation and mixing periods. The preparation time τ was chosen from a PPPI experiment having proton π pulses in preparation and mixing. A second PPPI search, in the presence of a magnetic field gradient (see Figs. 3.7b and d) and in the absence of these π's, allowed an independent choice for the mixing time τ'. The time T was then selected by maximizing the height of the desired echo at $t_2 = 0$.

3.5.2.3 Calculation of Relative Line Intensities

The excitation period decoupling also simplifies the calculation of relative line intensities. As described in Section 2.5 the intensities of individual multiple quantum lines are, in general, complex functions of the internal Hamiltonian and the r.f. pulses and timing parameters which characterize the preparation and mixing periods. In certain situations, however, the ^{13}C decoupling allows the intensities of the transitions of labeled molecules to be related both to one another and to those of the unlabeled molecules, regardless of the details of the excitation periods. The principles will be illustrated by the calculation of the relative intensities of the $n^I = 5$, $n^S = 0$ transitions shown in Figure 3.8b.

There are only two $n^I = 5$ coherences for the decoupled [1 - ^{13}C] benzene molecule or equivalently for the unlabeled molecule. These are known by symmetry to be associated with the operators

$$X^5_\alpha = \sum_i I^+_{0i} \prod_{j\neq i} I_{+j} = \frac{1}{2}|m^I = 3><m^I = -2, A_1(^{12}C)|, \tag{3.22a}$$

$$X^5_\beta = \sum_i I^-_{0i} \prod_{j\neq i} I_{+j} = \frac{1}{2}|m^I = 2, A_1(^{12}C)><m^I = -3|. \tag{3.22b}$$

The notation in the outer products specifies the proton Zeeman quantum number, the irreducible representation, and the applicable permutation group, which is labeled by ^{12}C or ^{13}C to indicate that the group is assumed to change to that of the unlabeled molecule when the ^{13}C is decoupled. For the [1 - ^{13}C] benzene molecule the permutation group is C_2 and effectively reverts to D_6 under decoupling. The factor of $\frac{1}{2}$ keeps the normalization constant with the undecoupled operators and may also be written as $\frac{1}{2}(S^+_0 + S^-_0)$.

At $t_1 = 0$, the Hamiltonian suddenly changes to $\mathcal{H}_1$. For the experimental sequences of Figure 3.7,

$$\mathcal{H}_1 = \mathcal{H}_{IS} + \mathcal{H}_{II}, \tag{3.23}$$

since the Zeeman terms are effectively removed by the π pulses at $\frac{t_1}{2}$. The eigenoperators under the Hamiltonian of Equation 3.23 with $n^I = 5$, $n^S = 0$ are

$$X^5_{\alpha,\pm} = S^\pm_0|m^I = 3><m^I = -2, A_1(^{13}C), \alpha, \pm|, \tag{3.24a}$$

$$X^5_{\beta,\pm} = S^\pm_0|m^I = 2, A_1(^{13}C), \beta, \pm><m^I = -3|. \tag{3.24b}$$

The eigenstates with index α or β (running from 1 to 4) must be numerically calculated by 4×4 diagonalizations within the totally symmetric $|m^I| = 2$, $|m^S| = \frac{1}{2}$ manifolds. The plus signs in Equations 3.24 refer to the $m^S = \frac{1}{2}$ manifold, the minus signs to $m^S = -\frac{1}{2}$.

The relative intensities of the observed $n^I = 5$, $n^S = 0$ lines can now be calculated in terms of inner products of the coupled and decoupled eigenoperators. This will be discussed for transitions indexed by α, though analogous expressions hold for those indexed by β. The ratio of the intensity of a transition of the ^{13}C-containing molecules to the corresponding transition of the unlabeled molecules can be expressed in terms of the mole fraction χ_{13} of labeled molecules and quantum mechanical traces as:

$$\frac{|I^5_{\alpha,\pm}(^{13}C)|}{|I^5_{\alpha}(^{12}C)|} = \frac{\chi_{13}|Tr[X^5_{\alpha,\pm}(^{13}C)]^{\dagger}X^5_{\alpha}(^{12}C)|^2}{(1-\chi_{13})|Tr[X^5_{\alpha}(^{12}C)]^{\dagger}X^5_{\alpha}(^{12}C)|^2} . \tag{3.25}$$

Since the $|m^I| = 3$ eigenstates are the same with and without decoupling, the traces can be simplified to

$$\frac{|I^5_{\alpha,\pm}(^{13}C)|}{|I^5_{\alpha}(^{12}C)|} = \frac{\chi_{13}}{(1-\chi_{13})} \times \frac{1}{2}|\langle m^I = -2, A_1(^{13}C), \alpha, \pm | m^I = -2, A_1(^{12}C)\rangle|^2 . \tag{3.26}$$

By the completeness property, there is a sum rule

$$\sum_{\alpha=1}^{4} \sum_{\pm} \frac{|I^5_{\alpha,\pm}(^{13}C)|}{|I^5_{\alpha}(^{12}C)|} = \frac{\chi_{13}}{(1-\chi_{13})} . \tag{3.27}$$

This simply states that the total intensities from the labeled and unlabeled molecules are in proportion to their mole ratio. This would not be the case had $\mathcal{H}_{IS}$ played a role in the excitation dynamics.

The expression for relative line intensities given in Equation 3.26 is easily evaluated. By symmetry, the $m^I = -2$ eigenstate of the decoupled molecule is the symmetric sum of the direct product states characterized by five spins down (β) and one spin up (α):

$$|m^I = -2,\ A_1(^{12}C)> = \frac{1}{\sqrt{6}}\,[\,|\beta\beta\beta\beta\beta\alpha> + |\beta\beta\beta\beta\alpha\beta> + |\beta\beta\beta\alpha\beta\beta>$$

$$+ |\beta\beta\alpha\beta\beta\beta> + |\beta\alpha\beta\beta\beta\beta> + |\alpha\beta\beta\beta\beta\beta>\,]. \qquad (3.28)$$

Once the various A_1 eigenstates of the coupled molecule with $m^I = -2$ are computed, each of the inner products $<m^I = -2, A_1(^{13}C), \alpha, \pm|m^I = -2, A_1(^{12}C)>$ is formed simply by summing the coefficients of the particular eigenstate, expressed in the direct product basis. Squaring the sum and multiplying by $\frac{1}{2}\,\chi_{13} = 0.45$ gives the relative intensity of each $n^I = 5$, $n^S = 0$ [1-^{13}C] benzene transition. On this same scale the $n^I = 5$ transition of the unlabeled molecules has an intensity of 0.05.

The resulting intensities for the lines of Figure 3.8a are shown as a stick spectrum in Figure 3.8b. The theoretical sum of the intensities in the five unobserved pairs is 8% of the total intensity. A similar, but simpler, analysis gives the relative intensities of the $n^I = 6$, $n^S = 0$ transitions also shown in Figure 3.8. The sum of the satellites is again related to the central transition from the unlabeled molecules by their respective mole fractions.

3.5.3 Two Step Excitation of $n^S = 1$ Coherence

The density operator prepared from I spin magnetization with S spin decoupling contains only coherences with $n^S = 0$. In order to introduce $n^S = \pm 1$ terms, two additional requirements have to be met. First, $\mathcal{H}_{IS}$ must be allowed to act for a period of time $\tau_{IS} \geq F_{iS}^{-1}$, and then an S pulse must be applied in order to change the n^S quantum number of the HMQ coherence from zero to ±1. Prior to the action of $\mathcal{H}_{IS}$, this pulse would have no effect because at the time that the decoupling is turned off, the S spin factor in each coherence is proportional to the identity $(S_0^+ + S_0^-)$.

When $\mathcal{H}_{II}$ is present along with $\mathcal{H}_{IS}$ during the period τ_{IS}, as in Figures 3.7c and d, the dynamics of the transfer of coherence to $n^S = \pm 1$ requires numerical calculation for a general value of n^I. The total I spin coherence $n^I = N$ is a special case, however. As noted in Section 3.4.3.2, this eigenoperator evolves according to the sum $\sum_i F_{iS}$ independent of $\mathcal{H}_{II}$. Thus, if at the time the decoupling is discontinued the $n^I = N$ coherence is given by

$$\rho_{N,0}(\tau) = \frac{1}{2}(S_0^+ + S_0^-) \prod_i I_{+i}, \tag{3.29}$$

at time τ_{IS} later it is given by

$$\rho_{N,0}(\tau + \tau_{IS}) = \frac{1}{2}[S_0^+ \exp(i\theta_{IS}) + S_0^- \exp(-i\theta_{IS})] \prod_i I_{+i}, \tag{3.30}$$

where

$$\theta_{IS} = 2\pi\tau_{IS} \sum_i F_{iS}. \tag{3.31}$$

For $\tau_{IS} = (4|\sum_i F_{iS}|)^{-1}$, $\theta_{IS} = \frac{\pi}{2}$ and Equation 3.30 simplifies to

$$\rho_{N,0}(\tau + (4|\sum_i F_{iS}|)^{-1}) = S_z \prod_i I_{+i}. \tag{3.32}$$

A $\frac{\pi}{2}$ pulse at the S spin Larmor frequency converts this into $n^I = N$, $n^S = \pm 1$ coherence with complete efficiency. As noted in Section 3.4.3.1, this coherence is invariant to both $\mathcal{H}_{II}$ and $\mathcal{H}_{IS}$ and thus gives a central (zero frequency) peak in the $n^I = N$ proton spectrum. Equation 3.30 was confirmed by completely transferring the $n^I = 6$, $n^S = 0$ ^{13}C satellites of Figure 3.8a into the central line when τ_{IS} was set equal to half the inverse of the satellite splitting.

The same pulse sequences also result in $n^S = \pm 1$ spectra for other values of n^I (Fig. 3.9 and Table 3-1). For these lines even a relative intensity calculation would require a computer-assisted exact dynamics calculation. Thus the assignments of Table 3-1 were made on the basis of frequency alone.

3.6 Scalar Heteronuclear Recoupled Interactions by Multiple Pulse

3.6.1 Introduction

In Section 3.4.3, the spectrum of the higher order heteronuclear multiple quantum coherences was discussed for an effective evolution Hamiltonian (Eq. 3.18) from which $\mathcal{H}_{II}^D$ had been removed. As described in Section 3.3.2 the multiple pulse sequences designed to remove $\mathcal{H}_{II}^D$ scale the heteronuclear interactions and I spin chemical shifts by a common factor $K \leq \frac{1}{\sqrt{3}}$. In fact, pulse sequences such as HW-8[78] (Fig. 3.4d) which remove $\mathcal{H}_{II}^D$ and result in a secular average Hamiltonian (for which n^I and n^S are conserved) scale down $\mathcal{H}_I^Z$ and $\mathcal{H}_{IS}$ by a factor of $\frac{1}{3}$. The scaling of $\mathcal{H}_{IS}$ in these experiments is certainly undesirable since it reduces the effective magnitude of the interactions being measured.

Although the assumption that n^I and n^S are both conserved during the evolution of an HMQ experiment was convenient for the analysis of Section 3.4.3, it is by no means a requirement of these experiments. Relaxation of this assumption permits the use of a wide variety of multiple pulse sequences for the removal of $\mathcal{H}_{II}^D$. Many of these scale down the parameters of $\mathcal{H}_{IS}$ by less than does the HW-8 sequence and, in addition, are designed for improved suppression of the homonuclear dipolar couplings[95-98]. In this section we introduce a new multiple pulse technique, scalar heteronuclear recoupled interactions by multiple pulse (SHRIMP), which removes $\mathcal{H}_{II}^D$ while scaling the parameters of $\mathcal{H}_{IS}$ by a

factor $K = \frac{1}{\sqrt{3}}$. The SHRIMP method has the advantage of generating HMQ spectra having properly phased lines whose relative intensities are both independent of excitation dynamics and easily calculated.

3.6.2 The SHRIMP Sequence

The SHRIMP technique involves irradiating both the I and S spins with the same sequence of r.f. pulses during t_1. This keeps their angular momentum components always parallel in the toggling frame. If we also require that the Zeeman terms $\mathcal{H}_I^Z$ and $\mathcal{H}_S^Z$ vanish, then the desired average Hamiltonian for the SHRIMP sequence is

$$\mathcal{H}_{I\cdot S} + \mathcal{H}_{II}^J = -\frac{1}{3}\sum_i 2F_{iS}\underset{\sim}{I}_i \cdot \underset{\sim}{S} - \sum_{i<j} J_{ij}\underset{\sim}{I}_i \cdot \underset{\sim}{I}_j. \qquad (3.33)$$

The first term is the average Hamiltonian resulting from $\mathcal{H}_{IS}$. The notation $\mathcal{H}_{I\cdot S}$ indicates that the interaction has taken on the operator form of a scalar coupling in spin space. This amounts to a recoupling of the I and S nuclei so that flip-flop terms normally suppressed by the large difference in Larmor frequencies are reintroduced.

At this point it is useful to clarify the meaning of the terms "size" and "scale factor" as they relate to a Hamiltonian such as $\mathcal{H}_{IS}$. We take as a measure of the magnitude of a particular interaction A the norm of the matrix which describes that interaction. Symbolically, this norm is written as $\|A\|$. It should be noted that a close analogy exists between the norm of a matrix and the property of length which can be associated with a vector in 3-dimensional geometric space. Formally, the norm of a matrix has the following defining properties[115]:

1) $\|A\| > 0$ unless $A_{ij} = 0$ for all i,j, in which case $\|A\| = 0$.

2) $\|aA\| = a\|A\|$ for every real number a.

3) $\|A+B\| \leq \|A\| + \|B\|$.

A convenient definition of the norm of an $(n \times n)$ matrix is

$$\|A\| = \left[\sum_{i,j} \frac{(A_{ij})^2}{n}\right]^{\frac{1}{2}} = [Tr(\frac{A^{\dagger}A}{n})]^{\frac{1}{2}} \quad . \tag{3.34}$$

Since $\|A\|$ is invariant under unitary transformations, the norm can be defined equivalently as the root-mean-square eigenvalue of the matrix A.

As we have seen, the unperturbed heteronuclear coupling between I and S spins takes the form $I_z S_z$. Under SHRIMP, this interaction becomes, instead, $\frac{1}{3}\,\underset{\sim}{I}\cdot\underset{\sim}{S}$. Since

$$\|\underset{\sim}{I}\cdot\underset{\sim}{S}\|^2 = \|I_x S_x\|^2 + \|I_y S_y\|^2 + \|I_z S_z\|^2 \tag{3.35a}$$

and

$$\|I_x S_x\| = \|I_y S_y\| = \|I_z S_z\|, \tag{3.35b}$$

the norm of $\mathcal{H}_{I\cdot S}$ is

$$\|\mathcal{H}_{I\cdot S}\| = \frac{1}{\sqrt{3}}\|I_z S_z\| \tag{3.36}$$

and the scale factor K describing this sequence is $\frac{1}{\sqrt{3}}$.

A particular pulse sequence which leads to the average Hamiltonian of Equation 3.33 is illustrated in Figure 3.10. It is describable in the ABC notation[97] as

$$(ABC)(C\bar{B}\bar{A})(\bar{A}B\bar{C})(\bar{C}\bar{B}A)(A\bar{B}\bar{C})(\bar{C}B\bar{A})(\bar{A}\bar{B}C)(CBA). \tag{3.37}$$

The letters indicate the toggling frame value of $U_{rf}^{-1}(I_z + S_z)U_{rf}$ and

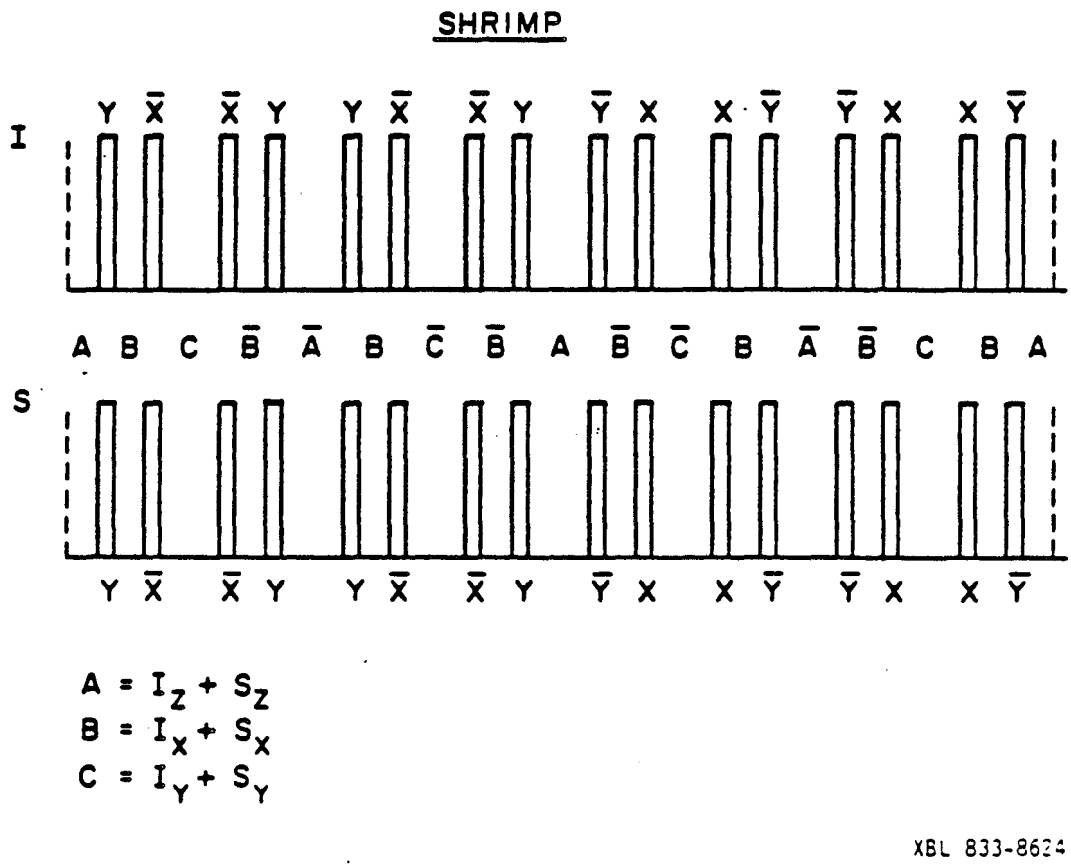

Figure 3.10. SHRIMP pulse sequence. SHRIMP removes homonuclear dipolar couplings ($\mathcal{H}^{D}_{II}$) while recoupling the I and S spins. The same sequence of r.f. pulses is applied to both spin species. This reintroduces heteronuclear flip-flop terms (of the form $I_{+i}S_{-}$) into the Hamiltonian $\mathcal{H}_{IS}$, which then takes the form of a scalar coupling. Parameters of this Hamiltonian are scaled by a factor of $1/\sqrt{3}$. The toggling frame value of $U_{rf}^{-1}(I_z + S_z)U_{rf}$ is indicated in ABC notation[97].

specify a sequence in which the same pattern of r.f. pulses is given both I and S spins. The sequence consists only of $\frac{\pi}{2}$ pulses and is compensated to give no contribution to the average Hamiltonian from $\mathcal{H}^{D}_{II}$, even for finite pulse lengths. Since it is symmetric, $\bar{\mathcal{H}}^{(1)}$ correction terms also vanish.

3.6.3 Evolution Under SHRIMP

The average Hamiltonian of Equation 3.33 has fundamentally different properties than either the unperturbed Hamiltonian or the previous multiple pulse Hamiltonian of Equation 3.18. The presence of heteronuclear flip-flop terms in the SHRIMP Hamiltonian means that the Zeeman quantum numbers of the individual spin species are not conserved. However, it is true that

$$[\underset{\sim}{I} + \underset{\sim}{S},\ \mathcal{H}_{I\cdot S} + \mathcal{H}^{J}_{II}] = 0. \tag{3.38}$$

This implies that the sum of the Zeeman quantum numbers is conserved and, in addition, that the Hamiltonian is isotropic in spin space. The principal consequence for HMQ experiments is that the sum $(n^{I} + n^{S})$ is conserved, though not the individual quantities.

An interesting consequence of Equation 3.38 is that the SHRIMP sequence can serve as a cross polarization scheme. It transfers any component of I magnetization to the corresponding component of S in much the same way that Hartmann-Hahn cross polarization[116] transfers the spin-locked component.

3.6.4 HMQ Spectroscopy Under SHRIMP

In this section, the consequences of using the SHRIMP Hamiltonian of Equation 3.33 as the evolution Hamiltonian $\mathcal{H}_1$ of an heteronuclear

multiple quantum experiment are discussed. Figure 3.11 shows the energy level diagram relevant to high order HMQ spectroscopy of partially oriented [1-^{13}C] benzene under the SHRIMP Hamiltonian. Unlike the situation depicted in Figure 3.6, subspectral analysis is not applicable.

The total spin coherence, characterized by $(n^I + n^S) = 7$, is still independent of all spin-spin couplings. The transitions characterized by $(n^I + n^S) = 6$ belong to the A_1 irreducible representation, since they all involve the totally symmetric states with $(m^I + m^S) = \pm\frac{7}{2}$. From the energy level diagram of Figure 3.11, there are apparently five pairs of such transitions. One pair has no splitting, however, and constitutes a degenerate central line. This is not peculiar to [1-^{13}C] benzene, but is in fact a general feature which follows from the commutator of (3.38). To see this, consider the operator formed from the total spin coherence through the action of the derivation-superoperator[117] generated by $(I_- + S_-)$:

$$[(I_- + S_-),\ S_+ \prod_i I_{+i}] = S_0^- \prod_i I_{+i} + S_+ \sum_i (I_{0i}^- \prod_{j\neq i} I_{+j}). \qquad (3.39)$$

This is clearly an $(n^I + n^S) = N$ operator. Its commutator with the SHRIMP Hamiltonian of Equation 3.33 is zero, however, as is most easily seen by noting that both terms on the left of Equation 3.39 do so commute. By induction, this argument can be extended to prove that there is a center line for every order $(n^I + n^S)$. In general, then, there are as many pairs of $(n^I + n^S) = N$ transitions containing information on $\mathcal{H}_{I\cdot S} + \mathcal{H}_{II}^J$ as there are distinct I spins. This number is N for an unsymmetrical molecule and 4 for [1-^{13}C] benzene. This is also the number of distinct heteronuclear couplings F_{iS}.

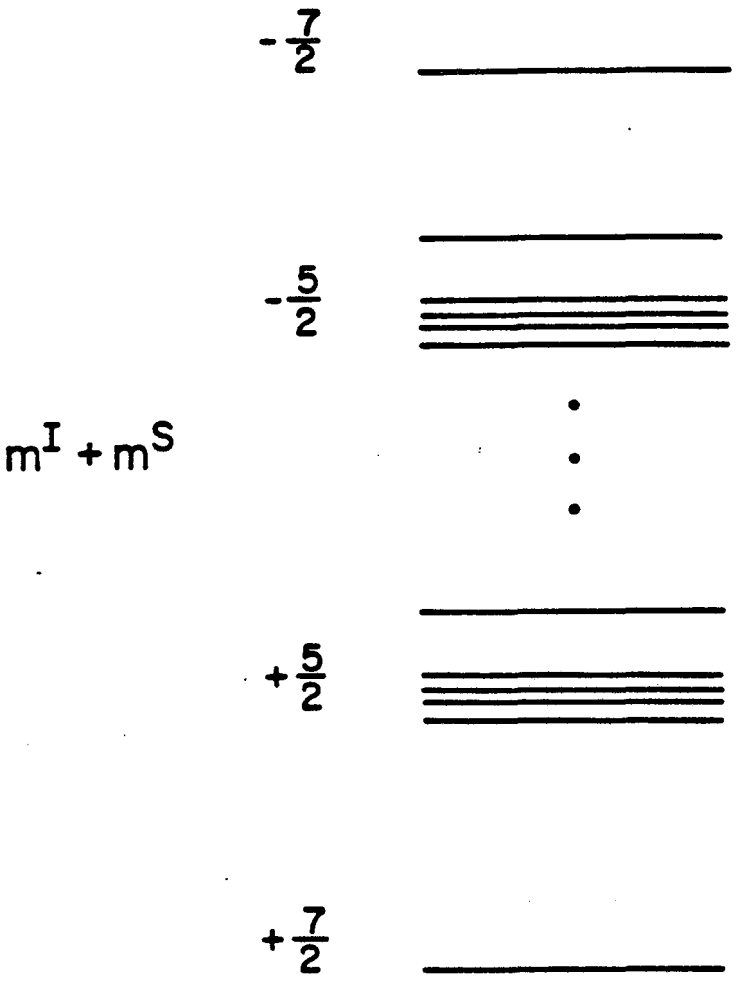

XBL 8110-7176 A

Figure 3.11. [1 - ^{13}C] benzene energy level diagram relevant to SHRIMP spectroscopy. During evolution under the SHRIMP pulse sequence (Fig. 3.10) the individual spin quantum numbers m^I and m^S, and hence the differences n^I and n^S, are not good quantum numbers of the system. The sums $(m^I + m^S)$ and $(n^I + n^S)$ are, however, conserved quantities.

We consider now the problem of exciting the $(n^I + n^S) = N$ SHRIMP coherences. For the same reasons as discussed in Section 3.5.2 it is desirable to decouple the S spins during preparation and mixing periods. Thus it is reasonable to consider at time $t_1 = 0$ the $n^S = 0$ operators prepared with decoupling. The conservation of $(n^I + n^S)$ under the SHRIMP Hamiltonian then requires that the initial condition be the proton total spin coherence $(n^I = N)$:

$$\rho(t_1 = 0) = X^N = \frac{1}{2} \prod_i I_{+i}. \tag{3.40}$$

During the evolution period this will evolve into other operators with $(n^I + n^S) = N$ so that at time t_1, additional terms of order $(n^I = N-1, n^S = 1)$ will be present. These need not lead to I magnetization in t_2, however, since decoupling will tend to destroy any $n^S = 1$ coherence and CTEF can be used to discriminate against $n^I \neq N$ coherence.

With these considerations it is possible to write the SHRIMP interferogram with initial condition $n^I = N$ as the autocorrelation function $\mathrm{Tr}([X^N(0)]^\dagger X^N(t_1))$. The fact that the signal can be written as a single autocorrelation function guarantees that all of the lines will appear with the same phase. The intensities are found to be, in analogy to Equation 3.26:

$$\frac{|I^N_{\alpha,\pm}(^{13}C)|}{|I^N(^{12}C)|} = \frac{\chi_{13}}{(1-\chi_{13})} \times \frac{1}{2} |\langle m^I + m^S = \pm\frac{(N-1)}{2},\ A_1(^{13}C),\ \alpha|$$
$$m^I = \pm\frac{N}{2},\ m^S = \mp\frac{1}{2},\ A_1(^{12}C)\rangle|^2. \tag{3.41}$$

A sum rule identical to Equation 3.27 holds. In Equation 3.41, the index α, which labels the distinct pairs of lines, runs from 1 to the number of

distinct I spins, plus one. As noted, one pair falls at the center and is thus degenerate with the signal from the unlabeled molecules. The other pairs, in principle, are sufficient to determine the unknown parameters F_{iS}.

3.7 Spreading Parameters in HMQ Spectroscopy with I Spin Detection

3.7.1 Motivation and Introduction

The discussion to this point has been for a single system consisting of N spins I and one spin S. In some situations, most notably that in which S represents ^{13}C at natural abundance, the sample consists of a collection of such systems. In such cases, it is important to be able to distinguish the transitions arising from each system. An effective way of doing this is to introduce a period in which the dynamics are determined by the chemical shifts of the S spins. These chemical shifts then serve as spreading parameters, which separate the spectra of the various systems and facilitate their assignment to particular molecular species.

One way of introducing S spin chemical shifts into heteronuclear multiple quantum spectra is to detect S spin magnetization (with I spin decoupling) during t_2, as was done in local field spectroscopy experiments. Because of the reduced signal-to-noise ratio associated with direct observation of the S spins, however, it is advantageous to introduce the evolution due to $\mathcal{H}_S^Z$ into t_1 instead. This can be done by following the evolution of an $n^S = \pm 1$ HMQ operator, but detecting I spin magnetization in t_2. Such an indirect measurement of $\mathcal{H}_S^Z$ has been demonstrated in the liquid state spectrum of $^{13}CH_3I$[111].

In previous discussions of the evolution of $n^S = \pm 1$ HMQ coherence, emphasis has been placed on dipolar evolution ($\mathcal{H}_{IS}$) with the Zeeman term $\mathcal{H}_S^Z$ being intentionally suppressed in the interest of removing the effect

of magnet inhomogeneity. In this section, we indicate how the previous pulse sequences may be augmented to achieve separation of the spectra arising from different species according to $\mathcal{H}_S^Z$. This can be done with a sequence which remains immune to any inhomogeneity of the Zeeman terms and, in addition, suppresses the signal from species which do not contain an S spin.

Experiments which begin by preparing the total spin coherence ($n^I = N$) of the I spin system are of particular interest. As discussed in Section 3.5.3, this term can be quantitatively converted into ($n^I = N$, $n^S = \pm 1$) coherence and also serves as the initial condition for HMQ spectroscopy under SHRIMP (Sec. 3.6.4). Figures 3.12a and b depict pulse sequences designed to measure the quantity $\sum_i F_{iS}$ for each S spin and to correlate this sum with the chemical shift ω_S of the S spin. These serve as a prelude to the sequence of Figure 3.12c in which both $\sum_i F_{iS}$ and ω_S are used to identify the HMQ transitions of the species containing that S spin.

A common feature of all of these sequences is that the evolution period is divided into two parts:

$$t_1 = t_{1a} + t_{1b}. \tag{3.42}$$

In a given experiment the ratio $\frac{t_{1a}}{t_{1b}}$ is held fixed as t_1 increases. The particular ratio used is chosen so as to allow resolution of all frequencies appearing in the Fourier transform with respect to t_1.

3.7.2 Correlation of $\sum_i F_{iS}$ with ω_S.

Each of the sequences of Figure 3.12 begins with the preparation of ($n^I = N$, $n^S = 0$) coherence under the preparation propagator U. In the

Figure 3.12. Pulse sequences for the correlation of heteronuclear coupling constants with a spreading parameter. In these sequences $x = (N\gamma_I + \gamma_S)/2N\gamma_I$. (a) This pulse sequence allows correlation of $\sum_i F_{iS}$ with the chemical shift ν_S of the ^{13}C nucleus involved. The initial condition of interest is the ($n^I = N$, $n^S = 0$) coherence. The resulting spectrum for this coherence is a triplet of lines from each different ^{13}C site. The splitting within each triplet is proportional to $\sum_i F_{iS}$, its center is proportional to the chemical shift of the carbon, ν_S. (b) Incorporation of a pulsed field gradient allows CTEF discrimination against all coherence not prepared as $n^I = N$. (c) This sequence allows separation of SHRIMP spectra by the chemical shift of the ^{13}C involved. Again, the initial condition of interest is ($n^I = N$, $n^S = 0$). A SHRIMP sequence (not drawn) is applied during t_{1a} and the time period τ_{IS} is fixed.

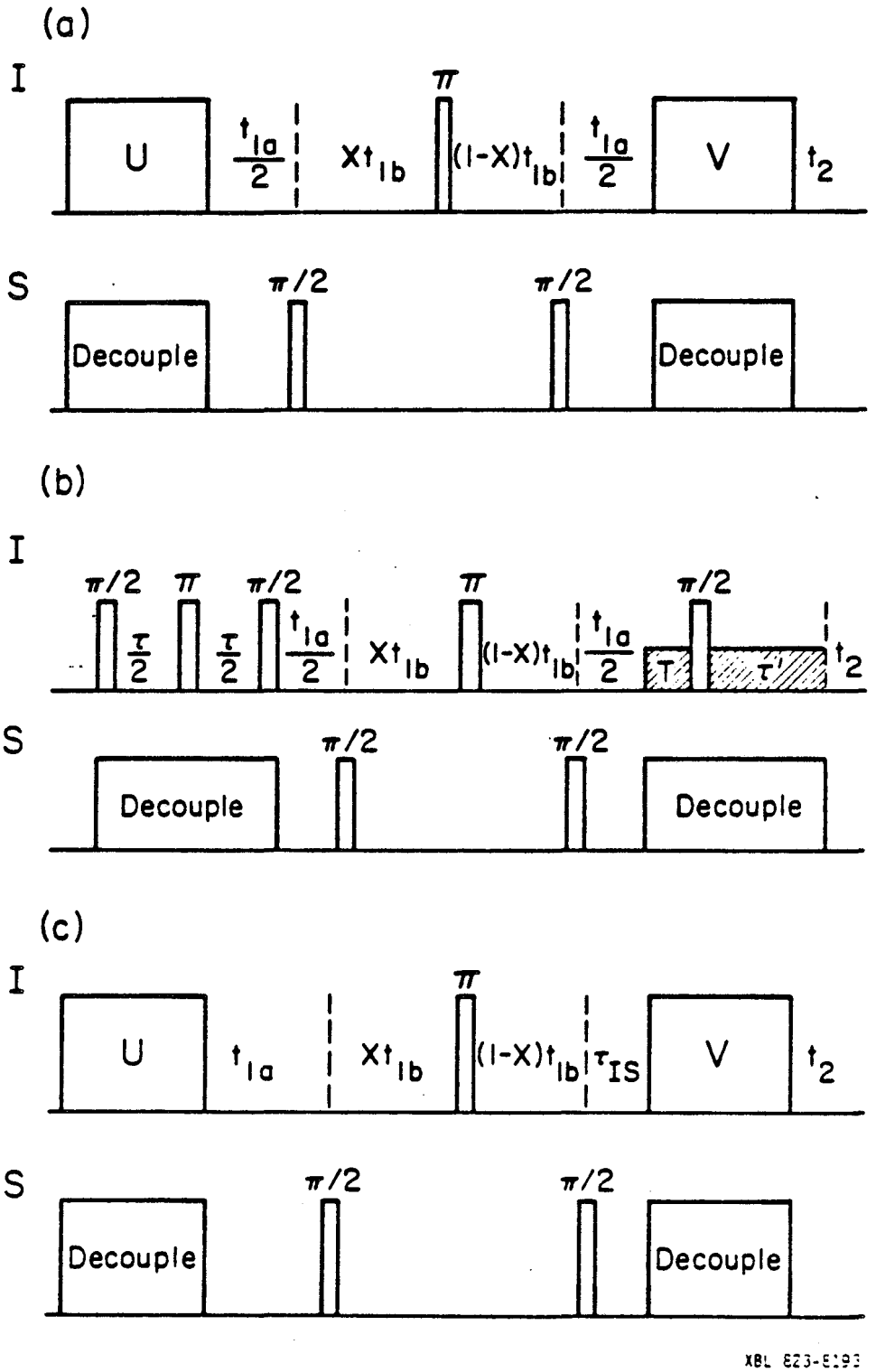
(a)
I
U
$\frac{t_{1a}}{2}$
Xt_{1b}
π
$(1-X)t_{1b}$
$\frac{t_{1a}}{2}$
V
t_2
S
Decouple
$\pi/2$
$\pi/2$
Decouple
(b)
I
$\pi/2$
π
$\pi/2$
$\frac{\tau}{2}$
$\frac{\tau}{2}$
$\frac{t_{1a}}{2}$
Xt_{1b}
π
$(1-X)t_{1b}$
$\frac{t_{1a}}{2}$
$\pi/2$
τ
τ'
t_2
S
Decouple
$\pi/2$
$\pi/2$
Decouple
(c)
I
U
t_{1a}
Xt_{1b}
π
$(1-X)t_{1b}$
τ_{IS}
V
t_2
S
Decouple
$\pi/2$
$\pi/2$
Decouple

XBL 823-8193

first experiment (Fig. 3.12a) this evolves according to $\sum_i F_{iS}$ (Eq. 3.19) for a time $\frac{t_{1a}}{2}$, is converted to ($n^I = N$, $n^S = \pm 1$) coherence for a time t_{1b}, and then back to $n^S = 0$ for a second period $\frac{t_{1a}}{2}$ before mixing to observable I magnetization.

The I spin π pulse during t_{1b} refocuses that coherence which spends time xt_{1b} with quantum numbers ($n^I = N$, $n^S = -1$) and $(1-x)t_{1b}$ with ($n^I = -N$, $n^S = -1$). The fraction x, given by

$$x = \frac{(N\gamma_I + \gamma_S)}{2N\gamma_I}, \tag{3.43}$$

is chosen to remove the effects of the inhomogeneous Zeeman terms for this coherence alone. Other coherences, including all those arising from systems not labeled by an S spin, may be suppressed by intentionally increasing the range of $\omega(\underset{\sim}{r})$ with a pulsed field gradient. As demonstrated below, further suppression of unwanted coherence can be achieved by shifting the relative phase of the S spin pulses in successive shots (Sec. 2.4.2).

The spectrum resulting from Fourier transformation with respect to t_1 is a triplet centered at

$$\left(\frac{t_{1b}}{t_1}\right)\left[-(\nu_S + \Delta\nu_S) + \left(\frac{\gamma_S}{\gamma_I}\right)\Delta\nu_I\right]. \tag{3.44}$$

The splitting between the outer lines of this triplet is

$$\left(\frac{t_{1a}}{t_1}\right)\left|\sum_i F_{iS}\right|. \tag{3.45}$$

This allows association of $\sum_i F_{iS}$ for a particular S spin with the chemical shift of that spin.

The ability to correlate $|\sum_i F_{iS}|$ with ν_S was demonstrated on the same sample of [1-^{13}C] benzene using the pulse sequence of Figure 3.12b. CTEF was used so that only magnetization resulting from $n^I = 6$ coherence was sampled. Four different experiments were performed, the phase of the first S spin $\frac{\pi}{2}$ pulse being incremented by 90° in each successive experiment. Data from these four experiments were combined so that only the triplet of lines belonging to $n^S = -1$ coherence was retained. The effect of an S spin chemical shift was simulated by changing the ^{13}C synthesizer frequency.

Figure 3.13a shows the positions of the three lines as a function of ^{13}C frequency offset, with the proton frequency set on-resonance. As expected, these lines move in unison as the frequency is varied, the change in line position with changing offset frequency being determined by the ratio $\frac{t_{1b}}{t_1} = 0.49$, as described by Equation 3.44. Figure 3.13b shows similar results of experiments in which the ^{13}C frequency is set on-resonance and the proton offset frequency varied. Again, Equation 3.44 is confirmed. Finally, the effect of varying the ratio $\frac{t_{1a}}{t_1}$ (Equation 3.45) is illustrated in Figure 3.13c. The results of these experiments demonstrate that by an appropriate choice of the ratio $\frac{t_{1a}}{t_1}$, separated triplets can be obtained and $\sum_i F_{iS}$ thereby correlated with ν_s for several inequivalent S spins, without ever detecting S spin magnetization.

3.7.3 Sorting of HMQ Spectra by Spreading Parameter

The correlation of $\sum_i F_{iS}$ with ν_S is useful in choosing the parameter τ_{IS} in the sequence of Figure 3.12c. This sequence begins with evolution of $n^I = N$ coherence under, for example, the SHRIMP Hamiltonian of Equation 3.33 for a time t_{1a}. Following a $\frac{\pi}{2}$ S pulse, evolution for time t_{1b}, as

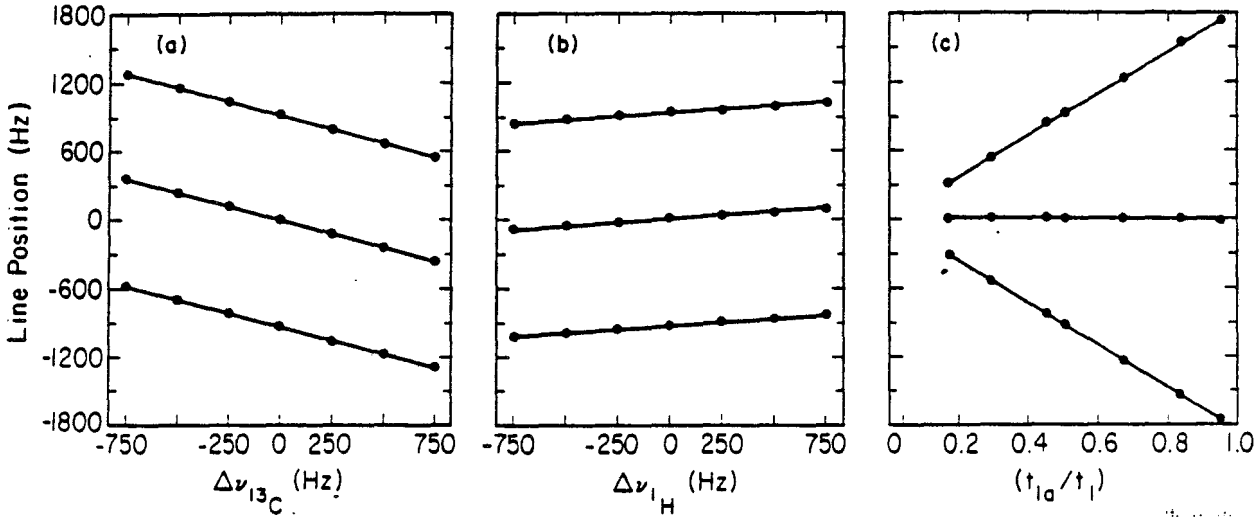

Figure 3.13. Line positions as a function of $\Delta\nu_{^{13}C}$, $\Delta\nu_{^{1}H}$, and (t_{1a}/t_1) in $n^I = 6$ spectra of partially oriented [1 - ^{13}C] benzene, collected with the pulse sequence of Figure 3.12b. The spectrum obtained in each experiment is a triplet of lines; the position of each of these lines is shown. All spectra were acquired with τ = 4.304 msec, T = 1.025 msec, and τ' = 4.266 msec. (a) $\Delta\nu_{^{13}C}$ dependence: Line positions as a function of ^{13}C frequency offset with ^{1}H frequency set on-resonance. Experiments were run with Δt_{1a} = 100 μsec, Δt_{1b} = 96 μsec. The slope of the least-squares fit to the position of each spectral line is 0.488; the theoretical value is $(\Delta t_{1b}/\Delta t_1) = 0.490$ (Eq. 3.44). (b) $\Delta\nu_{^{1}H}$ dependence: Line positions as a function of ^{1}H frequency offset with ^{13}C frequency set on-resonance. Experiments were run with Δt_{1a} = 100 μsec, Δt_{1b} = 96 μsec. The slope of the least-squares fit to the position of each spectral line is 0.120; the theoretical value is $(\gamma_S/\gamma_I)(\Delta t_{1b}/\Delta t_1) = 0.122$ (Eq. 3.44). (c) (t_{1a}/t_1) dependence: Line positions as a function of the ratio (t_{1a}/t_1) with both ^{13}C and ^{1}H frequencies set on-resonance. The center line, which contains no dipolar information, remains stationary as a function of the fraction (t_{1a}/t_1); the splitting between the outer lines of the triplet varies linearly with this parameter (Eq. 3.45).

in the sequence of Figure 3.12a, shifts the SHRIMP spectrum for each spin an amount proportional to ν_S. As t_1 is incremented the time τ_{IS} is held fixed. In the Fourier transform with respect to t_1, the intensity of a given set of SHRIMP lines, corresponding to the heteronuclear couplings to a particular S spin, varies as $\sin(\theta_{IS})$ as described by Equation 3.30. A pulsed field gradient during t_{1b}, phase shifting of S spin pulses, and CTEF can again be used to suppress unwanted coherence.

3.8 Conclusion

In this chapter, the measurement of heteronuclear dipolar couplings in molecules containing N spin-I nuclei and one spin-S nucleus has been considered. Several new approaches to the problem have been introduced and experimentally demonstrated. The exponential increase in spectral complexity with the size of the spin system is a problem which was unsolved by single quantum local field techniques. The multiple quantum methods demonstrated allow spectroscopy at the resolution of individual transitions for larger molecules than is otherwise possible.

Even when high-order multiple quantum coherence is observed, however, the rationale for removing the effect of homonuclear dipolar couplings still remains. This removal reduces the number of unknown parameters, thereby simplifying spectral interpretation and simulation. The usual approach is to irradiate only the abundant nuclei with a multiple-pulse line-narrowing sequence. A new approach which involves the irradiation of both spin species, SHRIMP, was introduced.

In addition to providing good spectral resolution, another desirable feature of any experiment designed for large molecules is that it generates spectra whose relative line intensities can be readily simulated. In general, this is difficult in multiple quantum experiments, because

of the complex dynamics of the excitation periods. The elimination of this problem by the separation of homonuclear and heteronuclear excitation was demonstrated for the high order spectra of [1-^{13}C] benzene. For the $n^I = 5$ spectrum, this calculation depended on the high molecular symmetry. Both the SHRIMP method and that of total spin coherence transfer echo spectroscopy (TSCTES) discussed in the next chapter lead to relative line intensities which are independent of the excitation periods, regardless of molecular symmetry.

In all of the experiments discussed, the final detection of magnetization is at the abundant spin frequency, since this typically gives greater sensitivity. Optimization of sensitivity may require selective excitation of high-order coherence (Sec. 2.5.4), exactly as in purely homonuclear experiments. The methods demonstrated in Section 3.7 allow heteronuclear multiple spectra to be labeled with the resonance frequency of the lower sensitivity heteronuclear spin without requiring that it be directly observed.

Chapter 4: TOTAL SPIN COHERENCE TRANSFER ECHO SPECTROSCOPY

In Chapter 2, several of the problems associated with existing multiple quantum NMR methods were described. These difficulties can complicate the interpretation of multiple quantum spectra and limit the accuracy of information which can be extracted from them. Among these are problems resulting from: (1) the sensitivity of MQ transitions to inhomogeneous broadening, (2) the complex dependences of MQ line intensities on both parameters of the spin Hamiltonian and timing parameters of the excitation sequence, and (3) the generally different and unknown phases of MQ spectral lines. These latter two problems were discussed in Sections 2.5 and 2.3 respectively, while the effects of inhomogeneous broadening ($\omega(\underset{\sim}{r})I_z$) during the evolution period t_1 are considered below. Solution of these problems has provided much of the motivation behind the development of total spin coherence transfer echo spectroscopy (TSCTES)[65,118] and it will be shown in this chapter how all three can be overcome by the TSCTES method.

In Section 4.1, a number of introductory topics are presented, including a consideration of the effects of π pulses in spin echo experiments, a description of the total spin coherence, and a review of coherence transfer echoes. Section 4.2 introduces the technique of total spin coherence transfer echo spectroscopy, describes several different TSCTES pulse sequences, and presents experimental results which demonstrate the TSCTES technique. The relative line amplitudes in TSCTES spectra, including phase, are considered in Section 4.3. In Section 4.4, we discuss absolute integrated line amplitudes in TSCTES spectra. The dependence of these amplitudes on r.f. flip angles, the number of protons in the spin system (N), and the multiple quantum order of interest (n^I)

are all considered. Various limitations on the applicability and information content of TSCTES, including the effects of diffusion, are described in Section 4.5.

4.1 Introductory Topics

4.1.1 Evolution Period Spin Echoes

As noted in Section 2.4.1, since the contribution of magnetic field inhomogeneity to the multiple quantum linewidth is proportional to the order of the transition n^{I}[53], it can be resolution limiting even in situations where it is negligible in the single quantum spectrum. This has led to the incorporation of selective[36] or non-selective[19,41] π pulses at the midpoint, $\frac{t_1}{2}$, of the multiple quantum evolution period (Fig. 2.4) in order to create a spin echo[119] at time t_1. While such an echo does remove effectively inhomogeneous broadening, it creates new difficulties, as discussed below.

In order to describe the effect of an evolution period π pulse, we first derive an expression for the signal observed in a multiple quantum spin echo experiment. With reference to Equation 2.8, this signal can be written as

$$S_\alpha(\tau,\tau',t_1) = \mathrm{Tr}(\rho(\tau,\tau',t_1)I_\alpha) \tag{4.1a}$$

$$= \mathrm{Tr}(V(\tau')\ \exp(-i\mathcal{H}_1\ \tfrac{t_1}{2})R\ \exp(-i\mathcal{H}_1\ \tfrac{t_1}{2})U(\tau)\rho(0)U^{\dagger}(\tau)\ \exp(i\mathcal{H}_1\ \tfrac{t_1}{2})$$

$$\times\ R^{\dagger}\ \exp(i\mathcal{H}_1\ \tfrac{t_1}{2})V^{\dagger}(\tau')I_\alpha), \tag{4.1b}$$

where R, the propagator for the π pulse at $\frac{t_1}{2}$, is given by

$$R = \exp(i\pi I_y). \tag{4.2}$$

Expanding in the eigenbasis of $\mathcal{H}_1$, Equation 4.1b can be simplified to

$$S_\alpha(\tau,\tau',t_1) = \sum_{i,j}\sum_{k,\ell} \alpha_{ji}(-\tau')\rho_{k\ell}(\tau)\langle i|R|k\rangle\langle \ell|R^\dagger|j\rangle \exp(i(\omega_{ji}+\omega_{k\ell})\frac{t_1}{2}). \tag{4.3}$$

This expression is discussed further in Sections 4.1.1.1 and 4.1.1.2 below.

The effect of a π pulse at $\frac{t_1}{2}$ is illustrated schematically in Figure 4.1. On the left, the prepared spin density operator existing during the first half of the evolution is depicted, for simplicity, by two arrows representing coherent superpositions of the connected eigenstates. After the π pulse, one of the two pictures on the right applies, depending on whether or not

$$[\mathcal{H}_1,\mathcal{H}_1'] = 0, \tag{4.4}$$

where

$$\mathcal{H}_1' = R\mathcal{H}_1R^\dagger. \tag{4.5}$$

$\mathcal{H}_1'$ is obtained from $\mathcal{H}_1$ simply by reversing the signs of all of the Zeeman terms ($\mathcal{H}_I^Z$).

4.1.1.1 $[\mathcal{H}_1,\mathcal{H}_1'] = 0$

The commutator of Equation 4.4 vanishes or is negligible when the chemical shift differences among the spins are zero or negligible compared to the spectral resolution. It also vanishes in the other extreme of weak coupling, where the chemical shift differences are much greater than the couplings between spins. This is because in the weak coupling limit, mutual spin-flip terms (of the form $I_{+i}I_{-j}$) may be dropped from $\mathcal{H}_1$. In either of these cases, Figure 4.1b applies after the π pulse. There is a one-to-one correspondence between coherences present before and after the π pulse.

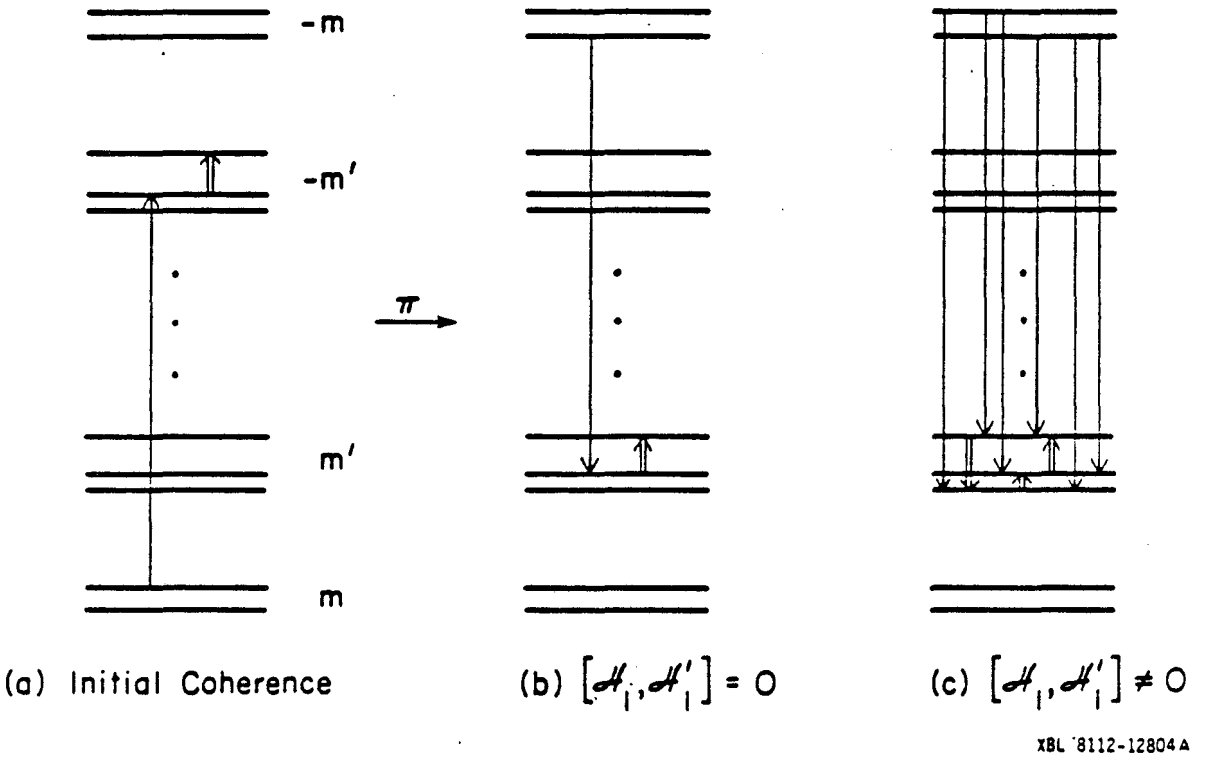

Figure 4.1. Coherence transfer due to a π pulse. (a) Two coherences existing before the π pulse are indicated by the single and double arrows. (b) When $[\mathcal{H}_1, \mathcal{H}_1'] = 0$ (Eq. 4.4), the π pulse transfers each coherence to a single other coherence between states of opposite Zeeman quantum numbers. (c) When $[\mathcal{H}_1, \mathcal{H}_1'] \neq 0$, the situation is more complicated. Several coherences arise from each of those present before the π pulse. This leads to a spectrum of many lines at frequencies which are averages of those occurring before and after the π pulse.

This one-to-one correspondence is evident from an examination of Equation 4.3. When $[\mathcal{H}_1,\mathcal{H}_1'] = 0$, the spin inversion state formed from the eigenstate $|k\rangle$,

$$|\bar{k}\rangle = R|k\rangle, \tag{4.6}$$

is itself an eigenstate of $\mathcal{H}_1$. Thus the only non-zero matrix element $\langle i|R|k\rangle$ is the one with $\langle i| = \langle\bar{k}|$. Similarly, the matrix element $\langle \ell|R^\dagger|j\rangle = 0$ unless $\langle \ell| = \langle\bar{j}|$. This allows the quadruple sum in Equation 4.3 to be collapsed to

$$S_\alpha(\tau,\tau',t_1) = \sum_{i,j} \alpha_{j\bar{i}}(-\tau')\rho_{i\bar{j}}(\tau)\exp(i(\omega_{j\bar{i}}+\omega_{i\bar{j}})\frac{t_1}{2}), \tag{4.7}$$

where the dummy index k has been relabeled as j.

In cases where the commutator $[\mathcal{H}_1,\mathcal{H}_1']$ vanishes, an average Hamiltonian (Sec. 3.2),

$$\bar{\mathcal{H}}_1^{(0)} = \frac{1}{2}(\mathcal{H}_1+\mathcal{H}_1'), \tag{4.8}$$

accounts accurately for the spectrum observed by Fourier transformation with respect to t_1. This spectrum, having transitions at frequencies $\frac{1}{2}(\omega_{j\bar{i}}+\omega_{i\bar{j}})$, is free of all Zeeman terms. In liquids such a limit is referred to as J-spectroscopy[120,121]; in anisotropic systems it has been used to describe multiple quantum echo spectra[19,41] of systems with small or zero chemical shifts. If the goal is to measure spin-spin couplings, this situation is satisfactory. However, the removal of inhomogeneous broadening is gained at the expense of chemical shift information, which may be of intrinsic interest or may at least be an aid to line assignments, particularly in liquids.

4.1.1.2 $[\mathcal{H}_1, \mathcal{H}_1'] \neq 0$

The situation is different when the commutator (4.4) is not negligible. This situation results when the chemical shift differences and spin-spin couplings are of comparable magnitude. In this case, the density operator after the π pulse is represented by Figure 4.1c. Many of the spin inversion states $|\bar{k}\rangle$ are no longer eigenstates of $\mathcal{H}_1$ and, for a given eigenstate $|k\rangle$, several of the matrix elements $\langle i|R|k\rangle$ may therefore be non-zero. From each coherence of order n^I prepared originally, there may be a transfer (via the π pulse) to several coherences of order $-n^I$. The resulting spectrum cannot be characterized by an average Hamiltonian and, in fact, contains more Fourier components (at frequencies $\frac{1}{2}(\omega_{ji} + \omega_{k\ell})$) than would be expected from any plausible energy level diagram. This is illustrated in Figure 4.2b, which shows a computer simulated single quantum spin echo spectrum of partially oriented acetaldehyde. This spectrum, which is symmetric about zero frequency, contains more than twice the number of lines seen in the normal single quantum spectrum, whose simulation is shown in Figure 4.2a. The observed line positions in the spin echo spectrum are at the averages of pairs of transition frequencies of the normal spectrum.

The spin echo spectrum is reasonably insensitive to chemical shifts, though they do enter into the line positions in an attenuated form. More troublesome is that the plethora of lines created complicates spectral analysis and reduces resolution. Analytical expressions have been derived for the single quantum[122-124] and multiple quantum[69] spin echo line positions and intensities of several small spin systems. In addition, a computer program has been written which is capable of calculating multiple quantum spin echo spectra of systems of up to seven coupled spins[51].

Figure 4.2. Simulated spectra of partially oriented acetaldehyde. Simulations of this AB_3 spin system are with parameters J_{AB} = 2.8 Hz, D_{AB} = -179.0 Hz, D_{BB} = 458.6, and ν_{AB} = 1360.9 Hz. (a) Normal single quantum spectrum, generated by computer program SQSPEC[51]. (b) Single quantum spin echo spectrum, generated by computer program SPECHO[51]. This spectrum, which is symmetric about zero frequency, contains more than twice the number of lines seen in the normal spectrum in (a).

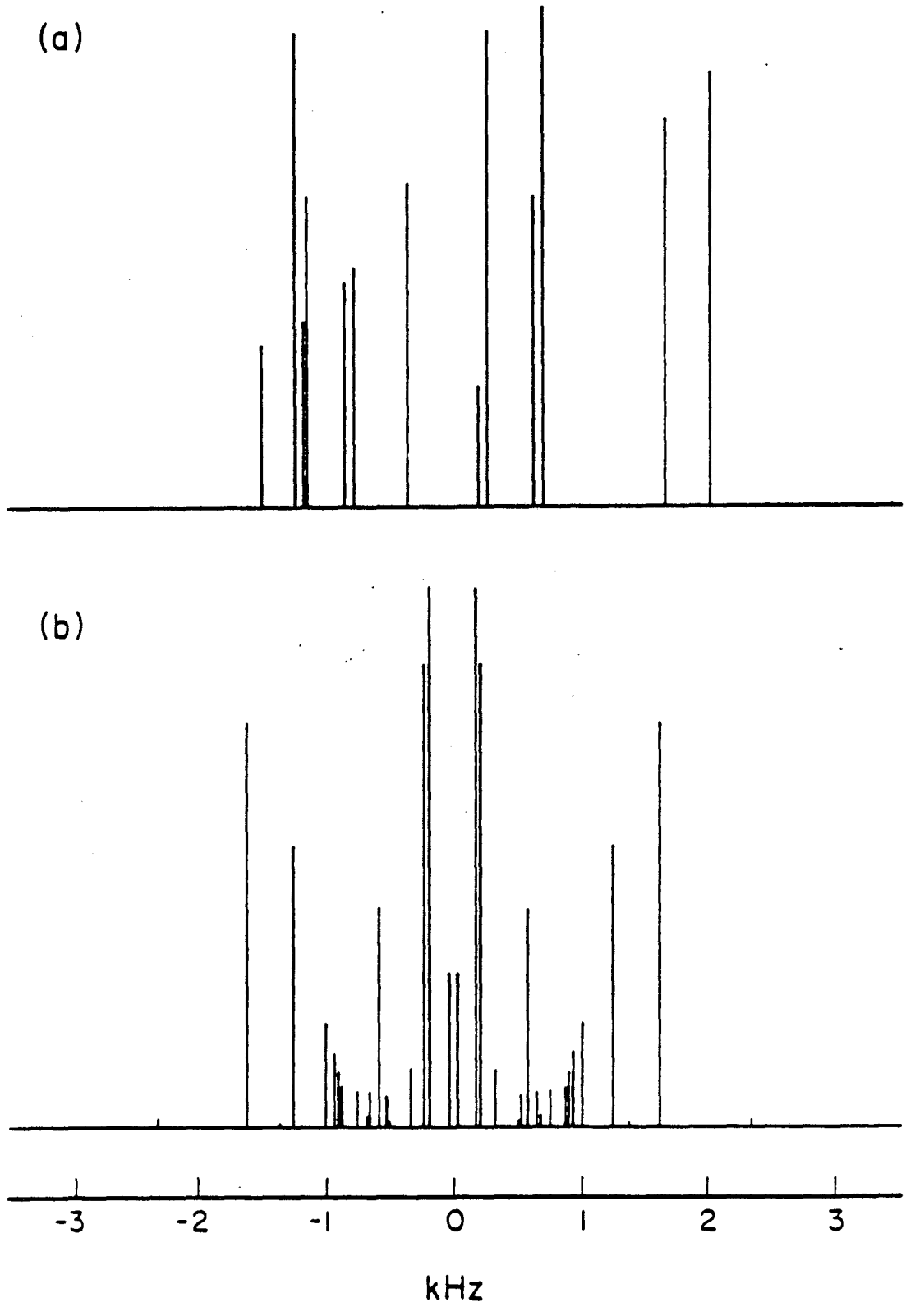

XBL 835-9607

4.1.2 Total Spin Coherence

4.1.2.1 Definition

The TSCTES method depends upon the unique properties of the total spin coherence, defined as the coherent superposition of the extreme eigenstates of a coupled spin system. This transition corresponds to the simultaneous flipping of all spins from down to up. Its operator may be written either in bra-ket notation or as the product of single spin operators. For a system of N spin-½ nuclei these forms are:

$$\left|\frac{N}{2}\right\rangle\left\langle\frac{-N}{2}\right| = \prod_{i=1}^{N} I_{+i}. \qquad (4.9)$$

The total spin coherence is one example of a spin inversion transition. Spin inversion transitions connect eigenstates which can be formed from one another by replacing all individual spin states $|\beta\rangle$ by $|\alpha\rangle$ and $|\alpha\rangle$ by $|\beta\rangle$.

4.1.2.2 Properties

Due to the bilinear nature of spin-spin couplings, coherences between spin inversion pairs commute with $\mathcal{H}_{II}^{D}$ and $\mathcal{H}_{II}^{J}$ and thus evolve independently of both. In addition, the total spin coherence (4.9) commutes with all chemical shift differences. Thus the total spin coherence evolves independently of all terms in the spin Hamiltonian except for the homogeneous and inhomogeneous Zeeman terms, $-(\Delta\omega + \omega(\underset{\sim}{r}))I_z$. It is this property which forms the basis of TSCTES experiments.

4.1.3 Coherence Transfer Echoes

Central to the TSCTES technique is the phenomenon of the coherence transfer echo[125,35,63]. In contrast to the Hahn spin echo[119], the coherence transfer echo involves a change in the magnitude of the order of

coherence, n^I, before and after the echo pulse. This effect has been demonstrated for a system of several coupled protons[63] and used for the suppression of signal from all but one order of coherence (coherence transfer echo filtering), as described in Section 2.4.2.4.

The TSCTES method uses the phenomenon of coherence transfer echoes to produce pure absorption phase multiple quantum spectra with homogeneous linewidths for any order n^I. The line positions for a system of coupled spins are the same as would be obtained in a perfectly homogeneous magnet. The relative line intensities are calculable from the eigenvectors of $\mathcal{H}_{INT}$ and are independent of the excitation dynamics. Thus this version of multiple quantum NMR overcomes all three of the problems described in the opening paragraph of this chapter.

4.2 TSCTES Pulse Sequences and Spectra

4.2.1 Generalized TSCTES Experiment

A generalized schematic diagram of the TSCTES experiment is shown in Figure 4.3a. The propagator U acts on $\rho(0) = I_z$ to prepare total spin coherence. Although it is possible to employ selective excitation methods (Sec. 2.5.4) to prepare only this coherence, the propagator U will, in general, also excite other multiple quantum orders. Means of suppressing that signal which does not originate as total spin coherence will be discussed below. Presently we focus on the evolution of the N-quantum coherence, whose coefficient is the density matrix element $\rho_{-N/2,N/2}$.

As mentioned in Section 4.1.2.2, the total spin coherence is sensitive only to the homogeneous and inhomogeneous Zeeman interaction, $-(\Delta\omega + \omega(\underline{r}))I_z$. This N-quantum coherence evolves freely for a time $\frac{nt_1}{N}$,

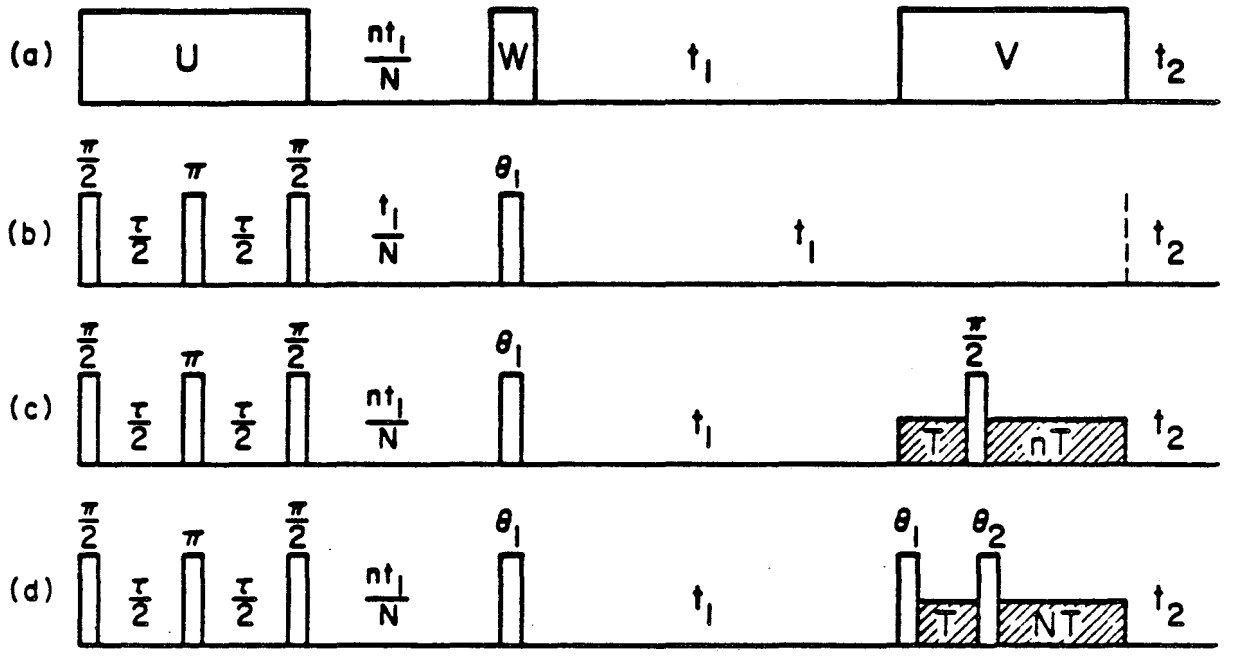

XBL 823-9465

Figure 4.3. TSCTES pulse sequences. N is the number of coupled protons in the spin system, -n the multiple quantum order of interest. (a) Generalized schematic of the TSCTES experiment. W represents a pulse or pulse sequence for transferring coherence from N-quantum to -n-quantum. (b) Single quantum (n = 1) TSCTES pulse sequence. Choice of the r.f. nutation angle θ_1 is discussed in Section 4.4.2. (c) Simple multiple quantum TSCTES sequence. The cross-hatched areas specify a pulsed magnetic field gradient for CTEF selection of -n-quantum coherence. In the present experiments, the static magnetic field inhomogeneity was such that no external gradient was required. (d) Phased-line multiple quantum TSCTES sequence. Coherence which is -n-quantum during t_1 is channeled back through the total spin coherence by the second θ_1 pulse before mixing to single quantum. CTEF and TPPI are both required to distinguish signal arising from the coherence transfer pathway of interest, as discussed in the text.

where -n is the order of the desired spectrum ($1 \leq n \leq N$). The linear dependence of dephasing rate on multiple quantum order causes $\rho_{-N/2,N/2}$ to accumulate a total phase factor of

$$\exp[+iN(\Delta\omega + \omega(\underset{\sim}{r}))\ \frac{nt_1}{N}\ ] = \exp(+in(\Delta\omega + \omega(\underset{\sim}{r}))t_1) \qquad (4.10)$$

during this time. Following this free evolution, a transfer of coherence takes place under the action of the homogeneous propagator W and the system evolves for an additional time t_1 at the frequencies of interest. For lines of order -n, the accumulated phase factor during t_1,

$$\exp(-in(\Delta\omega + \omega(\underset{\sim}{r}))t_1), \qquad (4.11)$$

just cancels the offset precession and inhomogeneous dephasing which occurred during $\frac{nt_1}{N}$, resulting in the formation of a coherence transfer echo[35,63]. The only modulation of this echo is due to the chemical shift differences and spin-spin couplings acting during t_1. Signal arising from coherence which is not N-quantum during $\frac{nt_1}{N}$ and -n-quantum during t_1 decays rapidly due to the inhomogeneous Zeeman interaction, $-\omega(\underset{\sim}{r})I_z$.

For $n \neq 1$, the echo modulation as a function of t_1 is not directly observable and the propagator V is required to mix the multiple quantum coherence back to single quantum coherence. Fourier transformation of the interferogram $S(t_1,t_2)$ with respect to t_1 yields the homogeneous -n-quantum spectrum.

4.2.2 Experimental Results

The experiments were performed on CH_3CHO dissolved in Eastman 15320 liquid crystal. The temperature was regulated at 26.0 ± 0.1°C and sampling of transverse magnetization occurred at $t_2 = 0$ only.

4.2.2.1 Single Quantum TSCTES

The homogeneous single quantum TSCTES spectrum shown in Figure 4.4b was obtained with the pulse sequence of Figure 4.3b. Parameter proportional phase incrementation (Sec. 2.5.5) was employed to choose a preparation time τ favorable for the excitation of the total spin coherence. Figure 4.4a is the normal one pulse single quantum spectrum and serves to illustrate the inhomogeneity of the static magnetic field. The simulation in Figure 4.4c confirms the sensitivity of the TSCTES spectrum to spin-spin couplings and chemical shift differences.

Figure 4.6a displays the single quantum TSCTES spectrum obtained with an initial value of $t_1 = 0$. In contrast to the magnitude spectrum of Figure 4.4b, this spectrum is presented in phase sensitive mode. All lines in this spectrum are either absorptive or emissive. Both this interesting phase property and the relative intensities of these spectral lines will be discussed in Section 4.3.3.

4.2.2.2 Multiple Quantum TSCTES

Figure 4.3c illustrates a pulse sequence used to collect multiple quantum TSCTES interferograms. CTEF is employed to select out that coherence which is -n-quantum during t_1. Two and three-quantum spectra of oriented acetaldehyde, obtained using this pulse sequence, are displayed in Figure 4.5. Within the spectral resolution (~2 Hz), all transition frequencies in these spectra are consistent with the internal Hamiltonian parameters of Figure 4.2.

Multiple quantum TSCTES spectra having phased lines of easily calculable relative intensities are obtained with the pulse sequence of Figure 4.3d. In contrast to the sequence in Figure 4.3c, coherence which spends time t_1 as -n is transferred back to the total spin coherence before being mixed to observable signal. Here CTEF serves to discriminate

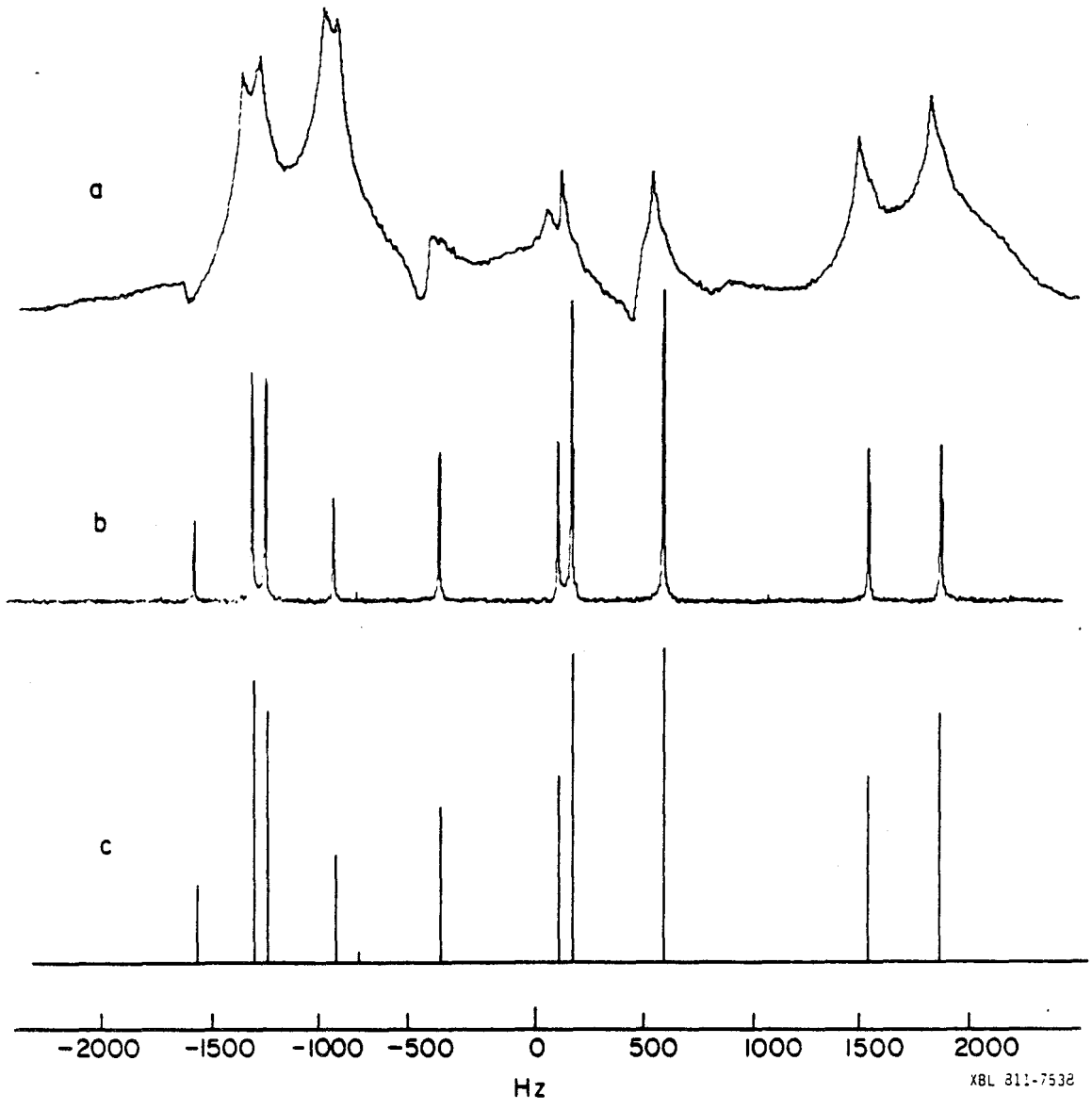

Figure 4.4. Single quantum magnitude mode spectra of partially oriented acetaldehyde. (a) The normal single-pulse Fourier transform spectrum, showing the inhomogeneity of the magnetic field to be greater than 1 ppm. (b) The single quantum TSCTES spectrum, obtained using the pulse sequence of Figure 4.3b, is the average of three 4096-point interferograms. These were collected with τ = 3.884 msec, Δt_1 = 200 μsec, θ_1 = 90°, and a recycle delay of 1 sec. (c) The simulation of this spectrum, generated with computer program NQECHO[51] using the same parameters as in Figure 4.2. Lines of E symmetry are absent because they do not correlate with the totally symmetric total spin coherence.

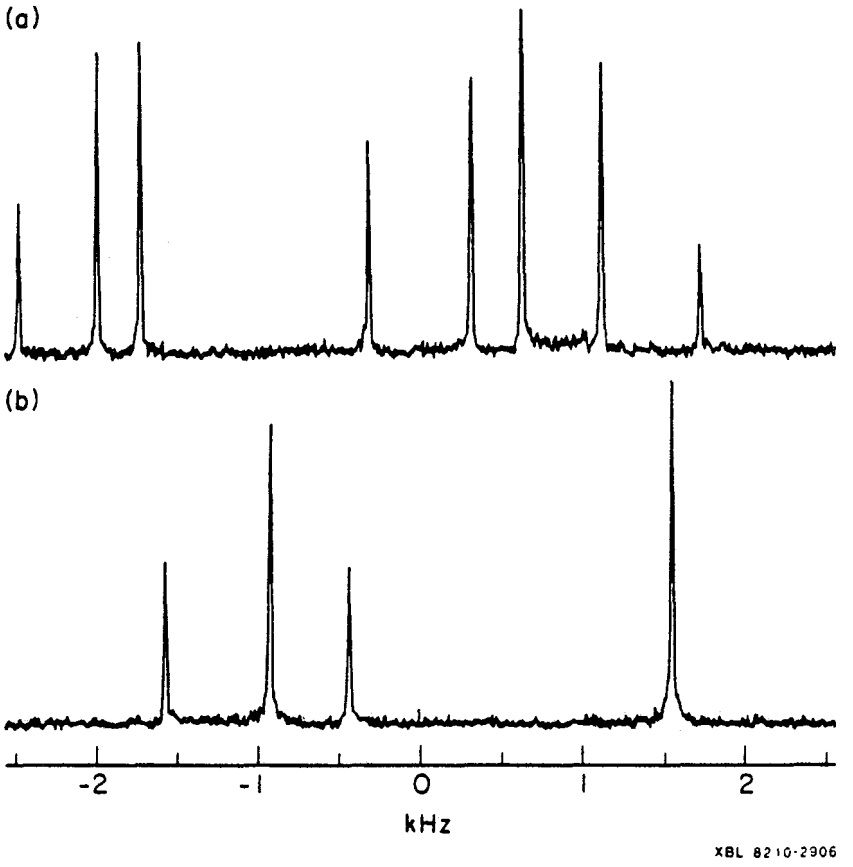

Figure 4.5. Multiple quantum TSCTES spectra of partially oriented acetaldehyde using the pulse sequence of Figure 4.3c. Each magnitude spectrum is the average of two 4096-point interferograms acquired with τ = 3.884 msec and a recycle delay of 2.1 sec. (a) The 2-quantum spectrum shows a total of 8 lines. For this spectrum T = 9.052 msec, Δt_1 = 160 μsec and θ_1 = 120°. Only a portion of the total bandwidth is displayed. (b) The 3-quantum spectrum contains 4 lines and was collected with T = 5.564 msec, Δt_1 = 200 μsec, and θ_1 = 139°.

Figure 4.6. TSCTES spectra of partially oriented acetaldehyde, displayed in phase sensitive mode, acquired with τ = 3.884 msec and a recycle delay of 2.1 sec. (a) The single quantum TSCTES spectrum shows all lines as either absorptive or emissive, as discussed in Section 4.3.3. The spectrum was collected using the pulse sequence of Figure 4.3b and is the average of three 4096-point interferograms with Δt_1 = 200 μsec, $(t_1)_o$ = 0, and θ_1 = 104°. The line positions in the simulated stick spectrum are the same as those in Figure 4.4c, the relative amplitudes being given by Equation 4.22. (b) The 3-quantum TSCTES spectrum collecting using the pulse sequence of Figure 4.3d. TPPI was used to separate out signals originating from different multiple quantum orders. This spectrum is the average of four 8192-point interferograms with T = 2.091 msec, Δt_1 = 20 μsec, θ_1 = 139°, and θ_2 = 104°. Line positions in the simulated stick spectrum were calculated based on the parameters given in Figure 4.2, and relative line amplitudes are given by Equation 4.24.

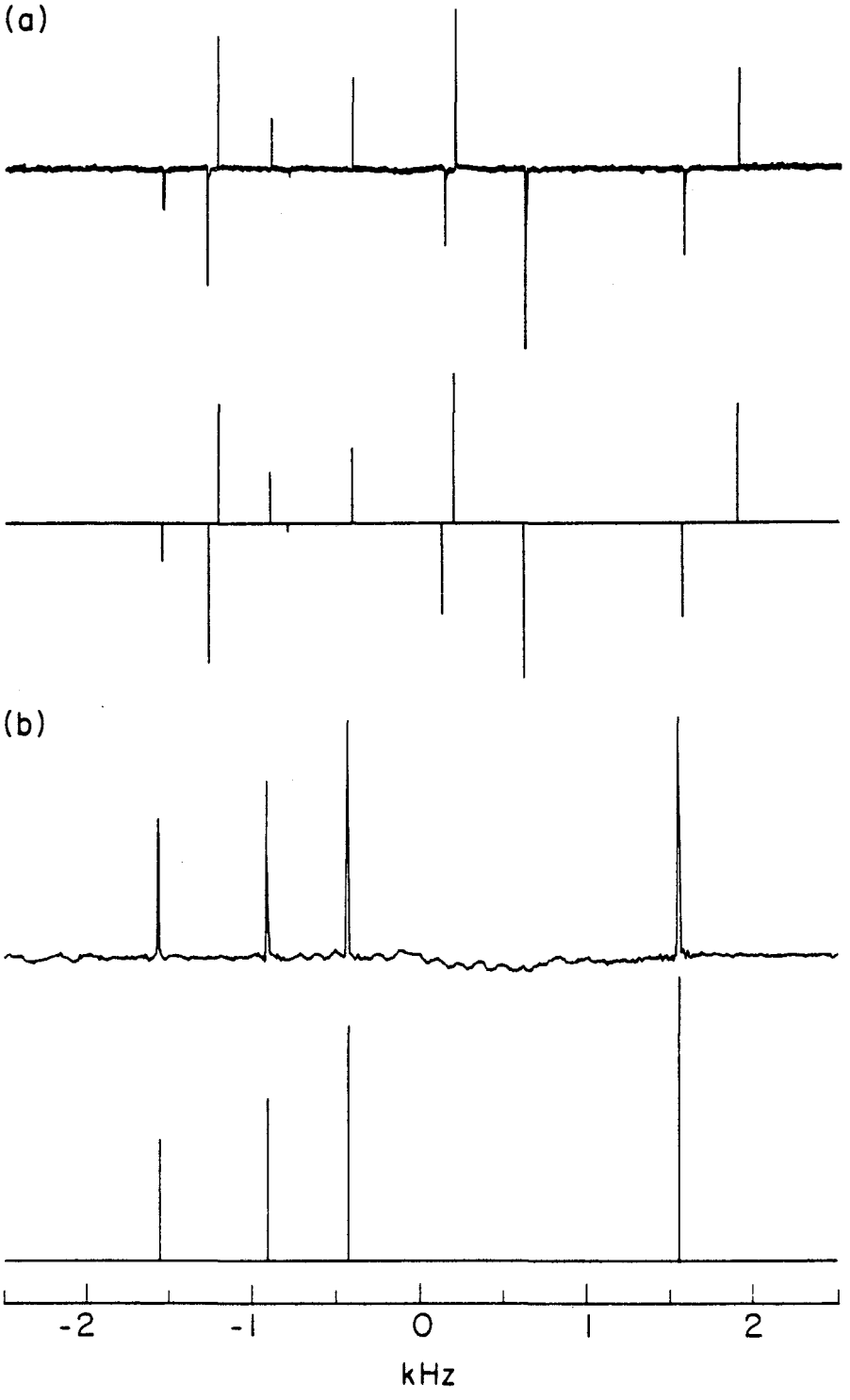

XBL 8210-2907

against coherence which is not N-quantum during time T. In addition to CTEF, a second "password" is required to separate out signal which originates as total spin coherence. That additional discrimination is necessary is most easily seen by considering a specific example.

Assume that the spectrum of interest is the 2-quantum TSCTES spectrum of a four spin system. The appropriate coherence transfer pathway can be schematically represented as:

$$4 \xrightarrow{\theta_1} -2 \xrightarrow{\theta_1} 4 \xrightarrow{\theta_2} -1. \qquad (4.12)$$

CTEF alone, however, cannot distinguish this desired pathway from the following alternate route:

$$2 \xrightarrow{\theta_1} -1 \xrightarrow{\theta_1} 4 \xrightarrow{\theta_2} -1, \qquad (4.13)$$

which also leads to spectral lines that are free of inhomogeneous broadening. The characteristic modulation properties of multiple quantum coherences under phase shifts of the r.f. irradiation (Sec. 2.4.2) can serve to distinguish these two cases from one another. The phased 3-quantum spectrum of Figure 4.6b was obtained using TPPI as the second password. This results in a clean separation of the signal contributions from the pathways (4.12) and (4.13) to different spectral regions.

4.3 Relative Line Amplitudes

4.3.1 Irreducible Tensor Operators

In the following sections on intensity and relative phase of TSCTES lines, it will prove useful to represent multiple quantum coherences as irreducible tensor operators. Irreducible tensor operators T_n^{ℓ} were introduced in Section 1.7 of this thesis. These tensor operators are normalized just as are outer products of normalized states:

$$Tr(T^{\ell}_{n}T^{\ell}_{-n}) = 1. \tag{4.14}$$

The total spin coherence can be represented as the tensor operator T^{N}_{N}:

$$T^{N}_{N} = |N/2><-N/2|. \tag{4.15}$$

According to Equation 1.64 the rotation of an irreducible tensor operator T^{ℓ}_{n} by an r.f. pulse of nutation angle θ and phase ϕ can be described by:

$$D(\theta,\phi)T^{\ell}_{n}\ D^{-1}(\theta,\phi) = \sum_{n'} T^{\ell}_{n'}d^{(\ell)}_{n',n}(\theta)\ \exp(i(n-n')\phi). \tag{4.16}$$

In the following discussion it will be the magnitude of the coefficient $d^{(\ell)}_{n',n}(\theta)$ and not the phase factor $\exp(i(n-n')\phi)$ which is important. Both factors will be common to all lines of a given observed spectral order n. The former will enter into the efficiency of the experiment, while the latter can be adjusted to unity by the choice of the r.f. phase or by overall phase manipulation of the complex data array.

4.3.2 General Form of the TSCTES Signal

As with any NMR experiment, the measured TSCTES signal is $Tr(\rho(t)I_{+})$ (Eq. 2.3). We shall first derive a general expression for the TSCTES signal based upon the schematic diagram of Figure 4.3a, and then consider the specific pulse sequences of Figures 4.3b and d.

We define the Hamiltonian $\mathcal{H}'_{INT}$ as

$$\mathcal{H}'_{INT} \equiv \mathcal{H}_{INT} + (\Delta\omega + \omega(\underline{r}))I_{z}, \tag{4.17}$$

the internal Hamiltonian minus the homogeneous and inhomogeneous Zeeman terms. It is assumed that TPPI in the preparation period and CTEF in the mixing period are used to select the coherence transfer pathway of interest.

Along with the coherence transfer echo formed at t_1, the labeling of signal with these two passwords allows us to determine the -n-quantum TSCTES signal from the evolution (during t_1) under $\mathcal{H}'_{INT}$ of a density operator $\rho^{(n)}(\tau)$ which is given at $t_1 = 0$ by

$$\rho^{(n)}(\tau) = \rho_{N/2,-N/2}(\tau)\mathrm{Tr}[(W|N/2><-N/2|W^{\dagger})T^N_n]T^N_{-n}. \qquad (4.18)$$

Taking the propagator W to be a strong y-pulse of flip angle θ_1 allows this density operator to be simplified to

$$\rho^{(n)}(\tau) = \rho_{N/2,-N/2}(\tau)\ d^{(N)}_{N,-n}(\theta_1)T^N_{-n}. \qquad (4.19)$$

The signal at $t_2 = 0$ can then be written as

$$S_\alpha(\tau,\tau',t_1,T) = \mathrm{Tr}(\exp(-i\mathcal{H}'_{INT}t_1)\rho^{(n)}(\tau)\ \exp(i\mathcal{H}'_{INT}t_1)\alpha(-\tau'-T));$$

$$\alpha = X,Y. \qquad (4.20)$$

Expanding Equation 4.20 in the eigenbasis of $\mathcal{H}_{INT}$ gives the TSCTES signal as an interferogram in t_1:

$$S_+(\tau,\tau',t_1,T) = \sum_{i,j} \rho^{(n)}_{ij}(\tau)(X_{ji}(-\tau'-T) + iY_{ji}(-\tau'-T))\ \exp(i\omega_{ji}t_1). \qquad (4.21)$$

In the general sequence of the form of Figure 4.3a and the particular sequence of Figure 4.3c, even the relative amplitudes of the different TSCTES lines of order n depend on the mixing period. For the sequences of Figures 4.3b and d, however, these relative amplitudes are independent of both preparation and mixing dynamics. It is these sequences which we now consider in greater detail.

4.3.3 Relative Single Quantum TSCTES Line Amplitudes

For the single quantum experiment (Fig. 4.3b), the propagator V is omitted because the -1-quantum coherence is directly observable during t_1.

Thus $I_+(-\tau'-T)$ is simply equal to I_+ and the intensity of a given line is given by the product

$$\rho_{N/2,-N/2}(\tau)\ d^{(N)}_{N,-1}(\theta_1)\langle i|T^N_{-1}|j\rangle\langle j|I_+|i\rangle. \qquad (4.22)$$

The first term in this expression is the coefficient of the total spin coherence prepared by the propagator $U(\tau)$. The second factor is a Wigner rotation matrix element, which expresses the efficiency with which single quantum coherence is prepared from the total spin coherence by a pulse of nutation angle θ_1. Optimal choice of this angle is discussed in Section 4.4.2. These first two factors are common to all lines. The third factor expresses the extent to which a particular transition i-j is represented in the resultant single quantum operator T^N_{-1}, while the final term is the normal magnetic dipole detection period matrix element.

As demonstrated in Figure 4.6a, all of the single quantum TSCTES lines are either absorptive or emissive. In addition, the sum of the lines in this spectrum is zero. Qualitatively this is easily understood. The signal immediately following the transfer of coherence W is rigorously zero, due to the orthogonality of T^N_{-1} and the detection operator I_+, which is a T^1_1 tensor operator. The point $t_1 = 0$ in the free induction decay therefore vanishes and, since this point is equal to the integral of the resulting spectrum, the sum of the spectral lines must be zero.

A quantitative treatment of relative line intensities and phases requires examination of the final two terms of the expression (4.22). The matrix elements $\langle i|T^N_{-1}|j\rangle$ are, to within a common phase factor, all real as are the elements of the detection matrix I_+. Thus all of the single quantum TSCTES lines have, to within a sign, a common phase. In addition, the algebraic signs of the elements $\langle i|T^N_{-1}|j\rangle$ alternate between + and - as the Zeeman quantum numbers m_i and m_j are changed by one[51].

In weakly coupled systems a similar relationship holds for the signs of the terms $\langle i|I_+|j\rangle$[51] and for these systems the positive and negative spectral lines originate in two orthogonal subspaces.

The simulation shown in the lower portion of Figure 4.6a is based upon the expression in (4.22). The matrices describing I_+ and the rotated total spin coherence in the eigenbasis of $\mathcal{H}_{INT}$ were computer calculated. The relative intensity and phase of each line was then determined by taking the product of the appropriate matrix elements. The common factor $\rho_{N/2,-N/2}(\tau)$ is discussed in Section 4.4.3.

4.3.4 Relative Multiple Quantum TSCTES Line Amplitudes

We turn now to the multiple quantum TSCTES pulse sequence of Figure 4.3d. Here the propagator V channels -n-quantum coherence back through the total spin coherence before the final mixing to detectable single quantum signal. The mixing thus serves the same purpose as the preparation: to interconvert total spin coherence and magnetization. Defining

$$\rho_{-N/2,N/2}(-\tau'-T) \equiv \mathrm{Tr}[(|N/2\rangle\langle -N/2|)I_+(-\tau'-T)], \tag{4.23}$$

we can write the coefficient of the i-j transition (Eq. 4.21) for the sequence of Figure 4.3d as

$$\rho_{ij}^{(n)}(\tau)(X_{ji}(-\tau'-T) + iY_{ji}(-\tau'-T)) = \rho_{N/2,-N/2}(\tau)\rho_{-N/2,N/2}(-\tau'-T) \times (d_{N,-n}^{(N)}(\theta_1))^2|\langle i|T_{-n}^{N}|j\rangle|^2. \tag{4.24}$$

The first three factors on the right are common to all lines of the chosen order. The first is the coefficient of the total spin coherence in the prepared density matrix $\rho(\tau)$, the second the coefficient of this same coherence in the "devolved" detection operator. The last two factors are both non-negative and real, ensuring that all lines will have a

common phase. The appropriate Wigner rotation matrix element comes into Equation 4.24 squared, because coherence is first transferred from N-quantum to -n and then back. For the same reason, the factor reflecting the extent to which the i-j transition is represented in T^N_{-n} enters as the magnitude squared. As in the single quantum case, the relative phases and intensities of all -n-quantum lines are independent of the propagators U, V, and W.

To simulate the 3-quantum TSCTES spectrum of Figure 4.6b, the density matrix resulting from rotation of the total spin coherence was computer calculated. Individual line intensities were then computed by taking the magnitude squared of the appropriate terms in this density matrix.

4.4 Absolute Integrated Intensities

4.4.1 Motivation

In the preceding section, the relative intensities of TSCTES lines were discussed. We address now the important question of absolute spectral intensity in TSCTES experiments. The overall intensity of a TSCTES spectrum depends upon: (1) the excitation of the total spin coherence (T^N_N), (2) the multiple quantum order of interest (-n), and (3) the efficient transfer of coherence $T^N_N \rightarrow T^N_{-n}$. The dependences on the first two of these will be discussed in Section 4.4.3. First, however, we consider the optimization of coherence transfer between multiple quantum orders.

4.4.2 Optimization of Pulse Angles

The dependences of the single and multiple quantum TSCTES line intensities on the pulse angle θ_1 of Figure 4.3 are given, respectively, by (4.22) and (4.24). In addition, for the sequence of Figure 4.3d, the

factor $\rho_{-N/2,N/2}(-\tau'-T)$ in (4.24) has an implicit factor $d^{(N)}_{N,-1}(\theta_2)$ describing the transfer of coherence $T^N_N \rightarrow T^N_{-1}$. The relevant Wigner rotation matrix element can be found in standard angular momentum texts[33,34]:

$$d^{(N)}_{N,-n}(\theta) = (-1)^{N+n}\left[\frac{(2N)!}{(N-n)!\,(N+n)!}\right]\left[\cos\left(\frac{\theta}{2}\right)\right]^{N-n}\left[\sin\left(\frac{\theta}{2}\right)\right]^{N+n}. \qquad (4.25)$$

Explicit tabulations of these coefficients have been given for $0 \leq N \leq 7$[126].

In order to demonstrate the dependence of coherence transfer efficiency on the r.f. nutation angle, two sets of 2-quantum TSCTES experiments were performed using the pulse sequence of Figure 4.3d. The first set involved varying the flip angle θ_1 with the value of θ_2 held constant ($\theta_2 = 104°$). For each value of θ_1, the sum of the line intensities in the 2-quantum spectrum was recorded. Figure 4.7a shows a plot of this total normalized spectral intensity as a function of θ_1. The solid line is the theoretical curve, described by the function $\sin^2\theta_1(1-\cos\theta_1)^2$. Figure 4.7b shows results from a second set of experiments in which flip angle θ_2 was varied with θ_1 constant ($\theta_1 = 120°$). The theoretical curve, described by the function $\sin^3\theta_2(1-\cos\theta_2)$, is also shown.

The expression for $d^{(N)}_{N,-n}$ given in Equation 4.25 is easily maximized to yield optimal values of the nutation angle θ, θ_{OPT}, for different values of N and -n. For the four spin acetaldehyde system (N = 4), θ_{OPT} equals 104° for n = 1, 120° for n = 2, and 139° for n = 3. Each of the TSCTES spectra displayed in Figures 4.5 and 4.6 were obtained with θ_1 (and, when relevant, θ_2) chosen according to this list.

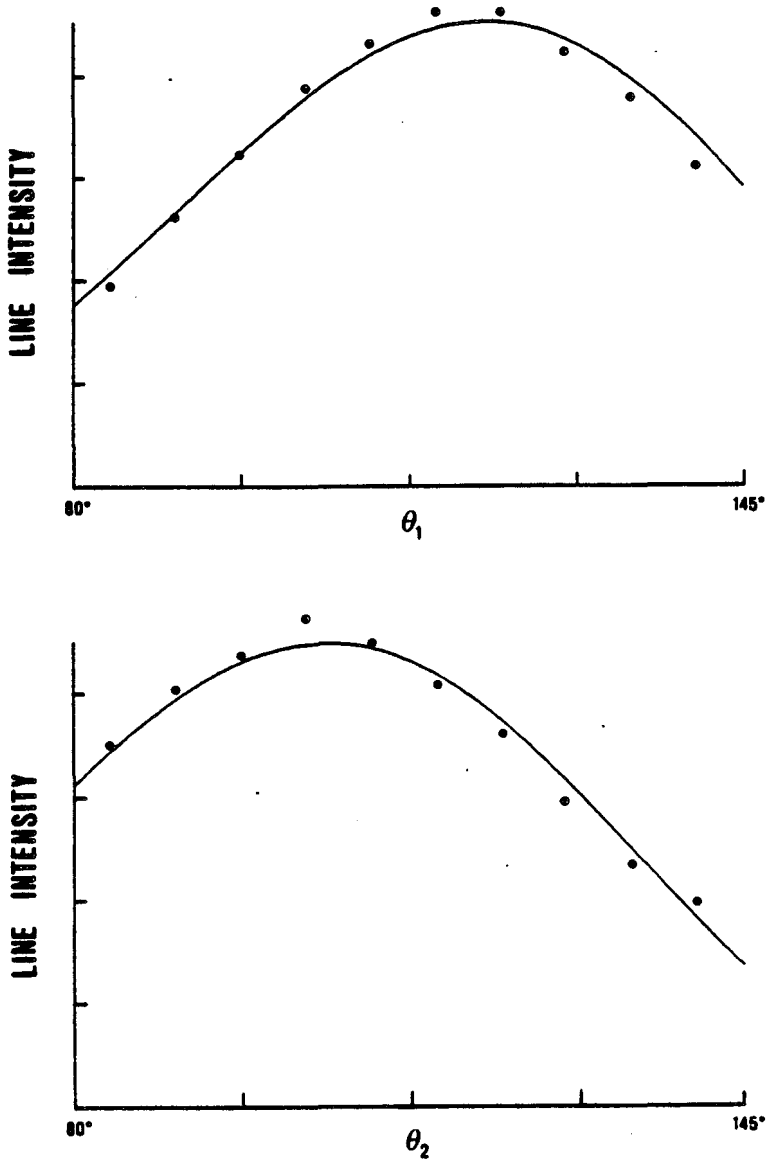

Figure 4.7. Dependence of 2-quantum line intensities on the r.f. nutation angles θ_1 and θ_2 of the pulse sequence in Figure 4.3d. Plotted line intensities are proportional to the sum of the magnitudes of the eight 2-quantum lines. (a) Line intensity as a function of θ_1 with $\theta_2 = 104°$. The theoretical curve is described by the function $\sin^2\theta_1(1-\cos\theta_1)^2$. (b) Line intensity as a function of θ_2 with $\theta_1 = 120°$. Here the theoretical curve is described by $\sin^3\theta_2(1-\cos\theta_2)$.

4.4.3 Dependence of Intensities on N and n

We derive in this section expressions for the absolute integrated and average TSCTES line intensities for the sequence of Figure 4.3d, expressed as a fraction of the total equilibrium magnetization. These intensities depend on both the number of spins, N, and the multiple quantum order, -n, observed.

The total spectral intensity for the sequence of Figure 4.3d, S(n,N), is found by summing (4.24) over all lines using the identity of Equation 4.14:

$$S(n,N) = \rho_{N/2,-N/2}(\tau)\rho_{-N/2,N/2}(-\tau'-T)(d^{(N)}_{N,-n}(\theta_1))^2. \qquad (4.26)$$

The maximum value of $\rho_{N/2,-N/2}(\tau)$ for initial condition $\rho(0) = I_z$ and any unitary preparation propagator $U(\tau)$ is $\frac{N}{2}$[20,47]. This is most easily seen by considering the two level system comprised of the $m^I = \pm \frac{N}{2}$ Zeeman levels. An N-quantum selective $\frac{\pi}{2}$ pulse transfers the entire population difference between these two states into total spin coherence. Similar arguments place an upper bound of $\frac{N}{2}$ on the magnitude of $\rho_{-N/2,N/2}(-\tau'-T)$ also. Substituting these maximum values into Equation 4.26, setting $\theta_1 = \theta_{OPT}$, and dividing by the total equilibrium magnetization, $Tr(I_z^2) = \frac{N2^N}{4}$, the optimum fractional magnetization, f(n,N), is found to be

$$f(n,N) = N2^{-N}(d^{(N)}_{N,-n}(\theta_{OPT}))^2. \qquad (4.27)$$

Finally, it is necessary to remember that the number of lines of order -n among which this magnetization will be shared also depends on N and n. In Equation 1.58b the number of n-quantum lines for a system of N spins-½, Z(n,N), was given for an unsymmetrical spin system as

$$Z(n,N) = \binom{2N}{N-n} . \qquad (4.28)$$

Dividing (4.28) into (4.27) gives the mean fractional magnetization per TSCTES line which can be detected in t_2. The logarithm (base 10) of this quantity is plotted in Figure 4.8 for $2 \leq N \leq 16$ and $n = N-1$ and $N-2$.

4.5 Limitations on TSCTES

4.5.1 System Size, System Isolation, and Linewidths

The results of Section 4.4, summarized by Figure 4.8, place an obvious signal-to-noise limitation on TSCTES. This is similar to that for other multiple quantum experiments discussed in previous chapters. For acetaldehyde and other small spin systems, the simple multiple quantum excitation sequences of Figures 4.3b-d are sufficient to excite a substantial amount of N-quantum coherence. For larger systems, there is increasing necessity for the selective excitation of the total spin coherence.

A more subtle requirement of the TSCTES experiment is that of system isolation. If the system is only approximately limited to N spins, the N-quantum transition will be broadened or split by interactions with other spins. This structure will then be convoluted into all lines of the TSCTES spectrum.

In this regard it should be noted that even when all lines are resolved Lorentzians, the TSCTES linewidth (FWHM), $\bar{\nu}_{\frac{1}{2}}^{ij}$, is given by

$$\bar{\nu}_{\frac{1}{2}}^{ij} = [(n/N)\nu_{\frac{1}{2}}^{N/2,-N/2} + \nu_{\frac{1}{2}}^{ij}], \qquad (4.29)$$

where $\nu_{\frac{1}{2}}^{ij}$ is the usual homogeneous linewidth for the i-j transition. Equation 4.29 expresses the fact that the irreversible dephasing of the total spin coherence is not removed from the dynamics by the echo.

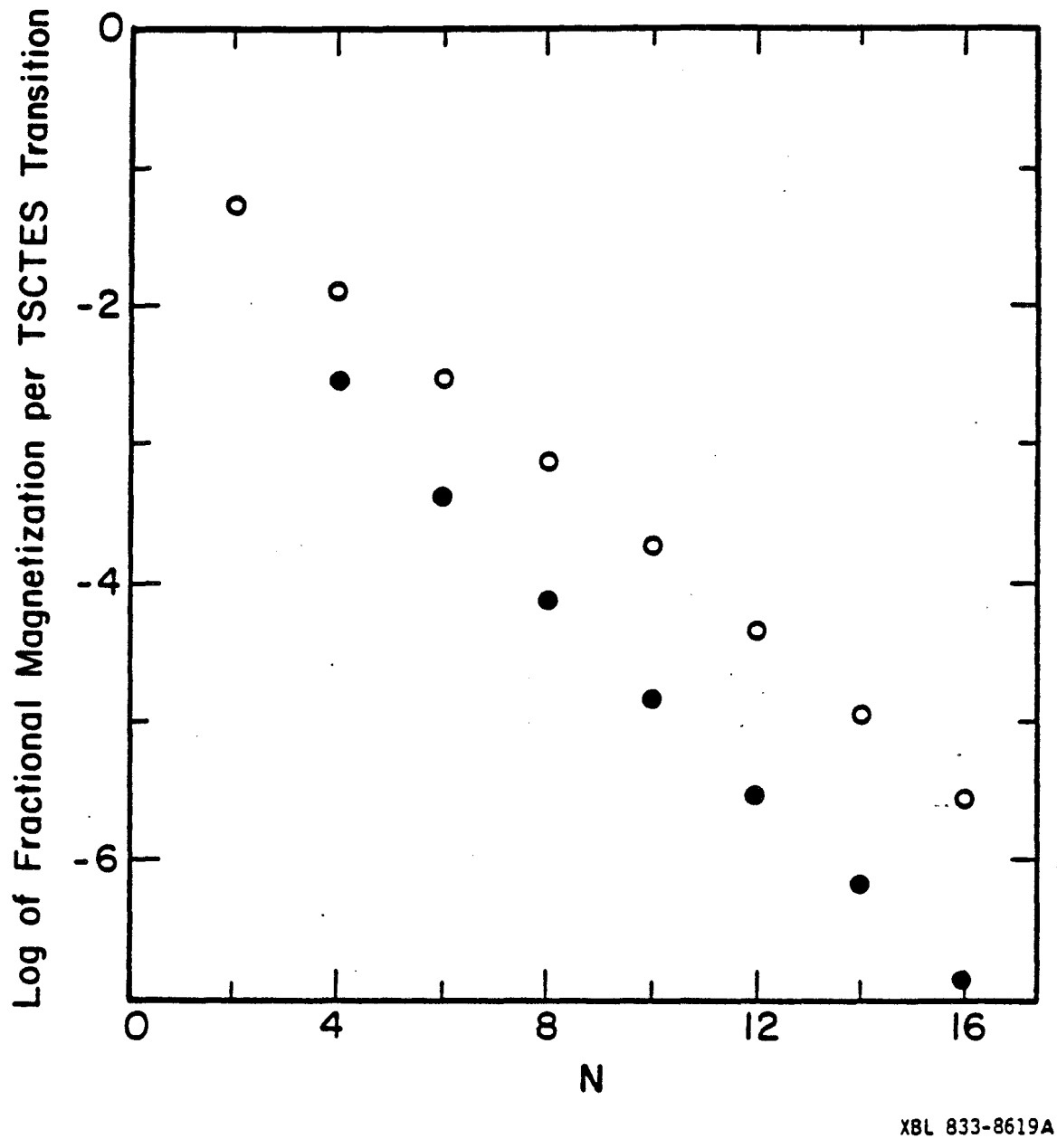

Figure 4.8. The logarithm (base 10) of the mean fractional magnetization per TSCTES transition, [f(n,N)/Z(n,N)], as a function of the number of spins N for observed orders n = N-1(○) and n = N-2(●). The calculation assumes optimum excitation periods and pulse angles for a TSCTES pulse sequence similar to Figure 4.3d. The decline in [f(n,N)/Z(n,N)] with increasing N is due to the greater number of -n-quantum transitions and the decreasing effectiveness of both exciting the total spin coherence and of transferring it to order -n and back.

4.5.2 Diffusion

As is the case for all echo techniques, TSCTES lines are susceptible to residual inhomogeneous broadening due to the effects of translational diffusion[119,127-130]. Molecular motion from one region of magnetic field to another during the evolution period imparts a random time dependence to the inhomogeneous Zeeman interaction and thus leads to an incomplete refocusing. In such a case, Equation 4.29 underestimates the linewidth.

In order to measure the effect of diffusion on linewidth, the magnetic field homogeneity was intentionally spoiled by misadjustment of the room temperature shims. Single quantum signal following a single pulse in the resultant field decayed in approximately 1 msec. Table 4-1 shows measured one, two, and three-quantum TSCTES linewidths for partially oriented acetaldehyde in this field. Also shown are the linewidths measured in standard spin echo experiments employing a single π pulse at the midpoint of the evolution period, $\frac{t_1}{2}$. TSCTES lines are seen to be more sensitive to the effects of diffusion.

To understand this effect the time period $\frac{nt_1}{N}$ and the Hamiltonian term $-\omega(\underset{\sim}{r})I_z$ must be explicitly reintroduced into the problem. The total spin coherence experiences an inhomogeneity of magnitude $-N\omega(\underset{\sim}{r})$ during the time $\frac{nt_1}{N}$, while -n-quantum coherence feels the inhomogeneity as $+n\omega(\underset{\sim}{r})$. If one treats the difference in magnitude between $N\omega(\underset{\sim}{r})$ and $n\omega(\underset{\sim}{r})$ as a time dependence in the size of the magnetic field inhomogeneity, Equation 5 of reference [128] can be used to compare the relative sensitivities of TSCTES and standard spin echo experiments to diffusion. Evaluation of this expression does predict the observed greater sensitivity to inhomogeneous broadening of TSCTES lines. A major contributing factor is the additional time period in TSCTES experiments, $\frac{nt_1}{N}$, over

Table 4-1

Linewidths of Multiple Quantum TSCTES and Standard Multiple Quantum Spin Echo Experiments for Partially Oriented Acetaldehyde in an Inhomogeneous Magnetic Field

Multiple Quantum Order (n)	TSCTES Linewidth (Hz)	Spin-echo Linewidth (Hz)
1	4	2
2	5	3
3	7	4
4	-	5

which the effect of diffusion must be considered. A more quantitative treatment of diffusional effects is difficult because these experiments were not performed in the presence of a well-defined magnetic field gradient. It is apparent, however, that diffusion will not seriously limit the resolution of TSCTES experiments except in extremely inhomogeneous static fields.

4.5.3 Information Content: Symmetry and Referencing

As already noted (Fig. 4.4), the lines observed with TSCTES always belong to the totally symmetric representation. This is because the total spin coherence itself has A_1 symmetry and any unitary propagator W only connects this coherence with other transitions of the same symmetry. For -(N-1)-quantum spectra this is not a problem because all such transitions are of A_1 symmetry. For lower orders this can be inconvenient, since transitions of other representations may be more sensitive to certain combinations of Hamiltonian parameters which one would like to extract from the spectra.

Finally, although TSCTES preserves chemical shift differences within a group of coupled spins, it is incapable of measuring differences between isolated systems. This places a limit on the technique's usefulness in mixtures and precludes the referencing of TSCTES spectra to an external standard.

4.6 Conclusion

The technique of total spin coherence transfer echo spectroscopy has been demonstrated for both single quantum and multiple quantum spectra. Spectra which are sensitive to both chemical shift differences and spin-spin interactions between coupled protons are obtained in the

absence of broadening due to inhomogeneity of the static magnetic field. In general, multiple quantum lines are of random phase and have relative intensities which are difficult to calculate, due to the complex dynamics of the excitation periods. Experiments which first excite and then channel signal back through the unique total spin coherence produce multiple quantum TSCTES spectra having phased lines and easily simulated relative intensities. The r.f. nutation angle dependence of coherence transfer processes has been analyzed by means of a tensor operator description and confirmed by experiment. An analysis of the line intensities shows that TSCTES should find numerous applications in coupled spin systems of moderate size.

The extension of TSCTES to heteronuclear systems consisting of several coupled protons and a ^{13}C nucleus is straightforward. Multiple quantum spectroscopy of these systems was discussed in Chapter 3. Heteronuclear TSCTES experiments in such systems may begin with excitation of the total spin coherence of the protons or of the combined proton/^{13}C spin system. In a manner analogous to that described here, heteronuclear TSCTES spectra can then be collected which are sensitive to carbon-proton couplings as well as proton-proton couplings and chemical shifts.

Chapter 5: APPLICATIONS OF HETERONUCLEAR BILINEAR ROTATIONS

In Chapter 3, we discussed the measurement of dipolar couplings in partially oriented molecules consisting of several coupled protons and a randomly placed ^{13}C nucleus. In this chapter, we consider various aspects of the NMR spectroscopy of such molecules in the liquid state, where the dipolar couplings are averaged to zero. In recent years, a variety of simple double resonance experiments have been performed which make use of the J-coupling between heteronuclear spins in liquids to perform useful site-selective manipulations. The problems approached include: (1) the transfer of polarization from one spin species to another[131-139], (2) the aforementioned creation of heteronuclear multiple quantum coherence[63,66,108-113], (3) observation of ^{13}C satellite spectra without interference from the much more abundant ^{12}C containing groups [140,141], (4) selection of carbon signal from ^{13}C nuclei having a particular number of directly bound protons[136,142-144], and (5) creation of certain non-equilibrium population distributions (J-order)[136,145,146]. These seemingly diverse experiments actually have a strong resemblance to one another. They all consist of irradiating one or both spin species with several strong r.f. pulses of nutation angle $\frac{\pi}{2}$ or π, separated in time by periods of free evolution on the order of $(J_{IS})^{-1}$, the inverse of the heteronuclear coupling constant between the spins of interest.

The purpose of this chapter is twofold. The first is to develop a density operator formalism for the dynamics of these double resonance experiments. We then use this formalism in the design of novel pulse sequences for the isolation of satellite spectra and for homonuclear decoupling of protons in liquids.

Throughout this chapter we shall continually emphasize the bilinear nature of the heteronuclear scalar coupling. In Section 5.1, the concept of a heteronuclear bilinear rotation is defined and various operator identities are collected. The usefulness of the bilinear rotation as a calculational tool is demonstrated in Section 5.2 by explicit calculation of the density operators which are prepared in several known experiments. In Section 5.3, the compensated heteronuclear bilinear π rotation (CHBπ), designed to be less sensitive to J_{IS} than a simple bilinear π rotation, is introduced. This relative insensitivity to J_{IS} is experimentally demonstrated and the CHBπ is applied to the problem of the selective detection of ^{13}C satellite proton spectra. Finally, the problem of homonuclear decoupling in liquids is examined in Section 5.4. A new decoupling technique which takes advantage of the heteronuclear scalar coupling bewteen a ^{13}C and its bound (satellite) protons, Bilinear Rotation Decoupling (BIRD)[147], is introduced and experimentally demonstrated.

5.1 Heteronuclear Bilinear Rotations

5.1.1 Isolated I_nS Spin Systems

We begin by reviewing the algebra involved in simple bilinear rotations of the components of spin angular momentum. Initially we shall be concerned with systems composed of a single ^{13}C nucleus (S spin) bonded to n magnetically equivalent protons (I spins). The spin Hamiltonian for the I_nS system is

$$\mathcal{H} = -(\Delta\omega^I + \omega(\underset{\sim}{r}))I_z - (\Delta\omega^S + \left(\frac{\gamma_S}{\gamma_I}\right)\omega(\underset{\sim}{r}))S_z + J'_{IS}I_zS_z. \qquad (5.1)$$

(For consistency with reference [147], the sign of the heteronuclear coupling has been reversed relative to Equation 1.51.) The homonuclear

scalar couplings, which commute with all components of I spin angular momentum, have been omitted from Equation 5.1 and can be rigorously ignored throughout this discussion.

It will prove convenient to remove the Zeeman terms in Equation 5.1 from the evolution by applying π pulses to both spin species. The simplest pulse sequence which does this and is cyclic (in the sense of average Hamiltonian theory) is

$$\frac{t}{2},\ (\pi_x^{I,S}),\ \frac{t}{2},\ (\pi_{\bar{x}}^{I,S}), \tag{5.2}$$

where $(\pi_x^{I,S})$ represents simultaneous π_x pulses applied to both I and S spins. The propagator for this sequence is

$$U(t) = \exp(-i\pi(I_x + S_x))\ \exp(-i\mathcal{H}\frac{t}{2})\ \exp(i\pi(I_x + S_x))\ \exp(-i\mathcal{H}\frac{t}{2}) \tag{5.3a}$$

$$= \exp(-iJ'_{IS}I_zS_zt). \tag{5.3b}$$

The term $J'_{IS}I_zS_z$ is the average Hamiltonian $\bar{\mathcal{H}}^{(0)}$ over the cycle defined by (5.2). In this case the effective Hamiltonian is equal to $\bar{\mathcal{H}}^{(0)}$, since the Hamiltonian commutes with itself at all times and all correction terms therefore vanish. Equation 5.3b shows that the Zeeman terms do not contribute to the evolution at time t.

If the pulse sequence of (5.2) is sandwiched between hard $\frac{\pi}{2}$ pulses applied to one or both spin species, the resulting propagator is of the form:

$$U(t) = \exp(-iJ'_{IS}I_pS_at); \tag{5.4}$$

$$p = x,y,z$$

$$a = x,y,z.$$

Since all I operators commute with all S operators, the propagator of Equation 5.4 describes a rotation about the "p"-axis for I operators and about the "a"-axis for S operators. For S operators the factor $(I_p J'_{IS} t)$ plays the role of an "angle" and we can write the effect of this propagator on the components of $\underset{\sim}{S}$ in the following general form:

$$\exp(-iJ'_{IS} I_p S_a t) S_a \exp(iJ'_{IS} I_p S_a t) = S_a, \tag{5.5a}$$

$$\exp(-iJ'_{IS} I_p S_b t) S_a \exp(iJ'_{IS} I_p S_b t) = S_a \cos(I_p J'_{IS} t) - S_c \sin(I_p J'_{IS} t), \tag{5.5b}$$

$$\exp(-iJ'_{IS} I_p S_c t) S_a \exp(iJ'_{IS} I_p S_c t) = S_a \cos(I_p J'_{IS} t) + S_b \sin(I_p J'_{IS} t). \tag{5.5c}$$

$p = x,y,z$; $a,b,c = x,y,z$ or cyclic permutation.

Formally equivalent expressions describe the effect of these propagators on the components of $\underset{\sim}{I}$. Equations 5.5a-c follow directly from the expansion of the exponentials and hold regardless of the number of equivalent protons bonded to the ^{13}C. To simplify the sine and cosine terms, however, we must take into account this number. Expressions for the three most common cases: IS, I_2S, and I_3S are given below. Derivations of these expressions can be found in Appendix C.

IS

$$\cos(I_p J'_{IS} t) = \cos\left(\frac{J'_{IS} t}{2}\right), \tag{5.6a}$$

$$\sin(I_p J'_{IS} t) = 2I_p \sin\left(\frac{J'_{IS} t}{2}\right); \tag{5.6b}$$

I_2S

$$\cos(I_p J'_{IS} t) = 1 + (\tfrac{1}{2} + 2I_{p1} I_{p2})(\cos J'_{IS} t - 1), \tag{5.6c}$$

$$\sin(I_p J'_{IS} t) = I_p \sin\left(\frac{J'_{IS} t}{2}\right); \tag{5.6d}$$

$$I_3S \quad \cos(I_p J'_{IS} t) = \cos^3\left(\frac{J'_{IS} t}{2}\right) - 4(I_{p1}I_{p2} + I_{p1}I_{p3} + I_{p2}I_{p3}) \times \sin^2\left(\frac{J'_{IS} t}{2}\right) \cos\left(\frac{J'_{IS} t}{2}\right), \tag{5.6e}$$

$$\sin(I_p J'_{IS} t) = 2I_p \sin\left(\frac{J'_{IS} t}{2}\right) \cos^2\left(\frac{J'_{IS} t}{2}\right) - 8I_{p1}I_{p2}I_{p3} \sin^3\left(\frac{J'_{IS} t}{2}\right). \tag{5.6f}$$

When the propagator (5.3) acts on proton (I) operators, only Equations 5.6a and 5.6b are relevant, with S_p replacing I_p. This is because a single ^{13}C nucleus is always assumed. An important special I spin analog of Equations 5.5b and c is the case $2\theta \equiv J'_{IS} t = 2\pi$ (Fig. 5.1):

$$\exp(-i2\theta I_p S_{a,b,c}) I_{q,r} \exp(i2\theta I_p S_{a,b,c}) = -I_{q,r}. \tag{5.7}$$

This will be termed a heteronuclear bilinear π rotation, since it has the property of inverting two components of $\underset{\sim}{I}$. This result holds for all systems I_nS, since each proton experiences the one ^{13}C in the same way. The important point to be made is that unlike an r.f. π pulse, the bilinear π rotation, resulting from the heteronuclear scalar coupling, is selective to those protons bound to a ^{13}C.

5.1.2 Coupling to Non-Satellite Spins

To this point, the discussion of bilinear rotations has been limited to an isolated I_nS group. Often the ^{13}C nucleus and its bound protons are coupled to other protons in the spin system, however. The full spin Hamiltonian for the system must, of course, include these couplings, which complicate the description of heteronuclear bilinear rotations. Nonetheless, with regard to bilinear π rotations, we will continue to treat the effective Hamiltonian as a pure bilinear coupling between the

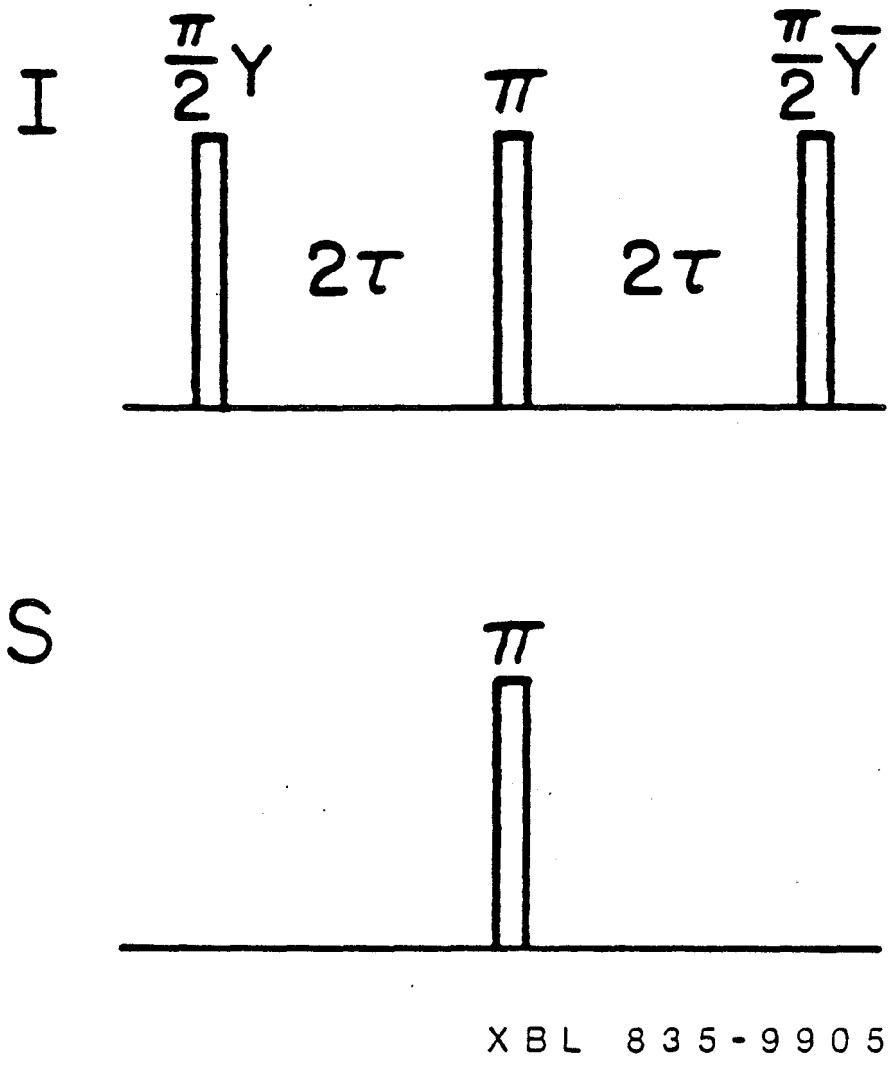

Figure 5.1. Simple Bilinear π Rotation. The strong proton π/2 pulses and periods of free evolution combine to produce a propagator of the form $U(t) = \exp(-iJ'_{IS}I_xS_zt)$. This corresponds to a rotation about the proton x-axis, with the nutation angle given by the product $J'_{IS}t/2$. Choosing $t = 4\tau = 1/J_{IS}$ results in a nutation angle of π radians.

^{13}C and its satellite protons, ignoring all couplings to non-satellite spins. Justification for this is provided by considering the relative magnitudes of the interactions involved.

Typical heteronuclear scalar couplings between a ^{13}C spin and its satellite protons range between 120 and 250 Hz and, for a large group of molecules, can be correlated with the degree of s-character in the ^{13}C-H bond[148], as illustrated in Table 5-1. For many molecules, long-range carbon-proton couplings and homonuclear proton scalar couplings range from 0 to 20 Hz, with the larger values usually found in compounds containing multiple bonds. Recall from Equations 5.5 and 5.7 that the timescale for the bilinear π rotation is determined by the heteronuclear coupling to the satellite protons, J'_{IS}. Because this coupling is generally an order of magnitude or more larger than all couplings to non-satellite protons, we assume throughout that the effect of these coupling is negligible on the bilinear π rotation timescale.

5.2 Application of Bilinear Rotation Formalism to Pulse Sequence Analysis

Having developed the concept of bilinear rotations, we now apply the operator formalism of Section 5.1 to the analysis of several recently published experiments. The experiments to be reviewed in this section involve the transfer of coherence between protons and ^{13}C nuclei. We will show how carbon and proton magnetization operators can be rotated into one another by successive application of propagators of the form of Equation 5.4.

Table 5-1

Representative Heteronuclear Couplings $J_{^{13}C-H}$ as a Function of ^{13}C Orbital Hybridization

Hybridization	$J_{^{13}C-H}$
sp^3	120 Hz
sp^2	160
sp	240

5.2.1 Enhancement of Carbon Signal

We begin by considering two pulse sequences which are useful for the enhancement of ^{13}C signal: INEPTR[134-136] and DEPT[138,139]. Both accomplish this enhancement by manipulation of the heteronuclear J-coupling to allow the magnetization of the protons, with their larger gyromagnetic ratio, to be converted into ^{13}C magnetization. These two techniques have the advantage over the nuclear Overhauser effect (NOE)[149,150] of being independent of relaxation mechanism.

5.2.1.1 INEPTR

The INEPT pulse sequence with refocusing, INEPTR, is illustrated in Figure 5.2. The first proton pulse establishes the initial condition $\rho(0)_+ = b_I I_y$. The remainder of this sequence is described by the propagator

$$U(2\tau+\Delta) = \exp(-i\mathcal{H}\tfrac{\Delta}{2})\ \exp(-i\pi(I_x+S_x))\ \exp(-i\mathcal{H}\tfrac{\Delta}{2})\ \exp(i\ \tfrac{\pi}{2}\ (I_y+S_y))$$
$$\exp(-i\mathcal{H}\tau)\ \exp(i\pi(I_x+S_x))\ \exp(-i\mathcal{H}\tau). \qquad (5.8)$$

In this propagator, phases for all pulses have been indicated for concreteness, though only those indicated in the figure are of consequence. By inserting the identity $[\exp(i\pi(I_x+S_x))\ \exp(-i\pi(I_x+S_x))]$ twice, the propagator of Equation 5.8 is easily simplified to

$$U(2\tau+\Delta) = \exp(-iJ'_{IS}I_zS_z\Delta)\ \exp(-i\ \tfrac{\pi}{2}\ (I_y+S_y))\ \exp(-iJ'_{IS}I_zS_z(2\tau)). \qquad (5.9)$$

The rightmost factor of this propagator acts on the initial condition $b_I I_y$ to give:

$$\rho(2\tau)_- = \exp(-iJ'_{IS}I_zS_z(2\tau))[b_I I_y]\ \exp(iJ'_{IS}I_zS_z(2\tau)) = -2b_I I_x S_z$$
$$\text{for } 2\tau = \frac{1}{2J_{IS}}\ . \qquad (5.10)$$

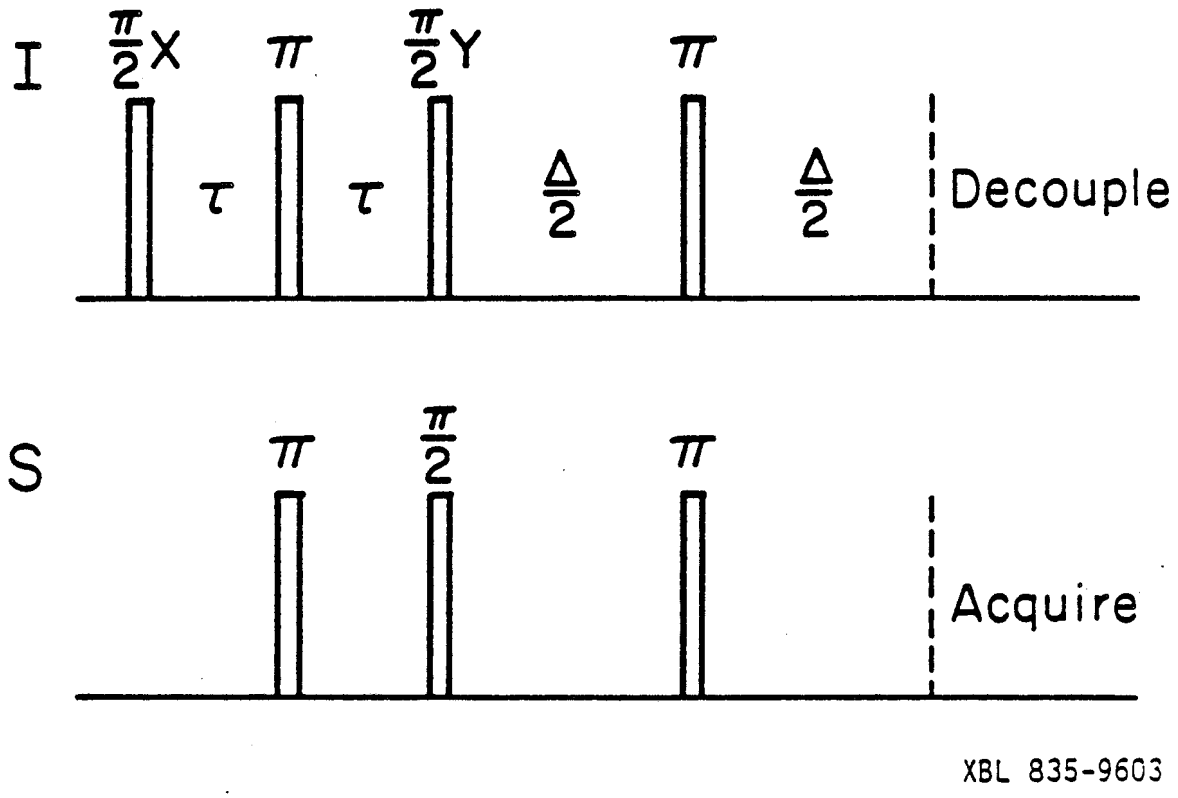

Figure 5.2. INEPTR[134-136] pulse sequence. Polarization is most efficiently transferred from protons to carbon for $\tau = 1/2J_{IS}$. An additional delay of Δ is required if a proton-decoupled free induction decay is to be collected. The optimal value of this delay depends upon the number of protons bound to the carbon.

It is convenient to treat the simultaneous $\frac{\pi}{2}$ pulses at time 2τ as if they occur sequentially. The density operator following the $(\frac{\pi}{2})_y$ proton pulse is

$$\rho(2\tau) = -2b_I I_z S_z, \tag{5.11}$$

which is recognized as describing J-order[136,145,146]. For an IS spin system, this sequence has inverted the populations of one of the two proton transitions. A $(\frac{\pi}{2})_y$ ^{13}C pulse completes the first half of this sequence, yielding

$$\rho(2\tau)_+ = 2b_I I_z S_x. \tag{5.12}$$

Due to the presence of the proton operator I_z, immediate proton decoupling will result in no observable carbon signal, since $Tr(S_+(I_z S_x))$ vanishes. A waiting period Δ is thus required, leading to the density operator

$$\begin{aligned}\rho(2\tau+\Delta) &= \exp(-iJ'_{IS} I_z S_z \Delta)[2b_I I_z S_x] \exp(iJ'_{IS} I_z S_z \Delta) \\ &= 2b_I I_z [S_x \cos(I_z J'_{IS}\Delta) + S_y \sin(I_z J'_{IS}\Delta)].\end{aligned} \tag{5.13}$$

To choose an optimal delay time Δ for IS, I_2S, and I_3S spin systems, the sine function in (5.13) must be expanded according to Equations 5.6b, 5.6d, and 5.6f, respectively. The optimal value is found by maximizing the coefficient of the operator I_p appearing in each of these expressions. The result is $\Delta_{OPT} = \frac{1}{2J_{IS}}$, $\frac{1}{4J_{IS}}$, and $(\frac{1}{\pi J_{IS}})(\tan^{-1}(\frac{1}{\sqrt{2}}))$ for n = 1, 2, and 3, respectively. The value of Δ_{OPT} for these and larger values of n have been given previously[151], without explicit density operator expressions. The ^{13}C signal enhancement due to INEPTR is $\frac{\gamma_I}{\gamma_S}$, $\frac{\gamma_I}{\gamma_S}$, and $1.16 \times (\frac{\gamma_I}{\gamma_S})$ for n = 1, 2, and 3 respectively. These values fail to reach (for $n \geq 2$) the theoretical maximum enhancement of $n^{\frac{1}{2}}(\frac{\gamma_I}{\gamma_S})$[152,153]. It is

interesting to note that this failure is accompanied by the appearance in the density operator of terms involving the products of spin operators. These would become heteronuclear multiple quantum coherence upon application of a proton $\frac{\pi}{2}$ pulse.

5.2.1.2 DEPT

An alternate technique for the enhancement of ^{13}C signal, Distortionless Enhancement Polarization Transfer (DEPT), is illustrated in Figure 5.3. For ^{13}C spectra acquired without proton decoupling, the DEPT sequence, as its name implies, provides the same enhancement for each line of the ^{13}C multiplet without phase distortion. As described in Section 5.1, the ^{13}C and ^{1}H π pulses in the DEPT sequence serve to remove the Zeeman terms from the Hamiltonian. In analyzing DEPT, we will assume that the Hamiltonian contains only the heteronuclear coupling $J'_{IS}I_zS_z$ though, for computational convenience, the proton π pulse at time τ will be omitted from the propagator.

The first proton pulse of the DEPT sequence establishes the initial condition $\rho(0)_+ = -b_I I_x$. The remainder of this sequence is described by the propagator

$$U(3\tau) = \exp(-iJ'_{IS}I_zS_z\tau)\exp(i\theta I_x)\exp(i\pi S_x)\exp(-iJ'_{IS}I_zS_z\tau) \times \exp(-i\frac{\pi}{2}S_x)\exp(-iJ'_{IS}I_zS_z\tau). \quad (5.14)$$

The rightmost factor of this propagator acting on $-b_I I_x$ yields:

$$\rho(\tau)_- = \exp(-iJ'_{IS}I_zS_z\tau)[-b_I I_x]\exp(iJ'_{IS}I_zS_z\tau) = -2b_I I_y S_z \quad \text{for } \tau = \frac{1}{2J_{IS}}. \quad (5.15)$$

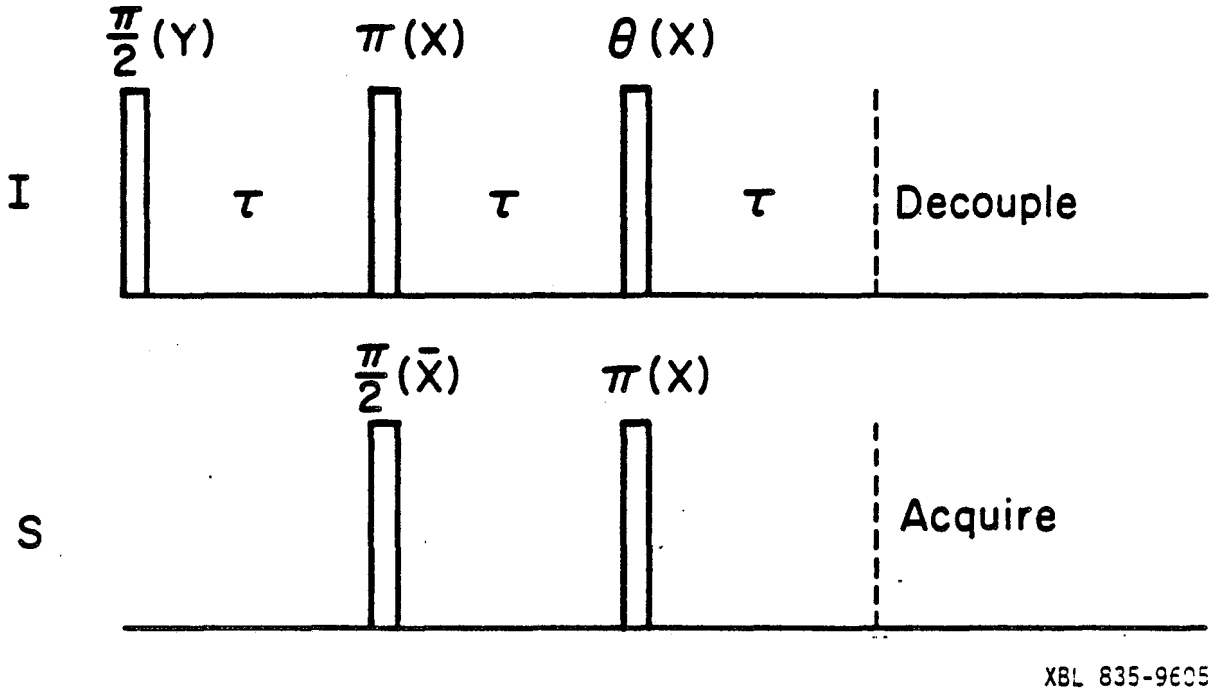

Figure 5.3. DEPT[138,139] pulse sequence for the transfer of magnetization from protons to carbon. The delay τ is chosen equal to $\frac{1}{J_{IS}}$. The optimal value of the flip angle θ depends upon the number of protons which are bound to the carbon, in much the same way as the delay Δ in the INEPTR sequence (Fig. 5.2).

Rewriting $\exp(-i\frac{\pi}{2}S_x)$ as $\exp(-i\pi S_x)\exp(i\frac{\pi}{2}S_x)$ allows the remainder of the propagator (5.14) to be rewritten as

$$U(3\tau) = \exp(-iJ'_{IS}I_zS_z\tau)\exp(i\theta I_x)\exp(iJ'_{IS}I_zS_z\tau)\exp(i\frac{\pi}{2}S_x). \quad (5.16)$$

For $\tau = \frac{1}{2J_{IS}}$, this expression can be further simplified to

$$U(3\tau) = \exp(i2\theta I_yS_z)\exp(i\frac{\pi}{2}S_x). \quad (5.17)$$

The density operator at time 3τ can now be computed as

$$\rho(3\tau) = \exp(i2\theta I_yS_z)\exp(i\frac{\pi}{2}S_x)[-2b_II_yS_z]\exp(-i\frac{\pi}{2}S_x)\exp(-i2\theta I_yS_z) \quad (5.18a)$$

$$= \exp(i2\theta I_yS_z)[-2b_II_yS_y]\exp(-i2\theta I_yS_z) \quad (5.18b)$$

$$= -2b_II_y[S_y\cos(2\theta I_y) + S_x\sin(2\theta I_y)]. \quad (5.18c)$$

The similarity between $\rho(3\tau)$ and the density operator prepared by the INEPTR sequence (Eq. 5.13) is readily apparent. In fact, by associating the flip angle 2θ with the INEPTR parameter $J'_{IS}\Delta$, we can use the considerations of Section 5.2.1.1 to choose optimum flip angles for IS, I_2S, and I_3S spin groups. This similarity between INEPTR and DEPT has been noted recently[139].

5.2.2 Suppression of Non-Satellite Proton Magnetization

We consider next two pulse sequences useful for the suppression of non-^{13}C-bonded (non-satellite) proton magnetization and suggest a third, related method. The first of these, illustrated in Figure 5.4a, has appeared in the literature in two slightly different forms[140,141]. Two experiments are performed, one with a ^{13}C π pulse at τ and a second with no ^{13}C pulse and the resulting free induction decays are cosubtracted.

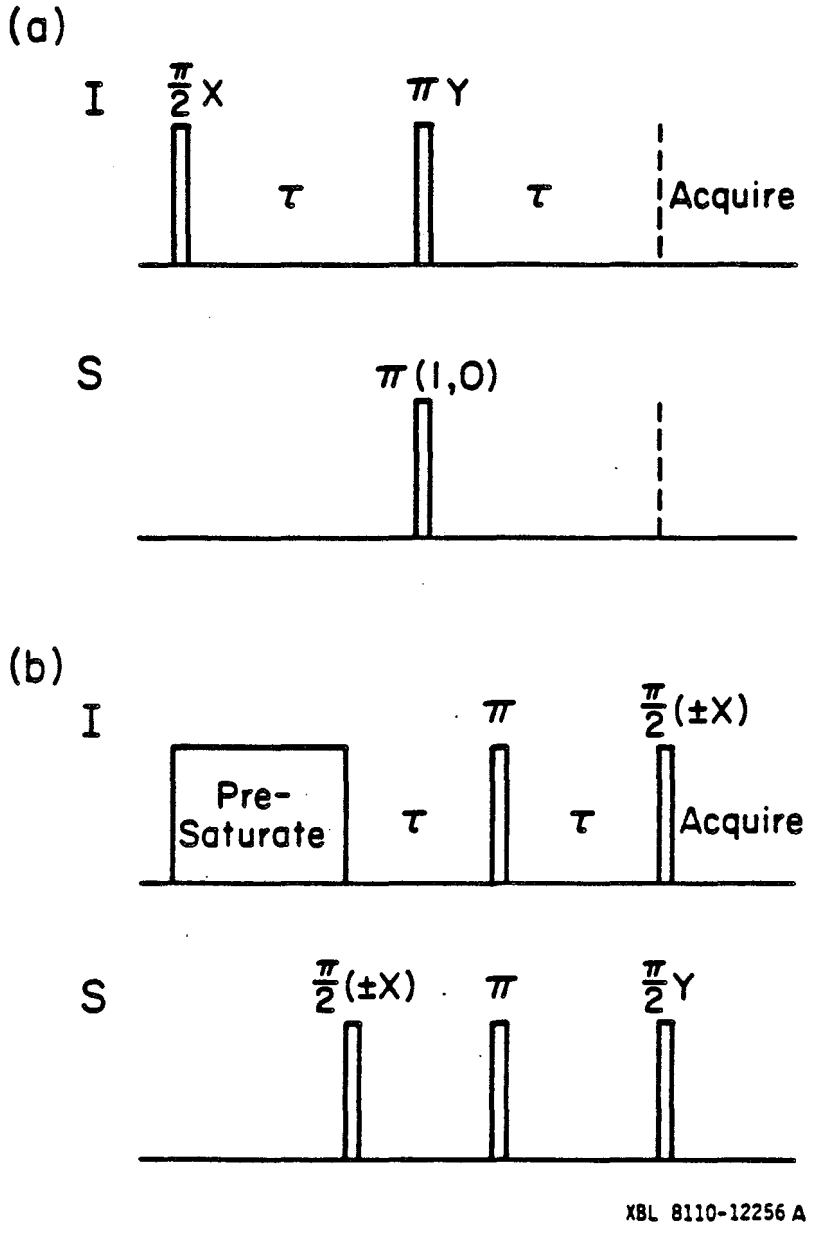

Figure 5.4. Pulse sequences for suppression of non-satellite proton magnetization[140,141]. (a) With $\tau = 1/2J_{IS}$, signal from experiments performed with and without the ^{13}C π pulse are subtracted from one another. (b) τ is chosen equal to $1/4J_{IS}$ and initial proton magnetization is saturated. Addition of signal from two experiments having the indicated pulse phases enhances suppression of non-satellite magnetization.

The initial density matrix following the proton $(\frac{\pi}{2})_x$ pulse is $\rho(0)_+ = I_y$. Non-satellite protons experience only the proton $(\pi)_y$ pulse at time τ, and for these spins $\rho_{NON}(2\tau) = I_y$. For the experiment with no ^{13}C pulse, the proton π pulse decouples protons from carbon, so that for satellite protons $\rho_{SAT}(2\tau)$ is also I_y. When π pulses are applied to both spins, however, the protons and carbon remain coupled and the protons experience a bilinear π rotation. This rotation inverts the spin operator for satellite protons: $\rho_{SAT}(2\tau) = -I_y$. (Formally speaking, a second pair of π pulses should be applied to the carbon and proton spins at 2τ as in (5.2) to fulfill the cyclic r.f. requirement of average Hamiltonian theory. Their omission changes nothing, however). Thus the signal attributable to satellite spins is of opposite sign in these two experiments, while non-satellite signal is of the same sign. Cosubtraction of the two free induction decays leaves signal only from ^{13}C-bonded protons.

A second method of suppression has been described[140] and is illustrated in Figure 5.4b. The presaturation period destroys all proton magnetization, leaving the system describable by the carbon operator S_z. Following the ^{13}C $(\frac{\pi}{2})_x$ pulse, $\rho(0)_+ = b_S S_y$ and the system then evolves under the now familiar $U(t) = \exp(-iJ'_{IS} I_z S_z t)$ propagator for a time $t = 2\tau = \frac{1}{2J_{IS}}$:

$$\rho(2\tau)_- = \exp(-iJ'_{IS} I_z S_z (2\tau))[b_S S_y] \exp(iJ'_{IS} I_z S_z (2\tau)) = -2b_S I_z S_x \quad \text{for } 2\tau = \frac{1}{2J_{IS}} . \tag{5.19}$$

Proton and carbon $\frac{\pi}{2}$ pulses rotate this density operator into

$$\rho(2\tau)_+ = 2b_S I_y S_z . \tag{5.20}$$

The important point is that only satellite protons experience this coherence transfer. We also note that a simultaneous 180° shift of the phases of the first ^{13}C pulse and the final ^{1}H pulse leaves the prepared density matrix unchanged, while any residual signal from non-satellite protons is inverted by the proton phase shift. Addition of free induction decays from experiments with phases x and $\bar{x}$ reinforces signal from satellite protons and further suppresses non-satellite magnetization.

The preceding sequence is effective in suppressing non-satellite proton magnetization, but sacrifices a factor of $\gamma_H/\gamma_C = 4$ in signal-to-noise by starting with ^{13}C magnetization. This sacrifice can be avoided in the following proposed double coherence transfer experiment. Satellite proton magnetization is first transferred to the carbons. The remaining proton magnetization, which is due to non-satellite protons, is then spoiled by a pulsed magnetic field gradient. Finally, the stored ^{13}C magnetization is transferred back to the protons for detection. The pulse sequence is illustrated in Figure 5.5.

This sequence will be analyzed for an IS spin system. The first half of the experiment is simply the INEPTR sequence with $\Delta = 2\tau$. From Equation 5.13, this sequence results in the density operator

$$\rho(4\tau)_- = b_I S_y. \tag{5.21}$$

A $(\frac{\pi}{2})_x$ ^{13}C pulse stores this magnetization along $-S_z$, and is followed by spoiling of all proton magnetization by application of a pulsed magnetic field gradient. Following this spoiling, a $(\frac{\pi}{2})_{\bar{x}}$ ^{13}C pulse restores carbon magnetization to the transverse plane:

$$\rho(4\tau + T)_+ = b_I S_y. \tag{5.22}$$

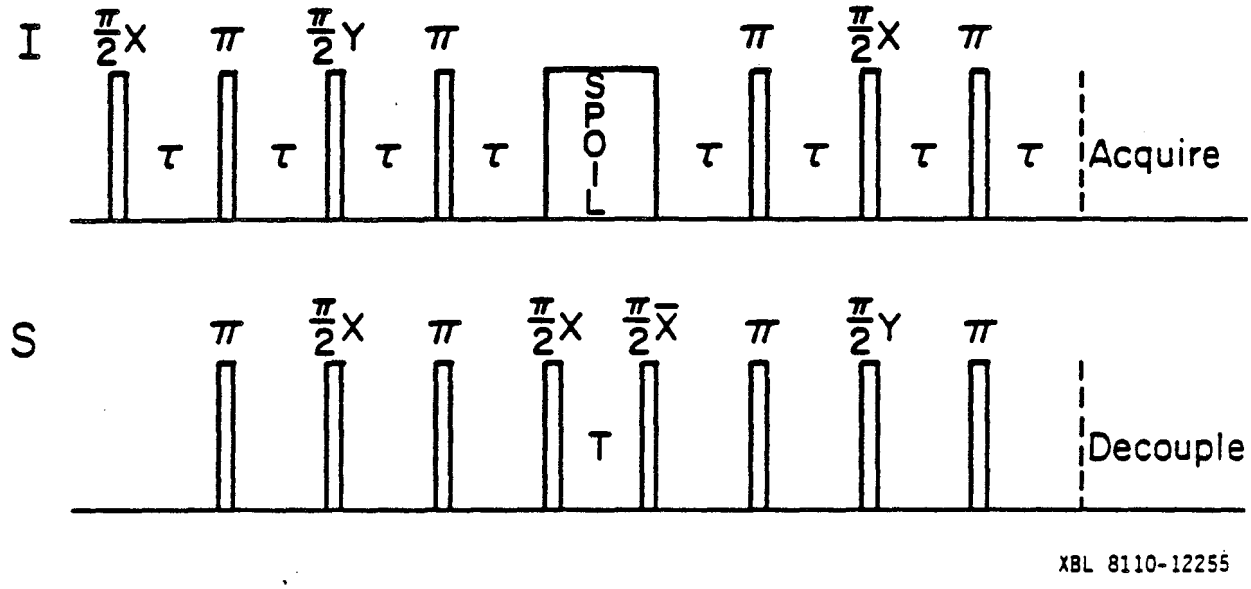

XBL 8110-12255

Figure 5.5. Proposed experiment for suppression of non-satellite proton magnetization. With $\tau = 1/2J_{IS}$, the first half of this experiment is simply INEPTR (Fig. 5.2). The "SPOIL" can be achieved by applying a pulsed field gradient. As discussed in Section 5.2.2, the remainder of this sequence is similar to that of Figure 5.4b. Signal-to-noise is enhanced by a factor of $\gamma_H/\gamma_C = 4$ over that experiment.

This is the same density operator as is produced by the initial $(\frac{\pi}{2})_x$ ^{13}C pulse of the previous sequence (Fig. 5.4b), except that the total magnetization has been enhanced by (γ_H/γ_C). Free evolution of the system proceeds as before and, following the proton and carbon $\frac{\pi}{2}$ pulses,

$$\rho(6\tau + T)_+ = 2b_I I_y S_z. \tag{5.23}$$

A final delay period of 2τ is required if the proton spectrum is to be acquired with ^{13}C decoupling. Phase shifting of the proton and carbon pulses can be easily incorporated into this sequence to provide further suppression of non-satellite signal.

5.3 Compensated Heteronuclear Bilinear π Rotations (CHBπ's)

5.3.1 Motivation

In many magnetic resonance experiments it is critical to be able to accurately adjust r.f. pulse flip angles. Particular problems may result in situations where the range of chemical shifts, finite sample size, and r.f. field inhomogeneity combine to cause different parts of the sample to experience different nutation rates and angles. Consideration of these problems has led to the use of composite r.f. pulses[154-156], whose effectiveness in compensating for a range of pulse lengths and resonance frequencies has been demonstrated. Recently, the general problem of off-resonance spin inversion has been treated comprehensively[157,158].

In heteronuclear bilinear rotations, the nutation frequency is proportional to J_{IS}. When two or more different coupling constants are present in a system, it becomes impossible to choose a single time such that all carbon-proton pairs experience the same rotation angle. This is similar to the observed sensitivity of cross polarization efficiency in

liquids to a distribution of scalar couplings[133,137]. In analogy to composite r.f. pulses, we introduce in this section compensated heteronuclear bilinear π rotations (CHBπ's).

5.3.2 Definition and Properties

Figure 5.6 illustrates an example of a CHBπ pulse sequence. The propagator for this sequence can be written as the product of three propagators, corresponding to alternate rotations about the y and x coordinate axes:

$$U(8\tau) = \exp(-iJ'_{IS}I_yS_z(2\tau))\ \exp(-iJ'_{IS}I_xS_z(4\tau))\ \exp(-iJ'_{IS}I_yS_z(2\tau)). \quad (5.24)$$

The time τ is chosen to result in a perfect bilinear π rotation for some representative scalar coupling, J°_{IS} ($\tau = \frac{1}{4J^\circ_{IS}}$). π pulses on both spin species again serve to remove the effects of all Zeeman interactions and chemical shifts.

A compensated bilinear π rotation is much less sensitive than the simple bilinear π of Figure 5.1 to misadjustments of τ. Its use allows effective bilinear π rotations to be given to carbon-proton pairs whose couplings vary over a range of values centered about J°_{IS}. This is important, because in many molecules the different scalar couplings between carbons and their satellite protons span a range of values. In Section 5.3.3, the relative insensitivity of the inversion efficiency of the CHBπ to bilinear nutation angle ($\frac{J'_{IS}t}{2}$) is demonstrated. Its use in a novel method for suppressing non-satellite proton signal is described in Section 5.3.4.

5.3.3 Insensitivity to Nutation Angle Misadjustments

The experiments described in this section were performed on samples

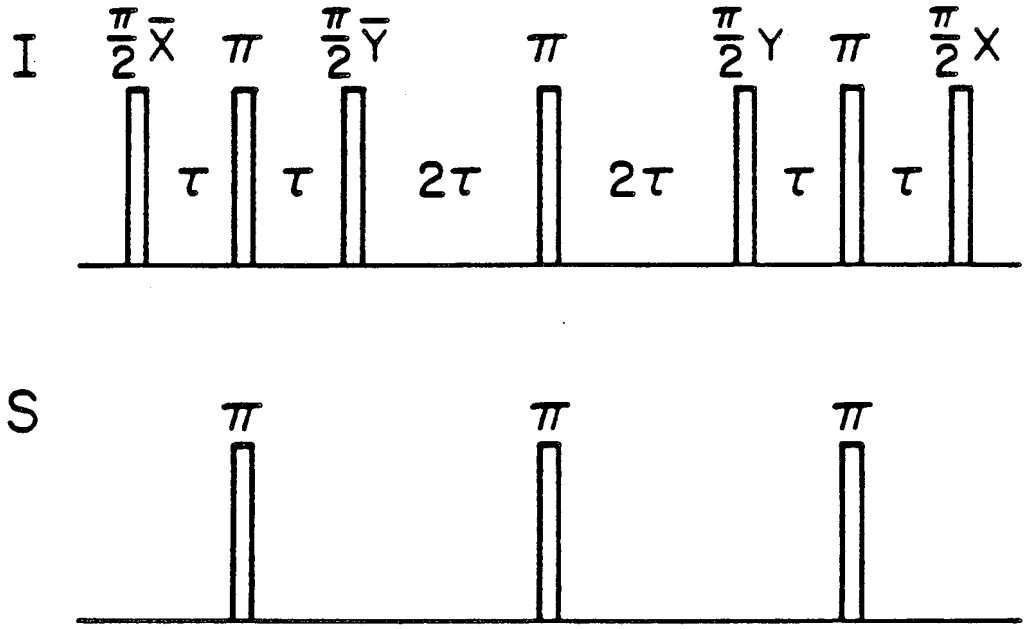

XBL 835-9904

Figure 5.6. Compensated bilinear π rotation, produced by alternate rotations about the proton x and y axes. The time period 4τ is chosen equal to $1/J^{o}_{IS}$ for some representative heteronuclear coupling J^{o}_{IS}. This sequence is much less sensitive to the exact value of J_{IS} than is the simple bilinear π rotation of Figure 5.1.

of benzaldehyde isotopically enriched with ^{13}C at the aldehyde carbon. Approximately 0.2% ditertbutylnitroxide was added to each sample to shorten its T_1 relaxation time.

To compare the sensitivities of simple and compensated bilinear rotations, two sets of experiments were performed on a sample which was 90% aldehyde carbon-13 enriched, using the pulse sequence of Figure 5.7a. One set was performed with U_π^x given by a simple bilinear π rotation (Fig. 5.1), a second set using a CHBπ (Fig. 5.6). Within each set of experiments, the delays between hard pulses making up the bilinear rotation were varied, corresponding to the variation in bilinear nutation angle which results in a sample having a range of J_{IS} values. The time $\frac{t_1}{2}$ was held fixed throughout and was chosen long enough (100 msec) to allow complete dephasing of magnetization due to magnetic field inhomogeneity. For these experiments this inhomogeneity was approximately 15 Hz (0.08 ppm).

The sequence of Figure 5.7a creates a spin echo at time t_1 for the ^{13}C-bound aldehyde protons only. Following acquisition of the second half of this echo during t_2, the free induction decay was Fourier transformed and the size of the signal due to the satellite aldehyde protons was measured. The results of these experiments are shown in Figure 5.8. Also shown are theoretical curves for inversion efficiencies as a function of bilinear nutation angle $\theta = \frac{J'_{IS}\tau}{2}$. Expressions for these efficiencies, which are derived in Appendix D, are given by

$$\frac{1}{2}(1 - \cos\theta) \tag{5.25a}$$

for simple bilinear rotations and

$$(\tfrac{1}{2})[(\cos\theta(1 + \sin^2(\tfrac{\theta}{2})) + \cos^2(\tfrac{\theta}{2}))^2 + (2\sin\theta\sin(\tfrac{\theta}{2}))^2]^{\frac{1}{2}} \tag{5.25b}$$

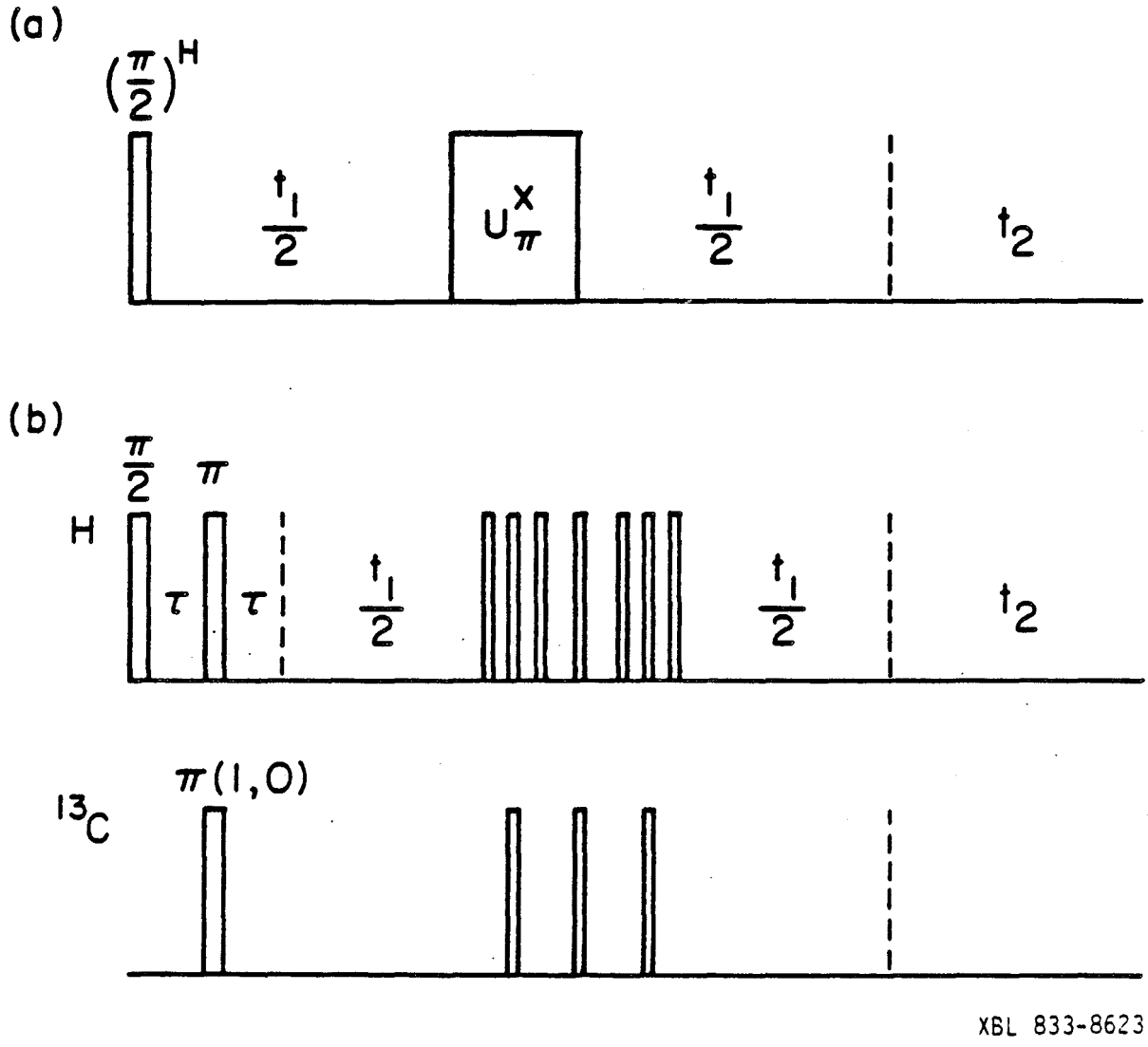

Figure 5.7. (a) Pulse sequence for demonstrating the relative insensitivity of CHBπ's to the value of J_{IS}. U_π^x represents either a simple π rotation (Fig. 5.1) or a CHBπ (Fig. 5.6). For satellite protons, the bilinear π causes a spin echo at time t_1, the second half of which is sampled during t_2. (b) Sequence for suppressing non-satellite magnetization, incorporating the sequence of Figure 5.4a at its beginning for enhanced suppression. The pulses at $(t_1/2)$ describe a CHBπ (Fig. 5.6).

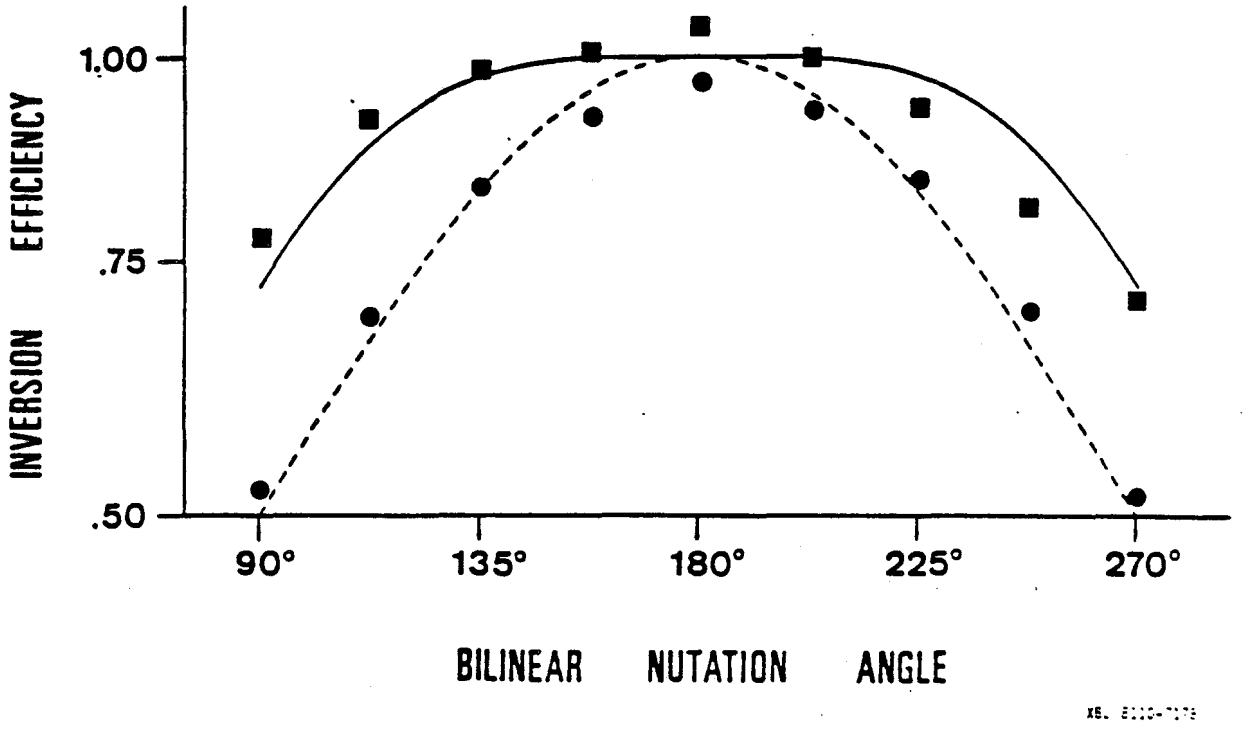

Figure 5.8. Comparison of inversion efficiencies of a simple bilinear π rotation (●) and a CHB (■) as a function of bilinear nutation angle. Data points represent the magnitude of the satellite proton signal for a sample of CH_3CHO, 90% enriched in the aldehyde carbon, for the experiment of Figure 5.7a (t_1 = 200 msec). The nutation angle was varied by changing the delays between the pulses making up the bilinear rotation. Theoretical curves are given by Equations 5.25a and 5.25b, respectively.

for compensated rotations.

The relative insensitivity of the CHBπ can be clearly seen in Figure 5.7, demonstrating that it can be used to give a good π rotation over a much wider range of heteronuclear J-couplings than the simple bilinear rotation. In particular, note that for a nutation angle misadjustment of 30%, the CHBπ still inverts with 96% efficiency, while the comparative figure for the simple rotation is only 79%.

5.3.4 Suppression of Non-Satellite Proton Magnetization

The use of a bilinear π rotation in the previous section to echo only the ^{13}C satellites suggests an additional way of suppressing magnetization from non-satellite protons. To demonstrate this, a pair of experiments were performed using the pulse sequence of Figure 5.7b on a benzaldehyde sample which was 10% carbon-13 enriched in the aldehyde carbon. This sequence, which is similar to that of Figure 5.7a, incorporates the sequence of Figure 5.4a at its beginning to enhance suppression of non-satellite magnetization. The spectrum resulting from this sequence with the ^{13}C π pulse at time τ included is shown in Figure 5.9b. Figure 5.9c was obtained by cosubtracting spectra obtained with and without this ^{13}C π pulse. The spectrum of Figure 5.9a, which is included for reference, was obtained in a similar experiment in which the bilinear π at $\frac{t_1}{2}$ was replaced by a single proton π pulse. Unlike the bilinear π rotation, which is selective to satellite protons, this π pulse echoes all of the proton magnetization at t_1, allowing a normal free induction decay to be collected in t_2.

As Figure 5.9 illustrates, the experiment of Figure 5.7b greatly enhances the relative size of the satellite signal, reducing the dynamic range problems often encountered when looking for satellites in natural

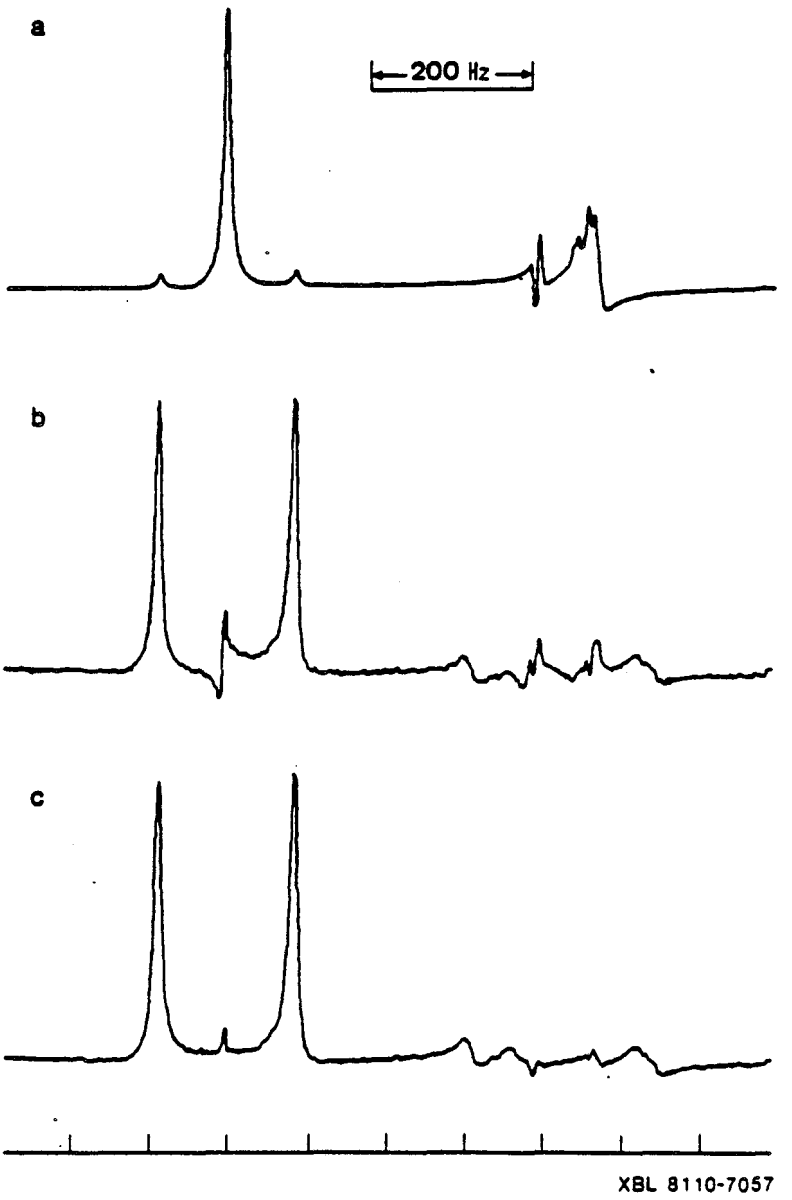

Figure 5.9. Demonstration of suppression of non-satellite proton magnetization for a sample of CH_3CHO, 10% enriched in the aldehyde carbon. (a) Spectrum obtained by sampling the second half of a normal spin echo, with t_1 = 200 ms. (b) Spectrum obtained using the pulse sequence of Figure 5.7b with the ^{13}C π pulse at τ included. Again t_1 = 200 msec and the second half of the echo was sampled during t_2. (c) Spectrum obtained by subtraction of signals collected with and without the ^{13}C π pulse at τ, using the sequence of Figure 5.7b.

abundance samples. We note that one could greatly reduce the required delay time t_1 through the use of a pulsed magnetic field gradient to cause more rapid dephasing of the magnetization. Also, as Figure 5.9 demonstrates, the proper choice of phase for the last ^{13}C pulse renders the satellite lines in-phase, independent of t_1. This is because the heteronuclear J-coupling, like the Zeeman interaction, can be removed from the evolution during t_1 by the bilinear π rotation.

5.4 Bilinear Rotation Decoupling (BIRD)

5.4.1 Background

Effective broadband proton homonuclear decoupling is a longstanding problem in the NMR of molecules in solution. As discussed in Chapter 3, the multiple pulse sequences designed to remove homonuclear dipolar couplings are ineffective in removing homonuclear J-couplings due to their scalar nature. In weakly coupled systems, methods of homonuclear decoupling are known. Spin tickling with a weak r.f. field[159] is possible for well-resolved multiplets. The method of J-δ spectroscopy[121,160] allows extraction of pure chemical shift spectra in weakly coupled systems by manipulation of a two-dimensional data array without actual decoupling during the evolution period. A similar method, which allows the recording of homonuclear decoupled absorption spectra without requiring the collection of a two-dimensional data array, has also been described[161].

In order to decouple a group of equivalent spins from all of its neighbors, one must be able to single out and manipulate that group independently of other spins in the system. As has been illustrated in previous sections of this chapter, the heteronuclear coupling between a carbon spin and its satellite protons provides a convenient means for doing this. The ^{13}C nucleus distinguishes the satellite protons from

all others and can be thought of as supplying a local decoupling field capable of nutating those protons to which it is coupled. In this section, a new method of homonuclear proton decoupling which takes advantage of the scalar coupling between protons and carbon is demonstrated. Our description of the technique will be in terms of the now familiar heteronuclear bilinear rotation and hence is termed Bilinear Rotation Decoupling (BIRD)[147].

5.4.2 Weakly Coupled Systems

In a weakly coupled system, a single bilinear rotation is sufficient to cause homonuclear decoupling. For simplicity we will assume that our spin system contains a single satellite proton, though this discussion is equally valid for a group of equivalent satellite protons. Weakly coupled systems are characterized by chemical shifts, a resonance offset, magnetic field inhomogeneity, and truncated homonuclear scalar couplings:

$$\mathcal{H} = -\sum_i \omega_i I_{zi} - (\Delta\omega + \omega(\underset{\sim}{r}))I_z - \sum_{i<j} J_{ij} I_{zi} I_{zj}. \qquad (5.26)$$

Labeling the satellite proton as spin "k", the effect of a bilinear π rotation can be written as (Eq. 5.7):

$$I_{zk} \rightarrow -I_{zk} \qquad (5.27a)$$

$$I_{zi} \rightarrow I_{zi}, \qquad i \neq k. \qquad (5.27b)$$

If this bilinear π is followed immediately by a strong proton π pulse, the overall effect is to invert the I_z operator associated with all protons <u>except</u> the one bonded to the ^{13}C.

Figure 5.10a illustrates the use of a bilinear π rotation and an adjacent strong π pulse to give the simplest BIRD pulse sequence. The

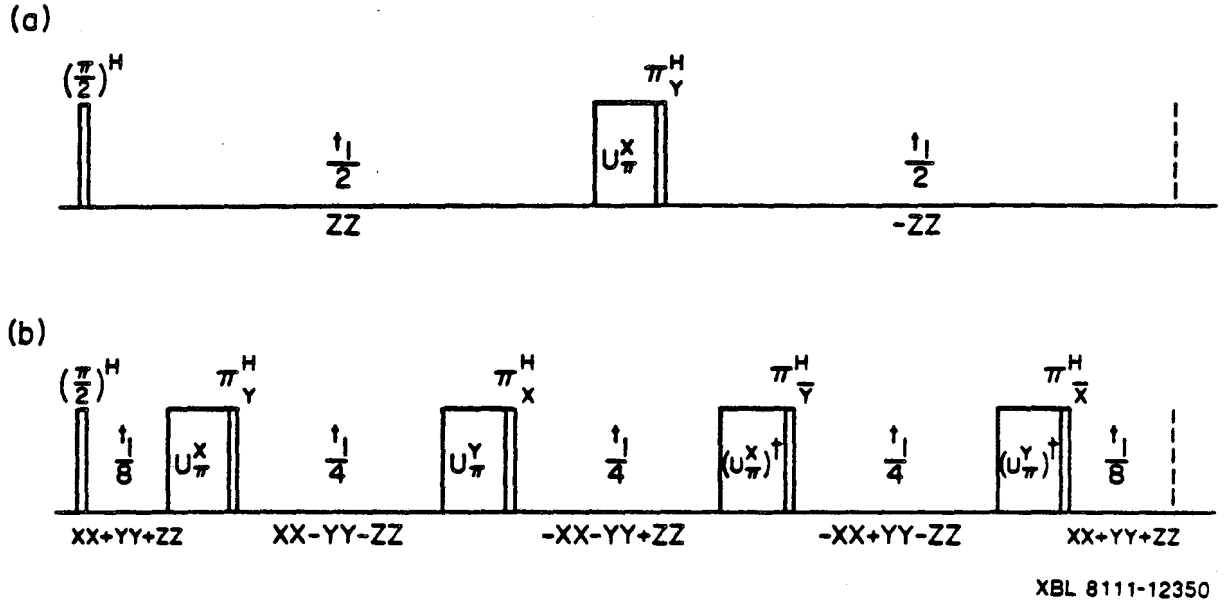

Figure 5.10. Pulse sequences for removal of J-couplings by BIRD. U^p_π represents a bilinear π rotation about the proton p-axis, π^H_p a strong proton π pulse of phase p. (a) A single bilinear π/strong π combination is sufficient for decoupling a weakly coupled system. Shown below the pulse sequence is the toggling frame value of the coupling $I_{zi}I_{zk}$ between satellite and non-satellite protons. The notation is $I_{pi}I_{pk} \equiv PP$. (b) Decoupling in strongly coupled systems requires a minimum of four bilinear π/strong π combinations. The toggling frame value of the proton-proton coupling $(\underset{\sim}{I}_i \cdot \underset{\sim}{I}_k)$ is shown below the pulse sequence.

box labeled U_{π}^{x} represents either a simple or compensated bilinear π rotation. As with the multiple quantum experiments of Chapters 2-4, the experiment is two-dimensional in that signal is sampled (at the point indicated by the broken line) as a function of t_1, which is incremented on successive shots. The BIRD spectrum is then obtained by Fourier transformation with respect to t_1.

As described in the discussion of Figure 5.4a (Sec. 5.2.2), application of average Hamiltonian theory to this simple BIRD sequence requires a second bilinear π rotation of opposite phase at time t_1. Its omission, however, can only effect the overall phase of the observed signal. In a toggling frame representation, a homonuclear coupling term $J'_{ik}I_{zi}I_{zk}$ during the first time period $\frac{t_1}{2}$ becomes $-J_{ik}I_{zi}I_{zk}$ in the second period $\frac{t_1}{2}$. The average Hamiltonian for this scalar coupling is zero, and since the Hamiltonian commutes with itself at all times, all correction terms to $\bar{\mathcal{H}}^{(0)}$ are zero. Similarly, the heteronuclear J-coupling also averages to zero. The chemical shift term for the satellite proton, $-\omega_k I_{zk}$, is preserved, however, along with the Zeeman terms $(-(\Delta\omega+\omega(\underset{\sim}{r}))I_{zk})$ for this spin. Two alternate representations of this version of the BIRD experiment using, respectively, energy levels and magnetization vectors, are given in Figure 5.11. In this figure, I labels a satellite proton and I' a non-satellite proton.

In practice a method is needed for detecting only that signal arising from satellite protons. One possibility, which is described further in Section 5.5, is to transfer coherence from protons to carbon at time t_1 and to then detect ^{13}C magnetization in t_2. For the experiments described here, selection of satellite signal was accomplished by substituting the pulse sequence of Figure 5.4a for the proton $\frac{\pi}{2}$ pulse at the start of the BIRD sequence. Cosubtraction of signals from

Figure 5.11. Schematic representation of BIRD using energy levels and magnetization vectors. A satellite proton is indicated by I, while I' represents a non-satellite proton. The sequence begins following a $\pi/2$ proton pulse with the proton spin vectors in the x-y plane(1). Free evolution of the system for a time $t_1/2$(2) causes precession of these vectors due to the chemical shift and heteronuclear coupling(3). A strong proton π pulse(4) rotates the magnetization vectors 180° about the pulse axis(5). For the I spin this also interchanges the identity of the spin vectors with respect to the ^{13}C. The bilinear π rotation(6), felt only by I, rotates that spin's magnetization vectors back, without interchanging their identities. Free evolution for an additional time $t_1/2$(8) brings these two vectors back into line(9), with preservation of the I spin chemical shift (δ_I) and without broadening due to coupling to other protons. The I' spin chemical shift ($\delta_{I'}$) has been removed by this sequence; the final width of its spin vector reflects the preservation of coupling to other protons not explicitly included in the energy level diagram.

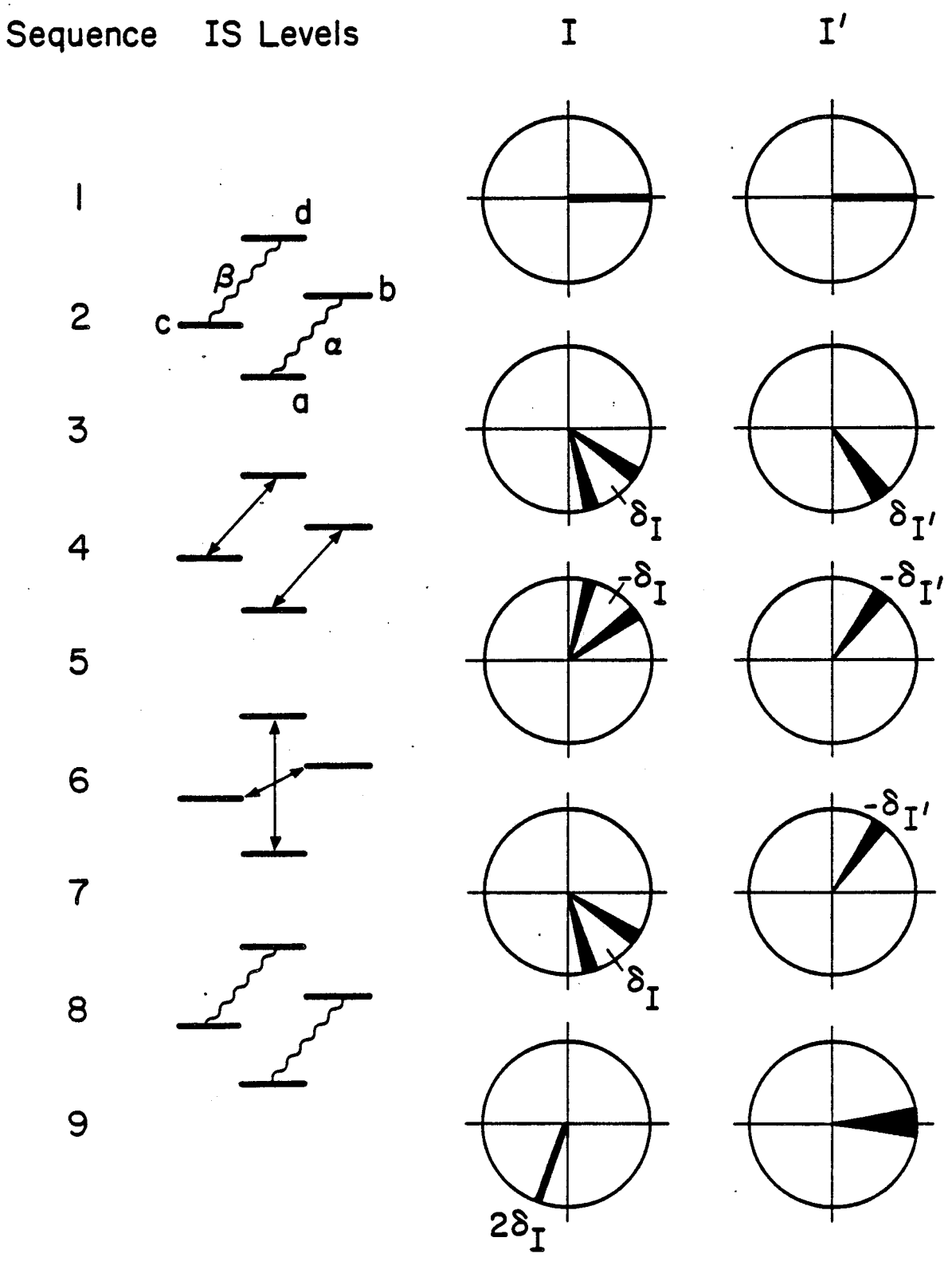
Sequence
IS Levels
I
I′
1
2
3
4
5
6
7
8
9
d
b
c
a
β
α
δ_I
$\delta_{I'}$
$-\delta_I$
$-\delta_{I'}$
$-\delta_{I'}$
$-\delta_I$
$2\delta_I$

XBL 824-8833

experiments with and without the ^{13}C π pulse at τ leads to reinforcement of satellite proton magnetization and cancellation of magnetization due to non-satellite protons.

As a demonstration of the BIRD method, Figure 5.12 shows the results of experiments performed on samples of 95% ethanol in water. In these experiments the samples were contained in 2 mm diameter sample bulbs and spun horizontally at 60-80 Hz. The linewidths of ~2 Hz in these spectra are dominated by residual magnet inhomogeneity. Figure 5.12a is the familiar proton spectrum of the methyl and methylene protons of ethanol. In Figure 5.12b we observe the same proton multiplets superimposed upon the much larger splittings due to the heteronuclear scalar couplings in an isotopically enriched sample. Figure 5.12c illustrates the BIRD spectrum of the same sample. All multiplet structure has been collapsed, while the chemical shifts are accurately preserved in the positions of the resulting singlet lines. Signal at the center of this spectrum is due to incomplete suppression of non-satellite proton magnetization.

5.4.3 Incorporation of BIRD into 2-D Experiments

One of the major advantages of BIRD is that the homonuclear decoupling is accomplished in a single time dimension and does not require accumulation and manipulation of a two-dimensional data array. This observation suggests the use of the BIRD sequence to provide decoupling in the t_1 dimension of a wide variety of different 2-D experiments. As an example, a pulse sequence for heteronuclear chemical shift correlation which incorporates BIRD decoupling is illustrated in Figure 5.13b.

The correlation of the chemical shifts of ^{13}C spins with those of protons coupled to the carbons was first suggested several years ago[131] and has since become a standard two-dimensional NMR technique[162,163].

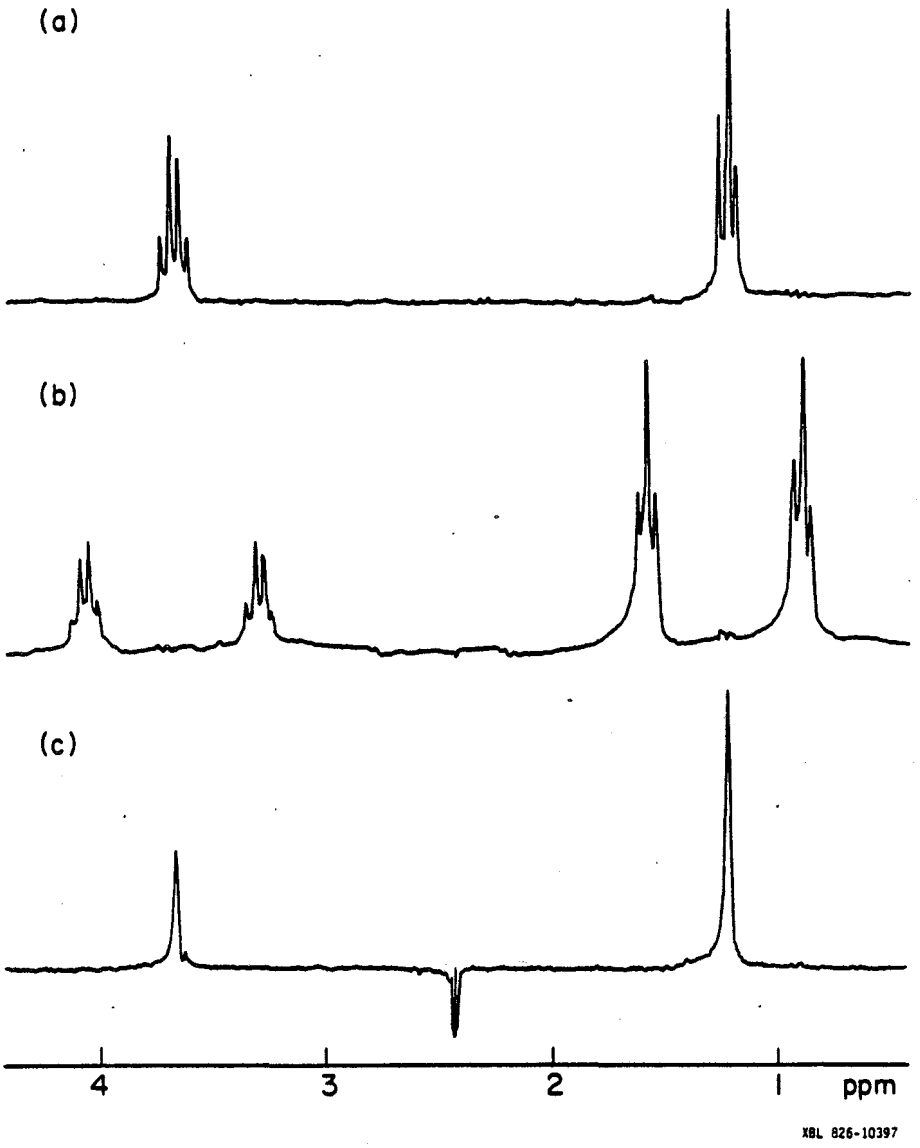

Figure 5.12. Spectra of ethanol illustrating removal of J-couplings by BIRD. Samples were spun horizontally at 60-80 Hz. (a) Normal spectrum of the methyl and methylene protons of unenriched ethanol in $CHCl_3$(1:2 v/v). (b) ^{13}C satellite spectra of [α-^{13}C] ethanol and [β-^{13}C] ethanol in $CHCl_3$(1:1:4 by volume, 90% isotopic purity at the labeled position). Non-satellite proton magnetization was suppressed, as described in the text. (c) BIRD spectrum of the ^{13}C enriched sample, collected using the pulse sequence of Figure 5.10a with a compensated bilinear rotation used as U_{π}^{x}. Non-satellite magnetization has again been suppressed.

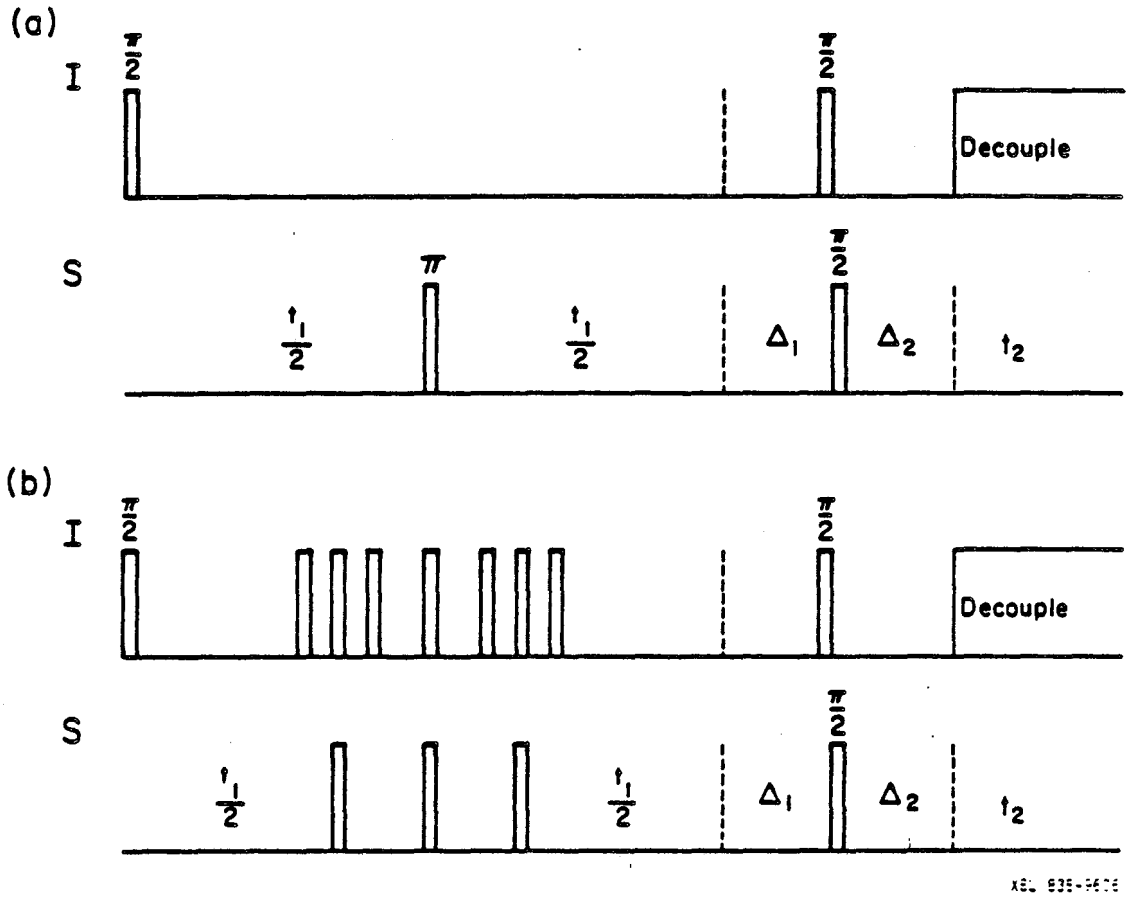

Figure 5.13. Heteronuclear chemical shift correlation pulse sequences. (a) Normal shift correlation[162,163], with evolution during t_1 determined by proton chemical shifts and homonuclear J-couplings. Delays Δ_1 and Δ_2 are chosen as in an INEPTR experiment. (b) Incorporation of BIRD sequence, which enhances spectral resolution by removing homonuclear J-couplings during t_1.

The basic pulse sequence for performing this experiment is illustrated in Figure 5.13a. The carbon π pulse in t_1 serves to decouple protons from carbons in this time dimension. The evolution of initial proton magnetization during t_1 is therefore determined by proton chemical shifts and homonuclear J-couplings. The delay periods Δ_1 and Δ_2 along with the $\frac{\pi}{2}$ pulses applied to both spin species serve to transfer proton magnetization to carbon magnetization via the heteronuclear scalar coupling, J_{IS}. To optimize this transfer, the delay Δ_1 is set equal to $\frac{1}{J_{IS}}$, while the optimal value of Δ_2 depends upon the number of satellite protons in the same way that the delay Δ did for the INEPTR experiment (Sec. 5.2.1.1). For each value of t_1, a proton decoupled ^{13}C free induction decay is then collected in t_2. Following double Fourier transformation, the 2-D spectrum correlates carbon chemical shifts in ω_2 with the chemical shifts and homonuclear J-couplings of satellite protons in ω_1.

The incorporation of BIRD into this sequence is achieved simply by replacing the ^{13}C π pulse at $\frac{t_1}{2}$ by a bilinear π rotation/strong proton π pulse combination (Fig. 5.13b). In this experiment, the same correlation between carbon and proton chemical shifts can be observed with the enhanced resolution afforded by homonuclear proton decoupling in ω_1. Heteronuclear chemical shift correlated spectra obtained with BIRD have been reported recently[164]. (A closely related experiment, which also incorporates a bilinear π rotation at the midpoint of the evolution period, and which is useful in discriminating between short-range and long-range heteronuclear J-couplings, has been described[165].) Incorporation of BIRD into other two-dimensional experiments is anticipated and should prove useful in enhancing spectral resolution, especially in studies of large spin systems.

5.4.4 Strongly Coupled Systems

It is interesting to consider the extension of BIRD to strongly coupled spin systems. Strongly coupled systems are usually considered those in which the scalar coupling between the protons is comparable in magnitude to the difference in chemical shifts between them. For satellite protons, however, strong coupling occurs when

$$\left|\omega_i - \left(\omega_k \pm \frac{J'_{IS}}{2}\right)\right| \simeq |J'_{ik}|. \tag{5.28}$$

The Hamiltonian describing the scalar interaction between strongly coupled spins is the untruncated J-coupling

$$\mathcal{H}^J_{II} = -\sum_{i<k} J'_{ik} \underset{\sim}{I}_i \cdot \underset{\sim}{I}_k. \tag{5.29}$$

Unlike the truncated scalar coupling, this term cannot be inverted with a single bilinear π rotation. In fact, a minimum of four bilinear π rotations, with appropriate phase shifts of the r.f. pulses, is required for decoupling. Figure 5.11b illustrates one simple pulse sequence for the removal of proton J-couplings in strongly coupled systems. In this figure, U^y_π refers to the propagator for a bilinear π rotation which inverts I_z and I_x for the satellite proton, while leaving I_y alone. U^y_π is related to U^x_π by a 90° phase shift:

$$U^y_\pi = \exp(-i\,\frac{\pi}{2}\,I_z)\,U^x_\pi\,\exp(i\,\frac{\pi}{2}\,I_z). \tag{5.30}$$

A strong proton π pulse of appropriate phase follows immediately after each bilinear rotation.

In order to calculate the effect of this four "pulse" sequence, average Hamiltonian theory is once again used. This calculation is performed in an interaction representation defined by the four bilinear π

rotations and accompanying proton π pulses. In this toggling frame, the value of

$$\underset{\sim}{I}_i \cdot \underset{\sim}{I}_k = I_{xi}I_{xk} + I_{yi}I_{yk} + I_{zi}I_{zk} \tag{5.31}$$

for the windows between bilinear rotations is indicated in Figure 5.13b. The notation used is that

$$I_{xi}I_{xk} \equiv XX \tag{5.32}$$

and cyclic permutations. The average Hamiltonian for these windows is found by summing:

$$\bar{\mathcal{H}}^{(0)} \propto (XX+YY+ZZ) + (XX-YY-ZZ) + (-XX-YY+ZZ) + (-XX+YY-ZZ) = 0. \tag{5.33}$$

Thus the coupling between the ^{13}C-bound proton "k" and all other protons vanishes to this order of approximation. The coupling of this satellite proton to the carbon spin also vanishes, on average, while its chemical shift is preserved.

5.5 Conclusion

In this chapter we have considered the liquid state spin dynamics of systems consisting of several protons and a ^{13}C nucleus. The concept of a bilinear rotation has been introduced and its usefulness as a calculational tool demonstrated. Of particular interest are bilinear rotation sequences having a bilinear nutation angle of π radians. The natural spread in the magnitude of heteronuclear coupling constants J_{IS} leads to an inevitable spread in bilinear nutation angles. Compensated bilinear π rotations, designed to be less sensitive to misadjusted timing parameters, have been introduced and their relative insensitivity to these errors demonstrated.

Compensated bilinear π rotations have been incorporated into new experiments to suppress non-satellite proton magnetization and to allow dynamic homonuclear proton decoupling in weakly coupled systems (BIRD). BIRD has an advantage over decoupling by spin tickling due to its broadband nature. As noted in Section 5.4.3, an advantage over J-δ spectroscopy is that decoupling is accomplished in real time in a single time dimension. One disadvantage of BIRD is that it is only sensitive to those protons bound in magnetically equivalent groups to ^{13}C spins. This lowers the available magnetization at natural abundance and means that protons in other binding environments do not appear in the BIRD chemical shift spectrum.

Appendix A: NMR IN LIQUID CRYSTAL SOLVENTS

Much of this work has been concerned with the NMR spectroscopy of molecules dissolved in liquid crystalline solvents. As described in Chapter 1, it is the combination of being partially oriented by a large magnetic field and rapid molecular diffusion which makes liquid crystals attractive NMR solvents. In this appendix, we review some of the properties of liquid crystals and of molecules dissolved in liquid crystal solvents. In particular, we show how the experimentally measured coupling constants and chemical shifts depend upon a set of parameters which describe molecular ordering with respect to the external magnetic field. The discussion in this appendix is limited to thermotropic liquid crystals - pure compounds which exhibit a mesophase within a particular temperature range.

Section A.1 discusses the structure of nematic liquid crystals and their interaction with an external magnetic field. In Section A.2, a quantitative treatment of ordering in liquid crystals is developed. The Saupe order tensor is defined and the complications involved in describing the ordering of non-rigid molecules are described. In Section A.3, the spin Hamiltonian for partially ordered systems is developed in terms of the order tensor, with emphasis on the required coordinate transformations. Spherical tensor operators are described in Section A.4 and the different spin Hamiltonian interactions are discussed in terms of these operators.

A.1 The Liquid Crystalline State

A.1.1 Structure and Classification of Mesophases

The liquid crystalline state was first reported nearly a century ago. Since that time, many compounds have been found to form this

mesophase, which is intermediate between liquid and solid. All compounds which exhibit the liquid crystal phase are composed of long rod-like molecules. Many texts have been written about the structure and properties of liquid crystals[166-168] and their use as NMR solvents has been reviewed[14,15]. The liquid crystal phase arises out of a tendency for the rod-like molecules' long axes to align parallel to one another. The preferred orientation of the long axes is described by a unit vector known as the director. There are actually several different liquid crystalline phases which are divided into three basic categories based upon their degree of molecular order: nematic, cholesteric, and smectic.

We will be concerned here with nematic liquid crystals, which exhibit the lowest degree of molecular ordering. There is no positional ordering of the centers of mass of the molecules in this mesophase, as illustrated schematically in Figure A.1a. A representation of the smectic A phase is shown, for contrast, in Figure A.1b. Many nematics form one or more other liquid crystalline phases as well. As the mesophase having the lowest degree of molecular ordering, however, the nematic is always the first formed upon cooling the isotropic liquid. The addition of a solute molecule depresses the nematic-to-isotropic transition temperature.

A.1.2 Orientation by External Magnetic Fields

In the absence of external constraints, ordering in nematic liquid crystals is limited to local domains and the orientation of the director varies continuously throughout the sample. This can change in the presence of an external magnetic field, however. Liquid crystal molecules interact with magnetic fields due to an anisotropy in their

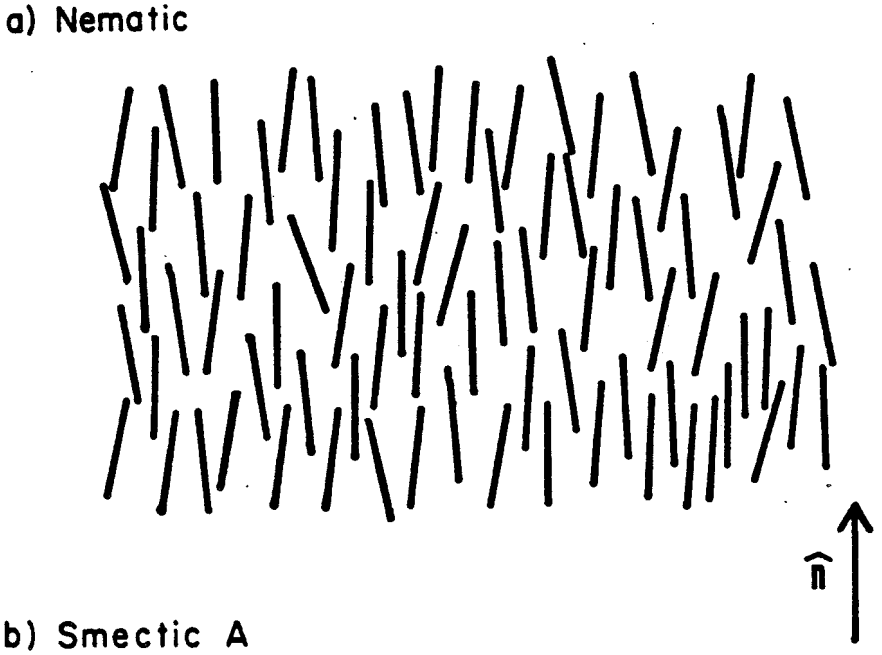

XBL 818-1765

Figure A.1. Pictorial representation of two thermotropic liquid crystal phases. Since the molecules in a liquid crystal are undergoing rapid fluctuations, this figure actually represents a snapshot taken at one particular instant in time. (a) In the nematic phase, the long axes of the rod-like liquid crystal molecules align preferentially along the director axis $\hat{n}$. (b) In addition to aligning along the director, molecules in the more highly ordered smectic A phase stack together in planes perpendicular to $\hat{n}$. (Figure courtesy of Steve Sinton.)

diamagnetic susceptibility. The free energy of this interaction is[14]

$$G = \frac{-\Delta\chi H_o^2(3\cos^2\theta - 1)}{6}, \qquad (A.1)$$

where H_o is the strength of the magnetic field, θ the angle between the field and director axes, and $\Delta\chi = \chi_{\parallel} - \chi_{\perp}$ is the anisotropy in the bulk diamagnetic susceptibility. The component $\chi_{\parallel}$ is that along the liquid crystal molecule's long axis while $\chi_{\perp}$ is the component perpendicular to it. For most thermotropic liquid crystals, including the Eastman 15320 used in all experiments described in this work, $\Delta\chi$ is positive and the free energy is lowered by alignment of the director with the direction of the magnetic field. In a magnetic field as large as 42 kGauss this alignment is complete, with the director parallel to the magnetic field throughout the sample.

Molecules dissolved in liquid crystals interact with the surrounding solvent. In an effort to minimize free energy, the solute molecules orient with respect to the liquid crystal in response to this interaction. In a magnetic field, the result is a net ordering of the solute molecules with respect to the field. It is surprising that molecules having tetrahedral symmetry such as CH_4 and $(CH_3)_4Si$ should have a preferred orientation in a liquid crystal. The NMR spectrum of dissolved tetramethylsilane does show a triplet of lines attributable to proton-proton dipolar couplings, however[169]. Possible explanations will be discussed in Section A.2.3.3.

The director specifies the direction of average orientation of the liquid crystal long axes and in a magnetic field points along the direction of the field. The individual liquid crystal molecules are hardly

static, however. In Section 1.3.2.1 we noted that rapid translational diffusion is taking place. In addition, the long axes of the liquid crystal molecules are fluctuating rapidly and temperature-dependently about the director. The director therefore represents a time or ensemble average and Figure A.1a an instantaneous snapshot of the nematic liquid crystal. The order parameters to be discussed in subsequent sections are themselves averages over these molecular fluctuations and acquire their temperature dependence from them.

A.2 Quantitative Description of Ordering

A.2.1 Saupe Ordering Tensor

In order to describe NMR spectroscopy in liquid crystals, a quantitative description of the partial molecular ordering in such systems must be introduced. More specifically, we ask how each of the spin Hamiltonian terms described in Chapter 1 must be modified to take into account this ordering. For the time being we assume that both the liquid crystal and any dissolved solute are rigid molecules. The problems posed by molecules undergoing large internal motions will be addressed in Section A.2.3. Recall that each of the interactions of $\mathcal{H}_{INT}$ can be described as a 3 x 3 second rank Cartesian tensor. In a high field experiment, the measured quantity is the laboratory frame zz component of this tensor. The task is one of expressing this quantity in terms of a molecule-fixed coordinate system defined by the axes x', y', z'.

Transformations from one coordinate system to another are described in many standard texts[32-34]. Specifically, the second rank tensor $\underset{\approx}{A}$ in the laboratory frame can be related to its form in a molecule-fixed coordinate system, $\underset{\approx}{A}'$, by the transformation matrix $\underset{\approx}{R}$:

$$\underset{\approx}{A} = \underset{\approx}{R}\underset{\approx}{A}'\underset{\approx}{R}^{\dagger} . \qquad (A.2)$$

(In this appendix primes are used to specify tensor interactions in a molecule-fixed axis system and not to indicate units of angular frequency. Couplings and chemical shifts are given throughout in units of rad·sec^{-1}. The author apologizes in advance for any confusion caused by this change in notation.) The tensor corresponding to each of the Hamiltonian interactions is real, so that $R^{\dagger} = R^{-1}$. We are interested in the zz component of $\underset{\approx}{A}$, given by:

$$(\underset{\approx}{A})_{zz} = \sum_{\alpha,\beta}^{x',y',z'} R_{z\alpha}R_{z\beta}A'_{\alpha\beta} = \sum_{\alpha,\beta}^{x',y',z'} A'_{\alpha\beta}\cos\theta_{z\alpha}\cos\theta_{z\beta}, \qquad (A.3)$$

where $\theta_{z\alpha}$ is the angle between the laboratory z-axis and the molecule-fixed α-axis ($\alpha = x',y',z'$). Following some algebraic manipulations, this can be written

$$(\underset{\approx}{A})_{zz} = \frac{1}{3}\sum_{\alpha,\beta}^{x',y',z'} A'_{\alpha\beta}(3\cos\theta_{z\alpha}\cos\theta_{z\beta} - \delta_{\alpha\beta}) + \frac{1}{3}\sum_{\alpha}^{x',y',z'} A'_{\alpha\alpha}$$

$$= \frac{2}{3}\sum_{\alpha,\beta} A'_{\alpha\beta}[\tfrac{1}{2}(3\cos\theta_{z\alpha}\cos\theta_{z\beta} - \delta_{\alpha\beta})] + \overline{A'}, \qquad (A.4)$$

where $\overline{A'}$ is the isotropic average of $\underset{\approx}{A}'$ ($\overline{A'} = \frac{1}{3}\,\mathrm{Tr}(\underset{\approx}{A}')$).

Finally, we must allow for the fluctuations about the director discussed in the previous section. This is done by averaging the angle-dependent terms of Equation A.4:

$$(A)_{zz} = \frac{2}{3}\sum_{\alpha,\beta} A'_{\alpha\beta}(\tfrac{1}{2}\langle 3\cos\theta_{z\alpha}\cos\theta_{z\beta} - \delta_{\alpha\beta}\rangle) + \overline{A'}$$

$$= \frac{2}{3}\sum_{\alpha,\beta} A'_{\alpha\beta}S_{\alpha\beta} + \overline{A'}. \qquad (A.5)$$

The matrix $S_{\alpha\beta}$ is the Saupe ordering matrix[170]. It can be readily seen that this matrix is both symmetric and traceless. Thus, for the uniaxial nematic mesophase there are a maximum of five independent, non-zero matrix elements or order parameters. These are traditionally taken to be S_{zz}, S_{xx-yy}, S_{xy}, S_{xz}, and S_{yz} (where the primes have been dropped). Each can range in value from -0.5 to 1.0 and all are zero for an isotropic liquid.

This formalism applies equally well to describing the ordering of a nematic liquid crystal or of molecules dissolved in it. The solute and solvent will be described by two different ordering matrices and there is, in general, no obvious way to relate these. In particular, one or another of these ordering tensors may be simplified due to molecular symmetry, as discussed below. It is generally true, however, that the more highly ordered a liquid crystal is, the greater will be the ordering of a dissolved solute molecule.

In molecules with symmetry, it is possible to reduce the number of non-zero order parameters by a judicious choice of the molecular axes x', y', z'. For example, in molecules containing an axis of rotation $C_n (n \geq 3)$, choosing z' along C_n results in a single non-zero order parameter, S_{zz}. Similarly, in molecules with a mirror plane, the choice of z' perpendicular to this plane reduces the number of order parameters to three: S_{zz}, $(S_{xx} - S_{yy})$, and S_{xy}. A complete table of the number of independent, non-zero order parameters required for molecules belonging to the different point groups has been given[171].

A.2.2 Spherical Harmonic Expansion

We mention briefly an alternate description of the ordering in nematic liquid crystals by means of a probability function. We define

the function $P(\theta,\phi)$ as the probability per unit solid angle that the director has polar angles θ and ϕ with respect to the molecule-fixed axis system x', y', z'. The problem then becomes one of evaluating $P(\theta,\phi)$. Snyder[172] has suggested expanding $P(\theta,\phi)$ in real spherical harmonics. The relevant ones are the 5 real functions of order $2(\ell = 2)$, the familiar d-orbitals. The expansion of $P(\theta,\phi)$ can be written as:

$$P(\theta,\phi) = (\frac{1}{4\pi}) + C_{3z^2-r^2}D_{3z^2-r^2} + C_{x^2-y^2}D_{x^2-y^2} + C_{xz}D_{xz}$$

$$+ C_{yz}D_{yz} + C_{xy}D_{xy}. \qquad (A.6)$$

In this equation the D's are the real representation of the five d-orbitals:

$$D_{3z^2-r^2} = (4\pi)^{-1}2^{-1}5^{\frac{1}{2}}(3\cos^2\theta - 1)$$

$$D_{x^2-y^2} = (4\pi)^{-1}2^{-1}15^{\frac{1}{2}}(\sin^2\theta\cos 2\phi)$$

$$D_{xz} = (4\pi)^{-1}15^{\frac{1}{2}}(\sin\theta\cos\theta\cos\phi) \qquad (A.7)$$

$$D_{yz} = (4\pi)^{-1}15^{\frac{1}{2}}(\sin\theta\cos\theta\sin\phi)$$

$$D_{xy} = (4\pi)^{-1}2^{-1}15^{\frac{1}{2}}(\sin^2\theta\sin 2\phi).$$

The five C's are motional constants which can be easily related to the elements of the Saupe ordering matrix. Again, symmetry can reduce the number of motional constants required to describe the ordering.

A.2.3 Non-Rigid Molecules

A.2.3.1 Exact Description

To this point the discussion has been limited to rigid molecules. Many liquid crystals and dissolved solutes are in fact non-rigid molecules,

undergoing rotations about carbon-carbon single bonds, rapid interconversion between different conformations, and/or vibrations. The problems of describing the ordering in such molecules and of determining how these motions ultimately effect the NMR spectrum have been the subject of considerable debate in the literature. As an illustration, we consider the ordering of a molecule which is interconverting between two or more different conformations.

Recall from Equation A.5 that for a rigid molecule the measurable component of a tensor interaction $\underset{\approx}{A}$ is given by:

$$(\underset{\approx}{A})_{zz} = \overline{A'} + \frac{2}{3} \sum_{\alpha,\beta} A'_{\alpha\beta} S_{\alpha\beta}. \tag{A.8}$$

The order parameter $S_{\alpha\beta}$ is $\frac{1}{2} \langle 3\cos\theta_{z\alpha}\cos\theta_{z\beta} - \delta_{\alpha\beta} \rangle$, where the brackets represent an average over all orientations of the molecule. In the case of a non-rigid molecule, the zz component of $\underset{\approx}{A}$ is properly written:

$$(\underset{\approx}{A})_{zz} = \overline{A'} + \frac{2}{3} \sum_{\alpha,\beta} \langle A'_{\alpha\beta} (\tfrac{1}{2}) (3\cos\theta_{z\alpha}\cos\theta_{z\beta} - \delta_{\alpha\beta}) \rangle. \tag{A.9}$$

In this equation the brackets represent averages over all internal motions and orientations of the molecule. When the intramolecular motion consists of rapid interconversion between n different conformations, this equation may be rewritten

$$(\underset{\approx}{A})_{zz} = \overline{A'} + \frac{2}{3} \sum_{n} \sum_{\alpha,\beta} P_n A'^{n}_{\alpha\beta} (\tfrac{1}{2}) \langle 3\cos\theta^{n}_{z\alpha}\cos\theta^{n}_{z\beta} - \delta_{\alpha\beta} \rangle$$

$$= \overline{A'} + \frac{2}{3} \sum_{n} \sum_{\alpha,\beta} P_n A'^{n}_{\alpha\beta} S^{n}_{\alpha\beta}, \tag{A.10}$$

where the superscript n refers to the n^{th} molecular conformation, P_n is the probability of this conformation, and the angular brackets again represent an orientational average.

A.2.3.2 Simplifying Approximations

While providing a formal solution to the problem, Equation A.10 also illustrates the difficulty in determining the structure and ordering of molecules undergoing internal motion. Up to 5n order parameters may be required, as well as probabilities and geometries for each of the n conformations. It is often difficult, if not impossible, to determine all of the unknown parameters from the NMR spectrum. In an effort to simplify this problem, it is often assumed that the average orientation of a non-rigid molecule is independent of its conformation. In mathematical terms, this assumption allows the following simplification of Equation A.10:

$$(\underset{\approx}{A})_{zz} = \overline{A'} + \frac{2}{3} \sum_{\alpha,\beta} \langle A'_{\alpha\beta} \rangle S_{\alpha\beta}, \qquad (A.11)$$

where $\langle A'_{\alpha\beta} \rangle = \sum_n P_n A'^{n}_{\alpha\beta}$ and the ordering is now described by a single set of order parameters. The simplification is referred to as "A-S separation"[173]. The problem is one of specifying the conditions under which this approximation is justified. Two different criteria have recently been described.

According to Burnell and deLange[173,174], the important factor is the relative timescales for internal motion and molecular reorientation. They consider ordering in the so-called weak-collision limit, in which conformational change involves no reorientation of the molecule as a whole (and both motions are assumed fast on an NMR timescale). Defining τ_v as the conformational lifetime and k as the rate of reorientation, they proceed to consider the limiting cases of slow interconversion ($k << \tau_v^{-1}$) and fast interconversion ($k >> \tau_v^{-1}$). In the fast interconversion limit, it is always possible to describe the ordering by a single set of "average" order parameters. In the limit of slow interconversion

one generally needs to specify a different set of order parameters for each conformation. Depending upon the symmetry of the molecule, it may be possible to choose a molecule-fixed axis system such that one set of order parameters suffices in this limit also, however.

Emsley and Luckhurst[175], on the other hand, argue that timescale arguments can be misleading and adopt instead a statistical mechanical approach. They treat the observed tensor components $(\underset{\approx}{A})_{zz}$ as equilibrium properties of the system which they evaluate in terms of inter- and intramolecular potentials. In their scheme, "A-S separation" is justified whenever the external potential is independent of internal molecular coordinates. Clearly the proper choice of molecule-fixed axis system is crucial in this regard. When an axis system which separates intermolecular potential from internal motion cannot be found, a single set of order parameters is no longer sufficient.

Recently, an attempt has been made to reconcile the relative timescales and equilibrium statistical mechanics points of view[176]. A complete description of the ordering of non-rigid molecules in the liquid crystalline phase is clearly a complex problem and many unanswered questions remain. In the general case described by Equation A.10, the number of unknowns to be determined greatly exceeds the number of independent dipolar couplings and the NMR spectrum must be supplemented with information from other sources. Often it may be possible to separate the effects of internal motion and molecular reorientation (Eq. A.11) or to make other simplifying approximations which make the problem more tractable. A more detailed treatment of the ordering of non-rigid molecules and of the role which multiple quantum NMR can play in elucidating this ordering can be found in the recent Ph.D. theses of Sinton[48] and Drobny[50].

A.2.3.3 Ordering of Molecules of High Symmetry

We return now to the ordering of molecules of high symmetry such as CH_4 and $(CH_3)_4Si$. For rigid molecules whose symmetry is described by the point groups T, T_d, O, or O_h all five order parameters are zero. Thus we expect them to show no preferred direction of orientation in a nematic solvent. Yet the NMR spectra of CD_4[177,178], $(CH_3)_4Si$[169], $(CH_3)_4C$[169] and other similar molecules show unmistakable anisotropic splittings as evidence of partial ordering.

Snyder and Meiboom[169] explained the observed $(CH_3)_4Si$ spectrum by postulating a distortion of the solute molecule due to an anisotropic pressure exerted by the liquid crystal solvent. Such angular deformations alone were unable to explain later experimental results for dissolved methane, however. An alternate explanation has been offered by Burnell and deLange[174] who suggest that the methane molecule is not tetrahedral at all instants in time due to normal vibrations of the C-H bonds. A coupling between these vibrations and molecular reorientation can then lead to a net ordering of the methane. This is very similar to the explanation of Emsley and Luckhurst[175] whose criterion for non-zero dipolar coupling in molecules of T_d symmetry is a dependence of the ordering potential on vibrational state.

The correct explanation for the ordering of molecules of high symmetry is probably a combination of solute distortion and vibration-reorientation coupling. The splittings observed in the spectra of these molecules, which reflect a solute-solvent interaction, are generally two or more orders of magnitude smaller than those typically seen for partially ordered molecules of lower symmetry. When analyzing the spectra of molecules dissolved in liquid crystals, it is usually assumed that interactions

between solute and solvent are negligible. The relatively small splitting seen in the spectra of molecules of T_d symmetry provides good support for this assumption.

A.3 The Spin Hamiltonian in Partially Oriented Systems

Equation A.5 expresses the measurable component of a tensor interaction $\underset{\approx}{A}$ in terms of the elements of that tensor in a molecule-fixed axis system ($A'_{\alpha\beta}$) and the components of the Saupe ordering matrix ($S_{\alpha\beta}$). In this section we consider this expression more explicitly for the three spin Hamiltonian interactions of interest in this work: scalar couplings, dipolar couplings, and chemical shifts.

A.3.1 Scalar Couplings

The scalar coupling is the easiest of the three interactions to describe. As discussed in Section 1.2.3.3, the anisotropic portion of the J-coupling is negligibly small for proton spin systems. The remaining isotropic coupling, given by $\frac{1}{3}\,\mathrm{Tr}(\underset{\approx}{J'})$, is a scalar which commutes with all rotations. The scalar coupling thus has no orientational dependence.

A.3.2 Dipolar Couplings

The dipolar coupling constant between spins i and j was given in Equations 1.43 and 1.45 as $(-\gamma_i\gamma_j\hbar/2r_{ij}^3)(3\cos^2\theta_{ijzz} - 1)$. This expression applies when spins i and j occupy fixed positions with respect to each other and the external magnetic field. At room temperature, rapid vibrational motion is occurring, however (a typical vibrational period is $\sim 10^{-13}$ sec), and the dipolar coupling must be averaged over this motion:

$$D_{ij} = \frac{-\gamma_i\gamma_j\hbar}{2} \langle (r_{ij}^{-3})(3\cos^2\theta_{ijzz} - 1) \rangle . \qquad (A.12)$$

Since the vibrational period is generally much shorter than the time for molecular reorientation, it is usually assumed that these two are uncorrelated (the validity of this assumption was discussed in Section A.2.3.2). This allows the two terms within the bracketed expression of Equation A.12 to be averaged separately:

$$D_{ij} = \frac{-\gamma_i\gamma_j\hbar}{2} \langle r_{ij}^{-3} \rangle \langle 3\cos^2\theta_{ijzz} - 1 \rangle, \qquad (A.13)$$

where only the angular factor is dependent on molecular reorientation.

We now evaluate the dipolar coupling constant D_{ij} in terms of the components of dipolar and ordering tensors expressed in a molecule-fixed axis system defined by x', y', z'. It is actually convenient to start in the principal axis system (PAS) of the dipolar tensor, defined by the axes a, b, c. Taking the c-axis along the internuclear vector, the dipolar interaction in this frame may be written:

$$D_{ij}(\text{PAS}) = \frac{-\gamma_i\gamma_j\hbar}{2} \langle r_{ij}^{-3} \rangle \begin{pmatrix} -1 & 0 & 0 \\ 0 & -1 & 0 \\ 0 & 0 & 2 \end{pmatrix}. \qquad (A.14)$$

This tensor is next transformed into the x', y', z' axis system. The component of this transformed tensor, $(D'_{ij})_{\alpha\beta}$, is:

$$(D'_{ij})_{\alpha\beta} = \sum_{\gamma\delta}^{x',y',z'} [D_{ij}(\text{PAS})]_{\gamma\delta} \cos\theta_{\alpha\gamma}\cos\theta_{\beta\delta}$$

$$= \frac{-\gamma_i\gamma_j\hbar}{2} \langle r_{ij}^{-3} \rangle [3\cos\theta_{\alpha c}\cos\theta_{\beta c} - \delta_{\alpha\beta}], \qquad (A.15)$$

where $\theta_{\alpha c}$ is the angle between the molecule-fixed axis α and the c-axis of the PAS, and the explicit ij subscript has been dropped from the angular terms. Finally, we combine the expressions for $(D'_{ij})_{\alpha\beta}$ with

elements of the Saupe ordering tensor to write the measurable zz component of the dipolar tensor as:

$$D_{ij} = \frac{-\gamma_i\gamma_j\hbar}{2} \langle r_{ij}^{-3} \rangle [\frac{2}{3} \sum_{\alpha,\beta}^{x',y',z'} (3\cos\theta_{\alpha c}\cos\theta_{\beta c} - \delta_{\alpha\beta})S_{\alpha\beta}], \qquad (A.16)$$

where we have used the fact that $\overline{D'_{ij}} = 0$. This equation may be expanded and rearranged to

$$D_{ij} = \frac{-\gamma_i\gamma_j\hbar}{2} \langle r_{ij}^{-3} \rangle [(3\cos^2\theta_{z'c} - 1)S_{z'z'} + (\cos^2\theta_{x'c} - \cos^2\theta_{y'c})(S_{x'x'} - S_{y'y'})$$
$$+ 4(\cos\theta_{x'c}\cos\theta_{y'c})S_{x'y'} + 4(\cos\theta_{x'c}\cos\theta_{z'c})S_{x'z'}$$
$$+ 4(\cos\theta_{y'c}\cos\theta_{z'c})S_{y'z'}]. \qquad (A.17)$$

Again, because the dipolar tensor for each pair of spins is diagonal in its own PAS, each angle in Equation A.17 has an implicit ij subscript.

A.3.3 Chemical Shifts

The expression for the chemical shift in partially ordered spin systems is

$$\omega_i = -\omega_o^i [\overline{\sigma'_i} + \frac{2}{3} \sum_{\alpha,\beta}^{x',y',z'} \sigma_{i\alpha\beta}S_{\alpha\beta}]. \qquad (A.18)$$

The first term on the right hand side of this equation, $-\omega_o^i\overline{\sigma'_i}$, is the isotropic chemical shift. In general, the chemical shift measured in the liquid crystalline phase will differ from that in an isotropic liquid. This difference, given by $\Delta\omega_i = \omega_i + \omega_o^i\overline{\sigma'_i}$, measures the anisotropy of the chemical shift.

Several factors can contribute to the anisotropy in the shielding at a particular nucleus i. Included among these are effects due to

surrounding electrons, neighboring nuclei, and the bulk properties of the sample as a whole. As discussed in Chapter 8 of Emsley and Lindon[14], it is often difficult to separate out the different contributions to $\Delta\omega_i$. Even when this is possible, interpretation of the chemical shift anisotropy in terms of molecular parameters is difficult.

A.4 Spherical Tensor Operators

A.4.1 Coordinate Transformations

The preceding sections have demonstrated the importance of transformations between coordinate systems. In the most general case, 3 such transformations are required to describe a second-rank tensor interaction in the liquid crystalline phase:

$$\text{PAS} \rightarrow \begin{matrix}\text{Molecule-fixed} \\ \text{Coordinate System}\end{matrix} \rightarrow \text{Director frame} \rightarrow \text{Laboratory frame.} \qquad \text{(A.19)}$$

For a nematic liquid crystal in high magnetic field, the director lies along the laboratory z-axis and the last of these transformations is unnecessary. To this point, all transformations have been expressed in Cartesian coordinates and have been given in terms of either a rotation operator ($\underset{\approx}{R}$) or the direction cosines of the angles between coordinate systems axes. In this section we demonstrate the use of spherical tensor operators in simplifying the general description of rotations. (The use of irreducible tensor operators to simplify the description of rotations in spin space was described in Section 1.7).

A complete description of coordinate transformations and spherical tensor operators can be found in several texts[30,32-34] and will not be repeated here. Before referring to these sources, the reader is warned that different authors use different conventions in their definitions of

rotation operators and coordinate systems, and care must be taken when comparing results between sources. The following discussion is based upon a right-handed coordinate system and is consistent with the rotation conventions of Silver[32].

A.4.1.1 Transformations in Geometric Space

The relationship between any two coordinate systems (x,y,z) and (x',y',z') can be specified by the Euler angles (α,β,γ) defined in the conventional way[32-34]. These three angles describe the successive rotations required to transform one coordinate system into the other. The rotation operator $R(\alpha\beta\gamma)$ is defined as

$$R(\alpha\beta\gamma) \equiv \exp(i\gamma\ell_z)\ \exp(i\beta\ell_y)\ \exp(i\alpha\ell_z), \tag{A.20}$$

where the angular momentum operators ℓ_y and ℓ_z are the "generators of infinitesimal rotations" about the y and z axes, respectively. This rotation operator describes the transformation of a function $f(\underset{\sim}{r})$ from one coordinate system to another:

$$f'(\underset{\sim}{r}) = R(\alpha\beta\gamma)f(\underset{\sim}{r}), \tag{A.21}$$

where $f'(\underset{\sim}{r})$ is the value of the transformed function and the positional coordinates $\underset{\sim}{r}$ are expressed in the new coordinate system.

The nine components A_{ij} of a second rank Cartesian tensor may be decomposed into a scalar of rank zero

$$\underset{\approx}{A}^0 = \frac{1}{3}\sum_i A_{ii}, \tag{A.22a}$$

an anti-symmetric tensor of rank one

$$\underset{\approx}{A}^1 = \frac{1}{2}(A_{ij} - A_{ji}), \tag{A.22b}$$

and a symmetric, traceless tensor of rank two

$$\underset{\approx}{A}^2 = \frac{1}{2}(A_{ij} + A_{ji}) - \underset{\approx}{A}^0. \tag{A.22c}$$

Each irreducible tensor operator of rank ℓ contains $(2\ell+1)$ independent components. When appropriately chosen, these $(2\ell+1)$ components A_n^ℓ transform among themselves under rotations according to

$$(A_n^\ell)' = R(\alpha\beta\gamma)A_n^\ell R^{-1}(\alpha\beta\gamma) = \sum_{n'=-\ell}^{\ell} A_{n'}^\ell \mathcal{D}^{(\ell)}_{n',n}(\alpha\beta\gamma), \tag{A.23}$$

where the $\mathcal{D}^{(\ell)}_{n',n}$ are elements of the Wigner rotation matrix of rank ℓ. Thus the transformation of a tensor operator $\underset{\approx}{A}$ from one coordinate system to another is greatly simplified by decomposing that operator into spherical tensor operators $\underset{\approx}{A}^\ell$. Expressions for the components A_n^ℓ of the spherical tensor operators which can be constructed from a second rank cartesian tensor $\underset{\approx}{A}$ are given in Table A-1.

For a series of coordinate transformations such as that shown in (A.19), Equation A.23 can be applied repetitively with different sets of Euler angles. In liquid crystals, we have seen that due to molecular fluctuations, the transformation from a molecule-fixed axis system to the director frame involves an ensemble or time average over orientation. In terms of spherical tensor operators, this average is achieved by substituting motionally averaged Wigner rotation matrix elements $\langle \mathcal{D}^{(\ell)}_{n',n}(\alpha\beta\gamma)\rangle$ in Equation A.23. The elements $\langle \mathcal{D}^{(\ell)}_{n',n}(\alpha\beta\gamma)\rangle$ can be expressed in terms of a set of motional constants similar to those introduced by Snyder[172] (Sec. A.2.2). These constants themselves can be directly related to the components of the Saupe ordering tensor.

Table A-1

Construction of Spherical Tensor Operators from the Components of a Second Rank Cartesian Tensor $\underset{\approx}{A}$

Spherical Tensor Operator Component	Cartesian Tensor Components
A^0_0	$-(1/\sqrt{3})(A_{xx}+A_{yy}+A_{zz})$
A^1_0	$-(i/\sqrt{2})(A_{xy}-A_{yx})$
$A^1_{\pm 1}$	$-(1/2)(A_{zx}-A_{xz} \pm i(A_{zy}-A_{yz}))$
A^2_0	$(1/\sqrt{6})(3A_{zz}-(A_{xx}+A_{yy}+A_{zz}))$
$A^2_{\pm 1}$	$\mp(1/2)(A_{xz}+A_{zx} \pm i(A_{yz}+A_{zy}))$
$A^2_{\pm 2}$	$(1/2)(A_{xx}-A_{yy} \pm i(A_{xy}+A_{yx}))$

A.4.2 More Spin Hamiltonians

In this final section, we express the dipolar coupling and chemical shift Hamiltonians in terms of spherical tensor operators. A more complete discussion of this subject may be found in Appendix A of Mehring[6]. In Equation 1.35, each Hamiltonian was written in terms of a second-rank Cartesian tensor:

$$\mathcal{H} = \underset{\sim}{X} \cdot \underset{\approx}{A} \cdot \underset{\sim}{Y} = \sum_{i,j} A_{ij} X_i Y_j. \tag{A.24}$$

Alternatively, this Hamiltonian can be expressed as the sum of the scalar products of irreducible tensor operators of rank 2, 1, and 0. The scalar product of two irreducible tensors can be written in terms of their respective components as

$$\underset{\approx}{A}^{\ell} \cdot \underset{\approx}{T}^{\ell} = \sum_{n=-\ell}^{\ell} (-1)^n A^{\ell}_n T^{\ell}_{-n}, \tag{A.25}$$

with a particular spin Hamiltonian then being given by

$$\mathcal{H} = \sum_{\ell=0}^{2} \sum_{n=-\ell}^{\ell} (-1)^n A^{\ell}_n T^{\ell}_{-n}. \tag{A.26}$$

In practice, the tensor operators $\underset{\approx}{A}^{\ell}$ and $\underset{\approx}{T}^{\ell}$ are generally chosen such that the former operate only on spatial variables and the latter solely on spin functions.

A.4.2.1 Dipolar Couplings

In the case of the dipolar coupling, the tensor $\underset{\approx}{A}^{\ell}$ is composed of the various elements of the Cartesian dipolar tensor $\underset{\approx}{D}_{ij}$. These are combined into the tensor components A^{ℓ}_n according to Table A-1. The

angular momentum operators in spherical tensor form are:

$$T_0^1 = I_z$$
$$T_1^1 = -\frac{1}{\sqrt{2}}(I_x + iI_y) \qquad (A.27)$$
$$T_{-1}^1 = \frac{1}{\sqrt{2}}(I_x - iI_y).$$

Irreducible tensor operators T_n^ℓ of rank 2, 1, and 0 are constructed from the angular momentum operators for spins i and j according to Equation 1.63 of Chapter 1.

A.4.2.2 Chemical Shifts

For the chemical shift, we first take the scalar product of the shift tensor $\underset{\approx}{\sigma}$ and the static field $\underset{\sim}{H}_0$. The resulting terms, $H_{\sigma x} = \sigma_{xz}H_0$; $H_{\sigma y} = \sigma_{yz}H_0$; $H_{\sigma z} = \sigma_{zz}H_0$, are combined into the three components of an irreducible first rank tensor A^1:

$$A_0^1 = H_{\sigma z}$$
$$A_1^1 = -\frac{1}{\sqrt{2}}(H_{\sigma x} + iH_{\sigma y}) \qquad (A.28)$$
$$A_{-1}^1 = \frac{1}{\sqrt{2}}(H_{\sigma x} - iH_{\sigma y}).$$

The scalar product of A^1 with the angular momentum tensor operators of Equation A.27 yields the chemical shift Hamiltonian in tensor form.

Appendix B: GAMMA HIGH-FIELD NMR SPECTROMETER

The experiments in this thesis were all performed on a home-built spectrometer operating at 182 MHz proton resonance. This spectrometer, the third constructed in our laboratory, is referred to as the "gamma" and is the subject of this appendix. In Section B.1 the spectrometer's magnet and shim system are discussed. Brief mention is made of the gamma's computer and its various peripherals in Section B.2. The low power electronics necessary to generate r.f. pulses of differing lengths and relative phases are the subject of Section B.3. Section B.4 is devoted to a discussion of high power r.f. amplifiers, while the sample probe and its related circuitry are described in Section B.5. The receiver and phase sensitive detector are discussed in Section B.6. The final two sections describe circuitry which is more digital in nature. Section B.7 deals with the sampling, analog-to-digital conversion and computer storage of audio frequency signals, while the gamma's 8-bit variable phase shifter and controller board are described in Section B.8.

B.1 Superconducting Magnet and Room Temperature Shims

B.1.1 The Magnet

The spectrometer is built around a persistent superconducting solenoid manufactured by Bruker Instruments. The magnet is operated at a field of approximately 42.7 kGauss. At this field, the resonance frequencies of the most commonly studied nuclei are:

^{1}H	182.00 MHz
^{13}C	45.77 MHz
^{2}H	27.94 MHz .

In addition to the main field, there are also three superconducting shims: One oriented along the direction of the main field (z) and two mutually orthogonal shims in the transverse plane (x and y, respectively). Current in these shims is adjusted by means of an external heater and a Hewlett-Packard 6259B DC Power Supply. Connection to the magnet is through a charging rod supplied by Bruker. The bore of the magnet is approximately 3.5 inches in diameter, with the center of the magnetic field located roughly 14 inches above the base of the bore tube (24 inches below the top of this tube).

B.1.2 Room Temperature Shim System

Contained within the magnet bore is a set of room temperature shims purchased from Cryomagnet Systems (Indianapolis, IN). The center of these room temperature shims is located 14.6 inches above the top of the bottom-mounting flange. The room temperature shim tube runs through the bore of the magnet and is secured by a locking ring on top. The top half of the shim tube can be replaced with a supplied spinner bearing to permit conventional z-axis sample spinning. A total of 14 different room temperature shims are provided: 6 axial shims (z^0, z^1, z^2,...z^5) and 8 radial shims (x, y, xy, $x^2 - y^2$, xz, yz, x^2z, y^2z). The axial shims are controlled by a matrix board supplied by Cryomagnets, the radial shims by a homebuilt power supply. At the present time, the room temperature shims provide no field-lock circuitry.

B.2 Gamma Computer System

B.2.1 Nova Computer and Peripherals

The operations of the gamma spectrometer are directed by a Data General NOVA2 minicomputer. This computer has a 16-bit word length and

32 kbyte of core memory. The computer is supported with a Diablo 4234 10 Mbyte dual-platter disk drive. Half of this storage is provided on a fixed platter, the remaining 5 Mbyte are on a removable pack. A Data General 6030 315 kbyte single density floppy drive allows data and programs to be transferred to floppy for long-term storage. The gamma's console is an ADM-3 CRT manufactured by Lear Siegler, the display scope is a Hewlett-Packard 1300 x-y Scope. A complete description of the spectrometer operating system SPEC has been provided[179].

B.2.2 EIA/TTL Toggle Box

In its normal configuration, the Main port of the spectrometer's console is connected to the Nova computer and the auxilliary (Aux) port is connected to the pulse programmer's microprocessor. Occasionally, however, it is necessary to interchange the connections to the Main and Aux ports. The EIA/TTL toggle box allows this to be done without actually having to swap cables. The box, whose schematic is shown in Figure B.1, has two different push-button selectable states: (1) Main-to-Nova, Aux-to-Microprocessor, (2) Main-to-Microprocessor, Aux-to-Nova. The box also contains a 4PDT switch which allows the Aux and Main port cables to be jumpered directly together, thereby removing the console from the circuit. This permits the console to be turned off once an experiment is started. In addition, the Aux port of the console may be disabled by means of a 2PDT switch.

B.3 Low Power r.f. Electronics

The experiments described in this work require the ability to generate r.f. pulses of various lengths and relative phases at both ^{1}H and ^{13}C carrier frequencies. (Since a wide variety of other nuclei can be studied, the non-proton frequency will be referred to as the X

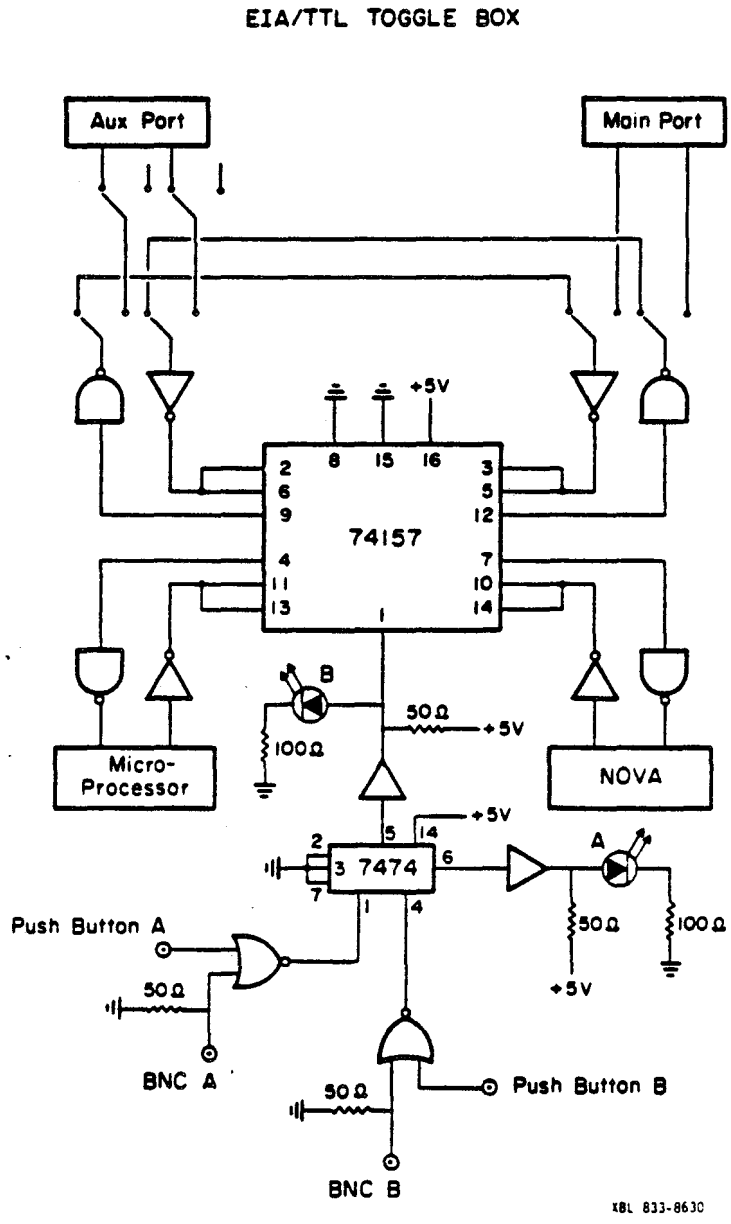

Figure B.1. EIA/TTL Toggle Box.

frequency throughout much of the remainder of this chapter.) The gamma is a dual channel spectrometer, capable of producing pulses at two different r.f. carrier frequencies simultaneously. In this section, the low power r.f. circuitry required to provide this capability is described. The opening and closing of all r.f. switches is controlled by TTL levels supplied by the spectrometer's microprocessor-based pulse programmer. Details concerning the construction and use of this pulse programmer are provided elsewhere[50,179]. Here we deal only with the various r.f. components and switches themselves.

We begin with an overview of the manner in which the r.f. pulses of appropriate length, phase, and carrier frequency are generated. As with most NMR spectrometers, phase generation on the gamma is performed at an intermediate frequency known as the IF. Pulses at this frequency are then mixed with a second frequency, the so-called local oscillator (LO), to generate the appropriate NMR frequency. On the gamma the IF is 30 MHz, the proton LO is 152 MHz, and the ^{13}C LO is 75.8 MHz.

One of the major advantages of generating pulses at the IF is the ease with which we may switch from one nuclear frequency to another. This is done by simply changing the frequency of the LO (along with a bandpass filter or two). The relative phase at the nuclear frequency is completely controlled by the generated IF pulse. Thus no adjustments to the phase-generating circuitry need be made upon switching carrier frequencies. An additional advantage to using an IF is that 30 MHz is a more convenient frequency at which to generate phase shifts than many nuclear frequencies, due to its relatively long wavelength.

B.3.1 IF/LO Generation

In its current configuration, the gamma spectrometer receives its

10 MHz reference signal from the back of a Programmed Test Sources PTS 40 frequency synthesizer discussed below. This 10 MHz signal is used as the external reference input to the gamma's X LO frequency synthesizer (Sec. B.3.2) as well as being the source of 30 MHz and 100 MHz frequencies. This is illustrated in Figure B.2, a schematic of the IF/^{1}H LO box. The generation of a 30 MHz signal is shown in the lower branch of this figure where, following amplification by an Anzac AM-102, the 10 MHz input is tripled to 30 MHz, and filtered. This 30 MHz signal, which will become the IF for both ^{1}H and X frequencies, is then sent to the LO/IF Generator (Fig. B.3).

The 10 MHz reference in the upper branch of Figure B.2 is used to generate the proton LO. A "times 10" circuit makes the 10 MHz into 100 MHz, which is then amplified by an AM-102 and fed into an Anzac MD-143 double-balanced mixer. The second input to this mixer is provided by doubling the output of a PTS 40 frequency synthesizer. This synthesizer, which operates over the range 0.1-40 MHz in 0.1 Hz steps, provides the means for adjusting the proton carrier frequency. The mixer output is amplified (Anzac AM-105), filtered (Texscan 4BC152/5), and split (Anzac TU-50) into two proton LO signals. One of these two is input to the ^{1}H Generator (Fig. B.6a), the other serves as the LO reference to the Receiver (Fig. B.9).

B.3.2 LO/IF Generator (Fig. B.3)

The 30 MHz output of the IF/^{1}H LO (Fig. B.2) is amplified by an AM-102, filtered, and split into three signals by a pair of Anzac THV-50's. These three IF signals are then fed, respectively, to the Phase Sensitive Detector (Fig. B.9b) and ^{1}H and X Quadrature Generators (Fig. B.4).

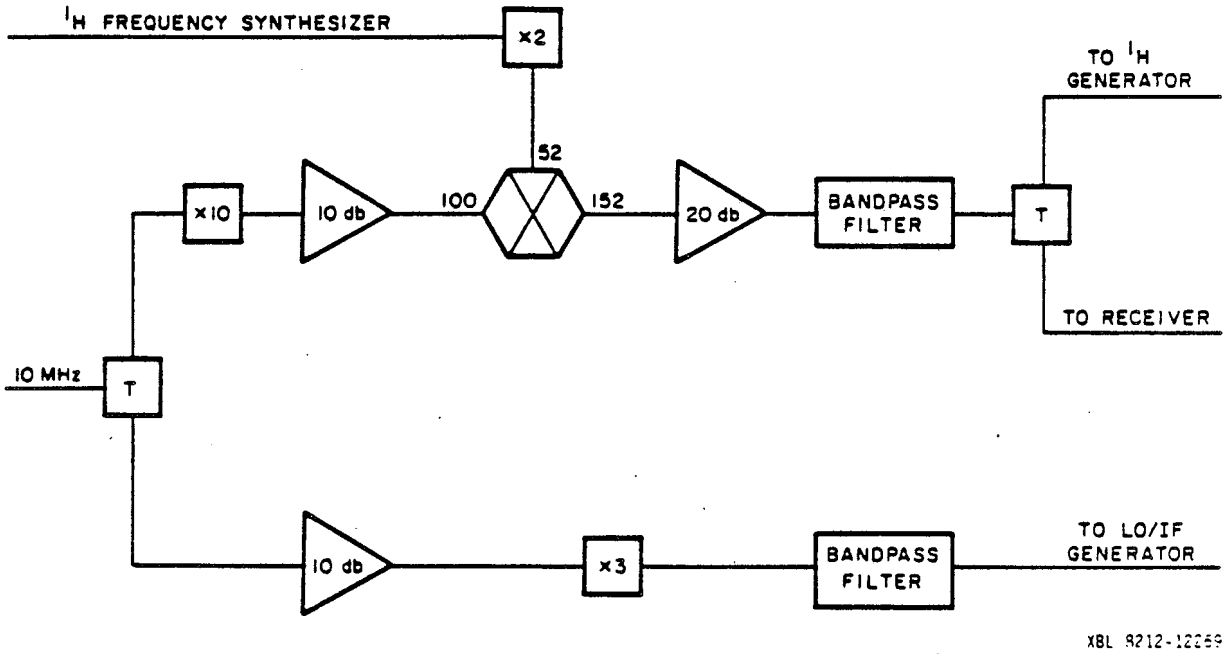

Figure B.2. IF/^{1}H LO Generator.

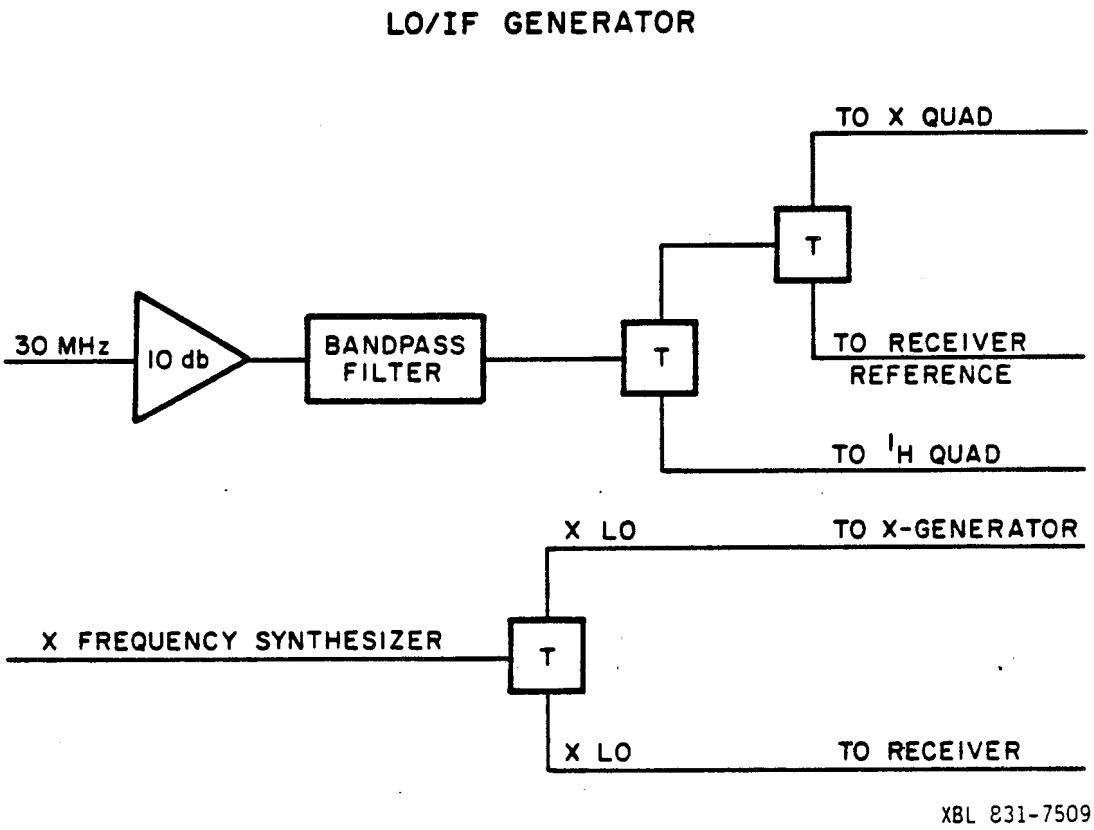

Figure B.3. X LO/IF Generator.

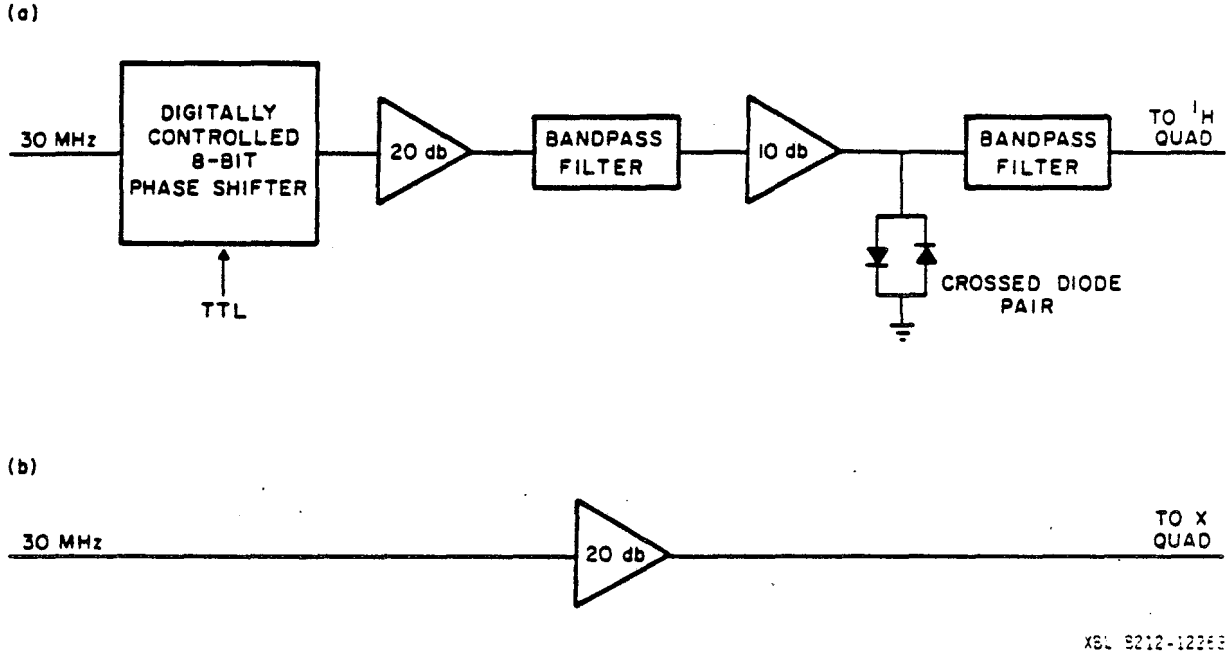

Figure B.4. IF Amplification. (a) ^{1}H channel. (b) X channel.

The X-frequency LO is generated directly by a Harris PRD Electronics 7828 frequency synthesizer, which operates over the range 0-80 MHz, is "click-settable" in steps of 1 kHz, and has a vernier dial adjustment over the range 0-999 Hz. The LO is split by a TU-50 into two signals which are fed to the X Generator (Fig. B.6b) and Receiver reference (if X signal is to be detected), respectively.

B.3.3 ^{1}H/X Quadrature Generation (Figs. B.4 and B.5)

Both the ^{1}H and X sides provide four r.f. channels having relative phases 0°, 90°, 180°, and 270°. These are labeled as y, $\bar{x}$, $\bar{y}$, and x, respectively. Quadrature generation is very similar for both ^{1}H and X frequencies and is illustrated in Figures B.4 and B.5. As indicated in Figure B.4b, the X frequency IF is simply amplified by an AM-105 before being split into its four phases. The proton IF, on the other hand, goes through a digitally controlled phase shifter (Sec. B.8), is amplified (AM-105), filtered, amplified a second time (AM-102), clipped with a pair of crossed diodes to ground, and filtered again (Texscan 3LD60/CC) before being split into its four phases.

Figure B.5 illustrates the Quadrature Generation boxes for both ^{1}H and X frequencies. The 30 MHz IF is split by a 0°/90° hybrid (Anzac JH-127) and then by a pair of 0°/180° hybrids (Anzac DV-50) to produce four mutually orthogonal phases. These are trimmed using 0-90° variable phase adjusters (Merrimac PSS-2-30) and 0-20 dB variable attenuators (Merrimac ARS-1) and fed into four sets of dual r.f. switches (Summit 571). Each of these pairs of switches is individually controlled by a TTL level supplied by the pulse programmer, allowing the desired pulse phase to be selected. The four r.f. lines are then recombined (Anzac DS-312) and, on the proton side, amplified (AM-102) before going to the ^{1}H or X Generator.

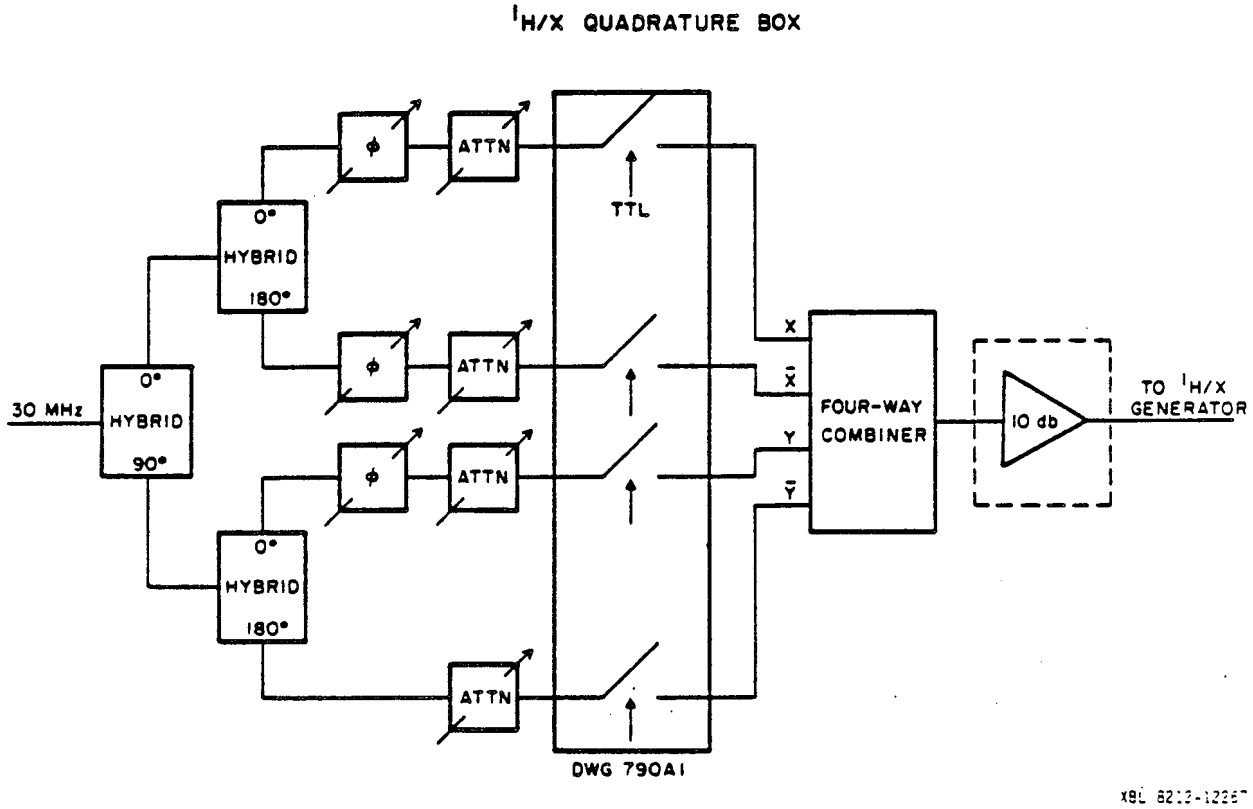

Figure B.5. Quadrature Generator. The gamma has two quadrature generation boxes, one on the proton side and one on the X side.

B.3.4 ^{1}H/X Generators (Fig. B.6)

The IF pulse from the proton quadrature box passes through a variable attenuator and is mixed with the proton LO (Fig. B.2) using an Anzac MD-143 mixer. After filtering (K & L Microwave 182/20), the resulting pulse at the ^{1}H carrier frequency is switched a second time (Daico SPST 100C1281A), passes through a capacitor (15 pf) to remove any DC offset, is amplified (AM-105), passes through a crossed pair of noise diodes, is filtered again (Texscan 3BD182/5-CC), and amplified (AM-102). A variable attenuator, consisting of a 10-turn 1 kΩ potentiometer to ground, allows the amplitude of the pulse to be fine-tuned before it is sent to the proton high-power amplifier.

The 30 MHz pulse on the X side is mixed with the X LO (Fig. B.3) using an Anzac MD-143. After filtering and amplifying (AM-105), the resulting pulse at the X carrier frequency is switched (pair of Summit 571 switches), amplified (AM-105), and trimmed (potentiometer to ground) before going to the X high-power amplifier.

B.4 High-Power Amplifiers

High-power amplification of the proton pulses is provided by an Amplifiers Research (AR 100L) broadband r.f. transmitter. With an input of ~1 V p-p this class A amplifier is capable of providing an output of 100-200 watts. This results in typical $\frac{\pi}{2}$ pulse lengths of approximately 5 μsec.

On the X side an Electronic Navigation Industries (ENI 350L) provides low power amplification. This class A amplifier supplies 50 dB of amplification over the frequency range 250 kHz - 105 MHz. The output of the ENI drives a Drake L-7 Linear Amplifier, a high-power tuned transmitter which has been modified to operate at frequencies of 16, 28, 46, and

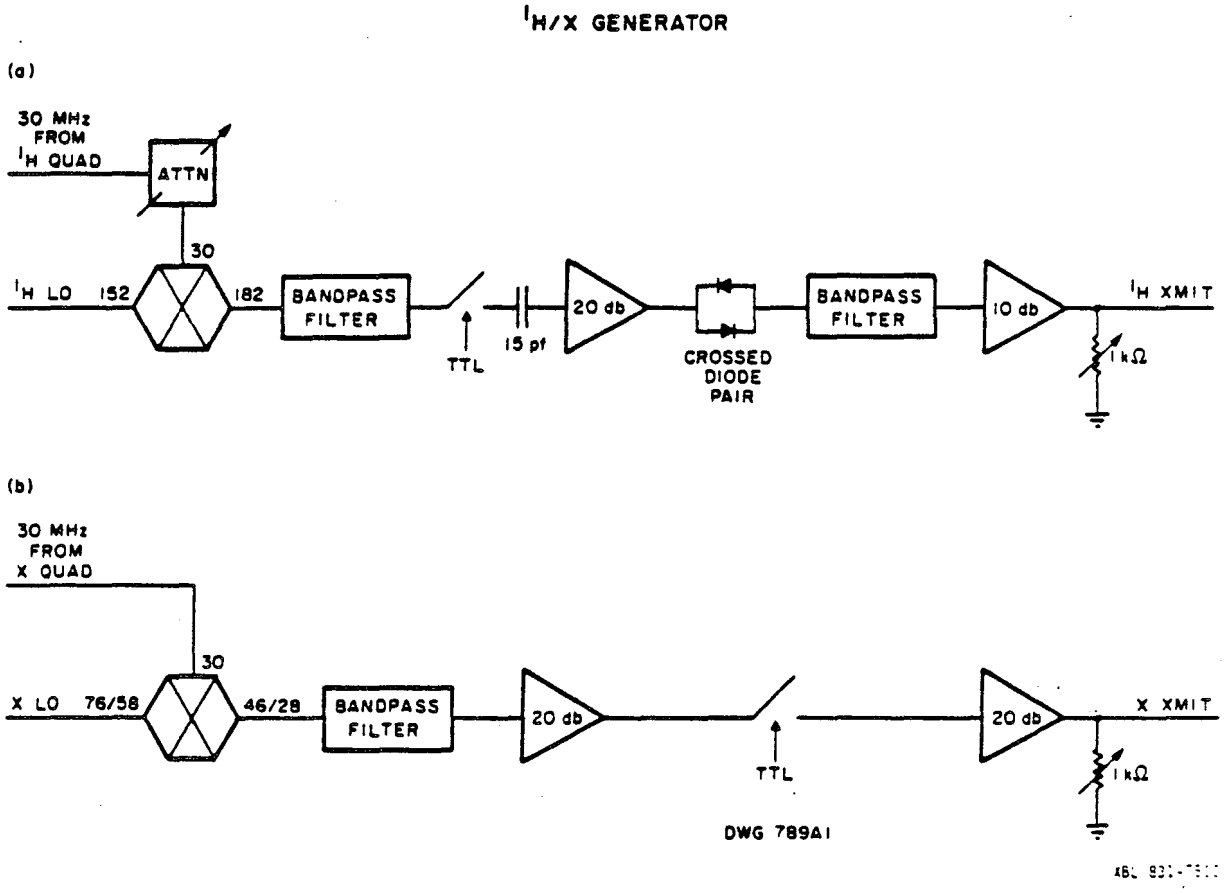

Figure B.6. ^{1}H/X Generators. (a) ^{1}H channel. (b) X channel.

56 MHz. In this configuration, a 1 V p-p input to the ENI results in an output in excess of 400 watts from the L-7. (One kilowatt or more of output may be obtained from the L-7 by driving it with a second AR amplifier.) Typically, a variable attenuator (Kay Elemetrics 432D) is placed on the input to the ENI to allow ^{1}H and X frequency pulse lengths to be more easily matched.

B.5 Probes

All of our probes are tuned L-C circuits designed to resonate at one or more nuclear frequencies. The probes used are of three basic types: (1) single-tuned, (2) double-tuned with two orthogonal coils, and (3) double-tuned with a single r.f. coil. The construction of probes for spinning samples at the magic angle is described elsewhere[12].

B.5.1 Single-Tuned Probes

Figure B.7a is the schematic drawing of a common probe circuit designed to resonate at a single frequency. High-power pulses are input to the probe from one of the transmitters. The tuning capacitor (C_1) is home-built, consisting of an inner cylindrical copper conductor and outer copper bell separated by a teflon dielectric. This capacitor is adjusted by sliding the inner conductor into and out of the dielectric. Matching capacitance (to 50 Ω impedance) is provided by one or more non-magnetic mica or ceramic capacitors (C_2)(commonly used caps include variable miniature ceramic disks manufactured by Erie and small, fixed-value capacitors made by American Technical Ceramics). The sample coil, a solenoid of 5-15 turns, is made from 18 or 20 gauge bare copper wire and has a diameter of 6-7 mm. At 180 MHz, the Q for this type of tuned circuit is typically ~100.

(a) Single-Tuned Probe

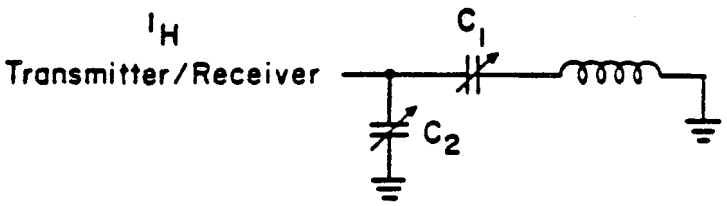

(b) Double-Tuned Probe

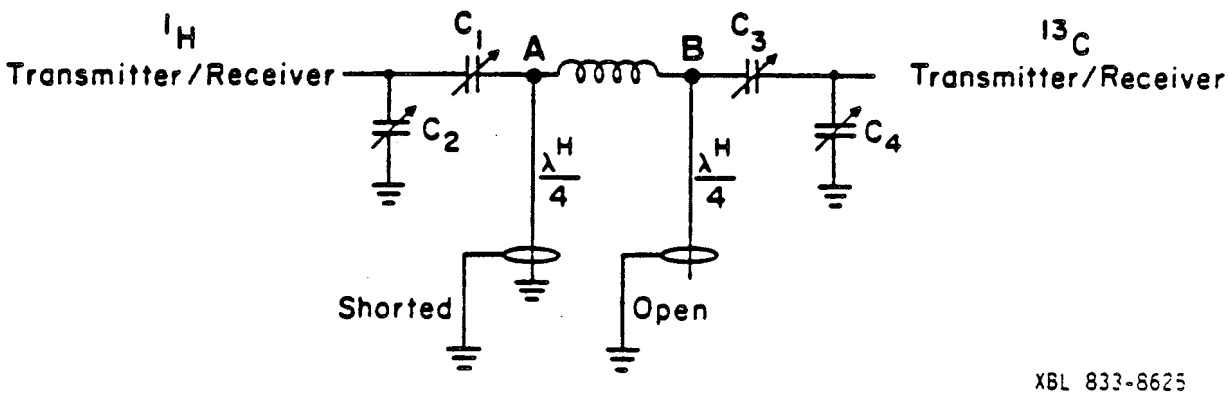

Figure B.7. NMR probes. (a) Single-tuned probe circuit. (b) Double-tuned single-coil circuit.

B.5.2 Double-Tuned Probe

Double resonance experiments, such as those described in Chapters 3 and 5 require a probe tuned to two different frequencies. One possible design makes use of two orthogonal r.f. coils. One tuned circuit in such a probe is identical to Figure B.7a, the other is similar except that a saddle-shaped Helmholtz coil, mounted outside of the proton solenoid,is the inductive element. The two tank circuits in this probe design share a common ground point. When the two r.f. coils are properly adjusted (to ensure orthogonality), good isolation between the two channels may be obtained. When used on the low frequency (X) side, Helmholtz coils are often found to break down at power levels in excess of ~200 watts.

For very high power applications, or when one is trying to accurately match proton and X power levels, it is convenient to adopt a double-tuned, single coil probe design[180,181]. The probe used for experiments in this work employs the transmission line circuit[180] illustrated in Figure B.7b. The tuning (C_1, C_3) and matching (C_2, C_4) capacitors in this circuit, as well as the coil itself, play the same roles as in a single-tuned probe. The two transmission lines are of length $\frac{\lambda^H}{4}$, where λ^H is the wavelength at the proton frequency within the coaxial cable. Point A in this circuit looks like a high impedance at the proton frequency while point B appears to be ground. At the X frequency, where the transmission lines are much less than one-quarter wavelength, the roles of A and B are reversed. In this manner, the same coil may be used for irradiation and/or detection at two different frequencies. Isolation between the two channels can be a problem with this circuit design. In this regard, one often starts with transmission lines which are longer

than $\frac{\lambda^H}{4}$ and trims them down until good isolation is achieved. Although it has been claimed that this probe design optimizes the signal-to-noise ratio at the low frequency at the expense of high frequency performance[182], the sensitivity of the proton channel was adequate for all experiments described herein.

B.5.3 Temperature Regulation

In Appendix A, the dependence of the ordering of a thermotropic liquid crystal on temperature was described. Because of this sensitivity, NMR probes used in studying these systems must be capable of carefully regulating the sample temperature. The probe used in this work has this capability. It is equipped with an evacuated double-walled glass dewar which screws directly onto the probe head. A copper-constantan thermocouple junction measures the temperature near the sample. Air is blown into the probe head by means of an evacuated transfer line which also serves as the probe's support rod. For high temperature studies, an external heater may be used to warm the air while low temperature studies may employ an ice bath, N_2 gas and a dry ice/ethanol bath, or N_2 gas bubbled directly from an ℓ-N_2 dewar for cooling. Fine temperature regulation is achieved by means of a small resistive heater which is placed within the probe's air transfer line. The temperature at the thermocouple junction is monitored by a digital temperature controller (Newport Laboratories). A home-built unit (Electronics Shop DWG 859A1) supplies current to the resistive heater anytime the temperature falls below a preset value. In this way temperature regulation to within $\pm 0.1^{\circ}C$ can be achieved.

B.5.4 Horizontal Sample Spinning

For the liquid studies of Chapter 5, the probe head was modified to

accommodate a horizontal sample spinner. The spinner, constructed of Delrin polymer, is a modification of the double-bearing, double-drive design used for magic angle spinning probes in our lab[12]. Spinning speeds of 0-150 Hz are achievable with this particular spinner. The liquid samples themselves were sealed in 4 mm diameter glass beads (Kontes 897020). Although Delrin sample tubes were machined, optimal resolution (~2 Hz) was obtained by placing the sample bead within a section of standard glass NMR tube fitted with Delrin end caps.

B.5.5 Receiver Protection and Noise Reduction

When high-power pulses are applied to the probe, care must be taken to protect the receiver preamplifier. In addition, the low-level noise produced by the high-power transmitters in their quiescent state can significantly degrade the signal-to-noise of an experiment. The circuit illustrated in Figure B.8 addresses both of these problems. Several crossed diode pairs placed after the bandpass filter help to block the transmitter noise. In practice, diode pairs are usually added until the observed noise level is approximately the same as that seen with the receiver input terminated to ground.

A pair of crossed diodes to ground attached to a quarter wavelength cable at the observed frequency protects the preamplifier. When a pulse is applied, these diodes open and the receiver appears as a high impedance to the transmitter, with the bulk of the power going directly into the probe. Typically a (distorted) signal of 0.5-1.0 V p-p leaks through to the preamp during a pulse.

B.6 Receiver

The gamma's receiver, which is set up for quadrature detection, is of the superheterodyne type. The Larmor frequency serves as a carrier

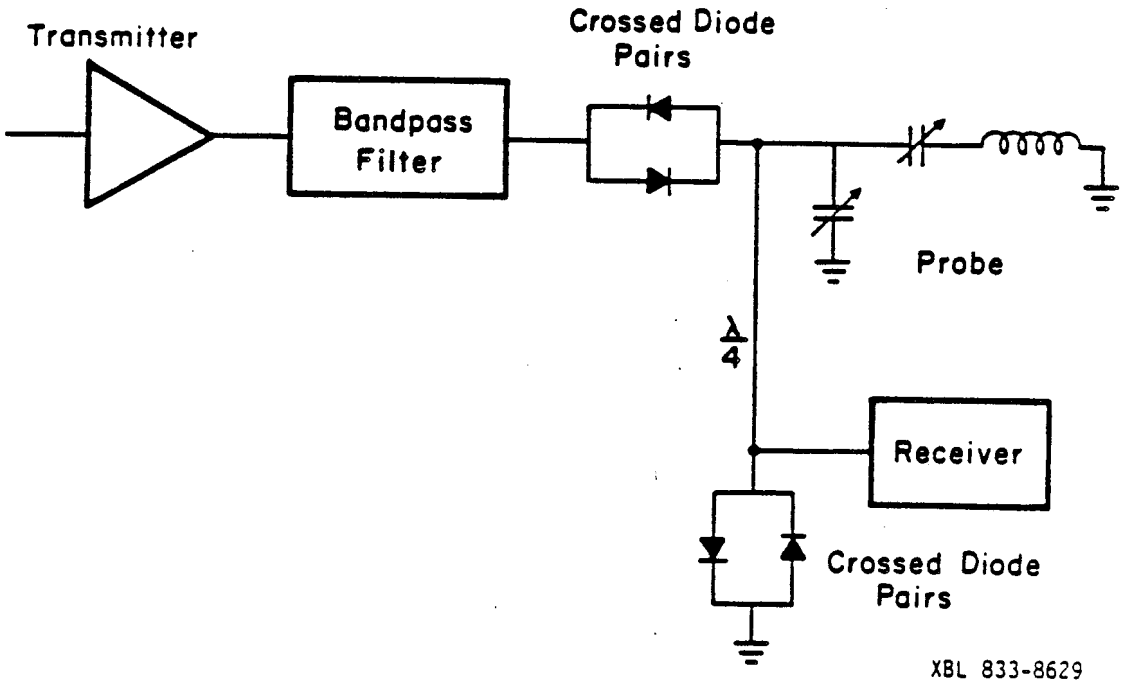

Figure B.8. Receiver protection and noise reduction circuitry.

for the signal of interest and is removed in a two-stage mixing process. The resultant audio frequency signal is a free induction decay in the rotating frame defined by the carrier frequency, ω, of the observed nucleus. By detecting signal in this manner, it is very easy to make the receiver a broadband device capable of detecting any nuclear frequency. The only requirement is that the preamplifier itself be a broadband unit.

B.6.1 Preamplifier/IF Amplifier (Fig. B.9a)

Upon coming from the probe, the nuclear signal is first amplified by a two-stage preamplifier. Since the noise figure of the receiver is almost completely determined by that of the preamp, the choice of preamplifiers is particularly important. The first stage of the preamp is an Avantek UTO 511 (Gain = 15 dB, Noise figure = 2.5 dB), the second stage an Avantek UTO 512 (Gain = 20 dB, Noise figure = 4 dB). Following amplification, the signal is filtered using a bandpass filter centered about the appropriate Larmor frequency. It is then mixed (Anzac MD-143) with the appropriate LO, amplified by a homebuilt amplifier (25 dB @ 30 ± 1 MHz), and sent to an IF strip amplifier (RHG Electronics Laboratory, EVT3010). This amplifier provides 20 dB of fixed gain plus 50 dB of variable gained controlled by a front panel-mounted potentiometer. The output of the IF strip is filtered (Texscan 4BM30/3-CC) and goes to the Phase Sensitive Detector.

B.6.2 Phase Sensitive Detector (Fig. B.9b)

At this point the signal of interest is riding upon a 30 MHz IF carrier. It is next split into two channels (Anzac TU-50), each of which is then input into an Anzac MD-143 mixer. The 30 MHz reference IF (Fig. B.3) goes through a variable delay line and is split into two

RECEIVER

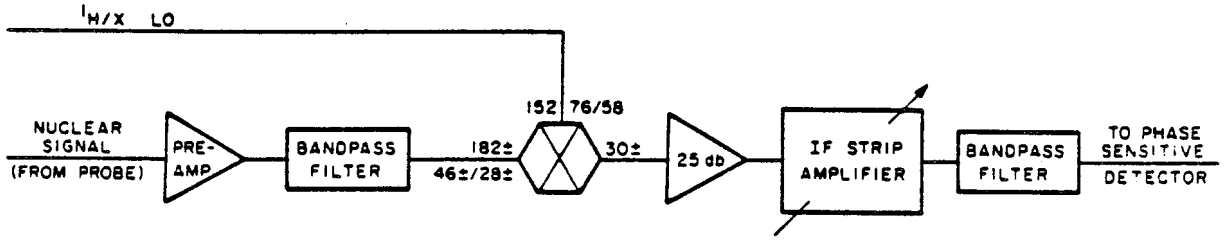

PHASE SENSITIVE DETECTOR

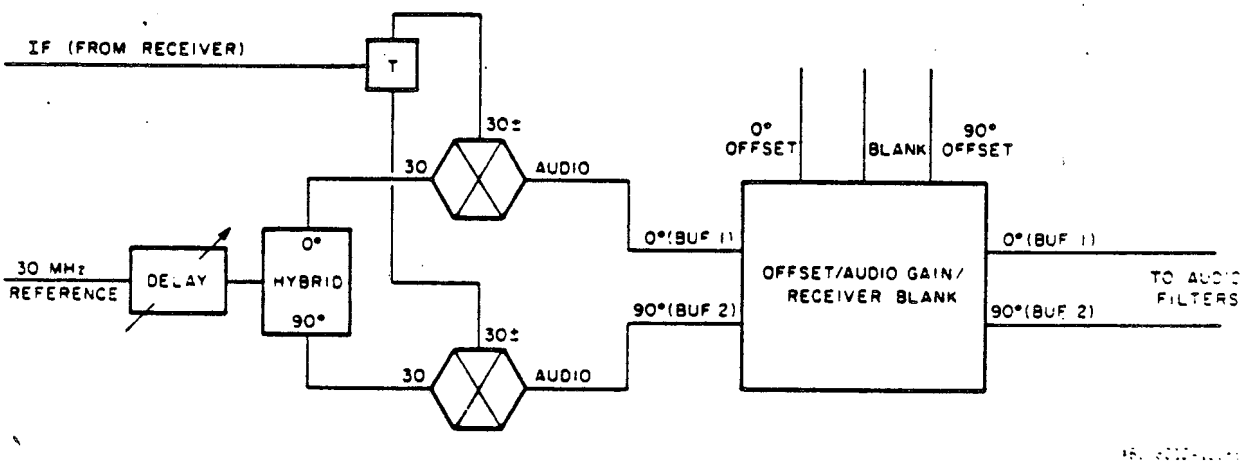

Figure B.9. (a) Receiver: Preamplifier/IF Amplifier.
(b) Phase-sensitive Detector. One channel of the box labeled Offset/Audio Gain/Receiver Blank is illustrated in Figure B.10.

channels (Anzac JH-127) having relative phases of 0° and 90°. Each of these channels becomes the second input to one of the above-mentioned mixers. The outputs of these mixers form two channels of audio signal, designated as 0°(Buffer 1) and 90°(Buffer 2) which then feed into the Offset/Audio Gain/Receiver Blank box.

B.6.3 Offset/Audio Gain/Receiver Blank

One of the two channels of the Offset/Audio Gain/Receiver Blank box is shown in Figure B.10. As its name implies, this box performs several different functions. Frontpanel-mounted potentiometers allow the d.c. offsets of the two channels of audio signal to be individually adjusted. In addition, this box provides a fixed amount of audio gain and contains two junction-FET analog switches for receiver blanking. These switches are normally open and must be closed by applying a HI TTL level (from the pulse programmer) to allow signal to be sampled.

The two channels of audio frequency signal then go to a set of audio filters (Rockland 452 Dual HI/LO). These filters have a maximum cutoff frequency of 100 kHz and provide 20 dB of switchable, optional gain. The output of the audio filters is sent directly to the Data Acquisition System.

B.7 Data Acquisition System

Figure B.11 provides an overview of the gamma's Data Acquisition System while Figure B.12 focuses in on the sample-and-hold and analog-to-digital converter (ADC) associated with each of the data channels. Signal from the output of the audio filters is input to the sample-and-hold (DATEL SHM-2). When a sampling pulse (TP1 from pulse programmer) is given, it causes the SHM-2 to hold its voltage level, which is then digitized by the ADC (Datel ADC-EH10B). This conversion process takes

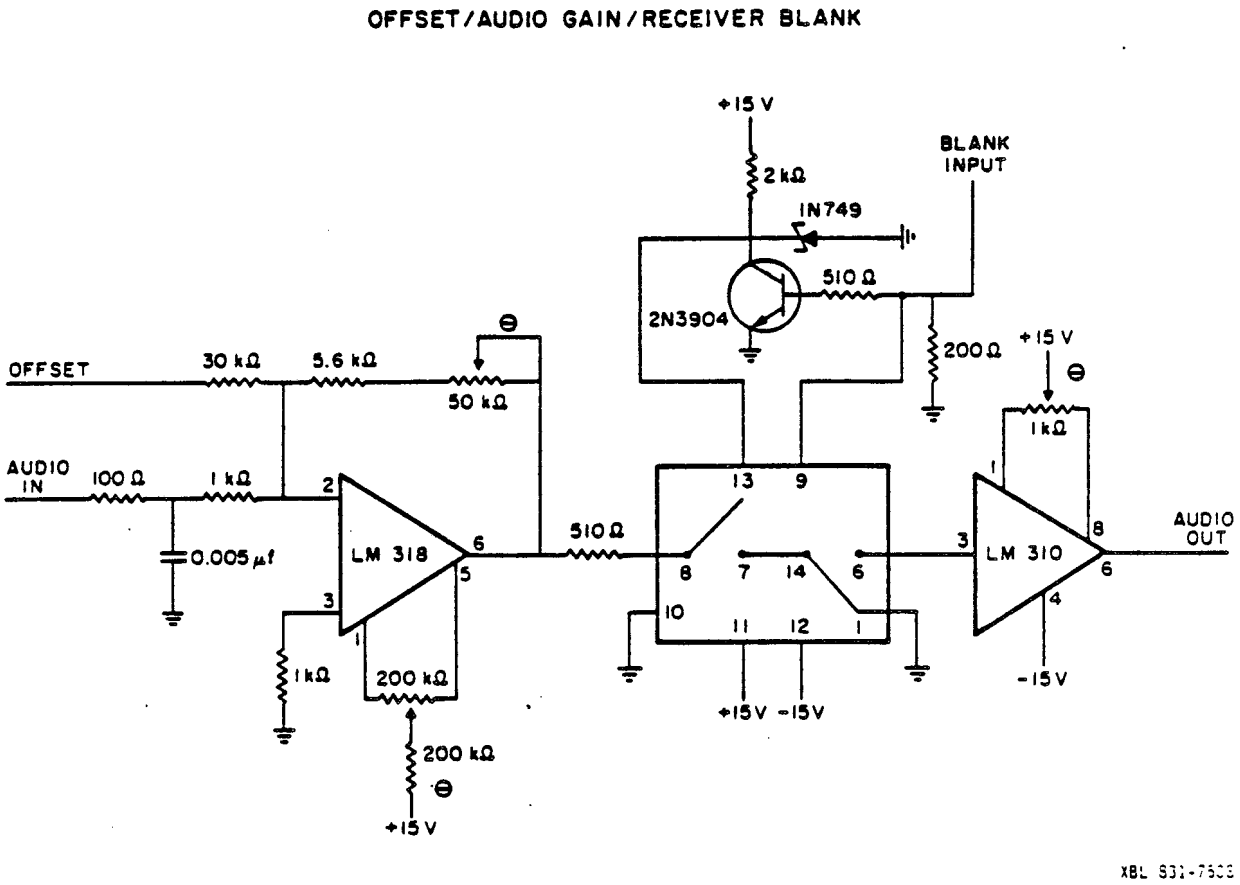

Figure B.10. Offset/Audio Gain/Receiver Blank box is part of the Phase-sensitive Detector shown in Figure B.9.

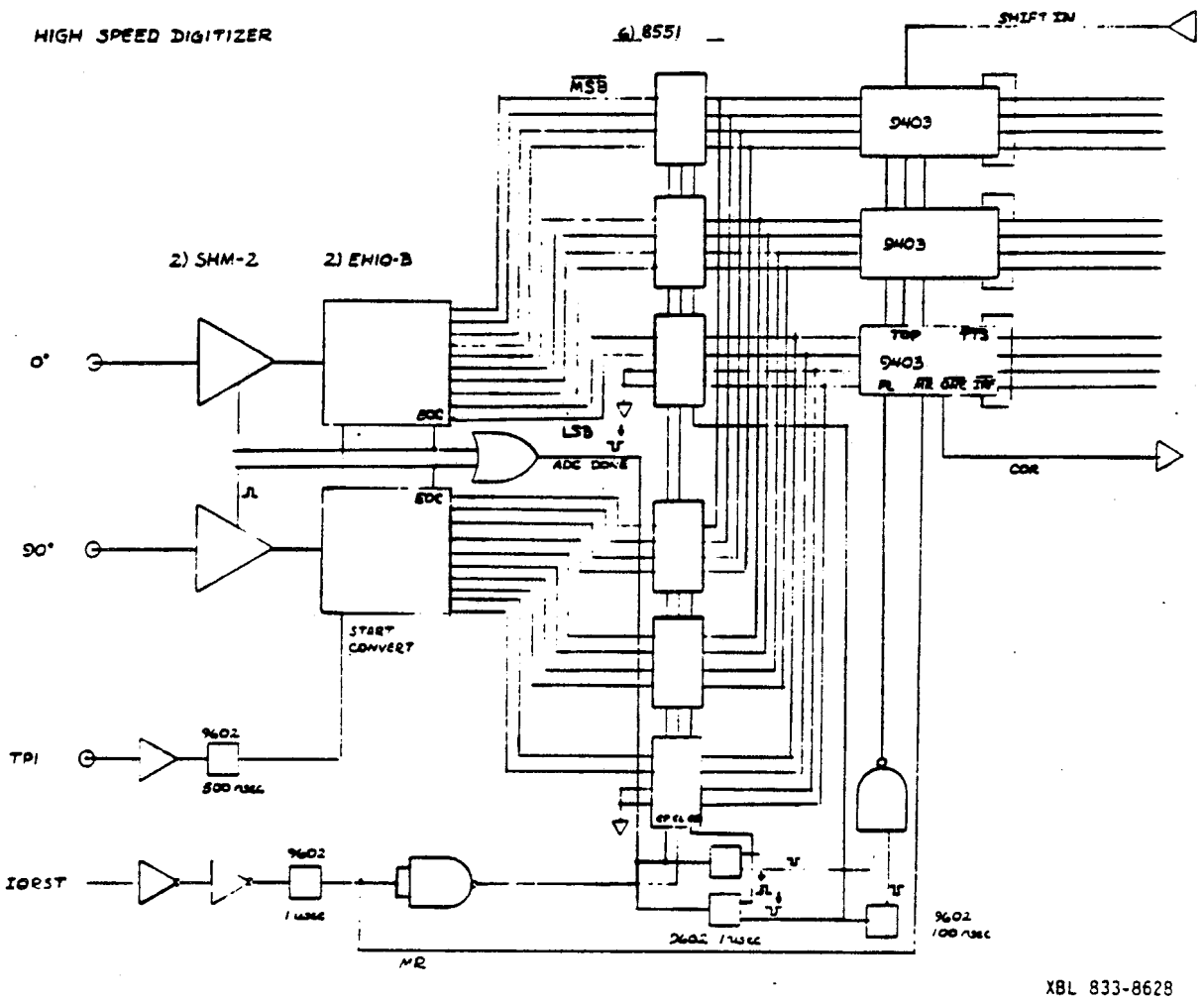

Figure B.11. Data Acquisition System. (Figure courtesy of Gary Drobny.)

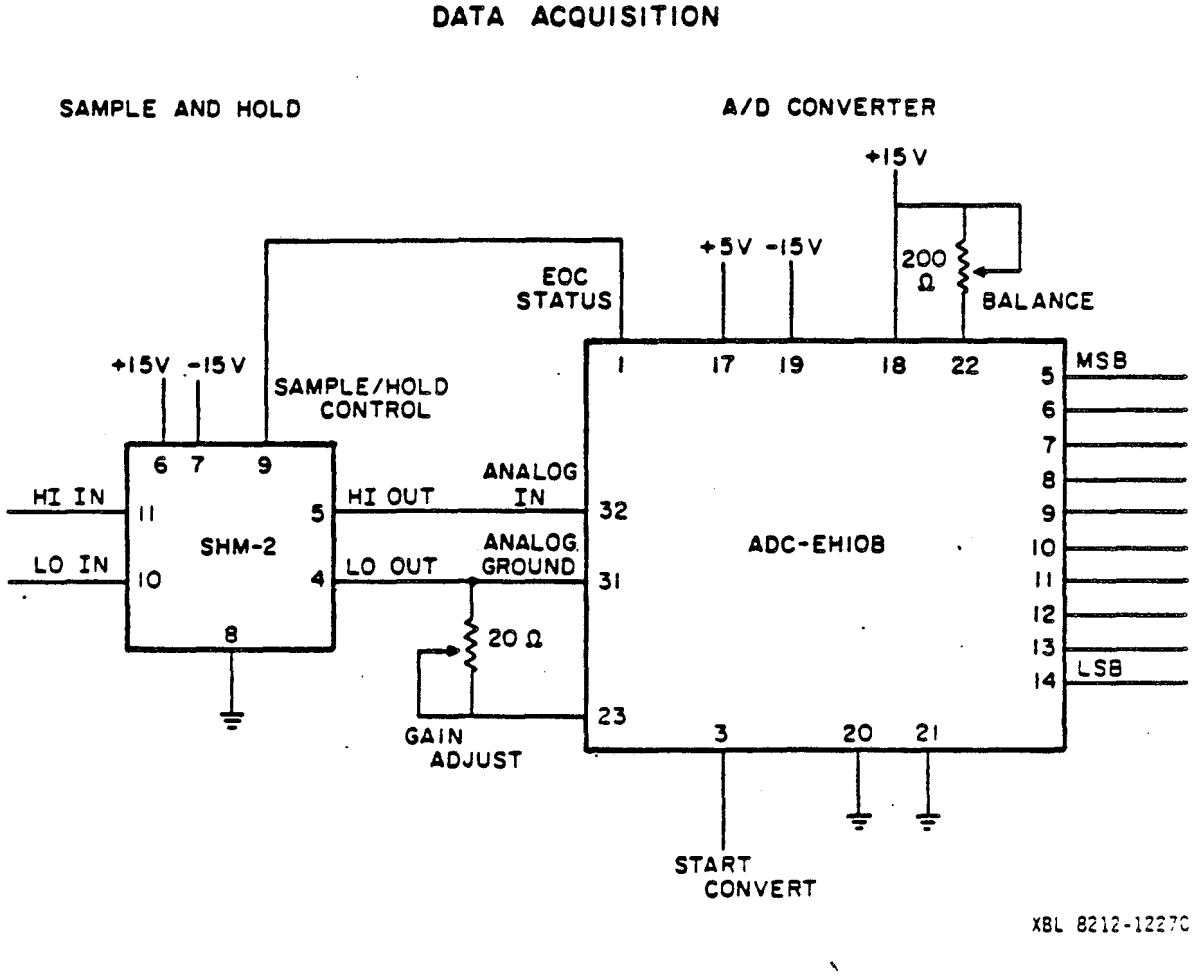

Figure B.12. Sample-and-Hold and Analog-to-Digital Converter. A closer look at a portion of the Data Acquisition System (Fig. B.11).

approximately 2 μsec, after which the SHM-2 goes back into sampling mode. The ADC-EH10B is a 10-bit ADC operated in bipolar mode which can accept analog signals within the range -5 V → +5 V.

The remainder of the circuitry of Figure B.11 is concerned with the transfer of the 10-bit digital words into the computer memory. The process, which involves taking the parallel outputs of the two ADC's and reading them into the computer in serial fashion has been described in detail[50]. The requirements of digitization and data transfer limit the maximum sampling rate to one complex data point every 5 μsec.

B.8 Digitally Controlled Phase Shifter

The Quadrature Generator (Fig. B.5) is capable of producing pulses having relative phases of 0°, 90°, 180°, and 270°. Often, multiple quantum experiments require pulses of other phases, however. Examples include experiments involving TPPI or PPPI, as well as those employing selective excitation sequences, as described previously. To accomplish these, the gamma has available a digitally controlled phase shifter (Daico 100D0898-30) which can generate phase shifts in units of $2\pi/256$ radians. The phase shifter, which operates at 30 MHz, produces a phase shift between its input and output which is specified by an 8-bit digital word. It has a settling time of approximately 2 μsec and is displayed schematically in Figure B.13.

The controller board for generating the appropriate 8-bit digital word is shown in Figures B.14 and B.15. The phase box can be operated in either of two different modes. In Manual mode, the phase shift $\Delta\phi$ is determined by the Manual set thumbwheel switches, with available settings ranging from $0\text{-}377_8$.

In Increment mode, the 8-bit word is the sum of control words from

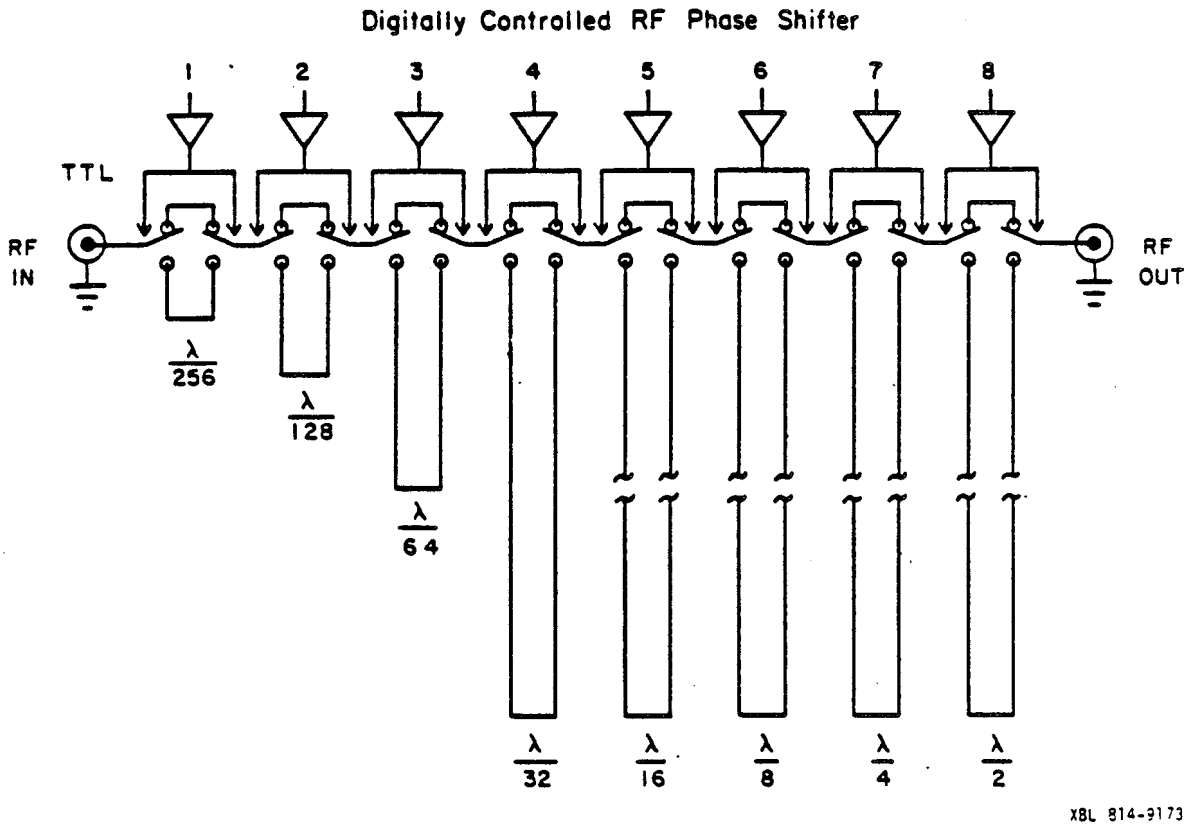

Figure B.13. Schematic representation of the Daico variable phase-shift unit. Phase-shifts, which are specified by an 8-bit digital control word, are generated by switching-in delay-line segments of appropriate lengths.

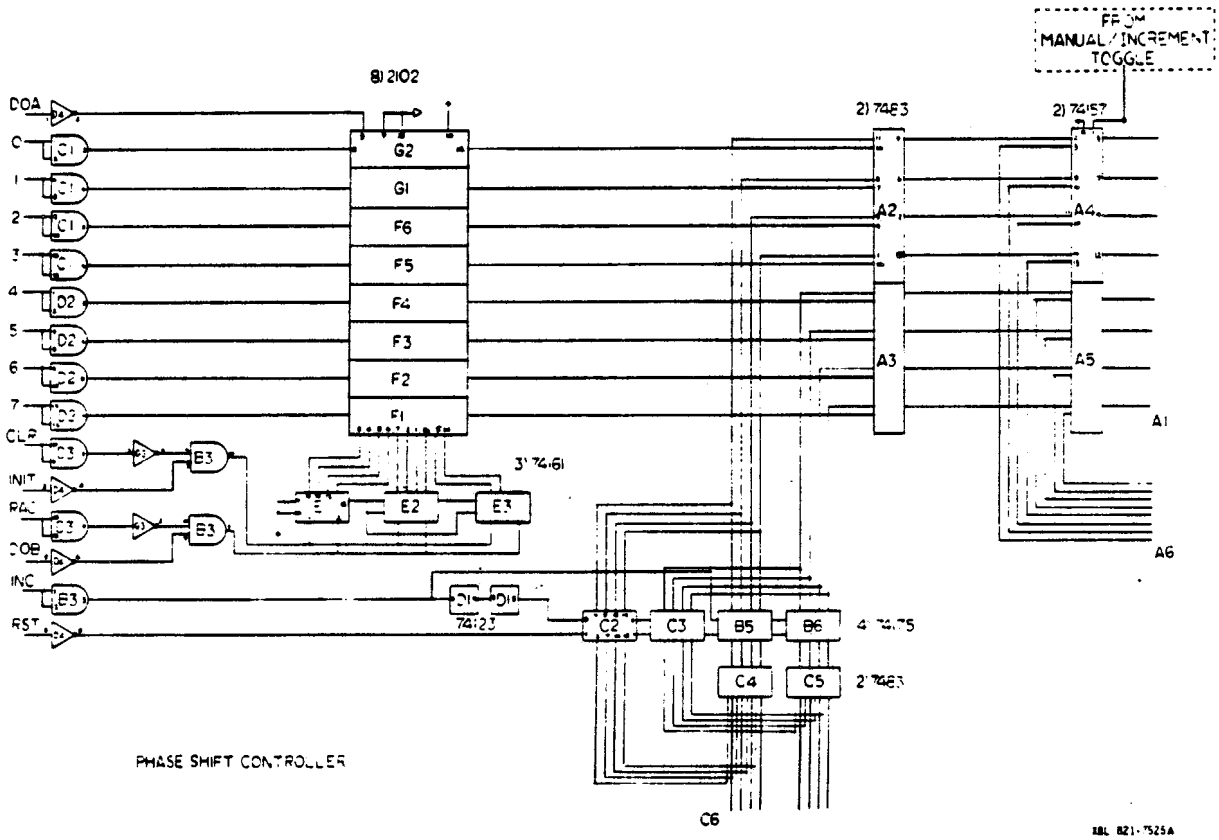

Figure B.14. Phase Box Controller Board. The box labeled "From Manual/ Increment Toggle" refers to the circuit shown in Figure B.15. (Figure courtesy of Gary Drobny.)

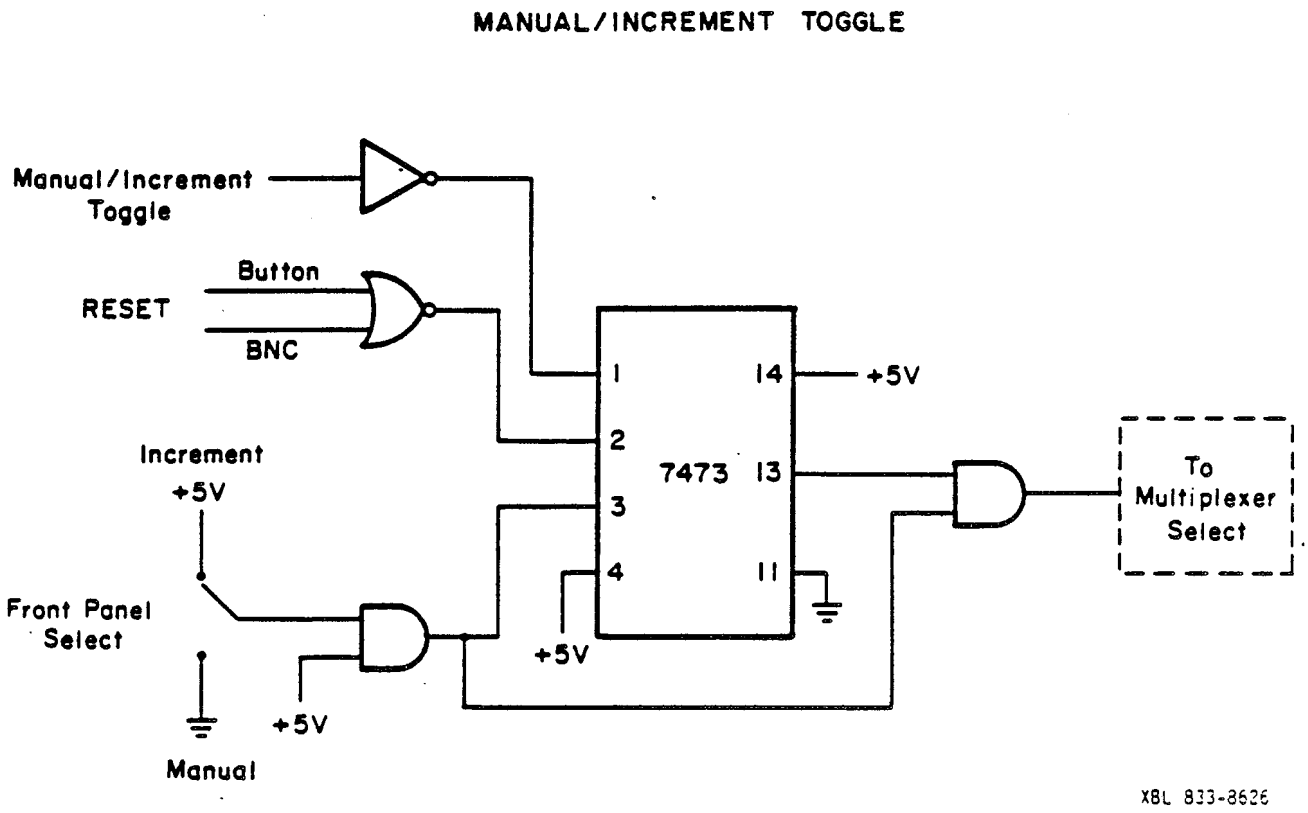

Figure B.15. Manual/Increment Toggle circuit controls the Multiplexer Select line on the Phase Box Controller Board (Fig. B.14).

two independent circuits: (1) an increment counter and (2) a RAM. The increment counter is stepped by an amount determined by the Increment thumbwheel switches each time the backpanel INC is strobed. This counter is reset to 0 by pulsing the backpanel RESET and is constructed as a "wrap-around" addition circuit so that overflows are automatically handled correctly. TPPI experiments are easily carried out in this way, with $\Delta\phi$ chosen as discussed in Section 2.4.2.2.

When a more intricate series of phase shifts is required, the available RAM circuitry can be used. The phase box RAM can accommodate a total of 1024 8-bit words. At the present time these must be loaded individually by hand, though a computer interface is planned. The RAM address counter is reset by strobing the backpanel RAC INIT, and is incremented with a pulse to the backpanel RAM. Any arbitrary pattern of phases may be programmed into and clocked out of the RAM. The 8-bit control word is always the sum of the current value of the increment counter and the current RAM word. A more detailed discussion of the phase box has been provided[50].

As currently configured, the proton IF feeds through the phase box immediately before being quadratured into four orthogonal phases (Fig. B.4). This is convenient for multiple quantum preparation sequences which require two or more different phases. However, some way is needed to switch between phase-shifted preparation period pulses and fixed-phase mixing period pulses. To do this, the toggle circuitry of Figure B.15 has been installed. Whenever the front panel select is set to Manual, the phase is determined by the value of the Manual set switches. In Increment mode, the control word can be toggled between the sum (Increment counter + RAM word) and the value of the Manual set switches by means of the backpanel Manual/Increment Toggle. In a typical multiple

quantum experiment, two toggle pulses are required per shot. The first, following the preparation period, toggles from phase-shifted to constant-phase pulses and the second, after the mixing period, restores the phase box to Increment mode before the next shot. The toggle circuitry can be reset by strobing the backpanel Manual/Increment Reset or by depressing the red frontpanel button.

Appendix C: EXPANSION OF TRIGONOMETRIC FUNCTIONS INVOLVING SPIN OPERATORS

As discussed in Section 5.1.1, the propagator $U(t) = \exp(-iJ'_{IS}I_pS_bt)$ appears to S angular momentum operators as a rotation about the "b"-axis. The effect of this propagator on the operator S_a was given in Equation 5.5b as:

$$U(t)S_a\,U^{-1}(t) = S_a\cos(I_pJ'_{IS}t) - S_c\sin(I_pJ'_{IS}t) \qquad (C.1)$$

In order to simplify this expression further we must expand the trigonometric functions. These expansions require that the number of equivalent I spins (protons) coupled to the S spin (^{13}C) be taken into account. This appendix sketches the expansion of $\sin(I_pJ'_{IS}t)$ and $\cos(I_pJ'_{IS}t)$ for IS, I_2S, and I_3S spin systems.

C.1 IS

For an IS spin system,

$$I_p^2 = \frac{1}{4} \qquad (C.2a)$$

$$I_p^3 = \frac{1}{4}I_p \qquad (C.2b)$$

or, more generally,

$$I_p^n = 2^{-n} \qquad \text{for n even} \qquad (C.3a)$$

$$I_p^n = 2^{(1-n)}I_p \qquad \text{for n odd.} \qquad (C.3b)$$

Substituting these identities into the power series expansions for sine and cosine yields Equations 5.6a and b:

$$\cos(I_pJ'_{IS}t) = \cos\left(\frac{J'_{IS}t}{2}\right) \qquad (C.4a)$$

$$\sin(I_p J'_{IS} t) = 2I_p \sin\left(\frac{J'_{IS} t}{2}\right) . \qquad (C.4b)$$

C.2 $\underline{I_2S}$

For the I_2S system,

$$I_p = I_{p1} + I_{p2} \qquad (C.5a)$$

$$I_p^2 = \frac{1}{2} + 2I_{p1}I_{p2} \qquad (C.5b)$$

or, more generally,

$$I_p^{(2n+1)} = I_p \qquad (C.6a)$$

$$I_p^{2n} = \frac{1}{2} + 2I_{p1}I_{p2}, \; n > 0. \qquad (C.6b)$$

Substituting these expressions into sine and cosine expansions yields Equations 5.6c and d:

$$\cos(I_p J'_{IS} t) = 1 + (\frac{1}{2} + 2I_{p1}I_{p2})(\cos J'_{IS} t - 1) \qquad (C.7a)$$

$$\sin(I_p J'_{IS} t) = I_p \sin(J'_{IS} t). \qquad (C.7b)$$

C.3 $\underline{I_3S}$

Finally, we consider the I_3S spin system, for which

$$I_p = I_{p1} + I_{p2} + I_{p3} = (I_{p1} + I_{p2}) + I_{p3}. \qquad (C.8)$$

The grouping together of I_{p1} and I_{p2} in this equation allows us to expand the sine and cosine terms using the trigonometric identities

$$\sin(x+y) = \sin(x)\cos(y) + \sin(y)\cos(x) \qquad (C.9a)$$

$$\cos(x+y) = \cos(x)\cos(y) - \sin(x)\sin(y) \qquad (C.9b)$$

to give

$$\cos(I_p J'_{IS} t) = \cos(J'_{IS} t(I_{p1} + I_{p2}))\cos(I_{p3} J'_{IS} t) - \sin(J'_{IS} t(I_{p1} + I_{p2}))\sin(I_{p3} J'_{IS} t) \quad \text{(C.10a)}$$

$$\sin(I_p J'_{IS} t) = \sin(J'_{IS} t(I_{p1} + I_{p2}))\cos(I_{p3} J'_{IS} t) + \cos(J'_{IS} t(I_{p1} + I_{p2}))\sin(I_{p3} J'_{IS} t). \quad \text{(C.10b)}$$

Equations (C.4) and (C.7) may now be used to expand the individual sine and cosine terms of Equation C.10:

$$\cos(I_p J'_{IS} t) = [(\tfrac{1}{2})(1 + \cos J'_{IS} t) + 2I_{p1} I_{p2}(\cos J'_{IS} t - 1)]\cos\left(\frac{J'_{IS} t}{2}\right) - 2(I_{p1} + I_{p2}) I_{p3} \sin\left(\frac{J'_{IS} t}{2}\right) \sin(J'_{IS} t), \quad \text{(C.11a)}$$

$$\sin(I_p J'_{IS} t) = (I_{p1} + I_{p2})\sin(J'_{IS} t)\cos\left(\frac{J'_{IS} t}{2}\right) + I_{p3}(1 + \cos J'_{IS} t)\sin\left(\frac{J'_{IS} t}{2}\right) + 4\, I_{p1} I_{p2} I_{p3}(\cos J'_{IS} t - 1)\sin\left(\frac{J'_{IS} t}{2}\right). \quad \text{(C.11b)}$$

Application of the double angle formulas

$$\sin(2x) = 2\sin(x)\cos(x) \quad \text{(C.12a)}$$

$$\cos(2x) = 1 - 2\sin^2(x) \quad \text{(C.12b)}$$

and collection of terms yields the final results given in Equations 5.6e and f:

$$\cos(I_p J'_{IS} t) = \cos^3\left(\frac{J'_{IS} t}{2}\right) - 4(I_{p1}I_{p2} + I_{p1}I_{p3} + I_{p2}I_{p3})\sin^2\left(\frac{J'_{IS} t}{2}\right)\cos\left(\frac{J'_{IS} t}{2}\right), \tag{C.13a}$$

$$\sin(I_p J'_{IS} t) = 2\, I_p \sin\left(\frac{J'_{IS} t}{2}\right)\cos^2\left(\frac{J'_{IS} t}{2}\right) - 8\, I_{p1}I_{p2}I_{p3}\sin^3\left(\frac{J'_{IS} t}{2}\right). \tag{C.13b}$$

Appendix D: BILINEAR π ROTATION INVERSION EFFICIENCIES

In Section 5.3.3 simple and compensated bilinear π rotations were compared with respect to their sensitivities to missets of the bilinear nutation angle $\theta(\theta = \pi J_{IS} t)$. For the experiment of Figure 5.7a, the size of the observed satellite proton signal provides a measure of the degree to which the bilinear rotation takes the operator $I_+ = I_x + iI_y$ into $I_- = I_x - iI_y$. Equations (5.25a and b) gave theoretical expressions for this inversion efficiency as a function of θ. In this appendix, these two equations are derived.

D.1 Simple Bilinear π Rotation

The propagator $U(\theta)$ for the simple bilinear π rotation

$$U(\theta) = \exp(-i2\theta I_x S_z). \tag{D.1}$$

Its effect on the operator I_+ is easily calculated:

$$\exp(-i2\theta I_x S_z) I_+ \exp(i2\theta I_x S_z) = I_x + iI_y \cos(\theta) + 2iS_z I_z \sin\theta \tag{D.2a}$$

$$= cI_- + dI_+. \tag{D.2b}$$

The inversion efficiency is given by the coefficient c of this equation, which can be computed as

$$c = \frac{\mathrm{Tr}(I_+(I_x + iI_y \cos\theta))}{\mathrm{Tr}(I_+ I_-)}. \tag{D.3}$$

The traces in Equation D.3 can be simplified as follows:

$$\mathrm{Tr}(I_+ I_-) = 2\mathrm{Tr}(I_x^2) \tag{D.4a}$$

$$\mathrm{Tr}(I_+(I_x + iI_y\cos\theta)) = \mathrm{Tr}(I_x^2 - \cos\theta I_y^2)$$

$$= [\mathrm{Tr}(I_x^2)](1-\cos\theta), \qquad \text{(D.4b)}$$

giving the coefficient c as (Eq. 5.25a):

$$c = (\tfrac{1}{2})(1-\cos\theta). \qquad \text{(D.5)}$$

D.2 Compensated Bilinear π Rotation

For the compensated bilinear π rotation, the propagator $U(\theta)$ is

$$U(\theta) = \exp(-i\theta I_x S_z)\exp(-i2\theta I_y S_z)\exp(-i\theta I_x S_z). \qquad \text{(D.6)}$$

Its effect on the operator I_+ is most easily calculated by considering the three factors on the right hand side of Equation D.6 sequentially:

$$\exp(-i\theta I_x S_z) I_+ \exp(i\theta I_x S_z) = I_x + iI_y\cos(\tfrac{\theta}{2}) + 2iI_z S_z \sin(\tfrac{\theta}{2}), \qquad \text{(D.7a)}$$

$$\exp(-i2\theta I_y S_z)[I_x + iI_y\cos(\tfrac{\theta}{2}) + 2iI_z S_z \sin(\tfrac{\theta}{2})]\exp(i2\theta I_y S_z)$$

$$= I_x(\cos\theta + i\sin\theta\sin(\tfrac{\theta}{2})) + iI_y\cos(\tfrac{\theta}{2}) + 2I_z S_z(i\sin(\tfrac{\theta}{2})\cos\theta - \sin\theta), \qquad \text{(D.7b)}$$

$$\exp(-i\theta I_x S_z)[I_x(\cos\theta + i\sin\theta\sin(\tfrac{\theta}{2})) + iI_y\cos(\tfrac{\theta}{2}) + 2I_z S_z(i\sin(\tfrac{\theta}{2})\cos\theta - \sin\theta)]$$

$$\times \exp(i\theta I_x S_z)$$

$$= I_x(\cos\theta + i\sin\theta\sin(\tfrac{\theta}{2})) + I_y(i\cos^2(\tfrac{\theta}{2}) - i\sin^2(\tfrac{\theta}{2})\cos\theta + \sin\theta\sin(\tfrac{\theta}{2}))$$

$$+ 2I_z S_z(i\sin(\tfrac{\theta}{2})\cos(\tfrac{\theta}{2})(1+\cos\theta) - \sin\theta\cos(\tfrac{\theta}{2})). \qquad \text{(D.7c)}$$

As before, the coefficient of I_-, c, can be computed as

$$c = \frac{\mathrm{Tr}[I_+(U(\theta)I_+U^\dagger(\theta))]}{\mathrm{Tr}(I_+I_-)}. \qquad \text{(D.8)}$$

The trace in the numerator of Equation D.8 can be simplified as follows:

$$\mathrm{Tr}[I_+(U(\theta)I_+U^+(\theta))] = \mathrm{Tr}(I_x^2)(\cos\theta + i\sin\theta\ \sin(\tfrac{\theta}{2}))$$

$$+ i\mathrm{Tr}(I_y^2)(i\cos^2(\tfrac{\theta}{2}) - i\sin^2(\tfrac{\theta}{2})\cos\theta + \sin\theta\ \sin(\tfrac{\theta}{2})), \quad \text{(D.9)}$$

giving the coefficient c as

$$c = (\tfrac{1}{2})[(\cos\theta + \sin^2(\tfrac{\theta}{2})\cos\theta - \cos^2(\tfrac{\theta}{2})) + 2i(\sin\theta\ \sin(\tfrac{\theta}{2}))]. \quad \text{(D.10)}$$

The magnitude of this coefficient, which gives the inversion efficiency of the compensated π rotation, is (Eq. 5.25b):

$$\tfrac{1}{2}\ [(\cos\theta(1+\sin^2(\tfrac{\theta}{2}))\ -\ \cos^2(\tfrac{\theta}{2}))^2 + (2\sin\theta\sin(\tfrac{\theta}{2}))^2]^{\frac{1}{2}} \quad \text{(D.11)}$$

REFERENCES

1. F. Bloch, W. W. Hansen, and M. Packard, Phys. Rev., 70, 474 (1946).

2. E. M. Purcell, H. C. Torrey, R. Pound, Phys. Rev., 69, 37 (1946).

3. A. Abragam, The Principles of Nuclear Magnetism, (Oxford, London, 1963).

4. C. Slichter, Principles of Magnetic Resonance, 2nd Ed., (Springer-Verlag, Berlin, 1978).

5. J. W. Emsley, J. Feeney, and L. H. Sutcliffe, High Resolution Nuclear Magnetic Resonance Spectroscopy, (Pergamon Press, Oxford, 1965). (2 vols.)

6. M. Mehring, Principles of High Resolution NMR in Solids, 2nd Ed., (Springer-Verlag, Berlin, 1983).

7. U. Fano, Revs. Mod. Phys., 29, 74 (1957); D. Ter Haar, Report of Progress in Physics, 24, 304 (1961).

8. R. C. Tolman, The Principles of Statistical Mechanics, (Oxford University Press, London, 1938).

9. J. von Neumann, Mathematical Foundations of Quantum Mechanics, (Princeton University Press, 1955).

10. F. J. Dyson, Phys. Rev., 75, 486 (1949).

11. U. Haeberlen, "High Resolution NMR in Solids: Selective Averaging," Advances in Magnetic Resonance, Supplement 1, (Academic Press, New York, 1976.)

12. R. Eckman, "Hydrogen and Deuterium NMR of Solids by Magic Angle Spinning," Ph.D. Dissertation, University of California, Berkeley, 1982 (published as Lawrence Berkeley Laboratory Report LBL-14200).

13. Y. S. Yen, "Multiple-Quantum NMR in Solids," Ph.D. Dissertation, University of California, Berkeley, 1982 (published as Lawrence Berkeley Laboratory Report LBL-15253).

14. J. W. Emsley and J. C. Lindon, NMR Spectroscopy Using Liquid Crystal Solvents, (Pergamon Press, Oxford, 1975).

15. P. Diehl and C. L. Khetrapal, "NMR Studies of Molecules Oriented in the Nematic Phase of Liquid Crystals," NMR Basic Principles and Progress, Vol. 1, (Springer-Verlag, Berlin, 1969).

16. A. Saupe and G. Englert, Phys. Rev. Lett., 11, 462 (1963).

17. G. Englert and A. Saupe, Z. Naturforsch, 19a, 172 (1964).

18. A. Pines, D. Wemmer, J. Tang, and S. Sinton, Bull. Am. Phys. Soc., 23, 21 (1978).

19. G. Drobny, A. Pines, S. Sinton, D. P. Weitekamp, and D. Wemmer, Faraday Division of the Chemical Society Symposium, 13, 49 (1979).

20. W. S. Warren, D. P. Weitekamp, and A. Pines, J. Chem. Phys., 73, 2084 (1980).

21. D. P. Weitekamp, "Time Domain Multiple Quantum NMR," Advances in Magnetic Resonance, Vol. 12, in press.

22. A. Wokaun and R. R. Ernst, Mol. Phys., 36, 317 (1978).

23. P. L. Corio, Structure of High Resolution NMR Spectra, (Academic Press, New York, 1966).

24. R. R. Ernst, W. P. Aue, E. Bartholdi, A. Höhener, and S. Schäublin, Pure Appl. Chem., 37, 47 (1974).

25. W. A. Anderson, Phys Rev., 104, 850 (1956).

26. J. I. Kaplan and S. Meiboom, Phys. Rev., 106, 499 (1957).

27. S. Yatsiv, Phys. Rev., 113, 1522 (1959).

28. G. Bodenhausen, "Multiple-Quantum NMR," Progress in NMR Spectroscopy, Vol. 14, (Pergamon Press, Oxford, 1981).

29. M.Hammermesh, Group Theory, (Addison-Wesley, Reading, 1962).

30. M. Tinkham, Group Theory and Quantum Mechanics, (McGraw-Hill, New York, 1964).

31. W. S. Warren and A. Pines, J. Am. Chem. Soc., 103, 1613 (1981).

32. B. L. Silver, Irreducible Tensor Methods, (Academic Press, New York 1976).

33. A. R. Edmonds, Angular Momentum in Quantum Mechanics, (Princeton University Press, Princeton, 1960).

34. M. E. Rose, Elementary Theory of Angular Momentum, (Wiley and Sons, New York, 1957).

35. H. Tanaka, T. Terao, and T. Hashi, J. Phys. Soc. Japan, 39, 835 (1975).

36. H. Tanaka and T. Hashi, J. Phys. Soc. Japan, 39, 1139 (1975).

37. A. Wokaun and R. R. Ernst, Chem. Phys. Lett., 52, 407 (1977).

38. S. Vega and Y. Naor, J. Chem. Phys., 75, 75 (1981).

39. S. Vega, J. Chem. Phys., 68, 5518 (1978).

40. A. Wokaun and R. R. Ernst, Mol. Phys., 38, 1579 (1979).

41. G. Bodenhausen, R. L. Vold, and R. R. Vold, J. Magn. Reson., 37, 93 (1980).

42. S. Sinton and A. Pines, Chem. Phys. Lett., 76, 263 (1980).

43. J. Tang and A. Pines, J. Chem. Phys., 72, 3290 (1980).

44. G. Drobny, A. Pines, S. Sinton, W. S. Warren, and D. P. Weitekamp, Phil. Trans. Royal Soc. London, A299, 585 (1981).

45. Y. S. Yen and A. Pines, J. Chem. Phys., 78, 3579 (1983).

46. D. E. Wemmer, "Some Double Resonance and Multiple Quantum NMR Studies in Solids," Ph.D. Dissertation, University of California, Berkeley, 1978 (published as Lawrence Berkeley Laboratory Report LBL-8042).

47. W. S. Warren, "Selectivity in Multiple Quantum Nuclear Magnetic Resonance," Ph.D. Dissertation, University of California, Berkeley, 1980 (published as Lawrence Berkeley Laboratory Report LBL-11885).

48. S. W. Sinton, "NMR Studies of Oriented Molecules," Ph.D. Dissertation, University of California, Berkeley, 1981 (published as Lawrence Berkeley Laboratory Report LBL-13604).

49. J. Tang, "Study of Correlations in Molecular Motion by Multiple Quantum NMR," Ph.D. Dissertation, University of California, Berkeley, 1981 (published as Lawrence Berkeley Laboratory Report LBL-13605).

50. G. Drobny, "NMR Studies of Liquid Crystals and Molecules Dissolved in Liquid Crystal Solvents," Ph.D. Dissertation, University of California, Berkeley, 1982 (published as Lawrence Berkeley Laboratory Report LBL-13736).

51. J. B. Murdoch, "Computer Studies of Multiple Quantum Spin Dynamics," Ph.D. Dissertation, University of California, Berkeley, 1982 (published as Lawrence Berkeley Laboratory Report LBL-15254).

52. J. Jeener, Ampere International Summer School, Basko Polje, Yugoslavia, 1971 (unpublished).

53. W. P. Aue, E. Bartholdi, and R. R. Ernst, J. Chem. Phys., 64, 2229 (1976).

54. R. Freeman and G. Morris, Bull. Mag. Reson., 1, 5 (1979).

55. R. Freeman, Proc. Royal Soc. London, A373, 149 (1980).

56. K. Nagayama, Adv. in Biophysics, 14, 139 (1982).

57. A. Bax, Two-Dimensional Nuclear Magnetic Resonance in Liquids, (Delft University Press, Delft, Holland, 1982).

58. W.-K. Rhim, A. Pines, and J. S. Waugh, Phys. Rev. Lett., 25, 218 (1970).

59. W.-K. Rhim, A. Pines, and J. S. Waugh, Phys. Rev. B, 3, 684 (1971).

60. G. Drobny, S. Sinton, J. Tang, D. Wemmer, D. Weitekamp, and A. Pines, in preparation.

61. J. Murdoch, W. S. Warren, D. P. Weitekamp, and A. Pines, J. Magn. Reson., to be submitted.

62. S. Vega and A. Pines, "Theory of Double-Quantum Coherence and High Resolution Deuterium NMR in Solids," Magnetic Resonance and Related Phenomena, H. Brünner, K. Hausser, and D. Schweitzer, eds., (Beltz-Offsetdruck, West Germany, 1976), p. 395.

63. A. A. Maudsley, A. Wokaun, and R. R. Ernst, Chem. Phys. Lett., 55, 9 (1978).

64. A. Bax, P. G. DeJong, A. F. Mehlkopf, and J. Smidt, Chem. Phys. Lett., 69, 567 (1980).

65. D. P. Weitekamp, J. R. Garbow, J. B. Murdoch, and A. Pines, J. Am. Chem. Soc., 103, 3578 (1981).

66. Y. S. Yen and D. P. Weitekamp, J. Magn. Reson., 47, 476 (1982).

67. A. Wokaun and R. R. Ernst, J. Chem. Phys., 67, 1752 (1977).

68. A. D. Bain and S. Brownstein, J. Magn. Reson., 47, 409 (1982).

69. M. A. Thomas and A. Kumar, J. Magn. Reson., 47, 535 (1982).

70. W. S. Warren, J. B. Murdoch, and A. Pines, J. Magn. Reson., to be submitted.

71. W. S. Warren, S. Sinton, D. P. Weitekamp, and A. Pines, Phys. Rev. Lett., 43, 1791 (1979).

72. W. S. Warren and A. Pines, J. Chem. Phys., 74, 2808 (1981).

73. W. S. Warren and A. Pines, Chem. Phys. Lett., 88, 441 (1982).

74. D. P. Weitekamp, J. R. Garbow, and A. Pines, J. Magn. Reson., 46, 529 (1982).

75. D. Jaffe, R. R. Vold, and R. L. Vold, J. Magn. Reson., 46, 475 (1982).

76. D. P. Weitekamp, J. R. Garbow, and A. Pines, J. Chem. Phys., 77, 2870 (1982).

77. J. S. Waugh, L. Huber, and U. Haeberlen, Phys. Rev. Lett., 20, 180 (1968).

78. U. Haeberlen and J. S. Waugh, Phys. Rev., 175, 453 (1968).

79. J. S. Waugh, Proc. Natl. Acad. Sci., 73, 1394 (1976).

80. R. K. Hester, J. L. Ackerman, V. R. Cross, and J. S. Waugh, Phys. Rev. Lett., 34, 993 (1975).

81. R. K. Hester, V. R. Cross, J. L. Ackerman, and J. S. Waugh, J. Chem. Phys., 63, 3606 (1975).

82. M. E. Stoll, A. J. Vega, and R. W. Vaughan, J. Chem. Phys., 65, 4093 (1976).

83. E. F. Rybaczewski, B. L. Neff, J. S. Waugh, and J. S. Sherfinski, J. Chem. Phys., 67, 1231 (1977).

84. R. W. Vaughan, Ann. Phys. Rev. Chem., 29, 397 (1978).

85. A. Höhener, L. Müller, and R. R. Ernst, Mol. Phys., 38, 909 (1979).

86. M. G. Munowitz, R. G. Griffin, G. Bodenhausen, and T. H. Huang, J. Am. Chem. Soc., 103, 2529 (1981).

87. T. Terao, H. Miura, and A. Saika, J. Chem. Phys., 75, 1573 (1981).

88. K. W. Zilm and D. M. Grant, J. Magn. Reson., 48, 524 (1982).

89. T. Terao, H. Miura, and A. Saika, J. Magn. Reson., 49, 365 (1982).

90. M. G. Munowitz and R. G. Griffin, J. Chem. Phys., 76, 2848 (1982).

91. M. Munowitz, W. P. Aue, and R. G. Griffin, J. Chem. Phys., 77, 1686 (1982).

92. M. G. Munowitz and R. G. Griffin, J. Chem. Phys., 78, 613 (1983).

93. J. Schaefer, E. O. Stejskal, R. A. McKay, and W. T. Dixon, J. Magn. Reson., 52, 123 (1983).

94. W. Magnus, Commun. Pure Appl. Math., 7, 649 (1954).

95. P. Mansfield, M. J. Orchard, D. C. Stalker, and K. H. B. Richards, Phys. Rev. B, 7, 90 (1973).

96. W.-K. Rhim, D. D. Elleman, and R. W. Vaughan, J. Chem. Phys., 58, 1772 (1973).

97. D. P. Burum and W.-K. Rhim, J. Chem. Phys., 71, 944 (1979).

98. D. P. Burum, M. Linder, and R. R. Ernst, J. Magn. Reson., 44, 173 (1981).

99. M. Lee and W. I. Goldberg, Phys. Rev. A, 140, 1261 (1965).

100. J. A. Reimer and R. W. Vaughan, Chem. Phys. Lett., 63, 163 (1979).

101. J. A. Reimer and R. W. Vaughan, J. Magn. Reson., 41, 483 (1980).

102. P. Diehl, H. Bösiger, and H. Zimmermann, J. Magn. Reson., 33, 113 (1979).

103. T. W. Shattuck, "Carbon and Deuterium Nuclear Magnetic Resonance in Solids," Ph.D. Dissertation, University of California, Berkeley, 1976 (published as Lawrence Berkeley Laboratory Report LBL-5458).

104. S. Vega, T. W. Shattuck, and A. Pines, Phys. Rev. A22, 638 (1980).

105. P. Brünner, M. Reinhold, and R. R. Ernst, J. Chem. Phys., 73, 1086 (1980).

106. M. Reinhold, P. Brünner, and R. R. Ernst, J. Chem. Phys., 74, 184 (1981).

107. S. Vega, Phys. Rev. A23, 3152 (1981).

108. M. E. Stoll, A. J. Vega, and R. W. Vaughan, Phys. Rev. A16, 1521 (1977).

109. M. E. Stoll, A. J. Vega, and R. W. Vaughan, J. Chem. Phys., 67, 2029 (1977).

110. P. M. Henrichs and L. J. Schwartz, J. Chem. Phys., 69, 622 (1978).

111. L. Müller, J. Am. Chem. Soc., 101, 4481 (1979).

112. V. W. Miner and J. H. Prestegard, J. Am. Chem. Soc., 103, 5979 (1981).

113. L. Müller, Chem. Phys. Lett., 91, 303 (1982).

114. A. Minoretti, W. P. Aue, M. Reinhold, and R. R. Ernst, J. Magn. Reson., 40, 175 (1980).

115. A. E. Taylor and W. R. Mann, Advanced Calculus, (Wiley and Sons, New York, 1972).

116. S. R. Hartmann and E. L. Hahn, Phys. Rev., 128, 2042 (1962).

117. C. N. Banwell and H. Primas, Mol. Phys., 6, 225 (1962).

118. J. R. Garbow, D. P. Weitekamp, and A. Pines, J. Chem. Phys., submitted for publication.

119. E. L. Hahn, Phys. Rev., 80, 580 (1950).

120. R. Freeman and H. D. W. Hill, J. Chem. Phys., 54, 301 (1971).

121. W. P. Aue, J. Karhan, and R. R. Ernst, J. Chem. Phys., 64, 4226 (1976).

122. A. Kumar and C. L. Khetrapal, J. Magn. Reson., 30, 137 (1978).

123. A. Kumar, J. Magn. Reson., 30, 227 (1978).

124. D. L. Turner, J. Magn. Reson., 46, 213 (1982).

125. I. Solomon, Phys. Rev., 110, 61 (1958).

126. H. A. Buckmaster, R. Chatterjee, and Y. H. Shing, Phys. Stat. Sol(a), 13, 9 (1972).

127. H. Y. Carr and E. M. Purcell, Phys. Rev., 94, 630 (1954).

128. E. O. Stejskal and J. E. Tanner, J. Chem. Phys. 42, 288 (1965).

129. J. F. Martin, L. S. Selwyn, R. L. Vold, and R. R. Vold, J. Chem. Phys., 76, 2632 (1982).

130. D. Zax and A. Pines, J. Chem. Phys., 78, 6333 (1983).

131. A. A. Maudsley and R. R. Ernst, Chem. Phys. Lett., 50, 368 (1977).

132. R. D. Bertrand, W. B. Moniz, A. N. Garroway, and G. C. Chingas, J. Am. Chem. Soc., 100, 5227 (1978).

133. G. C. Chingas, A. N. Garroway, R. D. Bertrand, and W. B. Moniz, J. Magn. Reson., 35, 283 (1979).

134. G. A. Morris and R. Freeman, J. Am. Chem. Soc., 101, 760 (1979).

135. G. A. Morris, J. Am. Chem. Soc., 102, 428 (1980).

136. D. P. Burum and R. R. Ernst, J. Magn. Reson., 39, 163 (1980).

137. G. C. Chingas, A. N. Garroway, R. D. Bertrand, and W. B. Moniz, J. Chem. Phys., 74, 127 (1981).

138. D. T. Pegg, D. M. Dodrell, and M. R. Bendall, J. Chem. Phys., 77, 2745 (1982).

139. D. T. Pegg, D. M. Dodrell, and M. R. Bendall, J. Magn. Reson., 51, 264 (1983).

140. R. Freeman, T. H. Mareci, and G. A. Morris, J. Magn. Reson., 42, 341 (1981).

141. M. R. Bendall, D. T. Pegg, D. M. Dodrell, and J. Field, J. Am. Chem. Soc., 103, 934 (1981).

142. C. LeCocq and J.-E. Lallemand, J. Chem. Soc. Chem. Commun., 12 (1981).

143. M. R. Bendall, D. M. Dodrell, and D. T. Pegg, J. Am. Chem. Soc., 103, 4603 (1981).

144. M. R. Bendall, D. T. Pegg, D. M. Dodrell, and D. M. Thomas, J. Magn. Reson., 46, 43 (1982).

145. A. N. Garroway and G. C. Chingas, J. Magn. Reson., 38, 179 (1980).

146. K. J. Packer and K. M. Wright, J. Magn. Reson., 41, 268 (1980).

147. J. R. Garbow, D. P. Weitekamp, and A. Pines, Chem. Phys. Lett., 93, 504 (1982).

148. Reference 5, Vol. 2.

149. A. W. Overhauser, Phys. Rev., 89, 689 (1953).

150. J. H. Noggle and R. E. Schirmer, The Nuclear Overhauser Effect, Chemical Applications, (Academic Press, New York, 1971).

151. D. T. Pegg, D. M. Dodrell, W. M. Brooks, and M. R. Bendall, J. Magn. Reson., 44, 32 (1981).

152. A. Pines, M. G. Gibby, and J. S. Waugh, J. Chem. Phys., 59, 569 (1973).

153. D. E. Demco, J. Tegenfeldt, and J. S. Waugh, Phys. Rev. B, 11, 4133 (1975).

154. R. Freeman, S. P. Kempsell, and M. H. Levitt, J. Magn. Reson., 38, 453 (1980).

155. M. H. Levitt and R. Freeman, J. Magn. Reson., 43, 65 (1981).

156. M. H. Levitt, J. Magn. Reson., 48, 234 (1982).

157. R. Tycko, Phys. Rev. Lett., submitted for publication.

158. J. Baum, R. Tycko, and A. Pines, J. Chem. Phys., submitted for publication.

159. W. A. Anderson, Phys. Rev., 102, 151 (1956).

160. K. Nagayama, J. Chem. Phys., 71, 4404 (1979).

161. A. Bax, A. F. Mehlkopf, and J. Smidt, J. Magn. Reson., 35, 167 (1979).

162. A. A. Maudsley, L. Müller, and R. R. Ernst, J. Magn. Reson., 28, 463 (1977).

163. G. Bodenhausen and R. Freeman, J. Magn. Reson., 28, 471 (1977).

164. A. Bax, N. M. Szeverenyi, and G. E. Maciel, presented at the 24th Experimental NMR Conference, Asilomar, California, 1983.

165. A. Bax, J. Magn. Reson., 52, 330 (1983).

166. G. W. Gray, Molecular Structure and Properties of Liquid Crystals, (Academic Press, New York, 1962).

167. P. G. deGennes, The Physics of Liquid Crystals, (Clarendon Press, Oxford, 1974).

168. S. Chandrasekhar, Liquid Crystals, (Cambridge University Press, Cambridge, 1977).

169. L. C. Snyder and S. Meiboom, J. Chem. Phys., 44, 4057 (1966).

170. A. Saupe, Z. Naturforsch, 20a, 572 (1965).

171. B. Bhagavantam and D. Suryanarayana, Acta. Cryst., 2, 21 (1949).

172. L. C. Snyder, J. Chem. Phys., 43, 4041 (1965).

173. E. E. Burnell and C. A. deLange, Chem. Phys. Lett., 76, 268 (1980).

174. E. E. Burnell and C. A. deLange, J. Magn. Reson., 39, 461 (1980).

175. J. W. Emsley and G. R. Luckhurst, Mol. Phys., 41, 19 (1980).

176. E. E. Burnell, C. A. deLange, and O. G. Mouritsen, J. Magn. Reson., 50, 188 (1982).

177. R. Ader and A. Loewenstein, Mol. Phys., 24, 455 (1972).

178. R. Ader and A. Loewenstein, Mol. Phys., 30, 199 (1975).

179. S. Sinton, J. R. Garbow, J. L. Ackerman, G. Drobny, D. J. Ruben, and A. Pines, "SPEC-DOC - A User's Guide to Spectrometer Software," (published as Lawrence Berkeley Laboratory Report PUB-3033), 1983.

180. V. R. Cross, R. K. Hester, and J. S. Waugh, Rev. Sci. Instrum., 47, 1486 (1976).

181. M. E. Stoll, A. J. Vega, and R. W. Vaughan, Rev. Sci. Instrum., 48, 800 (1977).

182. F. D. Doty, R. R. Inners, and P. D. Ellis, J. Magn. Reson., 43, 399 (1981).